



Max-Planck-Institut für Metallforschung
Stuttgart

Size and Shape Effects in Bioinspired Fibrillar Adhesives

Christian Greiner

Dissertation
an der
Universität Stuttgart

Bericht Nr. 208
Oktober 2007

Size and Shape Effects in Bioinspired Fibrillar Adhesives

Von der Fakultät Chemie der Universität Stuttgart
zur Erlangung der Würde eines Doktors der
Naturwissenschaften (Dr. rer. nat.) genehmigte Abhandlung

Vorgelegt von
Dipl.-Ing. Christian Greiner
aus Esslingen a.N.

Hauptberichter: Prof. Dr. E. Arzt
Mitberichter: Prof. Dr. F. Aldinger
Tag der mündlichen Prüfung: 30.10.2007

INSTITUT FÜR METALLKUNDE DER UNIVERSITÄT STUTTGART
und
MAX-PLANCK-INSTITUT FÜR METALLFORSCHUNG STUTTGART

Stuttgart, Juli 2007

Wer sich von der Wahrheit nicht besiegen lässt, wird vom Irrtum überwunden.
(Aurelius Augustinus, Confessiones)

Danksagung

Die vorliegende Arbeit wurde von Dezember 2004 bis Juli 2007 am Max-Planck-Institut für Metallforschung in Stuttgart angefertigt. Einige ihrer Teile wurden bereits in wissenschaftlichen Fachzeitschriften publiziert. So finden sich Teile von Kapitel 3 in *Advanced Materials*, die Ergebnisse von Kapitel 4 in *Langmuir* 23 (7), 3495-3502. Kapitel 5 ist bei *Langmuir* zur Veröffentlichung akzeptiert.

Es ist mir ein großes Anliegen an dieser Stelle denjenigen zu danken, die maßgeblich zum Gelingen dieser Arbeit beigetragen haben, sei es im beruflichen oder im privaten Umfeld.

Zu aller erst gilt mein Dank Herrn Prof. E. Arzt, in dessen Abteilung diese Arbeit entstanden ist. Ich bin sehr dankbar für die große Unterstützung, die ich während meiner gesamten Promotion durch ihn erfahren habe sowie für das stete Interesse an meiner Arbeit. Die zahlreichen Diskussionen zu meinen Ergebnissen werde ich als sehr motivierend in Erinnerung behalten.

Herrn Prof. F. Aldinger gilt mein Dank für die freundliche Übernahme des Mitberichtes.

Diese Arbeit wäre nicht das geworden was sie jetzt ist, ohne die großartige Unterstützung, die ich von Seiten meiner Betreuerin Dr. A. del Campo erhalten habe. Ich danke ihr für das sehr angenehme Zusammenarbeiten, dafür wie engagiert sie sich immer wieder für mich und meine Arbeit eingesetzt hat und nicht zuletzt für viele wissenschaftliche Diskussionen und Anregungen.

Vor allem die Entwicklung der in Kapitel 6 vorgestellten „Adhesion Design Maps“ wäre ohne die intensive Zusammenarbeit mit Prof. R. Spolenak von der ETH Zürich nicht möglich gewesen. Ich möchte ihm an dieser Stelle für die fruchtbaren Diskussionen zu diesem Thema und dem der Adhäsion im Allgemeinen herzlich danken.

Im Rahmen meiner Promotion hatte ich die Möglichkeit einige Wochen an der University of California Santa Barbara in Santa Barbara, USA zu verbringen. Diese Zeit mit ihren zahlreichen z.T. durchaus auch herausfordernden Diskussionen hat mir sehr geholfen das Gebiet der Adhäsion tiefer zu verstehen und gab mir wichtige neue Impulse. Hierfür möchte ich mich bei Prof. E. Kramer, Prof. K. Turner, Prof. J. Israelachvili sowie bei Dr. M. Northen bedanken.

Der gesamte experimentelle Teil der vorliegenden Arbeit beruht letztlich auf photolithographisch strukturierten Proben die im Reinraum der Abteilung Prof. von Klitzing des Max-Planck-Institutes für Festkörperforschung hergestellt wurden. Dass mir der Zugang zu dieser Einrichtung möglich war, ist das Verdienst von Frau M. Riek, an die ich an dieser Stelle, auch für die stete Hilfsbereitschaft und für die angenehme Atmosphäre im Reinraum, meinen Dank richten möchte. Das Stichwort Reinraum führt mich zu Kollegen, die mich das eine oder andere mal dorthin, und auch sonst durch die Zeit als Doktorand, begleitet haben: Dr. Ralf Kemkemer, Simon Jungbauer und Alexandra Goldyn.

Nicht zuletzt gilt mein Dank vielen Kollegen die mir mit Rat und Tat zur Seite standen oder mich durch Diskussionen zu neuem Nachdenken angeregt haben. Vor allem für letzteres gilt mein Dank meinem Büronachbarn Emerson De Souza. Für das ursprüngliche Entwickeln und Inbetriebnehmen des Adhäsionstesters „Basalt II“ danke ich Herrn Dr. Andrei Peressadko; Herrn Dr. Holger Pfaff für seine Vorarbeiten auf diesem Gebiet. Irma Álvarez möchte ich für ihre Arbeiten zu den „suction cups“ danken. An „meine“ Hiwis Melanie Mannsberger und Dirk Drotlef möchte ich meinen Dank für die Hilfe beim Auswerten der Messdaten richten. Nicht vergessen möchte ich Frau Hess, die mir eine große Hilfe war und viele administrative Stolpersteine aus dem Weg geräumt hat. Letztlich gilt mein Dank selbstverständlich allen Kollegen der Abteilung Arzt für das gute Zusammenarbeiten.

Eine Promotion stellt eine Aufgabe dar, die ich mir ohne Unterstützung auch im Privaten nicht vorstellen möchte. Für diesen Rückhalt, der mich auf verschiedenen Ebenen getragen hat und nicht zu unterschätzenden Anteil am Gelingen dieser Arbeit hatte, möchte ich aus tiefstem Herzen meinen Freunden Tillmann Seiffer, Martin Dautel und Dr. Wolfram Brodowski danken. In gleicher Weise war mir auch meine Familie eine starke Stütze, auf die ich mich die ganze Zeit über verlassen konnte. Mein herzlicher Dank an meine Eltern und meinen Bruder Markus.

Index

1	INTRODUCTION AND MOTIVATION	17
2	LITERATURE REVIEW	21
2.1	Contact Mechanics	21
2.1.1	The Hertz theory	21
2.1.2	The Johnson-Kendall-Roberts theory	23
2.1.3	The Derjaguin-Muller-Toporov theory	24
2.2	Research on Bioinspired Fibrillar Adhesives	25
2.2.1	Theoretical considerations	25
2.2.2	Fabrication methods	28
2.2.2.1	Manual cutting	28
2.2.2.2	Filling of commercial porous membranes	28
2.2.2.3	Filling of micromachined templates	30
2.2.2.4	Molding of photolithographic templates	32
2.2.2.5	Molding of plasma etched templates	33
2.2.2.6	Pattern transfer by plasma etching	36
2.2.2.7	Arrays of carbon nanotubes	37
2.2.2.8	Hierarchical structures by microfabrication and plasma etching	38
2.2.2.9	Direct drawing of micro and nanofibers	40
2.2.3	Summary of current literature	41
3	EXPERIMENTAL: FABRICATION OF PILLARS WITH CONTROLLED AND 3D TIP SHAPE ...	43
3.1	Introduction	44
3.2	Experimental	45
3.2.1	Photolithography	45
3.2.2	Soft lithography and inking	50
3.3	Results and Discussion	54
3.4	Conclusions	57

4	EFFECTS OF PILLAR RADIUS, ASPECT RATIO, AND PRELOAD.....	59
4.1	Introduction	60
4.2	Experimental	61
4.3	Results	63
4.4	Discussion	71
4.4.1	Condensation patterns for different array geometries	71
4.4.2	Backing contact and buckling of pillars during adhesion testing.....	71
4.4.3	Effective Young's moduli of patterned surfaces.....	72
4.4.4	Pull-off force versus preload	74
4.4.5	Pull-off force versus pillar radius.....	77
4.4.6	Pull-off force versus pillar aspect ratio	79
4.4.7	Comparison with biological systems.....	82
4.5	Conclusions	83
5	CONTACT SHAPE CONTROLS ADHESION OF BIOINSPIRED FIBRILLAR SURFACES.....	85
5.1	Introduction	86
5.2	Experimental	87
5.3	Results	91
5.3.1	Pull-off behavior	91
5.3.2	Compressive behavior	103
5.4	Discussion	105
5.4.1	Influence of tip shape on pull-off force.....	105
5.4.2	Size effect for different shapes: "splitting efficiency"	107
5.4.3	Preload dependence of pull-off force for different tip shapes.....	108
5.5	Conclusions	111
6	DESIGN CRITERIA FOR DRY ADHESIVE SYSTEMS: THE EFFECT OF SHAPE	113
6.1	Introduction	114
6.2	Review of Design Maps	115
6.2.1	What is the appropriate condensation criterion?	118
6.2.2	Minimal number of contacts	121
6.3	Design Maps for Punches.....	123
6.3.1	Contours of constant apparent contact strength	124

6.3.2	The limit of fiber fracture	125
6.3.3	The limit of ideal contact strength.....	125
6.3.4	Intersection with the conode.....	127
6.3.5	Condensation limit after Glassmaker <i>et al.</i>	128
6.3.6	Condensation limit after Persson.....	129
6.4	Surface Roughness in the Adhesion Design Maps for Flat Tips.....	130
6.4.1	Construction of adhesion design map.....	132
6.5	Design Maps for Toroidal Tips	135
6.5.1	Contours of constant apparent contact strength.....	135
6.5.2	The limit of fiber fracture	136
6.5.3	The limit of ideal contact strength.....	136
6.5.4	Intersection with the conode.....	138
6.6	Design Maps for Tapes.....	141
6.6.1	Contours of constant apparent contact strength.....	141
6.6.2	The limit of fiber fracture	142
6.6.3	The limit of ideal contact strength.....	143
6.6.4	Intersection with the conode.....	145
6.6.5	Limits and maps for other peel-off angles.....	146
6.7	Discussion.....	149
6.7.1	Critical number for change in hierarchy.....	149
6.7.2	Comparison of spheres and tapes	150
6.7.3	Discussion of adhesion design maps	152
6.7.4	What is the optimum shape?.....	154
6.7.5	Limitations and problems	159
6.8	Conclusions	161
7	SUMMARY AND OUTLOOK.....	163
8	APPENDICES	167
8.1	Appendix A: Additional Information to Chapter 3	167
8.2	Appendix B: Additional Information to Chapter 4.....	168
8.2.1	SEM micrographs of selected pillars structures	168
8.2.2	Load-displacement curves	169
8.2.3	Pull-off force and strength vs. preload for aspect ratio $\lambda = 2$	170

8.2.4	Tenacity	171
8.2.5	Pull-off force as a function of aspect ratio at radius $r = 10 \mu\text{m}$	172
8.2.6	Dependence of E^* on radius, height and aspect ratio	173
8.2.7	Critical contact radius and number of pillars in contact at a_{crit}	174
8.3	Appendix C: Additional Information to Chapter 5	176
8.4	Appendix D: Additional Information to Chapter 6	177
8.4.1	Design maps for tapes: detailed derivation	177
8.4.1.1	Contours of constant apparent contact strength	177
8.4.1.2	The limit of fiber fracture	178
8.4.1.3	The limit of ideal contact strength.....	179
8.4.2	Adhesion design maps for tapes at different peel-off angles	180
8.4.3	Adhesion design maps for spherical tip shape	184
8.4.4	Optimum design parameters for all three condensation limits.....	186
9	REFERENCES	191
10	DEUTSCHE KURZFASSUNG DER DISSERTATION	197
10.1	Motivation und Literaturüberblick	197
10.2	Experimentelles	199
10.3	Ergebnisse und Diskussion.....	202

Symbols and Abbreviations

Symbols

a	Contact radius or radius of small spheres (m)
a_{crit}	Critical contact radius according to spring model (m)
A_{app}	Apparent contact area (m ²)
A_c	Actual contact area (m ²)
A_f	Contact area of single fiber (m ²)
A_{proj}	Projected contact area of one contact (m ²)
A'_{proj}	Projected contact area of small contact (m ²)
b	Characteristic length of surface interactions (m)
C	Geometrical factor (-)
E	Young's modulus (Pa)
E^*	Reduced Young's modulus (Pa)
E_{eff}	Effective Young's modulus (Pa)
E_{opt}	Optimum Young's modulus (Pa)
f	Pillar packing density (-)
h	Pillar height or tape thickness (m)
k	Thermal conductivity (W/(m·K))
K	Reduced Stiffness (Pa)
n	Number of hemispheres in contact (-)
n_r	Refractive index (-)
$N(P_p)$	Number of pillars in contact at preload P_p (-)
N_{min}	Minimal number of small contacts for efficient splitting (-)
P	Compressive load (N)
P_c	Pull-off force (N)

P'_c	Pull-off force for split contacts (N)
$P_{c(max)}$	Maximum pull-off force according to spring model (N)
P_p	Compressive preload (N)
q	Shape parameter (-)
r	Pillar radius (m)
R	Fiber or sphere radius, or relative radius of curvature (m)
R'	Pillar radius after splitting (m)
R_{opt}	Optimal fiber radius (m)
S	Interpillar spacing (m)
T_g	Glass transition temperature (°C)
z_0	Equilibrium separation (m)
α	Peel-off angle of elastic tape (°)
α_c	Contact radius at pull-off (m)
α_t	Linear coefficient of thermal expansion (1/K)
γ	Work of adhesion (J/m ²)
γ'	Work of adhesion between two fiber tips (J/m ²)
γ_{eff}	Effective work of adhesion (J/m ²)
δ	Indenter displacement (m)
ε	Dielectric constant (-)
η	Viscosity (Pa·s)
$\lambda = h/2r$	Pillar aspect ratio (-)
λ_{opt}	Optimal fiber aspect ratio (-)
μ	Coefficient of friction, or Tabor parameter (-)
ν	Poisson's ratio (-)
ρ	Specific gravity (g/cm ³)
σ^*	Interfacial strength (Pa)
σ_{app}^{opt}	Ultimate apparent contact strength (Pa)
σ_c	Pull-off strength (Pa)
σ_f	Axial fiber stress (Pa)
σ_m	Tensile strength (Pa)
σ_{th}	Theoretical contact strength of van der Waals bonds (Pa)
σ_{th}^f	Theoretical fiber fracture strength (Pa)

Abbreviations

AFM	Atomic force microscope
CNT	Carbon nanotube
DMT	Derjaguin-Muller-Toporov
JKR	Johnson-Kendall-Roberts
MEMS	Micro electromechanical system
MWCNT	Multiwalled carbon nanotube
PC	Polycarbonate
PDMS	Polydimethylsiloxane
PI	Polyimide
PMMA	Polymethylmethacrylate
PS	Polystyrene
PVB	Polyvinylbutyral
PVS	Polyvinylsiloxane
RMS	Root mean square
SEM	Scanning electron microscope
UV	Ultraviolet
VdW	Van der Waals

Christian Greiner

Size and Shape Effects in Bioinspired Fibrillar Adhesives

Institute of Physical Metallurgy, University of Stuttgart and
Max Planck Institute for Metals Research, Stuttgart, 2007

207 pages, 45 figures, 7 tables

Abstract: Over the last years, the striking ability of geckos and several insects to cling to walls and ceilings has inspired large research efforts. The reasons for this interest is the strong and completely reversible adhesion of these dry adhesive systems, which is based on van der Waals interactions and thus universal on almost any kind of surfaces. Therefore the structures are not only interesting for fundamental science, but also for industrial application. Theoretical contact mechanical treatment of fibrillar systems has shown that the main physical principle behind their adhesion abilities is that of contact splitting, which states that the adhesion force increases upon splitting up one large contact into many small ones. Theory has also shown that the tip shape of the contacting fibers is of great importance for adhesion performance. Both influences – the one of size and the one of shape – were experimentally and theoretically treated in the present thesis. In order to allow for systematic and controlled adhesion experiments, elastomeric model systems were fabricated by soft molding techniques based on photolithographic master structures in the micrometer regime. Taking advantage of the filling mechanisms of the molding step and the viscosity of polydimethylsiloxane, it was not only possible to generate flat punch, but also hemispherical, concave, spatula- and mushroom-shaped pillars, and structures which resembled a flat punch, but with rounded edges. Systematic adhesion testing revealed that the adhesion strength increased with decreasing pillar diameter, as was theoretically predicted. This increase was found to be strongest for the mushroom-shaped pillars which also showed the highest overall adhesion values reaching the performance of geckos. The second highest gain upon contact splitting was found for spatular structures followed by hemispherical and flat punch-like tip shape. Also, the adhesion forces increased with increasing pillar aspect ratio. The “adhesion design maps” presented in this thesis, which were developed for different contact shapes, together with the conclusions drawn from the experimental data, will allow for a more strategic approach when designing fibrillar attachment systems in the future.

Christian Greiner

Size and Shape Effects in Bioinspired Fibrillar Adhesives

Institut für Metallkunde, Universität Stuttgart und
Max-Planck-Institut für Metallforschung Stuttgart, 2007

207 Seiten, 45 Abbildungen, 7 Tabellen

Kurzzusammenfassung: Geckos, aber auch einige Insekten und Spinnen besitzen die faszinierende Fähigkeit an der Wand und an der Decke laufen zu können. Diese starke, aber zugleich absolut reversible Haftung ist sowohl wissenschaftlich, als auch technisch von größtem Interesse. Sie basiert auf der Aufspaltung eines großen, in viele kleine Haftkontakte welche über van der Waals Wechselwirkungen mit der gegenüberliegenden Oberfläche in Kontakt treten. Theoretische Untersuchungen ergaben nicht nur die Vorhersage des Aufspaltungseffektes, d.h. dass viele kleine Hafthaare stärkere Haftkräfte erzeugen als einige wenige große, sondern zeigten auch an, dass die Endkontur der jeweiligen Haare einen starken Einfluss auf die Kontaktmechanik und die Stärke der Adhäsion haben sollte. Diese beiden Parameter, Größe und Kontur der Hafelemente, wurden in der vorliegenden Arbeit sowohl experimentell, als auch theoretisch untersucht. Um reproduzierbare und eindeutig interpretierbare Experimente zu ermöglichen, wurden Elastomeroberflächen mittels der sog. "Soft Lithography", basierend auf mikrostrukturierten Photolackoberflächen, hergestellt. Durch die geschickte Ausnutzung der Viskositäts- und Aushärteeigenschaften von Polydimethylsiloxan gelang es Modellsysteme solcher Haftsysteeme herzustellen. Diese hatten nicht nur die Kontur eines flachen Stempels, sondern waren auch halbkugel-, spatel- und pilzförmig. Auch konkave Strukturen und flache Stempel mit runden Kanten wurden erzeugt. Die systematische Untersuchung der Haftkräfte ergab, dass die Adhäsion für kleiner werdende Kontakte ansteigt. Dabei war die Zunahme für die pilzförmigen Haftkontakte am stärksten, gefolgt von den spatulären Strukturen, der hemisphärischen und der stempelförmigen Kontur. Die pilzförmigen Modellsysteme zeigten auch die höchsten absoluten Haftfestigkeiten, die jene des Geckos erreichten. Um die experimentellen Ergebnisse theoretisch abzurunden, werden "Adhesion Design Maps" für verschiedene Kontaktformen vorgestellt. Diese stellen Leitlinien für ein zukünftiges strategisches Entwickeln fibrillärer Adhäsive dar, welches zusammen mit den Schlußfolgerungen aus den Experimenten durch diese Arbeit erleichtert werden sollte.

1 Introduction and Motivation

“The woodpecker [...] can run up and down a tree in any way, even with the head downwards, like the gecko-lizard.”(1) With these words the great Greek philosopher Aristotle introduced the gecko into written language in the fourth century B.C. Since then humans wondered about the fascinating ability of this animal to walk and run along walls and even ceilings. But only with the emergence of electron microscopy in the 20th century was it possible to investigate the nanostructured topography of the gecko toe pads and to resolve their complicated ultrastructure (2-5). These pads are covered with long micron to nano sized hairs which terminate in so-called “spatulae”. These are about 20 nm thick and 200 nm wide and long (6). The hierarchical design of the entire structure is the key to the gecko’s adhesion behavior which enables strong and yet easily reversible attachment to almost any kind of surfaces.

In recent years, researchers have been able to theoretically understand and model aspects of the complex interplay of physical, chemical and engineering factors behind this outstanding adhesion performance, which is dominated by van der Waals forces with capillary contributions (6-9). One of the main results of these efforts has been the so-called “principle of contact splitting”, which states that, from the viewpoint of maximizing adhesion force, it is beneficial to split one large contact into many small subcontacts since by doing so an increase in overall pull-off force is predicted (10, 11). When moving away from the gecko and focusing on spiders and insects (like flies and beetles) with similar properties, different shapes were found for the contacting elements terminating the

individual hairs (called “setae”). This shape is band-like (spatular) in the case of the gecko, but can also be hemispherical or toroidal in other animals. For each of these shapes a different benefit for splitting a large contact into many small ones was theoretically predicted (12).

In part, the research in this field is driven by the enormous potential that is envisioned for artificial fibrillar adhesives. They would possess a high adhesion force on almost any kind of surface and could be easily detached without leaving behind any residue. Also, they would be self-cleaning. As a consequence, a “race” for fabricating the first – working – artificial, gecko-inspired adhesive has started, recently reviewed by del Campo and Arzt (13) and Chan *et al.* (14). This impetus has been possible through the rapid development of micro- and nanofabrication techniques experienced in the last years. But still, the intrinsic difficulties and the early stage of the research field limit the availability of artificial analogues with satisfactory adhesion performance. We are not even close to the desired smart structures for tunable adhesion or with self-cleaning properties, as they are demonstrated by the biological example. Another hindering factor is the complexity of the hierarchical biological structures that need to be understood and mimicked and the difficulty to reproducibly perform and interpret adhesion measurements.

The work presented here focuses on the fabrication and adhesion testing of microstructured surfaces possessing hairs, or rather pillars. With this approach several design parameters for artificial adhesives were investigated since merely copying nature is a poor approach for bioinspired design. Rather, the fundamental physics behind this kind of contact mechanical problem has to be understood. From there on, systematically designing artificial analogues, which might even be superior to their original biological counterparts, is envisioned. To gain this kind of understanding, the length, the diameter and the shape of

the pillars were varied systematically and independently. The results of the corresponding adhesion tests were compared with theoretical predictions. The main goal of this approach was to experimentally investigate whether the principle of contact splitting can be verified. Also different tip shapes were fabricated and their adhesion behavior was compared with theoretical predictions. Finally, the concept of “adhesion design maps” (15), which so far only existed for hemispherical contacts, was extended to other shapes. Thereby, another step towards efficient and rational design of bioinspired fibrillar adhesives was taken.

This thesis is organized in the following way: In chapter 2, the basic laws of contact mechanics will be presented and the current literature on fibrillar adhesives will be reviewed. Chapters 3 to 5 will deal with the fabrication and testing of elastomeric model systems. Chapter 6 will present the design and material selection principles developed in the context of adhesion design maps for different tip shapes. Finally, in chapter 7 a short summary of the thesis together with a brief outlook will be given. But now, we will have a look at the physics behind two contacting bodies.

2 Literature Review

In this chapter, the basic physical principles of contact mechanics will be introduced and explained, followed by a review of the up-to-date published literature on bioinspired fibrillar adhesives. This review will be organized by describing the individual fabrication approaches and by discussing the different methods to quantify adhesion and the subsequent adhesion performance of the structures.

2.1 Contact Mechanics

One of the first comments on a classical contact mechanics problem goes back to Sir Isaac Newton who in his 1704 published book “Opticks” stated that he observed a “clink-like” sound upon separating two contacting glass lenses. For the contact between them, he also observed a black contact zone and what later became known as Newton rings.

2.1.1 The Hertz theory

Even though the observations made by Isaac Newton clearly indicated that there are attractive forces present between two contacting bodies, even when contributions by electrostatics and magnetism can be excluded, the first step in establishing the field of contact mechanics was taken by Heinrich Hertz in 1881, without considering attractive forces between the two bodies. Hertz studied the stress distribution, the contact radius and the penetration depth for two elastic spheres in a frictionless contact, compressed by a force P (see Figure 2.1) (16).

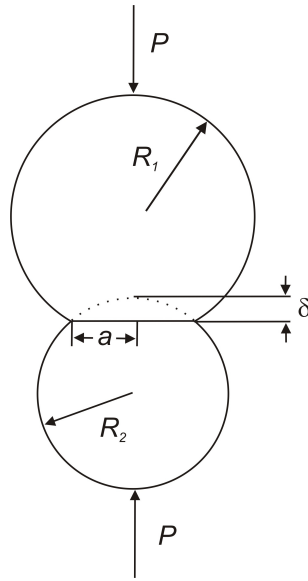


Figure 2.1: Frictionless contact between two smooth spheres (radii R_1 and R_2) compressed by the force P . This force leads to a circular contact area with radius a and a penetration depth δ .

The Hertzian theory for elastic contact assumes that the contact region – described by the contact radius a – is small compared to the radii of the contacting spheres R_1 and R_2 . It gives the following relation for a :

$$a^3 = \frac{3PR}{4E^*} \quad (2.1)$$

with R being the relative radius of curvature and E^* the reduced Young' modulus, both defined as:

$$\frac{1}{R} = \frac{1}{R_1} + \frac{1}{R_2} \quad (2.2)$$

$$\frac{1}{E^*} = \frac{1-\nu_1^2}{E_1} + \frac{1-\nu_2^2}{E_2} \quad (2.3)$$

where E_1 , ν_1 and E_2 , ν_2 are the Young's moduli and Poisson's ratios for sphere 1 and 2. From this starting point of two contacting spheres, the Hertzian theory has been extended

to other shapes, such as flat punches and cylinders. A thorough treatment of these and other cases can be found in the book written by Maugis (17).

2.1.2 The Johnson-Kendall-Roberts theory

Obviously, the biggest drawback of the Hertzian approach to contact mechanics is the neglect of attractive surface forces. This gap in the theoretical description was closed in 1971 when Johnson, Kendall and Roberts published their meanwhile famous paper on the surface energy and contact of elastic solids (18). Their approach, known as the JKR theory since, starts with the Hertzian description of the contact, but takes into account attractive van der Waals interactions inside the contact area. The theory balances elastic, potential and surface energies. In the presence of surface energy the contact area is predicted to be larger than in the Hertzian case. It is again described by the contact radius a (under fixed load conditions) (18):

$$a^3 = \frac{PR}{K} \left[1 + \frac{3\pi\gamma R}{P} + \sqrt{2 \frac{3\pi\gamma R}{P} + \left(\frac{3\pi\gamma R}{P} \right)^2} \right] \quad (2.4)$$

where γ describes the work of adhesion $\gamma = \gamma_1 + \gamma_2 - \gamma_{12}$, with γ_1 and γ_2 being the respective surface energies and γ_{12} the interfacial energy for the two contacting materials.

K is the reduced stiffness which is defined as:

$$\frac{1}{K} = \frac{3}{4} \left(\frac{1-\nu_1^2}{E_1} + \frac{1-\nu_2^2}{E_2} \right) \quad (2.5)$$

The contact sustains infinite stresses at its periphery. Due to the attractive forces, the contact area remains finite until a critical negative (tensile) load is applied which is found to be:

$$P_c = -\frac{3}{2}\pi\gamma R \quad (2.6)$$

When this force, known as the pull-off force P_c , is reached, the two spheres separate suddenly. For $\gamma=0$, the JKR solutions reduce to the Hertzian ones.

2.1.3 The Derjaguin-Muller-Toporov theory

The JKR theory was derived for soft spheres with large radii (compared to the contact area) and high adhesion energies. In 1975, Derjaguin, Muller and Toporov treated exactly the opposite case of a contact between hard solids, with small radii of curvature and low adhesion energies (19). In their approach – the DMT theory – they assume that the attractive forces inside the contact can be neglected and only consider van der Waals interactions outside the contact area. With these assumptions, the DMT results for the pull-off force P_c and the contact radius a are:

$$P_c = -2\pi\gamma R \quad (2.7)$$

$$a^3 = \frac{RP}{K} + \frac{2\pi\gamma R^2}{K} \quad (2.8)$$

It was the famous tribologist David Tabor who proposed that there should be a continuous transition between the two theories (20). In 1980, Muller *et al.* (21) showed that a single dimensionless parameter μ – known as the Tabor parameter – describes this transition. It is defined as follows (20):

$$\mu = \left(\frac{R\gamma^2}{E^* z_0^3} \right)^{1/3} \quad (2.9)$$

where z_0 represents the equilibrium separation of the two surfaces (usually taken to be between 0.3 and 0.5 nm). One finds that for $\mu > 5$ the JKR theory and for $\mu < 0.1$ the DMT theory applies. In all the cases discussed in the following chapters, where mainly elastomeric, thus soft surfaces, will be treated, the Tabor parameter is well above five, so that only the Johnson-Kendall-Roberts approach will be taken into account.

2.2 Research on Bioinspired Fibrillar Adhesives

2.2.1 Theoretical considerations

After the micro and nanostructure of biological attachment pads was resolved by electron microscopy, theories were developed to explain the split contact surface found in nature. One of the main results of these JKR-based contact mechanical considerations was the theory of “contact splitting”. Arzt *et al.* demonstrated an increase for the pull-off force by a factor of \sqrt{n} , when one large hemispherical contact (see Figure 2.2a) is split up into n subcontacts (10, 11):

$$P'_c = \sqrt{n}P_c \quad (2.10)$$

This finding can explain why heavier animals are equipped with finer attachment hairs. It describes the scaling relation between animal body mass and setae density very well over more than six orders of magnitude in mass (10, 22).

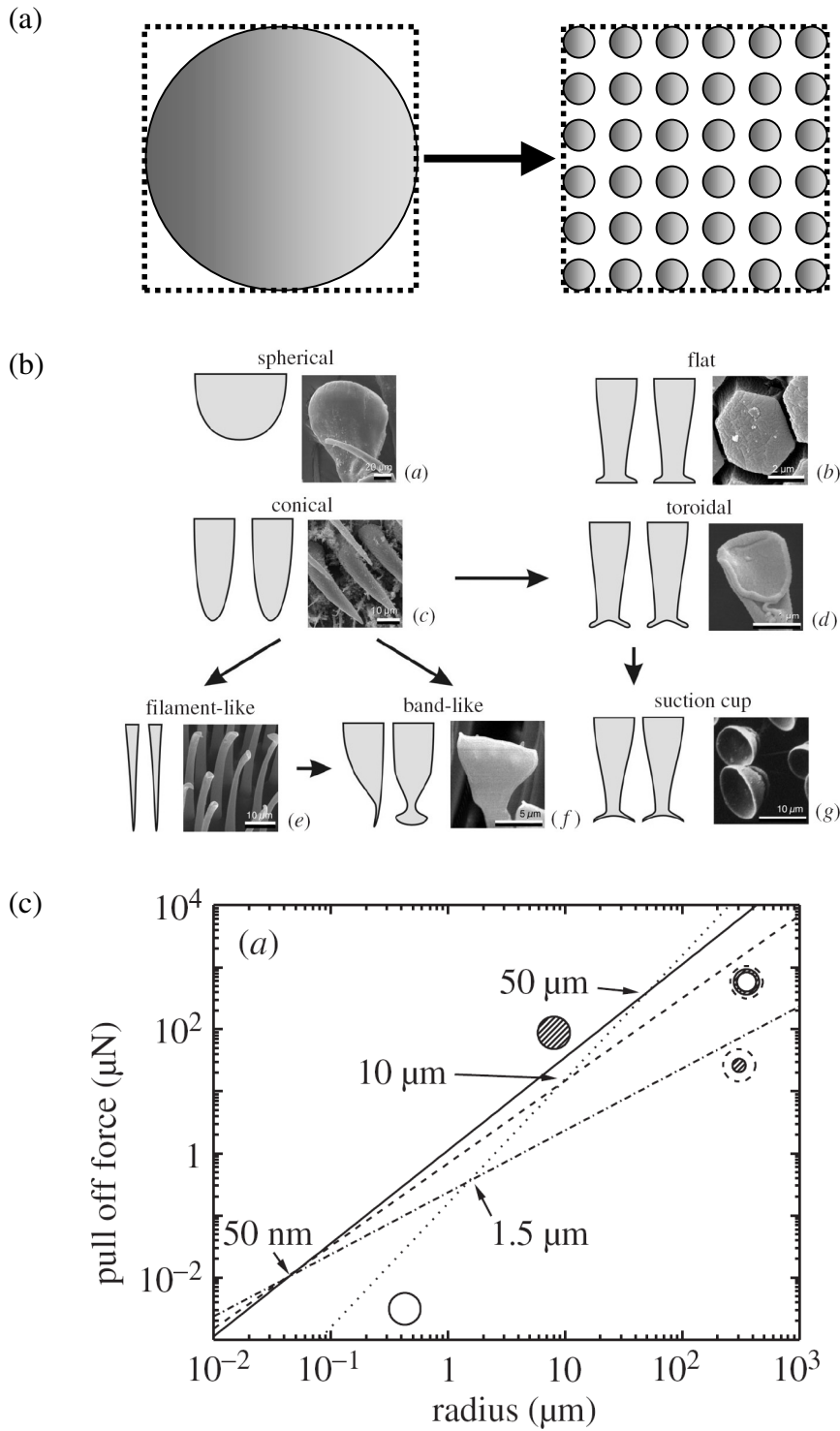


Figure 2.2: (a) Schematic to explain the principle of contact splitting: One large contact is split up into n smaller ones while keeping the projected contact area constant. (b) Shapes of attachment devices found in nature (picture taken from (12)). (c) Pull-off force vs. feature size for single contacts with various shapes demonstrating the different scaling behavior (taken from (12)).

As shown in Figure 2.2b, natural attachment systems exhibit not only hemispherical contact shapes, but a whole variety of contours (12). When treating these contours theoretically, Spolenak *et al.* found that different contact shapes also show different scaling relations between feature size and pull-off force (given by the slopes in Figure 2.2c) and thus different efficiencies for the process of contact splitting (12).

One would now think that for artificial fibrillar systems the minimization of feature radius and the highest packing density of fibers has to be the aim of any design since this, according to contact splitting, should yield the best adhesion performance. However, when investigating this in more detail, Spolenak *et al.* found that there are limitations to this approach. For example, fibers start to “condense”, build clusters and rather stick to one another than to the counter surface (15). This “fiber condensation” dramatically reduces the pull-off force generated by a fibrillar adhesive and has to be avoided by the design rules. These rules were visualized in so-called “adhesion design maps” which allow for a more strategic design of artificial structures, but to-date have only been constructed for hemispherical contacts (15).

Research groups all over the world embarked upon the task of fabricating such structures and characterizing their pull-off behavior. For both the fabrication and the measurement methods, a variety of techniques was developed and published in the literature. In the following, the publications will be grouped according to the fabrication method chosen and the adhesion results will be discussed in this context. At the end of the chapter a summarizing plot of all adhesion data published so far will be given.

2.2.2 Fabrication methods

2.2.2.1 Manual cutting

This simplest and crudest method imaginable to create fibrillar systems, which will be more on the millimeter range, was used by Glassmaker *et al.* (23), Chung and Chaudhury (24) and Ghatak *et al.* (25). The authors used polyvinylbutyral (PVB) or polydimethylsiloxane (PDMS) films and cut the surfaces with a razor blade. Glassmaker *et al.* brought the structures in contact with a glass slide by pressing them together on a hotplate. They measured very high pull-off strengths as a consequence of the resulting intimate contact between sample and reference surface (23).

2.2.2.2 Filling of commercial porous membranes

Filling a prefabricated porous template with a polymer melt, polymer precursor or a polymer solution is the fabrication method most frequently used to obtain arrays of pillars on a planar backing. After filling, the polymer is cooled down, cured or the solvent is evaporated. Subsequently, the structures are separated from the template either by demolding or by selective dissolution of the template. Templates with micro to nanometer sized pores of various dimensions are commercially available (e.g. anodic alumina membranes or track-etched polycarbonate (PC) membranes used in filtration technologies). In most cases commercial PDMS precursors (especially developed for microcontact printing) are used as polymer source. These systems have the advantage of easy handling and of rendering accurate reproductions of the template.

Sitti and co-workers (26-33), later Jin *et al.* (34) and more recently Kim *et al.* (35) used anodic alumina and PC membranes as templates, which were filled with PDMS (26, 28, 30), polyurethane (31), polyimide (27), a polystyrene (PS) solution (34), or a UV curable resin (35). Pore diameters ranged from 20 nm to 20 μm and pore densities from

10^5 to 10^8 cm^{-2} (30). The average membrane thickness was in the range of 5 to 60 μm . In most cases the membrane was chemically etched to release the fibers. Only low aspect ratio fibers and flexible PC membranes could be used to peel-off the template. Depending on the wetting properties of polymer and template, the fibers were hollow.

The advantages of this method are the availability of templates with different pore diameters, lengths and packing densities as well as the possibility of using different polymers for filling the membranes. It yields densely packed fibers with high aspect ratios and small diameters. Especially the filter membranes are very inexpensive as well. The major drawback of this structuring method is frequent fiber condensation as a consequence of the wet etch process needed to release the fibers from the template. The evaporating solvent exerts capillary forces on the individual fibers bringing them into contact with each other. In addition, the hairs often are of irregular length. Another problem of the wet etch process is that the polymer might be affected by the etching solution and the structures may lose their initial shape or collapse due to swelling or partial dissolution.

Applying this method, Jin *et al.* reported structured polystyrene surfaces with a water contact angle above 160° . Adhesive forces were determined by means of a highly sensitive micro electromechanical balance system which measured the force necessary to pull-off a water droplet from the nano fiber surface (34). Pull-off forces as high as 75 μN were reported and a dependence on the packing density of the fibers was found (34). As the volume of the water droplet used for the force measurements is unknown, an adhesion strength (force per contact area) cannot be calculated. With water as the counter surface for the measurements, contributions of capillary forces will be present. This is not discussed by the authors.

Kim *et al.* (35), who prepared the nanoporous molds themselves, also tried to quantify the adhesion behavior of their highly condensed fiber systems. Therefore, they glued a glass microsphere of 20 μm diameter to the end of an atomic force microscope (AFM) tip. By bringing the sphere in contact with the sample and measuring the force necessary to separate the two, they determined the adhesion performance. Kim *et al.* found that fibers with larger diameters and higher aspect ratios increased the pull-off forces. Especially the first results is in conflict with all theoretical predictions and with the results presented in this thesis. Since Kim *et al.* did not take into account any preload effect on the adhesion behavior (see the following chapters) and measured on highly condensed structures their results are the subject of substantial doubt.

2.2.2.3 Filling of micromachined templates

Peressandko and Gorb fabricated polyvinylsiloxane (PVS) pins by filling a steel template into which elliptic holes had been cut using a laser (36). The resulting elliptic pillars had a height of about 400 μm and a cross section of approx. $250 \times 150 \mu\text{m}^2$. With these structures adhesion experiments were performed bringing the pins into contact with a glass surface using a micromanipulator. The forces were measured with a load cell and the contact area was monitored with a video microscope. The authors showed that the adhesive force of the structured surface was higher than that of a flat control when normalizing the forces to the actual contact area, resulting in the so-called tenacity (36). Due to a limit in laser focusing, it is not possible with this method to fabricate smaller structures than the ones published, and the process is not very reproducible (37).

Sitti and Fearing indented a wax layer with an AFM tip and used the resulting hole pattern as template for molding with a silicone rubber or a polyester resin (26, 28, 29, 38). The adhesion properties of individual bumps were characterized using a tipless AFM

cantilever. Pull-off forces of approx. 180 nN for the silicone rubber and 290 nN for the polyester bumps were measured. Both results were compared to JKR theory and to calculations of the van der Waals forces. Good agreement between theoretical and experimental values was found (26). This fabrication approach is applicable for generating small pillars, but it is slow and not suitable for generating high aspect ratio structures, as well as it lacks control over the tip shape.

Together with Dr. Stanislav Gorb from the Max Planck Institute for Metals Research, the German company Gottlieb Binder GmbH (Holzgerlingen, Germany) developed a commercial, fibrillar dry adhesive. The exact processing technology remains unknown, but the structures are made out of PVS elastomer. The resulting pillars have a diameter of about 60 μm at the base, show mushroom-like tip shape (40 μm tip diameter) and are packed in a hexagonal fashion with approx. 40 % of the area being covered (39). So far two research groups investigated the tribological behavior of these structures (39-42). Bhushan and Sayer concentrated on friction and contact angle investigations (41), whereas Gorb *et al.* (39), Varenberg *et al.* (42) and Varenberg and Gorb (40) examined the adhesion properties in much detail. All adhesion measurements were performed with a home-built microtribometer setup (43), which allowed for testing in vertical and lateral direction and for a flat-on-flat contact scheme through a self-aligning system. The use of a high magnification video microscope allowed to visualize the contact area. When testing surfaces with pillars or with dimples (fabricated through punching flat PVS with a hollow needle) of different radii (20 to 120 μm), Varenberg *et al.* found that the pull-off force did not correlate systematically with the real contact area, but depended linearly on the real contact perimeter (42). This result so far lacks theoretical explanation but might be connected to the rather high surface roughness for these structures. In another study, Gorb *et al.* found out that for the flat-on-flat scheme used to quantify adhesion, pull-off force did

not depend on preload (39). The authors measured an adhesion force of up to 400 mN for the mushroom-shaped pillars which corresponds to a pull-off strength of about 60 kPa (39). In the same publication the authors performed peel tests and showed that after cleaning of a contaminated sample, a large part of the adhesion performance was recovered (39). More recently, Varenberg and Gorb studied the influence of shear on the pull-off behavior of these pillars (40). They found that the pull-off force could be switched on and off in close to binary fashion by moving the test stage by a certain lateral displacement (about 0.3 mm).

2.2.2.4 Molding of photolithographic templates

Photolithography allows the fabrication of templates with controlled and well-defined dimensions. Glassmaker *et al.* fabricated PDMS plate-like structures with diameters from 5 to 50 μm and a height of around 30 μm by casting PDMS prepolymer onto photolithographic templates (44). Crosby *et al.* applied the same technique and fabricated low aspect ratio PDMS structures with diameters and spacings between 50 and 500 μm (45). Thomas and Crosby also applied this technique to generate hole patterns with very interesting adhesion properties (46). To test adhesion, they utilized a custom-built setup which indented the test surfaces with a polished fused silica sphere (5 mm in radius). The contact area was monitored *in situ* using an inverted optical microscope. Crosby *et al.* normalized the measured adhesion force by the theoretically predicted one based on JKR theory. They reported a maximum in normalized pull-off force at about 200 to 250 μm structure radius with very little dependence on pillar spacing. The coupling between individual pillars and the applicability of the JKR theory were investigated as well.

The maximum aspect ratio of the structures fabricated by Crosby *et al.* was 0.08. Optical micrographs of the contact area during adhesion testing demonstrated that not only

the pillars but also the PDMS in-between them was in contact with the sphere. The normalized pull-off force was found to be smallest for the smallest pillars in the densest packing. This result is unexpected and might be due to an influence of the PDMS in-between the pillars, which in this case will contribute least.

Cheung *et al.* (47) in 2005 fabricated fibers out of SU-8, an epoxy based UV-sensitive photoresist, but did not systematically test adhesion performance. The same approach of generating SU-8 pillars with 17 to 25 μm in diameter and a length between 48 and 100 μm was chosen by Aksak *et al.* (48). Through inclined lithography, first published by Han *et al.* (49), they fabricated not only vertical pillars, but also structures under a tilt angle of 18° . Applying a double-molding step with a flexible silicon rubber which subsequently was vacuum-molded with a polyurethane, they transferred the original SU-8 into PU pillars, which were well suited for adhesion testing. To investigate the influence of the tilt angle on adhesion, the authors used a 12 mm diameter glass sphere and connected it to a load cell. The main result of a rather systematic study, which also took into account the preload dependence of the pull-off force, was that angled fibers showed less adhesion performance than vertical ones, but that their compliance was higher (48).

2.2.2.5 Molding of plasma etched templates

Plasma etching of prestructured wafers can be used for creating templates with high-aspect ratio holes. Glassmaker *et al.* applied an ion etching process on deep-UV photolithographically structured wafers to fabricate 10 μm deep and 1.2 μm wide holes with different lateral spacings (44). Replication of the templates with PDMS resulted in well-defined polymer pillars, which surprisingly did not collapse under their own weight. This contradicts claims published by Roca-Cusachs *et al.* stating that PDMS pillars should collapse when the aspect ratio exceeds five (50). The structures were tested in adhesion

against a flat glass slide and against a glass sphere while the contact area was monitored using an inverted microscope, which allowed for very controlled testing. Menon *et al.* applied a similar process to fabricate pillars with a diameter of 4 μm and 40 μm height. Adhesive forces were not measured (30).

Kustandi *et al.* recently submitted a paper in which they described the fabrication of fibrillar structures – minimal diameter 150 nm and maximum aspect ratio around 10 – relying on colloidal nanolithography (51). A monolayer of polystyrene spheres was used as a mask for an etching process leading to holes in a silicon wafer which subsequently were filled with polyparylene. Since wet etching of the silicon template often resulted in condensed pillar structures, the authors applied a dry etching process using XeF_2 gas. The authors measured the adhesive properties of their structures using a tipless silicon AFM cantilever. The adhesive force of a single fiber was calculated from this data. In order to ensure that static interactions did not play an important role, Kustandi *et al.* adhered a macroscopic piece of their structures to a glass slide and put it into an ionized atmosphere. They observed that the structures stayed attached to the glass and concluded that static forces were not significantly contributing to overall adhesion.

The fabrication method chosen by Kustandi *et al.* is suitable to manufacture fibrillar structures. Closer inspection of the published SEM micrographs reveals the presence of some fiber bundles, indicating that the dry etching process does not avoid condensation of fibers completely. Due to the self assembly process controlling the packing of polystyrene spheres, colloidal lithography is much faster than processes like e-beam lithography, but lacks their accuracy. By choosing different sphere diameters and varying other parameters, different fiber radii and pitches are possible. The entire process is still very time-consuming, and since it includes many different steps, is not expected to have a very

high yield. The published force-displacements curves are very irregular and with the setup used by Kustandi *et al.* the contribution of friction forces to overall adhesion, as well as the calculation of the pull-off force for one individual pillar, is not clear.

Several publications from the Sitti group also rely on fabrication approaches based on lithography and dry etching. In the earlier ones, the authors showed that this fabrication approach yields fibrillar structures but did not test adhesion (30, 47). More recently, Kim and Sitti fabricated polyurethane microfibers with spatula-like tips by molding a deep reactive ion etched silicon-on-insulator wafer (52). The resulting structures had a fiber diameter of 4.5 μm and a tip diameter of 9 μm . Fiber length was 20 μm and packing density around 44 % for the tips. The spatula-like shape was the result of an under etching approach once the etch reached the insulator layer. The adhesion behavior of these structures was tested with a 6 mm diameter glass sphere attached to a load cell, allowing very accurate measurements. The main results were a very high pull-off force of up to 60 mN and, even more important, an adhesion strength value as high as 180 kPa. This is in the regime of gecko adhesion. The fabrication approach chosen by Kim and Sitti allows high control over fiber diameter and length and to a certain degree also over tip shape. The whole process is fully integrable into standard microfabrication and areas up to entire wafers can be patterned. The drawback is that the wafer has to be etched away to release the structures in different etch media; this makes the process slow and expensive, and the template is lost. The adhesion testing was performed in a careful manner and preload effects were taken into account.

Applying a double-molding technique (53), Yoon *et al.* fabricated nano-size cone-shaped pillars out of PMMA with diameters of 50 nm at the top and three different heights which were not specified any further in their publication, but the aspect ratio did not

exceed two (54). The authors mainly tested friction properties, but in addition found that adhesion slightly increased with pillar aspect ratio. The adhesion tests were carried out with an AFM and a 1.25 μm diameter borosilicate ball clued to the tip. Even though the trend of increasing pull-off forces with feature aspect ratio seems plausible, close inspection of the SEM picture of the pillars given in the original publication reveals that the authors did not have control over the tip shape. The pillars are not homogeneous in height, so that the corresponding adhesion data does not allow for solid conclusions.

2.2.2.6 Pattern transfer by plasma etching

Plasma etching of prestructured surfaces can also be used for creating high-aspect ratio pillars directly on polymer layers. Usually, the polymer is coated with a patterned photoresist layer and a protective metallic film. After development, the system is exposed to an oxygen plasma which transfers the primary pattern into the polymer layer and thus extends the structuring into the third dimension. The process relies on different etch rates of the polymer and the metallic film on top of the photoresist, which acts as a mask during the etching process.

Geim *et al.* used polyimide films covered by a photoresist layer which was structured by electron beam lithography (55). After plasma etching, the resulting PI structures were transferred to a scotch tape. Pillars with diameters between 0.2 to 4 μm , heights ranging from 0.15 to 2 μm and different spacings from 0.4 to 4.5 μm were obtained. The adhesive properties of their structures were measured by atomic force microscopy with a custom-made flat cantilever (55). They found that the pull-off force was proportional to the density of hairs and had a weak dependence on the pillar height and diameter. Geim *et al.* stated that the pillar shape was less important (55). The adhesive properties of larger areas were tested using glass wedges and a laboratory balance.

The authors concluded that the adhesion increased with increasing contact area. When testing with the AFM, the authors always applied the same preload, which resulted in different contact areas when testing structures with different effective stiffnesses. In addition, not all pillars were in contact. Their conclusion that the adhesive force depended mainly on packing density and less on diameter, height and shape, contradicts theoretical predictions. Since they varied pillar radius, height and packing density at the same time and gave pull-off forces in arbitrary units with the contact area and the precise geometry of the indenter being unknown, the interpretation of their data is difficult, even though it seems to show an increase in pull-off force with decreasing pillar radius. With the microbalance experiments, a preload of more than 0.5 MPa was used, which seems quite high and might be the reason for the structures to stick. Hui *et al.* tried to reproduce the data collected by Geim *et al.* and measured other effects (56). Especially, they found a decrease in adhesion for the structured compared to the unstructured polyimide surface. Since Hui *et al.* backed their structures with PDMS rather than scotch tape, they argue that viscoelastic contributions might have affected Geim's results (56).

2.2.2.7 Arrays of carbon nanotubes

The idea of creating synthetic adhesive structures with carbon nanotubes was realized by Yurdumakan *et al.* (57) and Zhao *et al.* (58). Yurdumakan *et al.* chemically deposited multiwalled carbon nanotubes (MWCNT) on top of a silicon wafer and completely embedded them in polymethylmethacrylate (PMMA). The PMMA sheet was then peeled off the silicon wafer and partially dissolved in acetone (57). The resulting structures were entangled carbon nanotube bundles of around 50 nm diameter, which were irregular in length. Every individual tube had a diameter of approx. 10 nm. Varying the time of exposure to the solvent, different aspect ratios of the carbon nanotubes sticking out of the PMMA were possible. The authors performed adhesion measurements on these

structures by using a standard scanning probe tip. The pull-off force per area is reported to be about two orders of magnitude higher than that for a gecko seta (16 000 kPa compared to about 100 kPa). Yurdumakan *et al.* explain the high adhesion strength by a combination of van der Waals forces and energy dissipation in the carbon nanotubes during elongation due to their material properties (57). The high pull-off strengths obtained most probably are a consequence of frictional forces acting when testing such an irregular surface with an AFM tip. Their hypothesis that energy might be dissipated in the fibers does not seem to explain the very high adhesion values.

Zhao *et al.* (58) synthesized their structures – MWCNTs – by chemical-vapor-deposition on silicon substrates. The tubes had heights between 5 and 10 μm . For measuring adhesion, the samples were pressed against a laboratory balance with a preload of about 20 N and then retracted. The authors measured adhesion strengths of 120 kPa. In repetitive experiments Zhao *et al.* found that the adhesion performance decreased over time as some nanotubes lost contact to the substrate. Interestingly, another result was that pull-off force increased with decreasing fiber height, an effect not understood or explained by the authors and against theoretical considerations. In general, the adhesion performance found by the authors is impressive but might be an artifact due to very high preloads.

2.2.2.8 Hierarchical structures by microfabrication and plasma etching

The fabrication of hierarchical biomimetic adhesives was demonstrated by Northen *et al.* (59-61). The authors fabricated square silicon dioxide platforms with 2 μm thickness and an edge length of 100 to 150 μm using the BOSCH process. The platforms were supported by silicon pillars with 1 μm thickness and 50 μm height. After the platforms had been fabricated, they were coated with a photoresist layer and treated with an oxygen plasma for 5 minutes. This resulted in the generation of nanoscale fibrils on the polymer

surface which were 2 μm tall and 50 to 200 nm wide. The authors attributed this growth to electrohydrodynamic instabilities of polymer films in an electrical field according to the mechanism investigated by Russell *et al.* (62, 63). Contact angle measurements were performed on hydrophilic and hydrophobic samples. Hydrophobicity was achieved by a CF_4 plasma treatment. Adhesive properties of the hierarchical structures were tested with a Hysitron Triboindenter and a spherical aluminum tip having a root mean square (RMS) roughness of 500 nm, thus called “rough” by the authors (59). Additionally, an aluminum flat punch of 5 mm diameter (RMS roughness of 2.5 μm) was used for adhesion testing (60). The adhesive force was found to be zero for flat photoresist, increased when the photoresist was plasma treated and was highest when the photoresist nanorods were situated on top of the silicon dioxide platforms. In the last two cases, adhesion was found to be strongly dependent on applied normal preload which in the case of the spherical indenter was explained by an increase in contact area. When testing the hydrophobic compared to the hydrophilic nanorods, an increase in adhesion was found; this was explained by an increase in nanorod diameter through plasma treatment and a conformational change in the rods under applied pressure which was not found in the hydrophilic ones (59). When testing with a flat punch, similar results as for the spherical indenter were found, but no influence of the applied load was measured (60). Over five iterations the pull-off force for the nanorods on top of the silicon dioxide platforms remained stable, whereas it decreased significantly for the ones on the solid substrate. This behavior was explained by the flexibility of the platforms which was thought to prevent permanent damage of the nanorods (60).

This fabrication method is capable of manufacturing hierarchical structures up to the overall area of a silicon wafer resulting in 2,500 SiO_2 platforms on a 100 mm wafer (60). It is based on complex and sophisticated processing for micro electromechanical systems

(MEMS). It requires excellent cleanroom facilities and extensive experience in microfabrication techniques. The formation of nanoscale fibers through plasma treatment is a very interesting method to structure polymer surfaces, which could easily be upscaled, but suffers from a lack in theoretical understanding of the fibril formation process. The adhesion data show much scatter which the authors justify by the rough nature of the spherical aluminum tip. One would expect less noise in the data due to the very well defined adhesion test setup. Although the authors do not mention the sphere displacement into the test surface, it was more than 3 μm (64). With this indentation depth it is very likely that no individual pillars are left, but that they all are pressed into the SiO_2 surface. Thus, not the adhesive properties of individual nanorods but of several compressed ones were tested, which might explain the scatter in the data. Certainly, JKR theory for individual fibers should not be applied as was done by the authors. The measured pull-off forces, especially when compared to the other approaches, were very low. More recently, Northen *et al.* developed a switchable adhesive which allows to control adhesion via a magnetic field (65, 66), but again the overall adhesion was relatively small.

2.2.2.9 Direct drawing of micro and nanofibers

This method, although no paper has been published so far, is used to mimic fibrillar adhesives (67) and it holds the potential for successfully fabricating such structures (68-71). The process relies on the stretching of a polymer melt (68, 70), or a polymer solution (69-71). After the elongation, the polymer is either cooled or the solvent is evaporated. No adhesion data have been published.

2.2.3 Summary of current literature

In order to give a well-arranged and easy to grasp overview over the current efforts to fabricate fibrillar dry adhesives and especially to visualize the adhesion performance, in Figure 2.3, the published adhesion strength data (pull-off force per apparent contact area) is plotted vs. the feature size.

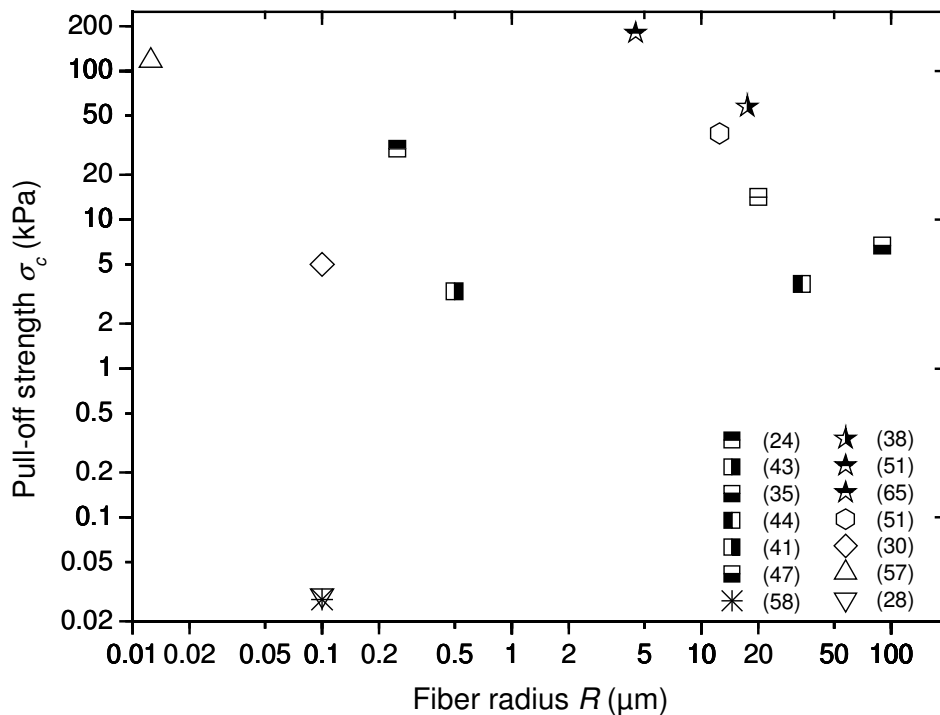


Figure 2.3: A comparison of the up-to-date published adhesion strength (pull-off force per area, σ_c) data versus the fiber radius.

The literature review demonstrates that many different approaches for the fabrication of bioinspired fibrillar adhesives have been developed and applied. This results in structures with a wide range of pillar radii and aspect ratios. As well, a whole variety of materials has been used, ranging from soft elastomers to very stiff carbon nanotubes. The adhesion properties of these structures have been investigated applying a broad range of test methods, e.g. AFM and nanoindenter based techniques. This diversity in structures, materials and test methods shows very little systematics and, as the interpretation of the

test data is not consistent, makes a quantitative comparison difficult. When using an adhesive, the most important characteristic is the adhesion force that is generated per area. This measure is called pull-off strength and is the best parameter to compare between individual adhesives. The pull-off strength however is rarely specified in publications specifically or it cannot be worked out with the information given in the papers, making it very difficult to determine systematic trends in the published data. Therefore, the present thesis focuses on the fabrication of well-defined model systems (mainly presented in chapter 3) and systematic adhesion testing. The results of these tests will be the main topic of chapters 4 and 5, concentrating on a systematic study of size (chapter 4) and shape (chapter 5) effects, which so far is missing in the literature. Chapter 6 will round off the experimental results with theoretical design guidelines for different contact shapes, developed in the form of adhesion design maps.

3 **Experimental: Fabrication of Pillars with Controlled and 3D Tip Shape**

Abstract – A new method for the fabrication of structured polymer surfaces possessing pillars with controlled 3D tip shapes resembling those found in biological attachment devices is reported. The fabrication strategy exploits the filling mechanism of 2D lithographic templates, combined with inking and printing steps using elastomeric precursors with various viscosities and crosslinking kinetics. Homogeneously structured areas about one square centimeter in size were obtained which allow reproducible and reliable testing of the adhesion behavior. With these structures it is possible to investigate the influence of contact shape (chapter 5) on the adhesion of structured surfaces and pave the road to a better understanding of biological attachment systems and to optimum designs of artificial analogues.

3.1 Introduction

The literature review given in the previous chapter clearly illustrates the need for systematic adhesion testing on well-controlled fibrillar model systems allowing the investigation of size and shape effects on dry adhesion. The structures published so far, with only two exceptions (39, 52), all terminated in flat punch-like pillars. In contrast, the tips of the fine hairs in biological systems show different shapes: spherical, conical, filament-like, band-like, sucker-like, flat and toroidal tips (see Figure 2.2b and (12)). At least as important, many biological structures are built with several levels of hierarchy. Although recent theoretical work already points out the importance of the tip shape (in particular the importance of a compliant tip, as in the gecko spatulae), this factor has not been considered in the artificial systems up to now (12). The main reason is the intrinsic difficulty and scarce availability of 3D micro and nanofabrication methods to obtain such structures over medium size areas (several cm^2) required for adhesion testing. This fact presently limits further achievements in this area.

In this chapter, a strategy which allows the fabrication of different 3D microstructured surfaces resembling those found in the attachment pads of different animals is presented (Figure 3.1). The method provides flexibility in the choice of dimensions, 3D shape, feature packing and polymer material from which the structured surfaces are fabricated. The obtained contact shapes were: pillars terminated with flat (a), spherical (b), mushroom-like (c) and spatula (d) tips, tips with concave shape (e), and pillars with split terminals (f).

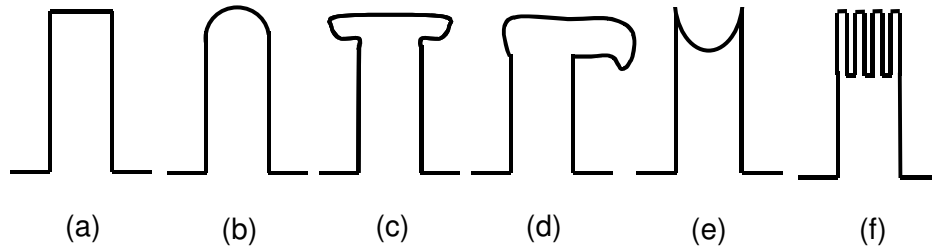


Figure 3.1: Different contact shapes obtained and tested (except for (f)).

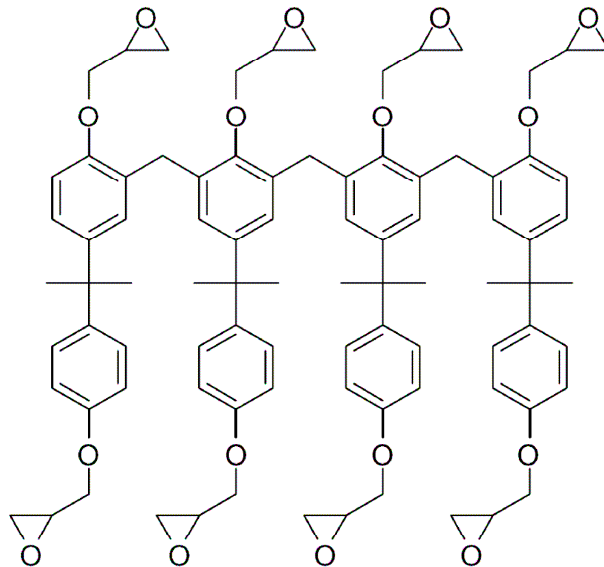
3.2 Experimental

3.2.1 Photolithography

In a first step, a suitable fabrication route for the 2D masters had to be chosen. This method had to yield well-defined structures, allow control over pillar radius and aspect ratio, be reasonable fast and be able to generate structures over large enough areas for reproducible adhesion testing. The method of choice was contact photolithography with SU-8 as photoresist. SU-8, first developed by Shell Chemicals for IBM, is an epoxy-based negative tone photoresist for the fabrication of high aspect ratio structures. It can be exposed by ultraviolet light, electrons (e-beam lithography) and X-rays (72, 73). Conventional spin-coating allows resist thicknesses between 1 and 300 μm . Multilayer coatings yield thicknesses up to 2 mm (72). After curing, SU-8 has a Young's modulus of 4.9 GPa, a glass transition temperature above 200°C and a degradation temperature above 380°C (74). These, and other physical properties, are summarized in Table 3.1. Figure 3.2 presents the molecular structure of SU-8.

Table 3.1: Physical properties of the SU-8 photoresist (74).

Property	Value
Young's modulus, E (postbake at 95°C)	4.02 GPa
Young's modulus, E (hardbake at 200°C)	4.95±0.42 GPa
Biaxial modulus of elasticity, $E/(1-\nu)$	5.18±0.89 GPa
Film stress (postbake at 95°C)	16-19 MPa
Maximum stress (hardbake at 200°C)	34 MPa
Coefficient of friction, μ (postbake at 95°C)	0.19
Glass temperature, T_g (unexposed)	~ 50°C
Glass temperature, T_g (fully crosslinked)	> 200°C
Degradation temperature (fully crosslinked)	~ 380°C
Coefficient of thermal expansion, α (postbake at 95°C)	52±5.1 ppm/K
Polymer shrinkage upon crosslinking	7.5 %

**Figure 3.2:** Chemical structure of the Bisphenol A Novolak epoxy oligomer contained in SU-8 formulations. Eight reactive epoxy functionalities allow a high degree of cross-linking after photoactivation.

Photolithography is a complex multi-step processing route. Depending on the resist thickness and the actual conditions in the cleanroom, all steps require well optimized processing parameters in order to yield optimum structures and maximum resolution, especially when fabricating high aspect structures. The processing steps for standard photolithography are schematically shown in Figure 3.3.

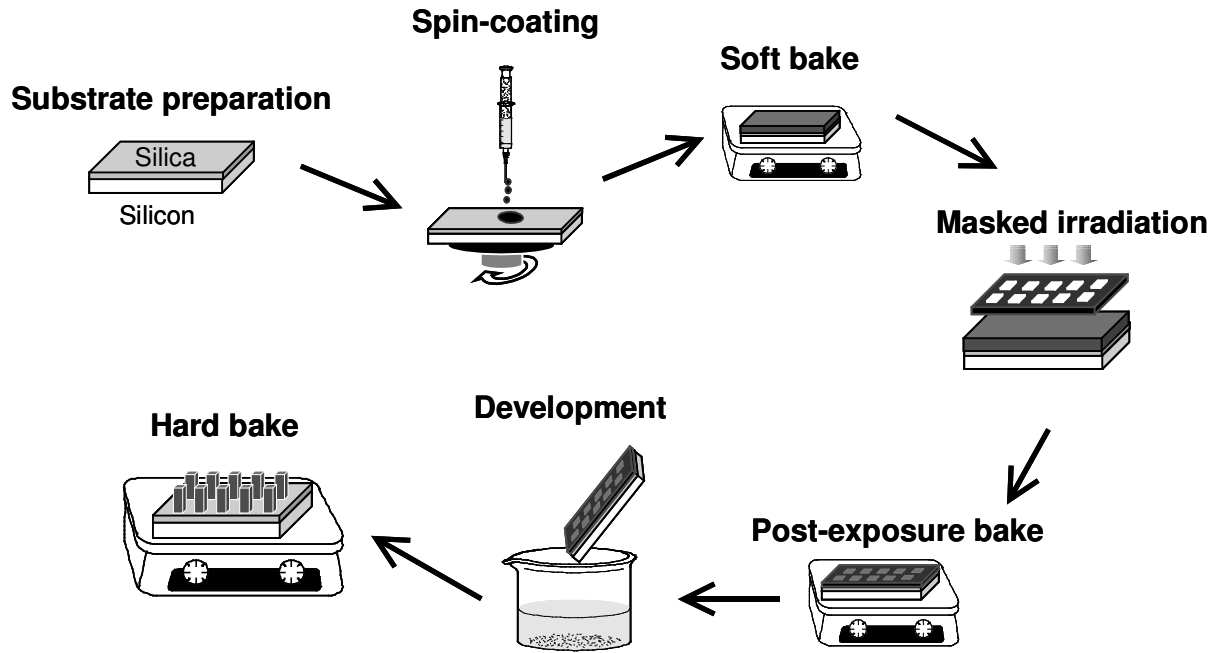


Figure 3.3: Photolithographic steps with the negative tone photoresist SU-8.

In the following the processing will be detailed. A tabular summary of the actually used processing parameters to obtain SU-8 structures with different thicknesses is given in Table 3.2.

Materials and equipment: Silicon Wafers (100 orientation) were provided by Crystec (Berlin, Germany), SU-8 types 2, 5, 25, 50 and 2075 covering a thickness range from 1.5 to 200 μm , and the developer mr-dev 600 were provided by Micro Resist Technology (Berlin, Germany). Masks were provided by ML&C (Jena, Germany) in quartz with 0.8 x 0.8 cm^2 chrome patterned fields.

Lithographic SU-8 templates: Wafers were first cleaned in piranha solution (5:1 $\text{H}_2\text{SO}_4:\text{H}_2\text{O}_2$) overnight and rinsed with deionized water. The wafers were transferred into the cleanroom and rinsed with acetone and blown dry with nitrogen before lithographic processing. A filter WG 320 supplied by Edmund Optics (Karlsruhe, Germany) was used for cutting off irradiation wavelengths below 320 nm, which is

important since SU-8 is very sensitive to smaller wavelengths resulting in a strong negative profile and limited resolution. Lithography with SU-8 was performed using a mask aligner Karl Suss MJB3 (Garching, Germany). The structured surfaces were characterized using a white light interferometer ZYGOLOT New View 5000, scanning electron microscopes Hitachi S4800 and LEO 1530 VP, and a contact angle equipment from Data Physics OCA H 150 Plus.

Table 3.2: SU-8 characteristic processing times (in minutes) for different variants and film thicknesses.

Resist Thickness (μm)	2.5	5	10	20	40	50	60	80
SU-8 resist type	2	5	5	25	25	50	50	50
Spin-coating 5 s at 500 rpm + 60 s at (rpm)	1150	2050	970	1750	900	1710	1490	1200
Soft bake (min) at 65°C	1	1	2	3	5	6	7	8
(min) at 95°C	3	3	5	7	15	20	22	26
Exposure time (s)	10.5	12.0	13.5	23.0	30.5	39.8	42.8	44.4
Post-exposure bake (min) at 65°C	1	1	1	1	1	1	1	1
(min) at 95°C	1	1	2	3	4	5	6	8
Development (min)	1	1	2	4	6	6	7	9
Hard bake	30 min at 150°C							

The lithographic masters fabricated in the present study contained arrays of high aspect ratio cylindrical holes. Their lateral dimensions ranged from 2 to 50 μm in diameter and aspect ratios from 1 to 6.

Two step lithography: Lithographic fabrication by superposition of coating and irradiation steps enabled the fabrication of hierarchical structures like the ones shown in Figure 3.4 using traditional 2D setups and alignment markers on the mask for guiding superposition. In a first step, a pattern with 50 μm structures was imaged on a 40 μm thick film. After a second coating step, seven features with 9 μm diameter were imaged on the top of each 50 μm feature. Development was performed in a single step after the second irradiation. See Figure 3.4 for a schematic of the processing steps.

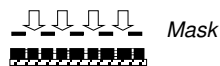
1) Coating photoresist, soft bake



4) 2nd masked irradiation



2) Masked irradiation



5) Development



3) Coating new photoresist layer



6) Soft molding, demolding

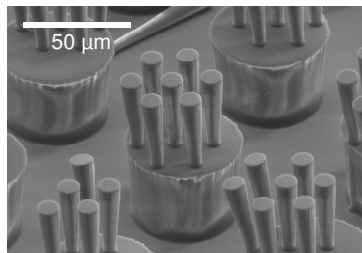


Figure 3.4: Schematic processing steps for the fabrication of hierarchical model systems and SEM picture of real structure.

3.2.2 Soft lithography and inking

Since SU-8 is a rather stiff polymer, it is close to impossible to reproducibly measure its adhesion properties. Therefore, the SU-8 master structures were replicated with polydimethylsiloxane (Sylgard 184, Dow Corning, MI, USA), the standard material for soft lithography (75, 76). The high chemical and mechanical stability of SU-8 makes it an optimum material to be used as master for molding soft elastomers. Several mechanical and other physical properties of Sylgard 184 PDMS are summarized in Table 3.3.

Table 3.3: Physical properties of Dow Corning Sylgard 184 PDMS (77-81).

Property (as cured)	Value
Young's modulus, E	1.2-2.0 MPa
Tensile strength, σ_m	6.2 MPa
Durometer hardness	50 Shore A
Viscosity, η	3900 mPa·s
Specific gravity, ρ	1.03 g/cm ³
Thermal conductivity, k	0.18 W/(m·K)
Linear coefficient of thermal expansion, α_l	$310 \cdot 10^{-6}$ 1/K
Dielectric constant, ϵ	2.65
Refractive index, n_r	1.430

The fabrication strategy is based on complete (Figure 3.5a) or partial soft molding (Figure 3.5e) on 2D masters made by lithography with elastomeric precursors with various viscosities, followed in some cases by inking (Figure 3.5b) and printing (Figure 3.5c, d) steps. The SU-8 masters were filled with different elastomeric precursors: Sylgard 184, President, Provil novo and P2. Filling with Sylgard 184 afforded arrays of pillars with flat ends (Figure 3.5a) and diameters between 2 and 50 μm . The dimensions reproduced accurately those of the templates.

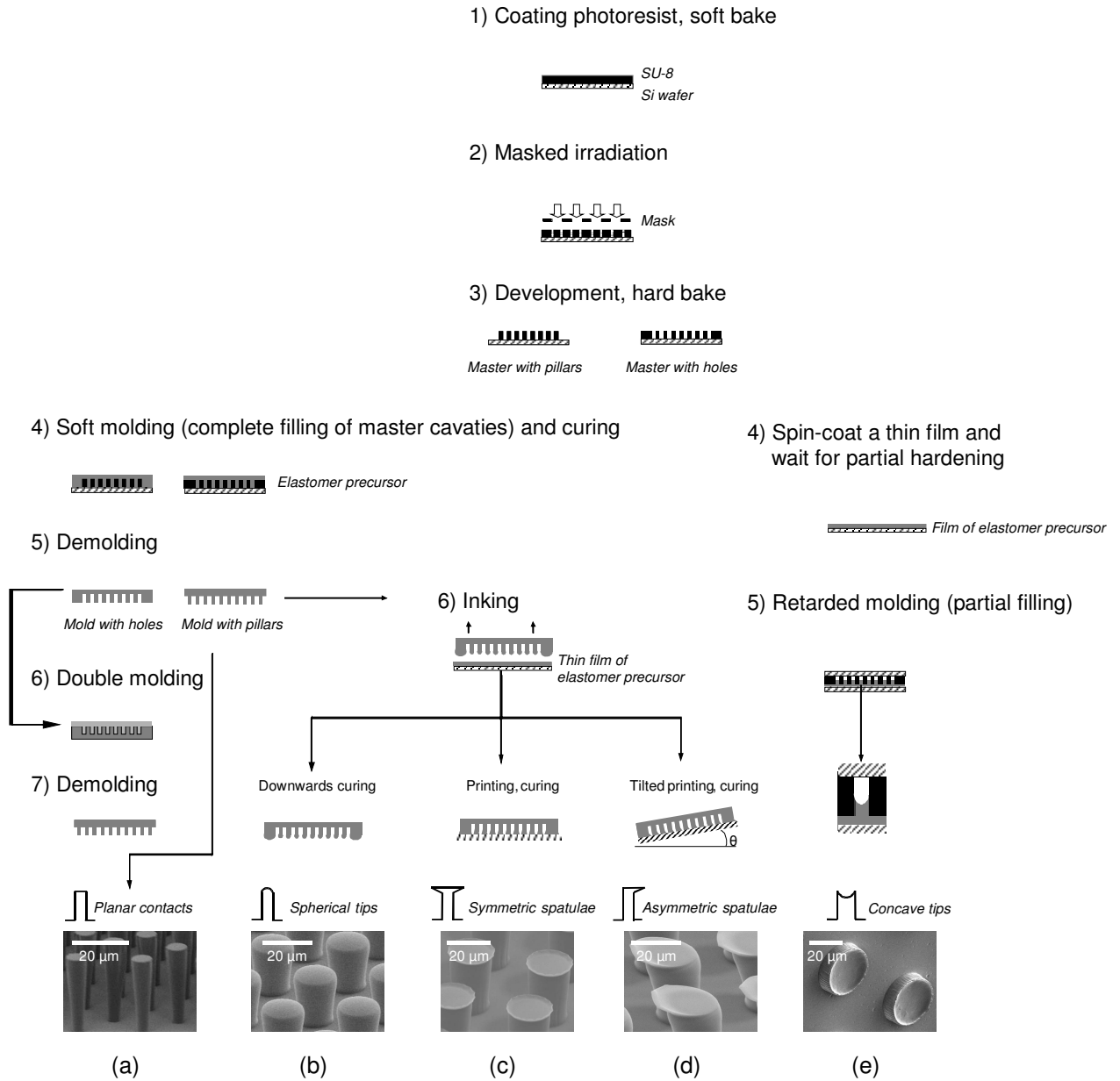


Figure 3.5: Overview of the fabrication strategies and SEM micrographs showing examples of the structures obtained.

Arrays of pillars with spherical and spatular tips were obtained by inking the Sylgard 184 structured substrates in a thin film ($\sim 6 \mu\text{m}$) of Sylgard 184 precursor (Figure 3.4b, c, d). A small drop of precursor remained on the top of the pillars. Curing of the array in upside-down orientation yielded hemispherical tips as a consequence of gravity and surface tension acting on the fluid drop (Figure 3.4b). The curvature of these structures depended on the thickness of the spin-coated film and was characterized by white light interferometry. Alternatively, the inked stamps were pressed against a flat substrate and

then cured. This rendered pillars with a flexible and flat roof. The tip diameter was a function of the spin-coated film's thickness (Figure 3.4c). The roofs could be symmetric or asymmetric depending on the tilt of the substrate during curing (Figure 3.4c, d).

Molding was also performed with elastomeric impression silicones used in the dental clinic for making denture impressions: Provil Novo, President and P2 (see below for details). These materials possess higher initial viscosities and much faster crosslinking kinetics (full crosslinking after 6 minutes at room temperature) than Sylgard 184 (fully crosslinking takes 48 hours at room temperature). They were supplied as two component systems which start crosslinking upon mixing. By soft molding these materials, pillars terminated by concave tips were obtained. The exact mechanism for the formation of this tip shape was investigated by Irma Álvarez in her diploma thesis. She provided the samples investigated in the present work. The dimensions of the resulting structures depended on the material, the delay time for starting the soft molding process after mixing the components and on the cavity dimensions of the master (diameter and height). Exact details for each step and process of the fabrication approach are given below.

Materials and equipment: Hexadecafluoro-1,1,2,2,-tetrahydrooctyltrichlorosilane was bought from ABCR (Karlsruhe, Germany). The dental impression elastomers P2 and Provil Novo Light Body were supplied by Heraeus Kulzer Dental (Hanau, Germany) together with the necessary mixing tools. President Light Body was purchased from Coltène Whaledent (Langenau, Germany). Modralit 3K was purchased from Dreve Dentamid GmbH (Unna, Germany), Sylgard 184 from Dow Corning (MI, USA).

Silanization of the SU-8 templates: Perfluorination of the SU-8 patterned wafers was performed by silanization with Hexadecafluoro-1,1,2,2-tetrahydrooctyltrichlorosilane. Silanization over the gas phase was conducted in an evacuated desiccator for 30 minutes using 20-50 μl of the fluoroderivative. The wafers were baked for 30 minutes at 95°C in vacuum to stabilize the coating by increasing lateral crosslinking and by reaction with free OH groups at the resist surface. Silanization increased the contact angle of the silicon wafer from 10° to 113° and for the cured SU-8 from 73° to 115°.

Soft molding on lithographic templates: A 10:1 ratio of Sylgard 184 prepolymer and crosslinker was mixed, degassed and poured on the silanized SU-8 structured wafer. Curing 14 h at 65°C under light vacuum ensured complete filling of the template and formation of accurate elastomeric negatives. Careful peel-off of the negative from the mold was necessary especially with high aspect ratios to avoid template damage.

Inking: A 10:1 ratio of Sylgard 184 prepolymer and crosslinker was mixed, degassed and spin-coated onto a silicon wafer to obtain film thicknesses $\sim 6 \mu\text{m}$. Typical spinning rate and time was 9000 rpm for 100 s. Higher spinning speeds were not achievable with the equipment available for this thesis. Previously molded Sylgard arrays of pillars were inked in the spin-coated film and cured upside-down in an oven during 14 hours at 65°C. A nearly hemispherical cap formed at the top of the pillars as a consequence of gravity and surface tension. The dimensions and radii of curvature were characterized by white light interferometry.

Printing: The inked patterns were pressed against a perfluorosilanized wafer before curing for obtaining mushroom- and spatula-like structures. Curing of the assembly was performed in horizontal and tilted arrangements in an oven during 14 hours at 65°C.

Retarded molding with Provil Novo and President: A 1:1 ratio of polymer base and catalyst paste were mixed for 30 seconds. Homogeneous ~ 0.5 mm thick films were prepared by spin-coating the mixture on a silicon wafer during different times. Delay times ranged between 4 and 6 minutes. The SU-8 mold was deposited vertically against the film and pressed with a 250 g weight. The systems were allowed to harden for at least 10 minutes.

Retarded molding with P2: The mixture of the polymer base and the catalyst paste were deposited on a silicon wafer via a mini-extruder provided by the supplier. Approx. 0.5 mm thick films were prepared by dragging a spatula across the mixture. The SU-8 mold was deposited vertically against the film and pressed with a 250 g weight. Delay times ranged between 1 and 5 minutes. The system was allowed to harden for at least 10 minutes.

3.3 Results and Discussion

Arrays of pillars terminating in flat (Figure 3.1a), spherical (b), mushroom-like (c), spatula (d) and concave tips (e) and pillars with hierarchical structure (f) were obtained. The method does not require use of complex 3D structuring techniques like multiphoton, holographic lithography, or nanomachining with focused ion beam (82, 83). Its flexibility and wide applicability rely on the fact that it exploits intrinsic polymer properties to obtain pillar patterns with well-defined 3D tip shapes from simple 2D arrays of holes. Homogeneously structured areas of one cm² were obtained which will allow reproducible and reliable testing of adhesion properties (see the following two chapters).

The shape of the structures was reproducible, controllable and remained constant across the whole patterned field. These effects were not unique for these systems, but were

general to any filling process and could be exploited for controlled 3D micro and nanopatterning using simple 2D molds (84). A recent work has been published where Sylgard 184 pillars of different heights were obtained by controlled incomplete filling of 2D molds, but no information on the tip shapes was given (85).

The low Young's modulus of the Sylgard 184 material limits the aspect ratio of the pillars that can be obtained (75). Gravity, adhesion and capillary forces exert stress on the pillars and may cause them to collapse. In fact, pillar collapse was observed in pillars with aspect ratios > 5 , in accordance to theoretical predictions (50, 86-92). Higher aspect ratios can be obtained by molding with harder materials, e.g. composite PDMS (90, 91, 93), bilayer PDMS (91, 92, 94), photocurable PDMS (53, 95), polyolefins (96), PDMS with polymer-reinforced sidewalls (97), fluoropolymers (95, 98, 99), photocurable perfluoropolyethers (100), photocurable fluorinated organic-inorganic hybrids (95, 101-105) or photocurable polyurethane acrylates (106, 107).

Arrays of PDMS pillars were also fabricated by double molding of SU-8 masters containing arrays of pillars. This method was applied to the cases where SU-8 masters with holes could not be obtained, due to limits in lithographic resolution. In a first step, Sylgard 184 molds containing arrays of holes were fabricated, silanized with a perfluorosilane, cured at high temperature, and refilled with Sylgard 184 precursor. After curing at lower temperatures and careful peel-off, a positive replica of the initial SU-8 pillar pattern was obtained. That the shape of those pillars was slightly different from the one obtained by direct molding will be discussed and demonstrated to be important for the adhesion performance in chapter 5.

The inking and printing steps were successfully performed manually for pillars with diameters between 2 and 50 μm and heights above 5 μm . Shorter pillars got completely dipped in the 6 μm thick Sylgard 184 film during printing and an inhomogeneous film covering the whole structure was obtained. Thinner Sylgard 184 films could not be obtained (the maximum spinning rate was 9000 rpm). In the cases where inking and printing failed, a continuous film connecting all pillars, or inhomogeneously distributed patches of elastomeric precursor bridging groups of pillars were obtained (see Figure 8.1 in appendix A). This was a consequence of misalignment between the pillar array and the precursor film during printing. It is believed that the use of a positioning stage to control printing depth, printing force and vertical pull-out would lead to significant improvements in the homogeneity.

In order to understand the filling mechanism and the forces driving the formation of tips with concave shape, the influence of the following processing parameters on the final shape was tested independently: applied external pressure, mold surface energy, polymer film thickness, initial precursor viscosity, the cavity geometry of the master (diameter and depth of the holes), as well as the crosslinking kinetics. This was the work of Irma Álvarez during her diploma thesis (84). No differences were found in molded structures obtained under different external pressures (applied weights from 120 to 500 g), from different film thicknesses (between 0.2 and 1.5 mm, well above structure height), or from molds with different surface energies (perfluorinated against non-perfluorinated molds with contact angles 73° and 115° respectively). Note that the contact angles of the materials in cured state are not significantly different: President 94° , Provil Novo 90° , PDMS 108° , and P2 62° .

3.4 Conclusions

In this chapter a novel approach to fabricate bioinspired adhesive surfaces with different 3D microtopographies using a single rigid 2D mold and combining micromolding and printing/inking approaches is described. The interplay of polymer viscosity and curing kinetics during mold filling has been exploited, thereby overcoming the need of expensive master molds for each variant. This fabrication approach does not require any complex 3D patterning technique or special equipment and can be extended to the fabrication of 3D nanostructured surfaces by using micro and nanopositioning stages instead of manual inking and printing. Arrays of pillars terminated with flat, spherical, concave, mushroom- and spatula-like tips and hierarchical structures have been obtained. Even though they are meant as model systems, they strikingly well resemble the shapes found in natural attachment organs. Adhesion studies on these structures will be presented in the following two chapters.

4 **Effects of Pillar Radius, Aspect Ratio, and Preload**

Abstract – Inspired by biological attachment systems, micropatterned elastomeric surfaces with pillars of different heights (between 2.5 and 80 μm) and radii (between 2.5 and 25 μm) were fabricated. Their adhesion properties were systematically tested and compared with flat controls. Micropatterned surfaces with aspect ratios above 0.5 are found to be more compliant than flat surfaces. The adhesion significantly increases with decreasing pillar radius and increasing aspect ratio of the patterned features. A preload dependence of the adhesion force has been identified and demonstrated to be crucial for obtaining adhesives with tunable adherence.

4.1 Introduction

The attachment pads of many insects and geckos are covered with long micro to nanosized hairs with characteristic shapes and mechanical properties. This remarkable surface topography enables these animals to firmly attach to and easily detach from almost any kind of surface. Much recent work has been directed to a theoretical understanding and modeling of the complex interplay of physical, chemical and engineering factors behind this adhesion mechanism (6, 7, 10, 108, 109). However, the role of many of these parameters still remains unclear.

As nature reveals, this adhesion concept promises enormous application potential. As a consequence, research efforts have turned to obtaining artificial, bioinspired adhesives (55). First, simplified analogues consisting of microsized vertical pillars with modest aspect ratios were obtained by soft molding elastomeric precursors on microfabricated templates, by hot-embossing polymer melts with microfabricated masters, by lithographically structuring resist films, or by direct drawing polymer fibers (24-26, 34, 39, 45, 52, 55, 56, 58, 59, 110). Nanosized pillars with higher aspect ratios were also fabricated by filling nanoporous membranes with polymer solutions or low-viscosity precursors (26) or as vertically oriented multiwall carbon nanotubes (57, 58). Judging the progress is made difficult by the fact that questionable adhesion tests, e.g. with AFM tips, are sometimes employed. Also, few detailed and systematic studies (44, 45, 55, 56, 59) of fibrillar adhesives are available.

The manufacture of more complex structures, closer in design and performance to those in nature, is still a difficult task with state-of-the-art micro and nanofabrication technologies. In addition, the difficulty of performing and interpreting adhesion tests on patterned surfaces complicates the analysis of published data and the extraction of significant experimental information. In this context, this work focuses on the fabrication and testing of elastomeric model surfaces possessing pillars with controlled shape and material properties. The pillar arrays were made by soft molding polydimethylsiloxane (PDMS, Sylgard 184) on patterned SU-8 films on Si wafers. The radius (r), the height (h) and the aspect ratio ($\lambda = h/2r$), of the pillars were systematically and independently varied. The influence of these parameters on the adhesion properties of the surface will be described and compared with theoretical predictions. The discussion of the results presented in this chapter will contribute to a better understanding and more accurate identification of the relevant factors responsible for adhesion in biological systems and will guide the design of bioinspired artificial analogues.

4.2 Experimental

Soft molding of Sylgard 184 was performed on arrays of holes made by lithographic patterning of thick SU-8 films as described in chapter 3. The high chemical and mechanical stability of SU-8 makes it an optimum system for molding soft polymers. The dimensions of fabricated Sylgard 184 pillars ranged from $r = 2.5$ to $25 \mu\text{m}$ in radius and $h = 2.5$ and $80 \mu\text{m}$ in height. The aspect ratio λ was between 0.5 and 4. The interpillar distance was identical to the pillar diameter and the packing geometry was hexagonal or square. The resulting pillar packing density was 22.7 % for the hexagonal and 19.6 % for the square patterns. The patterned area was $0.8 \times 0.8 \text{ cm}^2$ for each geometry.

The adhesion performance of the hexagonal patterned surfaces and flat controls was tested by recording load-displacement curves obtained with a home-built indentation equipment (111). This apparatus consists of a glass spring mounted on a piezoelectric crystal (P-611 NanoCube from Physik Instrumente, Karlsruhe, Germany) and coupled to a hexapod nanopositioning stage (F-206 from Physik Instrumente, Karlsruhe, Germany). A sapphire sphere with a diameter of 5 mm provided by Goodfellow (Huntingdon, U.K.) was glued to the free end of the glass spring. Using a spherical tip solves the problem of possible misalignment between probe and surface occurring in flat-flat contacts. The patterned sample was placed on the positioning stage and the sphere was brought in contact. After compressive preloading, the sphere was retracted at a constant rate of 1 $\mu\text{m/s}$ until pull-off occurred. The maximum vertical displacement of the piezo was 100 μm and the positioning accuracy was 1 nm. The stage had a maximum travel range of 12 mm with an accuracy of 100 nm. Spring deflection during contact was monitored via a laser interferometer (SP 120 from SIOS, Ilmenau, Germany). Calibration of the spring allowed conversion of the deflection into force. Using a spring with stiffness 130 Nm^{-1} , forces up to 4 mN could be measured with a resolution of 1 μN . Data collection was performed with a Labview software package. The sapphire sphere was cleaned with high-purity ethanol before each test.

Since the mechanical properties of polymers may change over time, all adhesion experiments were performed on one-day old samples fabricated under the same experimental conditions. The laboratory temperature ($\sim 22^\circ\text{C}$) and humidity ($\sim 20\%$) were registered for each measurement. A minimum of five measurements was performed for each data point. For comparison, adhesion tests under the same conditions were also conducted with flat specimens.

4.3 Results

Arrays of elastomeric pillars with dimensions ranging from 1 to 25 μm in radius and 2.5 and 80 μm in height could be successfully fabricated. SEM images of selected arrays are shown in Figure 4.1 (see also Figure 8.2 in appendix B). Fig. 4.1b is a close-up of Fig. 4.1a which exhibits flat-ended punches with sharp contours. Condensation (lateral collapse) of pillars was observed in arrays with aspect ratio greater than 3 for all pillar radii (see condensation patterns in Figure 4.1c and 4.1d). The demolding step during fabrication seemed to be critical for avoiding condensation. In fact, arrays with λ up to 4 and radius $r > 2.5 \mu\text{m}$ showing no evidence of condensation could be obtained by careful demolding (Figure 4.1a). Condensation occurs when the adhesive forces between pillar tips in contact overcome the forces required for bending the pillar. Theoretical models predict critical aspect ratios for condensation between 2.5 and 5.2 for pillars with $r = 2.5 \mu\text{m}$, and between 5.4 and 11.2 for pillars with $r = 25 \mu\text{m}$, assuming $E = 2.6 \text{ MPa}$, packing density 0.2267, and $\gamma_{\text{PDMS-PDMS}} = 0.044 \text{ Jm}^{-2}$ (see (26, 44, 50, 88, 112)). These values agree with the experimental data.

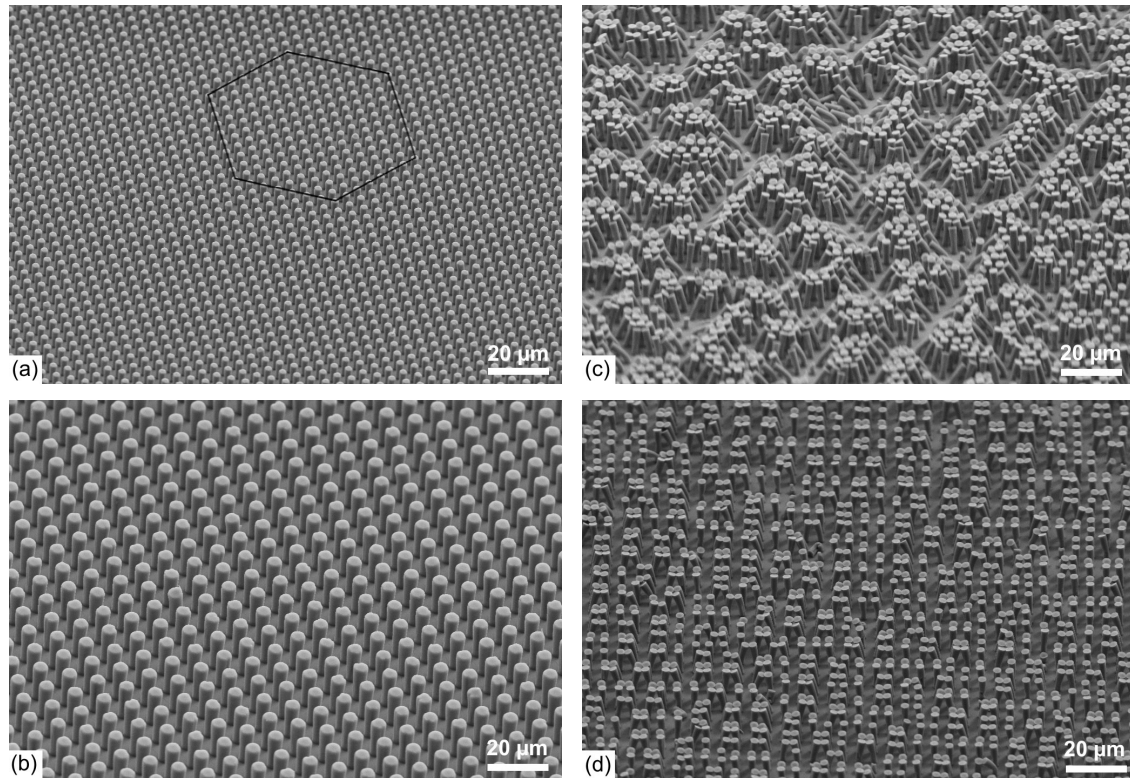


Figure 4.1: SEM micrographs showing arrays of pillars made by soft molding Sylgard 184 on SU-8 photolithographic templates. Pillars have a radius of $2.5\ \mu\text{m}$ and a height of about $20\ \mu\text{m}$. The minimum interpillar distance is $5\ \mu\text{m}$. The hexagonal symmetry is highlighted by the superimposed line. Specimens were coated with $10\ \text{nm}$ Au/Pd before taking pictures. Micrographs (a) and (b) show pillars in hexagonal packing. In (c) and (d) images of collapsed pillars with hexagonal and cubic symmetry are shown. A characteristic distribution of clusters was observed depending on the packing symmetry. See Figure 8.2 in appendix B for images of additional patterns.

The geometry of the adhesion tests is depicted in Figure 4.2, together with a representative experimental force-distance curve obtained on patterned surfaces with pillars with $r = 25\ \mu\text{m}$. Additional curves at different preloads can be seen in Figure 8.3 in appendix B. During loading, the curves initially show a non-linear response related to the change in the stiffness as the number of pillars in contact increased. No significant approach-retraction hysteresis could be noticed as an indication that the deformation of the sample is predominantly elastic and viscoelastic effects, while present, can be neglected. During retraction, the curves showed several points of instability where the force changed abruptly. The resulting saw-tooth profile was associated with isolated detachment events of the peripheral pillars in the contact area. These effects were not seen when measuring

adhesion to a planar surface. The final detachment event gives the value of the pull-off force (P_c).

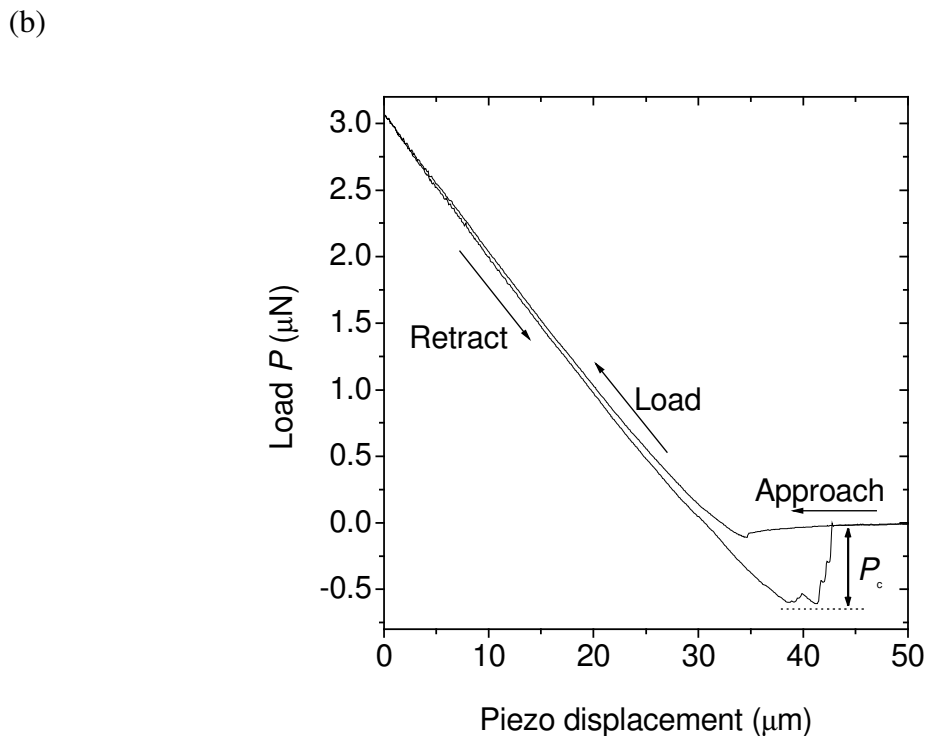
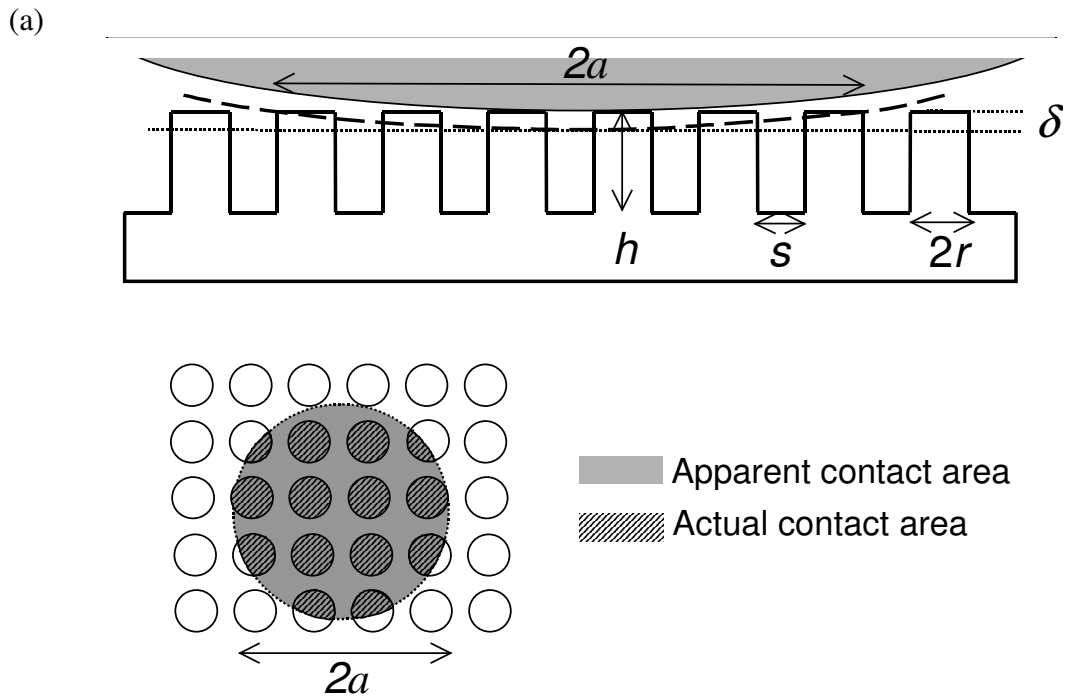


Figure 4.2: Details of the test procedure: (a) Schematic of the adhesion test geometry: δ indentation depth, a radius of projected contact area, r pillar radius, h pillar height, s spacing between pillars. The lower schematic shows a plan view of the adhesion test. Note that in actual tests $a \gg r$ unlike in this simplified schematic. (b) Load-displacement curve obtained from a patterned surface with $r = 25 \mu\text{m}$ and $\lambda = 1$. A saw-tooth profile can be observed during retraction before pull-off occurs. See Figure 8.3 in appendix B for additional data.

The influence of the fabrication procedure, the environmental conditions (temperature and humidity), and the experimental parameters (indentation rate, preload) on the adhesion results were first tested and later carefully controlled to allow meaningful comparison of data obtained from different specimens. The time elapsed between the fabrication process and the adhesion measurements was critical for reproducibility. Because Sylgard 184 hardens upon storage, older samples show more than twice the Young's modulus than as-prepared samples and therefore different load-indentation curves (80). Changes in humidity can also influence the experimental P_c values as liquid bridges around the contact areas result in higher adhesion. Meniscus forces on patterned surfaces depend on the geometry and radius of the contact surfaces, the hydrophobicity of the materials and the number of contact points (109, 113-115). To exclude meniscus effects as an additional variable, all measurements were performed at 20 % humidity.

Figure 4.3 shows the experimental value of P_c for different compressive preloads on flat and patterned samples with constant $\lambda = 1$. It is seen that for flat samples P_c does not vary significantly with the preload. In contrast, P_c increases significantly with the preload for patterned surfaces until a plateau is reached. This increase is more pronounced for pillars with smaller radii; for $r = 2.5 \mu\text{m}$, P_c increases up to five times with increasing preload. Patterns with higher λ were also measured and gave similar profiles (data shown in appendix B).

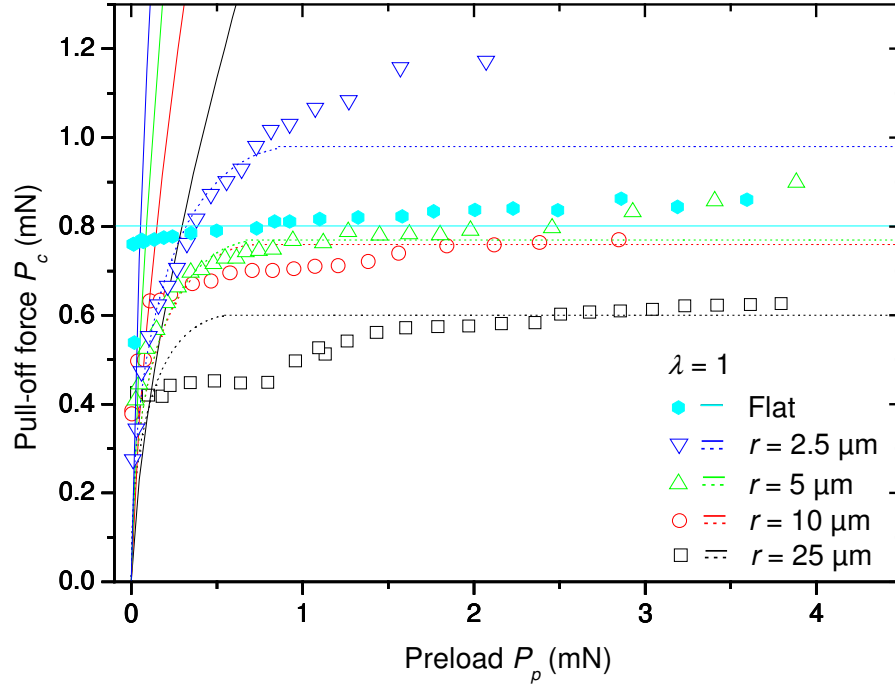


Figure 4.3: Dependence of the pull-off force, P_c , on the preload, P_p , in adhesion experiments on flat and patterned surfaces with pillars of different radii and constant aspect ratio λ of 1. The solid lines represent the theoretical values according to contact splitting theory assuming JKR behavior (10) ($E^* = 1.43 \text{ MPa}$, $\gamma = 0.068 \text{ Jm}^{-2}$). The dotted lines represent the theoretical values according to the spring model (116). The experimental error is within the size of the symbols.

Patterned surfaces with decreasing pillar radius showed higher P_c at any preload, in agreement with the contact splitting principle (10). The flat surface showed higher P_c at low preloads than the patterned ones. This is mainly due to its higher actual contact area (Figure 4.2), which outweighs adhesion enhancement due to split contact at low preloads. At preloads exceeding 0.4 mN, P_c of patterned surfaces with $r = 2.5 \mu\text{m}$ surpassed that of the flat surface.

A more meaningful parameter to compare adhesion performance is given by the pull-off strength, σ_c , which is obtained by dividing P_c by the apparent contact area, πa^2 . This area is different for each preload value and can be calculated from the experimental indentation depth by simple geometrical considerations. Figure 4.4a shows how σ_c decreases with increasing preload in both flat and patterned surfaces.

Figure 4.4b represents the same data as a function of the maximum indenter displacement δ divided by the pillar height h . Higher σ_c is clearly obtained for patterned surfaces with smaller pillar radius.

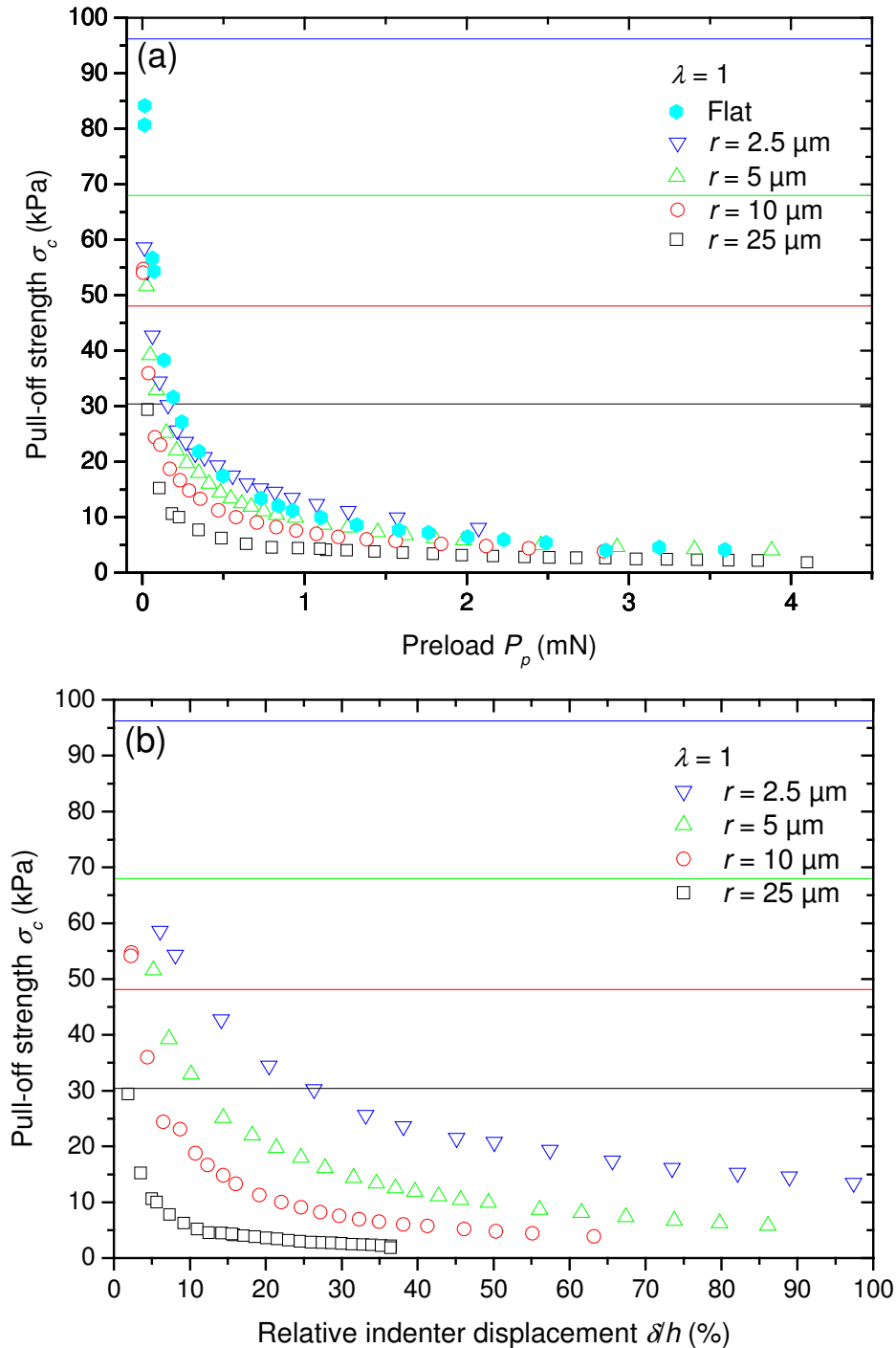


Figure 4.4: Dependence of the pull-off strength σ_c (force per apparent contact area) on preload: (a) Variation of σ_c with preload for adhesion experiments on planar and patterned surfaces with pillars of different radius and $\lambda = 1$. (b) The same data as in (a) but represented in terms the relative indenter displacement δh . The solid lines represent the theoretical values according to contact splitting theory assuming JKR behavior (10) ($E^* = 1.43 \text{ MPa}$, $\gamma = 0.068 \text{ Jm}^{-2}$). The experimental error is within the size of the symbols.

The benefit of patterning on adhesion performance can be also expressed in terms of the adhesion force divided by the actual contact area (tenacity). The tenacity of the patterned surfaces is in all cases higher than the tenacity of the flat surface, even for the largest pillars with $r = 25 \mu\text{m}$ (see Figure 8.5 in appendix B).

Similar experiments were performed on samples with pillars of various heights maintaining a constant pillar radius. Figure 4.5 shows the results obtained for pillars with $r = 5 \mu\text{m}$. A clear increase in P_c is observed at any preload when λ increases. The same tendency was observed in patterns with radius 10 and $2.5 \mu\text{m}$ (see appendix B Figure 8.6 for data on the $10 \mu\text{m}$ radius pillars). The patterns with $\lambda > 2$ show higher P_c than the flat samples at preload values above 0.25 mN or indentation depths above $2.5 \mu\text{m}$.

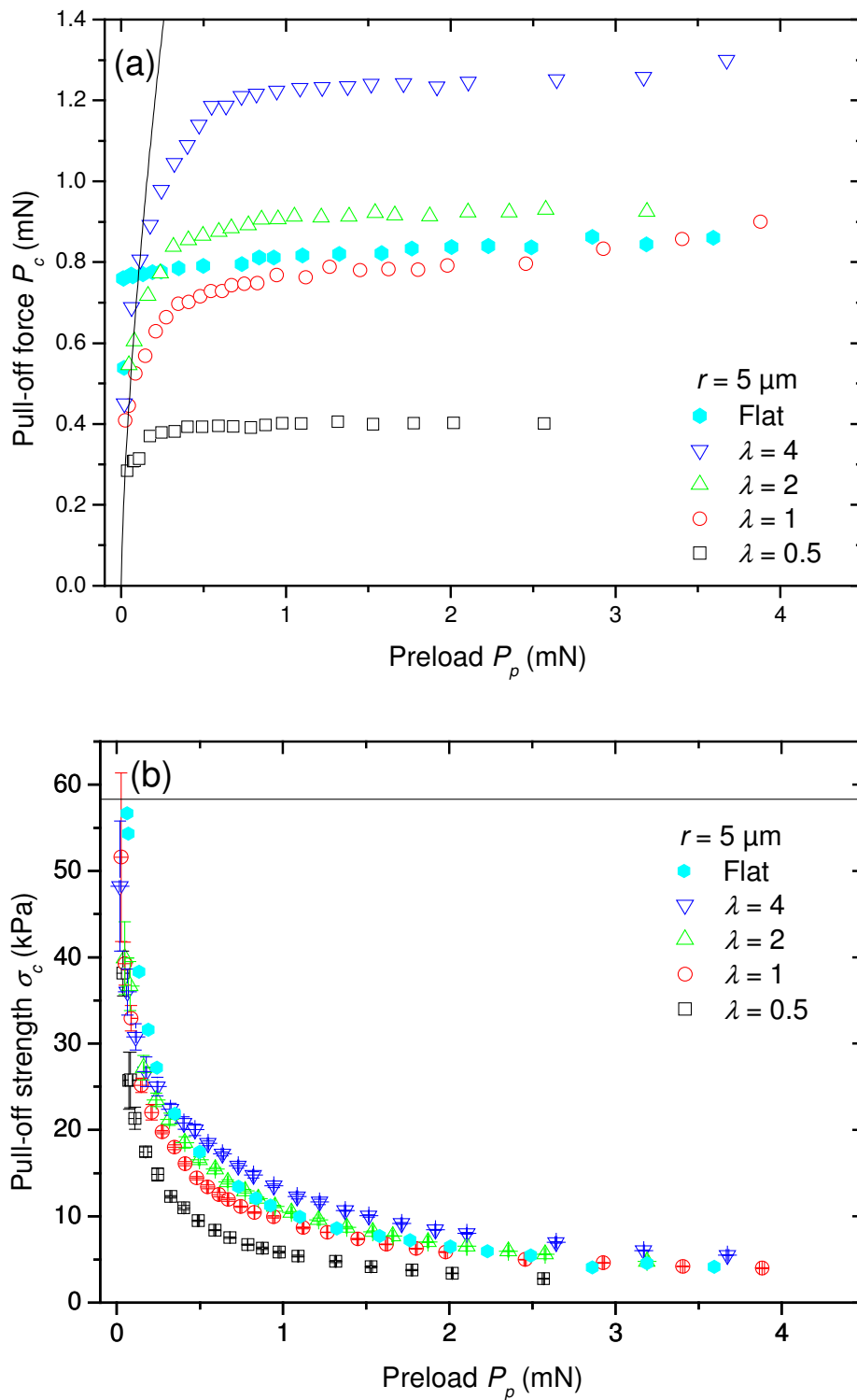


Figure 4.5: The influence of the aspect ratio on adhesion of patterned surfaces. Data correspond to pillar patterns with radius $5 \mu\text{m}$ and different heights, measured at different preloads. Solid lines correspond to theoretical values according to the JKR theory. The experimental error in the upper graph is within the size of the symbols.

4.4 Discussion

This study reports the first systematic results of radius and aspect ratio effects on the adhesion of micropatterned fibrillar surfaces. Several quantitative observations were made which will be discussed in turn.

4.4.1 Condensation patterns for different array geometries

Interesting condensation patterns with clusters of different sizes were observed for equal inter-pillar spacing depending on the array symmetry. On average, hexagonal lattices afforded bigger clusters than cubic lattices (Figure 4.1). Taking into account that condensation is detrimental to adhesion, square packing of pillars seems to be more advantageous than hexagonal packing in this respect. This has indeed been observed in biological systems (in most gecko species setae are arranged in cubic symmetry (27)) and is in agreement with theoretical modeling (27). However, there will be an obvious trade-off with the actual contact area: Because of the higher fiber packing density, a hexagonal lattice would be preferred provided that condensation can be avoided by other means.

4.4.2 Backing contact and buckling of pillars during adhesion testing

The load-displacement curves do not show any significant evidence of contact between the sphere and the backing from which pillars protrude, even at indentation depths well above the pillar height. This result agrees with data reported by Crosby *et al.* (45), who observed such contact only in the case of low aspect ratio pillars with large separations. The condition for contact with the backing has also been modeled theoretically (88, 89). If applied to the pattern geometries, backing contact would happen

in pillars with less than 1 nm height, three orders of magnitude smaller than the smallest pillar height (2.5 μm).

Buckling of high aspect ratio pillars at high preloads is another issue to be considered. Buckling would cause loss of contact between the pillar end and the sphere and would, consequently, reduce adhesion (44). The theoretical buckling criterion (88) predicts a minimum compressive load required for buckling (41 mN), which is well above the maximum preload (~ 4 mN), even for the pillars with the highest aspect ratio. For this reason, buckling events can be neglected in the experiments discussed here.

4.4.3 Effective Young's moduli of patterned surfaces

The compressive parts of the load-displacement curves were analyzed using the Hertz theory of elastic contact (16) (see section 2.1.1). When applied to a patterned surface, this approach will be valid if the contact region is considerably larger than the pillar radius, and if the extracted Young's modulus is interpreted as effective quantity (44). With these assumptions, the loading cycle of the load-displacement curves can be fitted with the Hertzian indentation model following

$$P = \frac{4}{3} E^* \sqrt{R} \delta^3 \quad (4.1)$$

where P is the applied compressive load, $E^* = E/(1-\nu^2)$ the effective Young's modulus of the surface, $\nu = 0.5$ Poisson's ratio, R is the radius of the indenting sphere and δ the indentation depth. All indentation curves from planar and patterned surfaces fitted well to this expression and the obtained values of E^* are represented in Figure 4.6 (see also Figure 8.7 in appendix B). Flat and patterned surfaces with short pillars ($h = 5 \mu\text{m}$) show the highest effective modulus, with similar values at around 1.4 MPa. Increasing the pillar

height at constant r causes a significant decrease in E^* , down to 0.6 MPa in the case of $h = 100 \mu\text{m}$. The drop of E^* is more pronounced for $\lambda < 2$ and less significant at higher values. The pillar radius does not seem to influence E^* significantly as might be expected from arrays with equal packing density.

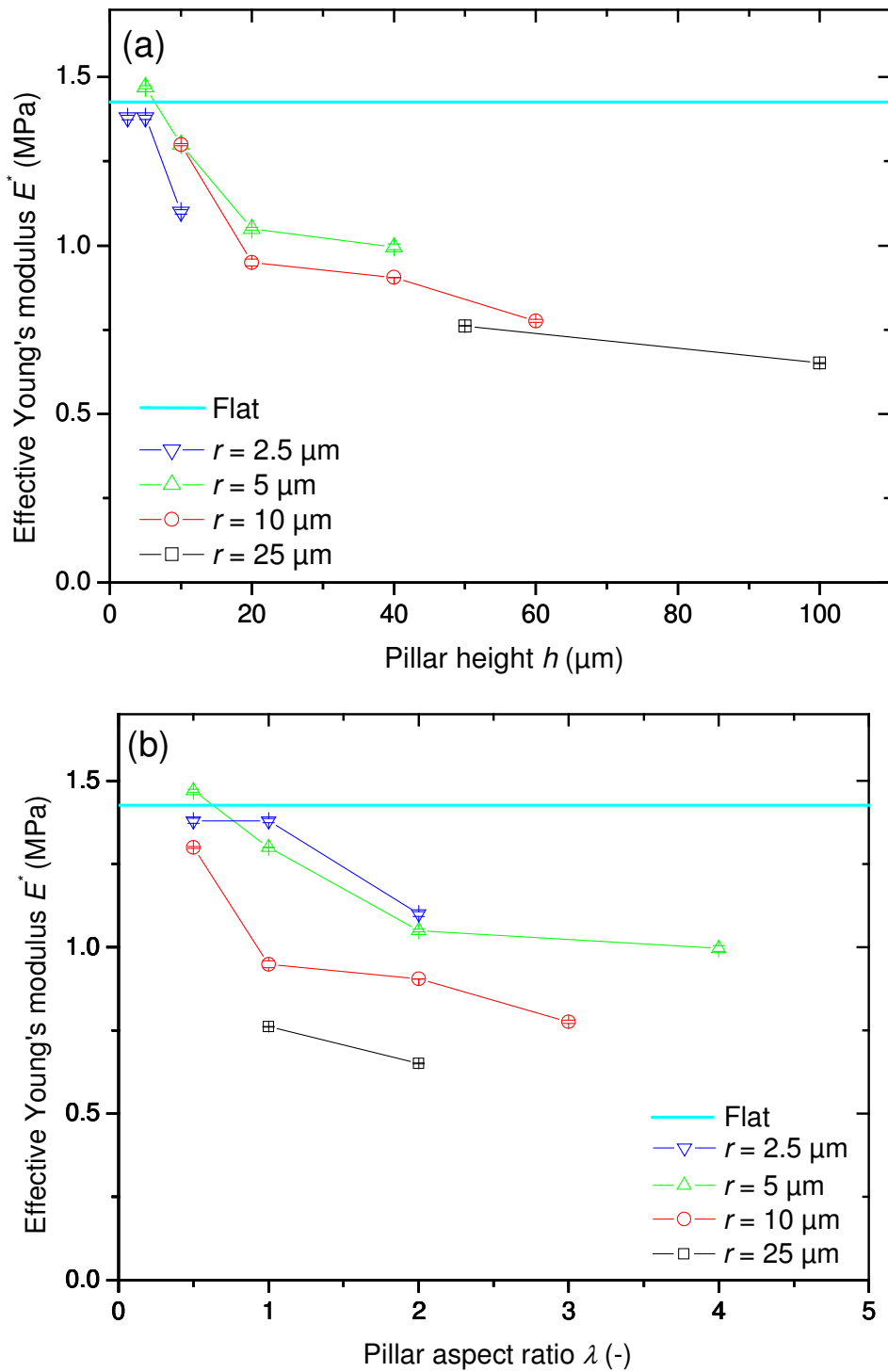


Figure 4.6: Variation of the effective Young's modulus E^* with pillar height and aspect ratio for arrays with different radius. E^* was calculated by fitting the loading curves with the Hertzian indentation model.

According to the results presented in this chapter, patterned surfaces are significantly more compliant than flat ones only for aspect ratios above 0.5. For plate-like fibrillar PDMS structures with a minimum λ of 0.6, other authors also reported a reduction of effective modulus with increasing aspect ratio (44). It is not immediately obvious why low λ patterned surfaces (with packing density 22.7 %) have similar modulus values as flat controls. The author believes that the backing material also contributes to the mechanical deformation of the surface during indentation and, for this reason, the actual contact area may not influence E^* in low λ patterns.

An increasing pillar height at constant radius seems to enhance compliance more than a decrease in pillar radius at constant height. These results are difficult to compare with similar studies in literature (44) since there the height was kept constant and the width of plate-like structures was varied. The result of Glassmaker *et al.* (44) that the effective modulus decreases with decreasing structure radius, or width in their case, is qualitatively also found in the data presented here.

4.4.4 Pull-off force versus preload

The pull-off force does not vary significantly with the preload in flat samples (Figure 4.3). This observation is in accordance with the Johnson-Kendall-Roberts (JKR) theory, which predicts a value of P_c independent of preload and modulus (18):

$$P_c = -\frac{3}{2}\pi\gamma R \quad (4.2)$$

where γ is the work of adhesion and R the radius of a sphere adhering to a plane. Taking $R = 2.5$ mm and the experimental value $P_c = 78$ mN, the work of adhesion for the non-patterned PDMS surface amounts to $\gamma = 0.068$ Jm⁻².

In contrast, P_c increases with preload in patterned surfaces up to a saturation level. The author attempts to describe this behavior by the JKR-based contact splitting theory (10). According to this model, P_c would be given by (10, 12):

$$P_c(P_p) = N(P_p) \sqrt{8\pi E^* r^3 \gamma} \quad (4.3a)$$

where

$$N(P_p) = \frac{f\pi\alpha^2}{\pi r^2} \quad (4.3b)$$

is the number of pillars in contact at preload P_p . The square-root factor in eq. 4.3a is the standard solution for an adhering flat punch; it is applicable only when the punch has higher modulus than the counter surface (117). For an elastic pillar in contact with a stiff indenter, as is the case here, the pull-off force is reduced by ca. 10 % and this equation can still be used as a first-order approximation (12). The theoretical pull-off strength can be derived by dividing $P_c(P_p)$ by the apparent contact area at a certain preload. Since the area fraction of pillars in the case here is constant, the theoretical σ_c should not show any dependence on preload. The results of the JKR theoretical predictions for P_c and σ_c are represented as solid lines in Figures 4.3 and 4.4. Obviously, this model does not describe the experimental observations.

The JKR model assumes that all pillars in contact are in tension at the pull-off event, which is not the case for a spherical indenter. A theoretical model which describes this case has been recently proposed (116). It models the contact between the pillar pattern and the spherical indenter as an array of independent elastic springs attached to a rigid hemisphere and compressed against a flat surface. During unloading, the springs at the periphery of the contact area are elongated, while the springs near the center of the contact remain in compression. When the outer springs reach the maximum elongation, they detach from the surface. As a consequence, the contact radius (and therefore the number of attached springs) decreases gradually during retraction. The contact holds until the remaining springs are no longer able to compensate the pulling force. This occurs at a critical contact radius, a_{crit} , at which the rest of the springs detach simultaneously. The pulling force at this point is the plateau force $P_{c(max)}$ and is given by (116):

$$P_{c(max)} = \frac{\pi E^*}{4Rh} a_{crit}^4 \quad \text{if } a \geq a_{crit} \quad (4.4)$$

where h is the spring (or pillar) height and E^* is the effective elastic modulus as discussed above. Note that $P_{c(max)}$ is independent of the preload and that this expression is only valid if a_{crit} has been reached during loading. Otherwise, P_c is smaller and given by (116):

$$P_c(P_p) = 2\sqrt{P_{c(max)}P_p} - P_p \quad \text{if } a \leq a_{crit} \quad (4.5)$$

It is evident that the spring model describes the experimental data qualitatively well (see dotted lines in Fig. 4.3). P_c increases with preload until it reaches a saturation level, above which P_c remains constant ($P_{c(max)}$). The discrepancy between the experimental and the theoretical plateau forces can be attributed to the error in determining a_c (see Fig. 4.8

below), which enters with the power of 4 (eq. 4.4). This error might originate in the coupling between the pillars which is neglected by the spring model.

These data suggest an interesting mechanism for tuning the effective adhesion performance of a patterned surface by modulating the applied preload. Note that wider P_c tuning ranges are possible in patterns with smaller pillar radii (Figure 4.3).

4.4.5 Pull-off force versus pillar radius

As shown in Figures 4.3 and 4.4, a decrease in the pillar radius causes a significant increase in pull-off force and strength. This is more clearly illustrated in Fig. 4.7a, where the pull-off strength is plotted against the pillar radius, on log-log scales, for three different preload values. The slope of these data defines the potential for improving σ_c by scaling the contact size and has been termed “splitting efficiency” (10, 12). Larger absolute values of the slopes result in higher gains in P_c by splitting the contact. Slopes between -0.40 and -0.46 were obtained, very close to the theoretical value predicted by the contact splitting theory (12) for pillars with flat ends, i.e. -0.50 (shown as dotted line in Fig. 4.7a). The good agreement between the JKR-based theoretical prediction and the experiments suggests that this theory can be used to explain adhesion of patterned elastomeric surfaces.

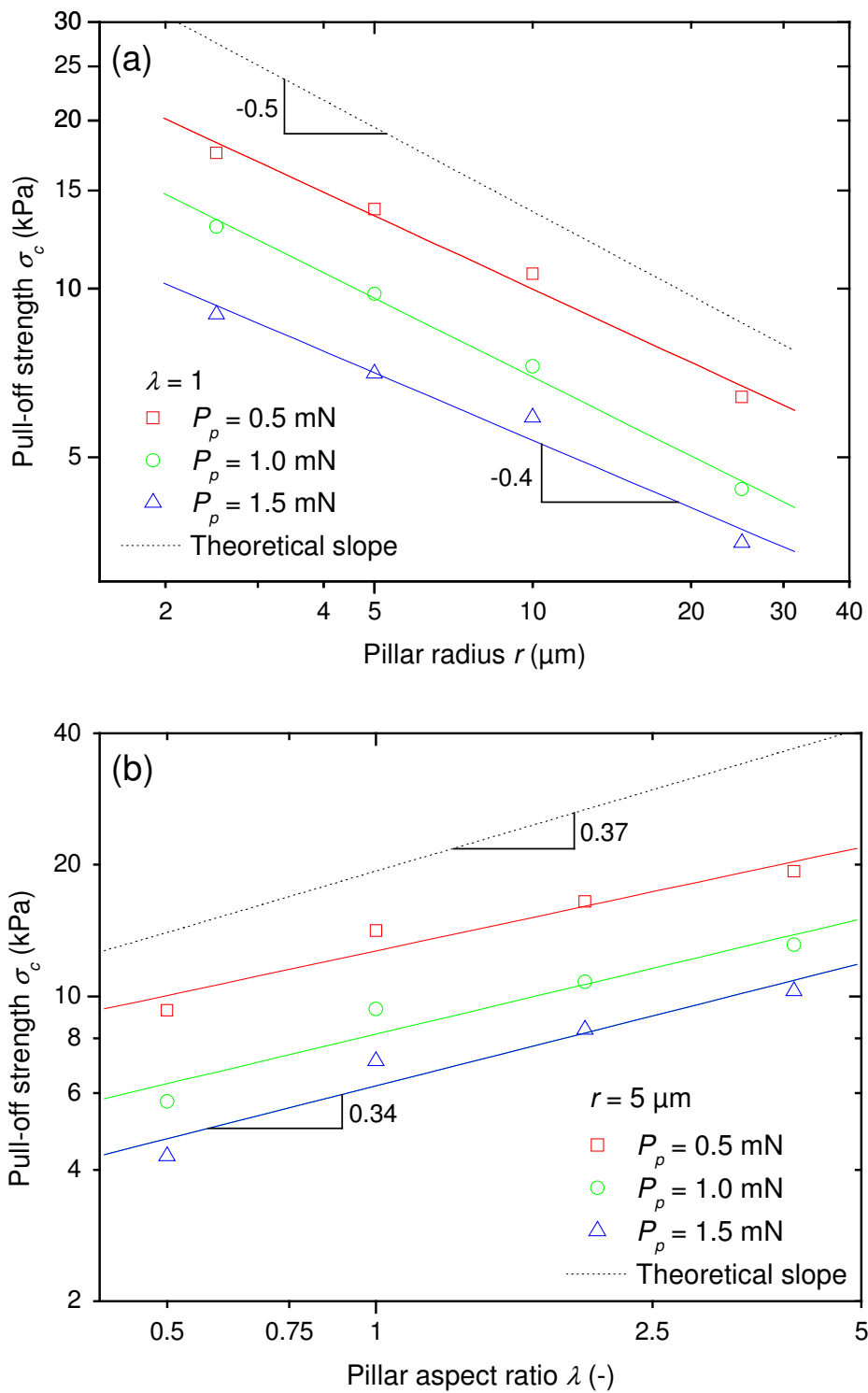


Figure 4.7: Pull-off strength as a function of pillar parameters: (a) σ_c vs. pillar radius showing the beneficial effect of smaller pillars. (b) σ_c vs. aspect ratio. In both plots, dotted lines represent the expected theoretical slope (12, 118).

4.4.6 Pull-off force versus pillar aspect ratio

Figure 4.5 has shown a 3-fold increase in P_c (at high preloads) when the aspect ratio was raised from 0.5 to 4. The increased adhesion of patterns with high λ has been attributed to a higher elastic energy dissipated at pull-off (24, 118-120), in analogy to the mechanism of crack propagation in rubbery materials (120). Assuming full dissipation, the elastic energy stored has to be added to the work of adhesion, resulting in an effective work of adhesion:

$$\gamma_{eff} = \gamma + \frac{f\sigma^*r}{E}\lambda \quad (4.6)$$

Taking a value for the interfacial strength, σ^* , typical for a soft, good adhesive ($\sigma^* = 1$ MPa (118)), and taking the experimental values $E^* = 1.43$ MPa, $\gamma = 0.068$ J/m² and $f = 0.2267$, the values of γ_{eff} corresponding to $\lambda = 0.5$ and 4 were calculated, resulting in $\gamma_{eff}(\lambda = 0.5) = 0.464$ J/m² and $\gamma_{eff}(\lambda = 4) = 3.239$ J/m². As in eq. 4.3a, P_c is expected to scale with the square root of the work of adhesion. This results in a theoretical 2.6-fold increase in P_c , when going from $\lambda = 0.5$ to 4, close to the experimental value. Figure 4.7b represents the increase in σ_c with increasing λ at three different preload values. The expected theoretical slope (0.37) according to the mentioned theories is also represented as dotted line.

Published data for the influence of the aspect ratio on the adhesion of patterned surfaces are scarce and contradictory. With some scatter range, no influence of λ on the adhesion of polyvinylbutyral fibrils with $E = 3.4$ MPa, radius 1 mm and λ between 1 and 15 was reported (23). A decrease in the adhesion force of pillar structures with $r = 100$ nm with increasing λ was also published (113), although measurements were performed only

at aspect ratios of 1 and 3 . The author believes that the data of this thesis represent the first systematic values for the increase of adhesion by increasing λ .

Finally, the influence of λ on a_{crit} and the number of pillars in contact at a_{crit} according to the spring model are addressed. These parameters can be extracted from the value of $P_{c(max)}$ as shown in Figure 4.8 (and Figure 8.8 in appendix B). At constant radius, a_{crit} and the number of pillars in contact at a_{crit} increase with increasing height or λ . For patterns with $r = 5 \mu\text{m}$, the critical radius is found to be $a_{crit} = 39 \mu\text{m}$ for $\lambda = 0.5$ and $a_{crit} = 91 \mu\text{m}$ for $\lambda = 4$. This increase is more pronounced for small radii and is almost imperceptible in pillars with $r = 25 \mu\text{m}$. This means that, in order to reach the maximum pull-off force of a patterned surface with high aspect ratio features, higher preloads are required than for low λ features. Taking the preload dependence of P_c as an effective mechanism to modulate adhesion performance, high λ patterns will thus offer a much wider modulation range than low λ patterns. Since fitting the data presented in Fig. 4.3 with the spring model is not perfect and the critical contact radius is sensible to small changes in the saturation value of the pull-off force, the a_{crit} values have rather large error bars as can be seen in Figure 4.8a.

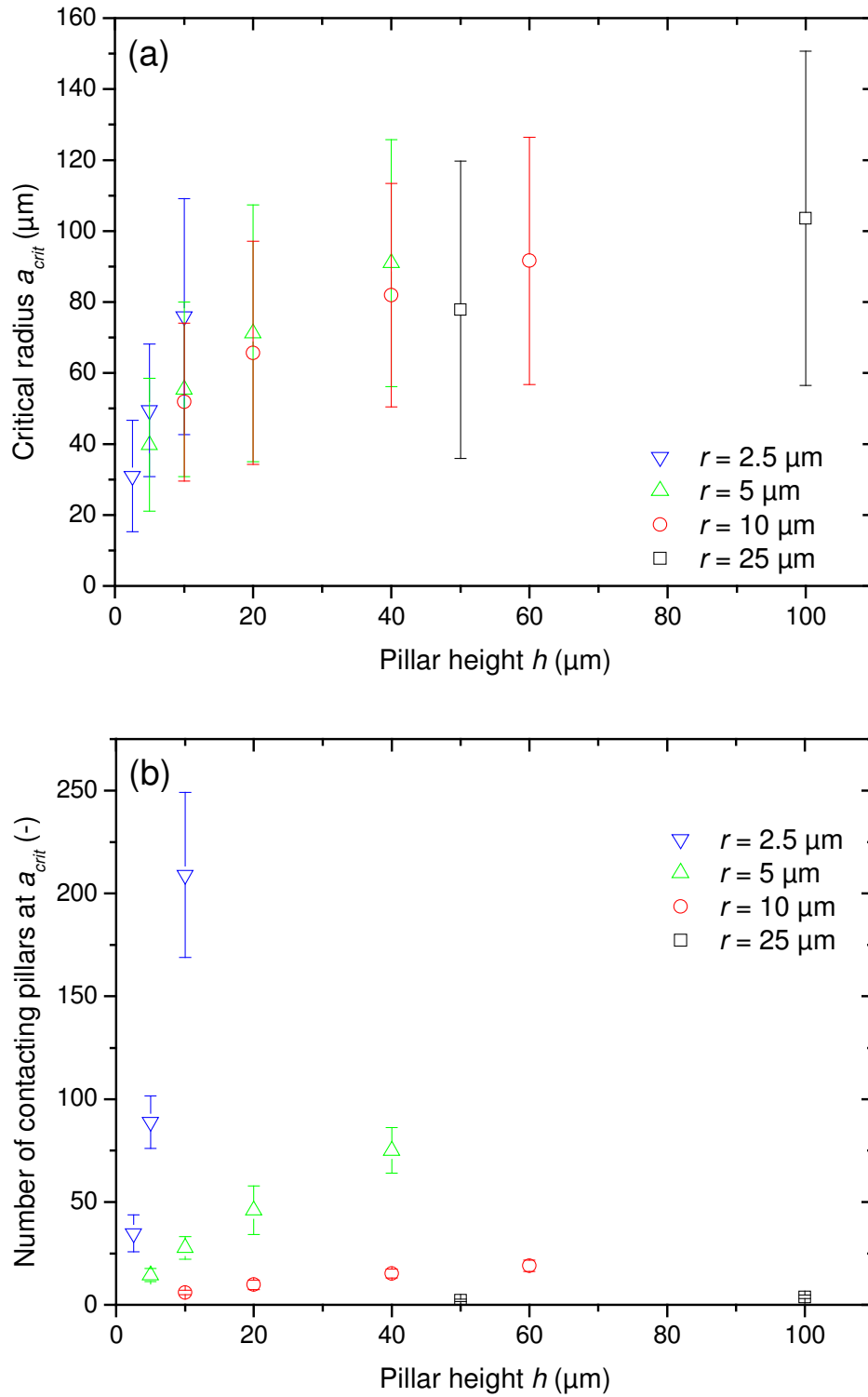


Figure 4.8: Critical contact radius a_{crit} and number of pillars in contact at a_{crit} for different pillar radii and heights. The values were determined by fitting the P_c vs. P_p data with the spring model (116).

4.4.7 Comparison with biological systems

Microscopy studies have demonstrated that the fibrillar attachment pads of flies, spiders and geckos show fibrils (“setae”) with decreasing radii with increasing animal body mass (10, 22). Whereas micron dimensions of the fibrils are sufficient for reliable attachment of flies or beetles, geckos must resort to sub-micron structures to ensure adhesion. The results of this thesis have demonstrated that adhesion enhancement by contact splitting is also applicable to artificial fibrillar structures. However, in spite of the adhesion improvement observed in the micropatterned surfaces with decreasing pillar radii, these still demonstrate lower P_c than flat controls in some cases (see Figure 4.3, low preload values). Patterns with smaller radii or more densely packed pillars are required to take real advantage of a split contact surface. In biology, packing densities of about 30 % are found in the hairs of the attachment pad of flies with hair radii around 1 μm (121, 122).

Gecko setae are not made of a soft material, as PDMS, but of harder β -keratin with a Young’s modulus around 1 to 3 GPa. This makes the setae mechanically stable even at aspect ratios up to 100 without showing condensation. As a consequence of the high aspect ratio, the effective Young’s modulus of the surface is decreased to 100 kPa (123). This value is 6 times lower than that of the patterned surfaces with an aspect ratio of 4. Such a high compliance enables the gecko to adhere also to rough surfaces, where adhesion behavior to the artificial structures of this thesis remains yet to be determined.

A preload dependence of the pull-off force has also been found in adhesion measurements performed on the attachment pads of the great green bush cricket (124). The authors point out that this mechanism may enable controlled attachment and detachment in animal locomotion (116, 124). According to the results discussed here, the high aspect ratio of the fibrils also contributes positively to this capability. High aspect ratio fibrils

require larger preloads to reach the maximum pull-off force than low aspect ratio fibrils; hence animals with high aspect ratio hairs will be able to modulate their adhesion force within a much wider range than those with low λ hairs. Artificial high λ structures thus remain a worthwhile challenge for microfabrication.

4.5 Conclusions

Sylgard 184 PDMS surfaces were microstructured with pillars of different radii (2.5 to 25 μm) and aspect ratios (0.5 to 4). Adhesion tests with a spherical probe indenter at different preloads were carried out. The data provide systematic and quantitative evidence of the positive influence of reducing the radius and/or increasing the fibril height on adhesion. The main results can be summarized as follows:

- *Size effect*: The pull-off strength σ_c increased with $r^{-0.4}$, where r is the pillar radius (at constant aspect ratio). This splitting efficiency is in good agreement with the JKR-based theoretical prediction of -0.5.
- *Aspect ratio effect*: The pull-off strength σ_c increased with $\lambda^{0.3}$, where λ is the aspect ratio of the pillars (at constant pillar radius). This increase in adhesion is attributed to higher elastic energy dissipation at pull-off with higher aspect ratio fibers.
- *Preload dependence*: For the spherical probe surface used, the compressive preload affects the adhesion force and strength; this dependence is more significant in high λ patterns, which allows modulating adhesion within wider ranges. This effect can be explained by a previous model (116).

- *Optimum patterns:* The highest pull-off forces can be expected for pillars with small radii and high aspect ratios, while avoiding their adhesive condensation. This highlights again the need for a trade-off between geometrical and elastic parameters as illustrated e.g. in adhesion design maps (15).
- *Data comparison:* The preload dependence can obscure comparison of adhesion data obtained by different groups as measurements are usually performed with different indenter geometries and at different preloads. It is suggested that the entire P_c vs. preload curve or its saturation value should be represented for meaningful comparison.

5 Contact Shape Controls Adhesion of Bioinspired Fibrillar Surfaces

Abstract – Following a recent bioinspired paradigm, patterned surfaces can exhibit better intermolecular adhesion than flat contacts. Previous studies have verified that finer contact structures give rise to higher adhesion forces. This study reports on the effect of contact shape, which was varied systematically in fibrillar PDMS surfaces, produced by lithographic and soft molding methods. For fiber radii between 2.5 and 25 μm , it is found that shape exerts a stronger effect on adhesion than size. The highest adhesion is measured for mushroom-like and spatular terminals, which attain values 30 times in excess of the flat controls and similar to a gecko toe. These results explain the shapes commonly found in biological systems, and help in the exploration of the parameter space for artificial attachment systems.

5.1 Introduction

Patterned surfaces, with a large number of regular micro to nanoscale features, are of increasing scientific interest because of their enhanced adhesion properties. Inspired by the attachment pads of insects and geckos (7-9, 125, 126), theoretical contact and fracture mechanics models (10, 23, 56, 127-129) have been established for fibrillar adhesion. First artificial analogues were produced as proof of principle, with mixed results with regard to adhesion performance (24-26, 34, 45, 55-59, 110).

To advance the subject and to provide a rational basis for the creation of superior surfaces, systematic studies of the different design parameters are required. So far, mainly the effects of fibril size, for a constant flat punch-like tip shape, have been investigated in detail (see chapter 4). In that study, the principle of contact splitting, which favors a large number of smaller contacts over a small number of large ones (10, 11), was validated.

However, nature provides a variety of contact shapes, ranging from spherical to conical, filament-like, flat, toroidal and concave terminals (12). Two recent experimental reports (39, 52) have stressed the significance of shape also in artificial systems; however in systematic terms, this degree of freedom so far has been largely neglected in the design of artificial analogues.

The objective of the present study is to provide the first experimental and systematic evidence of the role of contact shape in adhesion of split contact surfaces. For this purpose, different lithographic and soft molding methods were combined to fabricate elastomeric surfaces (Sylgard 184) patterned with micropillars of different shapes (flat, spherical,

concave, mushroom-type and spatular terminals) and dimensions. Their adhesion behavior was systematically characterized in terms of tip shape and pillar radius, and compared with theoretical predictions. Indeed, a strong effect of shape was identified which can overshadow the influence of size.

5.2 Experimental

Pillar arrays with different terminal shapes were obtained by combination of soft molding, inking and printing steps using elastomeric precursors and lithographic masters, as described in chapter 3. The dimensions of the fabricated structures ranged from $r = 2.5$ to $25 \mu\text{m}$ in radius and $h = 5$ and $50 \mu\text{m}$ in height. In all structures the aspect ratio was set to $\lambda = 1$ to allow comparison of the results. The interpillar distance was identical to the pillar diameter and the packing geometry was hexagonal. The resulting pillar packing density was 22.7 %. The patterned area was $0.8 \times 0.8 \text{ cm}^2$ for each geometry. The fabrication of pillars with different tip shapes has been presented in chapter 3. To make it easier to comprehend this chapter, parts of the fabrication approaches will be repeated in the following paragraphs.

Fabrication of pillars with flat tips by soft molding on SU-8 lithographic templates:

A 10:1 ratio of Sylgard 184 prepolymer and crosslinker was mixed, degassed and poured on the silanized SU-8 patterned wafer. Curing for 14 hours at 65°C in light vacuum ensured complete filling of the template and fabrication of accurate replicas. Careful demolding was necessary to avoid template damage. The total thickness of the elastomer samples was 7 mm in all cases. Further details on the procedure can be found in chapters 3 and 4.

Fabrication of pillars with spherical terminals by inking: A 10:1 ratio of Sylgard 184 prepolymer and crosslinker was mixed, degassed and spin-coated onto a silicon wafer to obtain film thicknesses below 6 μm . Previously soft molded Sylgard arrays of pillars were inked in the spin-coated film and cured upside-down in an oven during 14 hours at 65°C. A nearly hemispherical cap formed at the top of the pillars as a consequence of gravity and surface tension. The dimensions and radii of curvature were characterized by white light interferometry and are specified in Table 5.1.

Fabrication of pillars with mushroom-like terminals by soft molding on quenched lithographic molds: Lithographically structured wafers with holes were processed as in chapter 4, but using rapid cooling after soft, post-exposure and hard bake. Rapid cooling (by putting the hot wafers on a glass petri dish at room temperature) seemed to cause stresses in the SU-8 layer due to the mismatch in the thermal expansion coefficients of resist and wafer. As a consequence, delamination occurred at the edge of the holes. Soft molding Sylgard 184 on these templates rendered pillars with a thin, compliant ring, resembling a mushroom profile.

Fabrication of pillars with mushroom-like terminals by printing: The inked patterns were pressed against a perfluorosilanized wafer before curing in an oven during 14 hours at 65°C. Special care had to be taken to maintain the wafer in horizontal position for obtaining symmetric mushroom-like tips.

Fabrication of spatula-like terminals by tilted printing: The inked patterns were pressed against a perfluorosilanized wafer before curing. Curing of the assembly was performed in tilted arrangement in an oven during 14 hours at 65°C. Tilting slightly shifts the pillars from their initial printed position and creates an asymmetric terminal profile.

Fabrication of pillars with rounded edges by double molding: Sylgard hole patterns were first obtained by soft molding on SU-8 masters and then silanized by vapor exposure in vacuum to Hexadecafluoro-1,1,2,2-tetrahydrooctyltrichlorosilane for 30 minutes, followed by a second curing step at 200°C during 8 hours. After this treatment, a 10:1 ratio of Sylgard 184 prepolymer and crosslinker was cast and cured at 65°C for 14 h. The silanization and curing steps at 200°C are essential for avoiding sticking of the cured and fresh Sylgard 184. The pillars obtained after demolding had the expected dimensions but rounded edges, presumably as a consequence of the perfluorinated layer hindering wetting of the cavity corners by the Sylgard 184 precursor.

Fabrication of pillars with concave tips by soft molding with Provil Novo and P2: A 1:1 ratio of Provil Novo base paste and catalyst paste was mixed for 30 seconds and deposited on a silicon wafer. In the case of P2, the polymer base paste and catalyst paste were mixed in a mini-extruder provided by the supplier. Homogeneous ~ 0.5 mm thick films with different viscosities were prepared by spin-coating on a silicon wafer for defined times (between 4 and 6 minutes when using Provil Novo and between 1 and 4 minutes when using P2). Subsequently, the SU-8 mold was deposited vertically against the film and pressed with a weight having a mass of 250 g. The system was allowed to harden for 10 minutes. Pillars of decreasing height and with increasing concave profile were obtained by increasing the spin-coating time. The dimensions and radii of curvature for each case were characterized by white light interferometry (Table 5.1). This, as well as the replication of the pillars in PDMS (described below) was work performed by Irma Álvarez during her diploma thesis. She provided the samples tested here.

Replication of the pillars with concave tips in Sylgard 184: The concave structures obtained from Provil Novo were replicated in Sylgard 184 by using Modralit 3K as intermediate material for obtaining a negative copy. Subsequent soft molding Sylgard 184 on the Modralit 3K mold gave accurate replicas. The concave structures obtained from P2 were replicated in Sylgard 184 by using Provil Novo as intermediate material and a perfluorosilanzed layer to avoid sticking of Sylgard 184 to Provil Novo.

Adhesion measurements: Using the same procedure as reported previously in chapter 4, the adhesion performance of the hexagonal patterned surfaces and flat controls was tested by recording load-displacement curves obtained with a home-built indentation equipment (111). A sapphire sphere with a diameter of 5 mm was pressed against the patterned sample and retracted at a constant rate of 1 $\mu\text{m/s}$ until pull-off. The experimental value of the pull-off force, P_c , was extracted from the minimum of the retraction curves. Spring deflection during contact was monitored via a laser interferometer, which allowed us to measure forces up to 4 mN and 25mN – depending on the spring stiffness – with a resolution of 1 μN . Data collection was performed with a Labview software package. The sapphire sphere was cleaned with high-purity ethanol before each test.

Since the mechanical properties of polymers may change over time, all adhesion experiments were performed on one-day old samples fabricated under the same experimental conditions, unless specified. The laboratory temperature ($\sim 22^\circ\text{C}$) and humidity ($\sim 20\%$) were registered for each measurement. A minimum of 5 measurements was performed for each data point. For control purposes, adhesion tests under the same conditions were also conducted with flat specimens.

5.3 Results

5.3.1 Pull-off behavior

Figure 5.1 shows SEM images of representative patterned surfaces: pillars with flat, spherical, flat with rounded edges, mushroom, spatular and concave terminals. A more detailed description of the fabrication processes and structures can be found in the previous two chapters. The radii and curvatures of the different tips, as characterized by white light interferometry are given in Table 5.1 (see Figure 8.9 in appendix C for an example of a whitelight profile for spherical tips). It is seen that the fabrication process rendered homogeneous, well-defined structures. The pillars exhibit smooth surfaces in contrast, for example, to the structures investigated by Varenberg *et al.* (42).

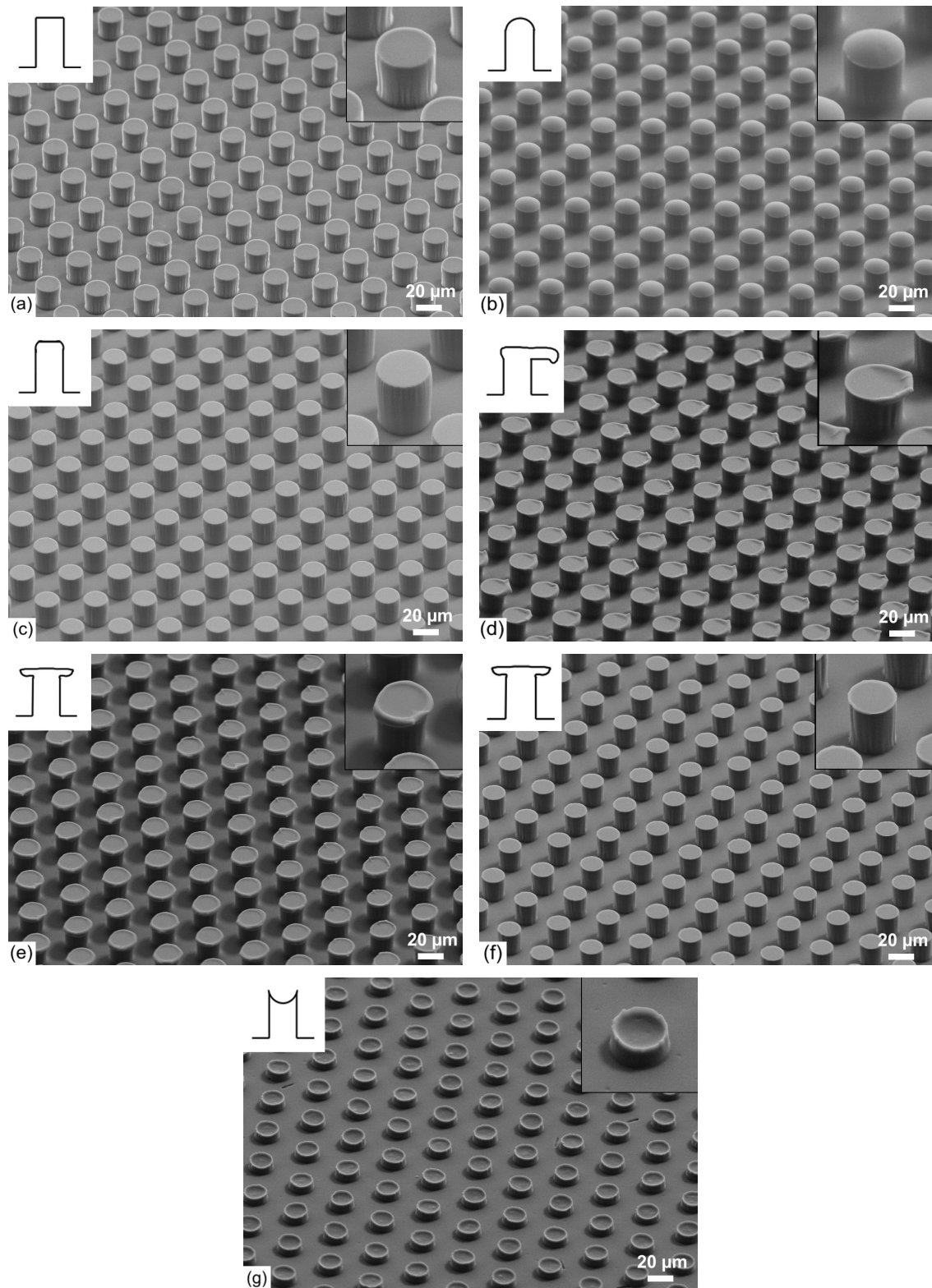
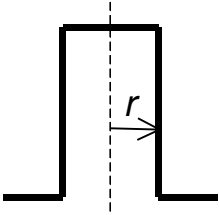
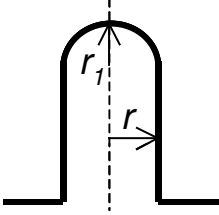
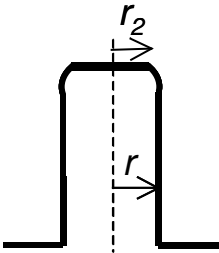
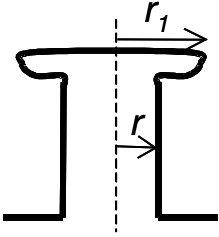
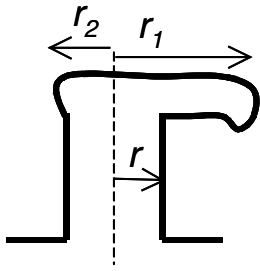
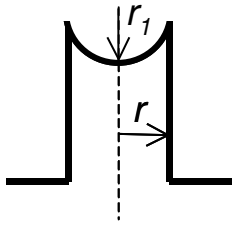


Figure 5.1: SEM images of selected patterns with different tip shapes: (a) flat, (b) spherical, (c) flat with rounded edges, (d) spatular, (e) mushroom (inked/printed), (f) mushroom (molding), (g) concave tips. Pillars have a radius of $10\ \mu\text{m}$ and a height of about $20\ \mu\text{m}$ except for pillars terminating in concave shapes (height $9\ \mu\text{m}$). Specimens were coated with $10\ \text{nm}$ Au/Pd before taking pictures.

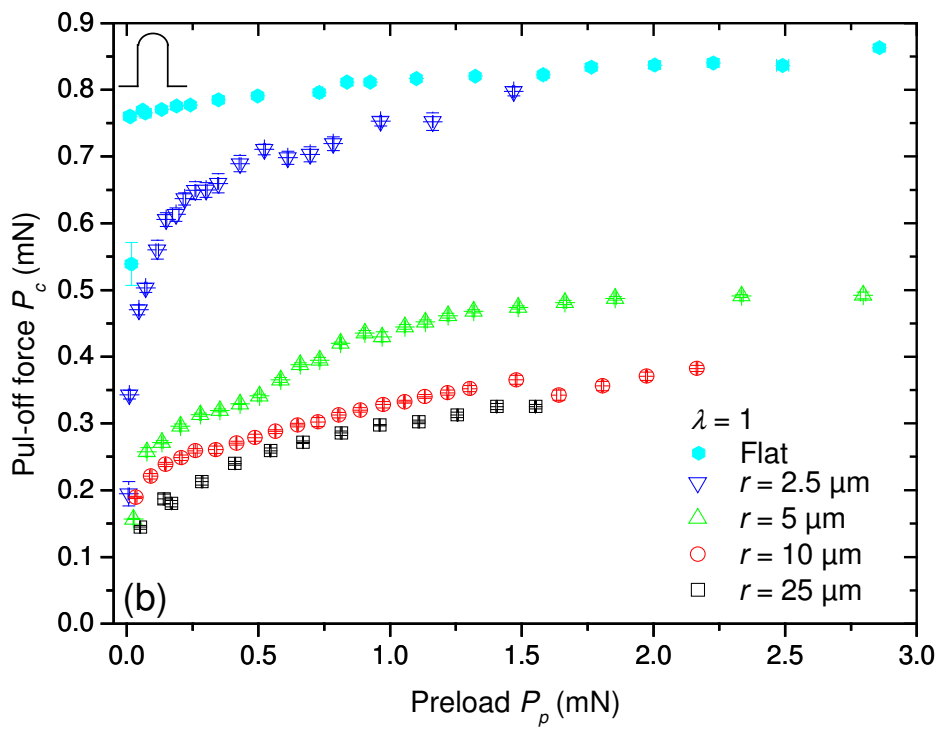
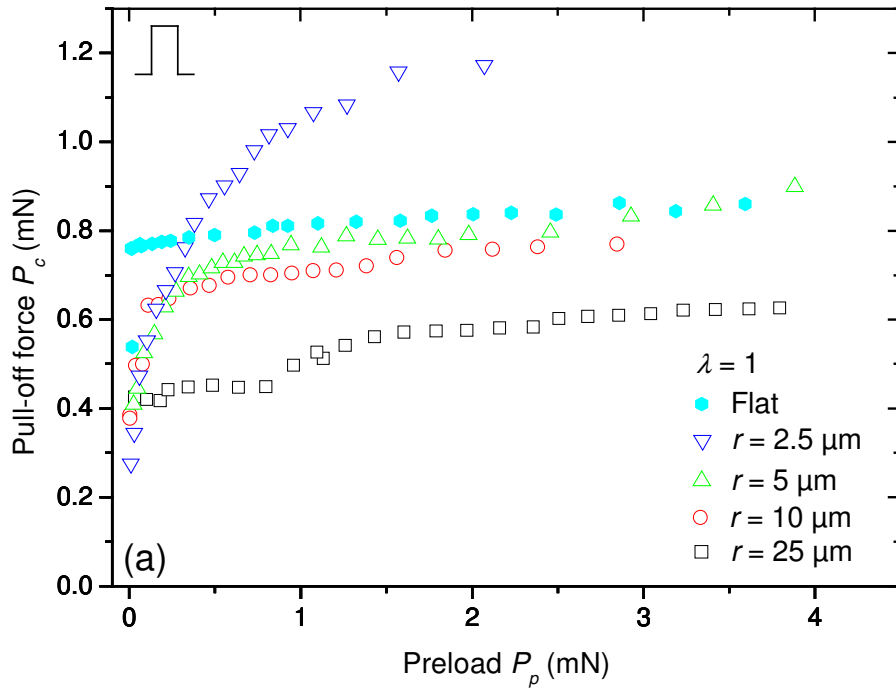
Table 5.1: Shapes and dimensions of the surface patterns, including mechanical parameters: The effective Young's modulus E^* was determined from the compressive behavior and the splitting efficiency corresponds to the slope of the data in Fig. 5.7.

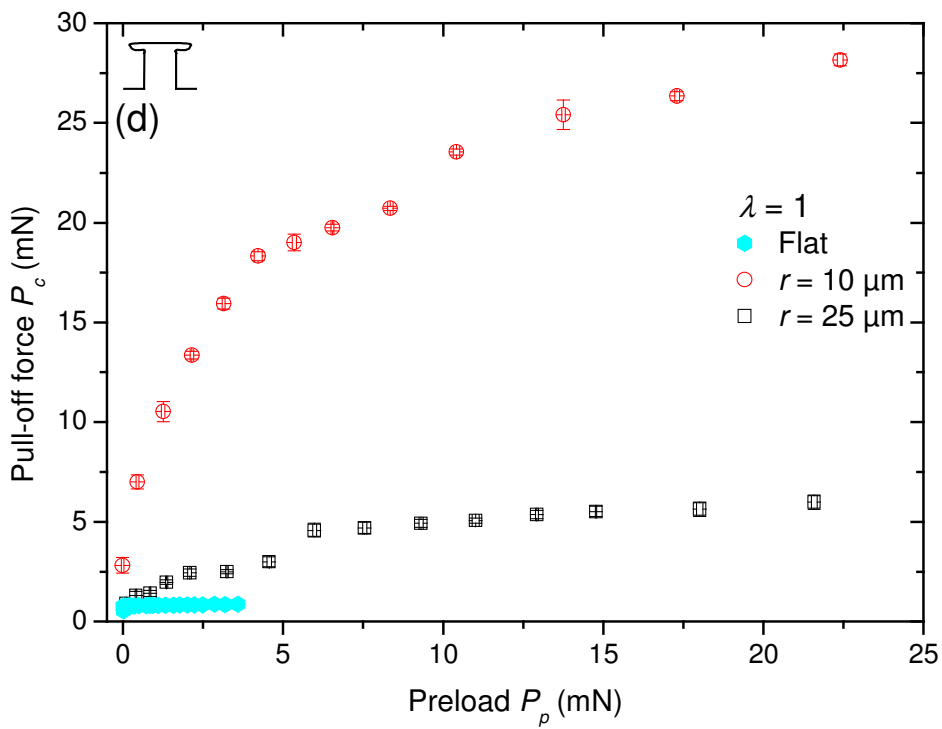
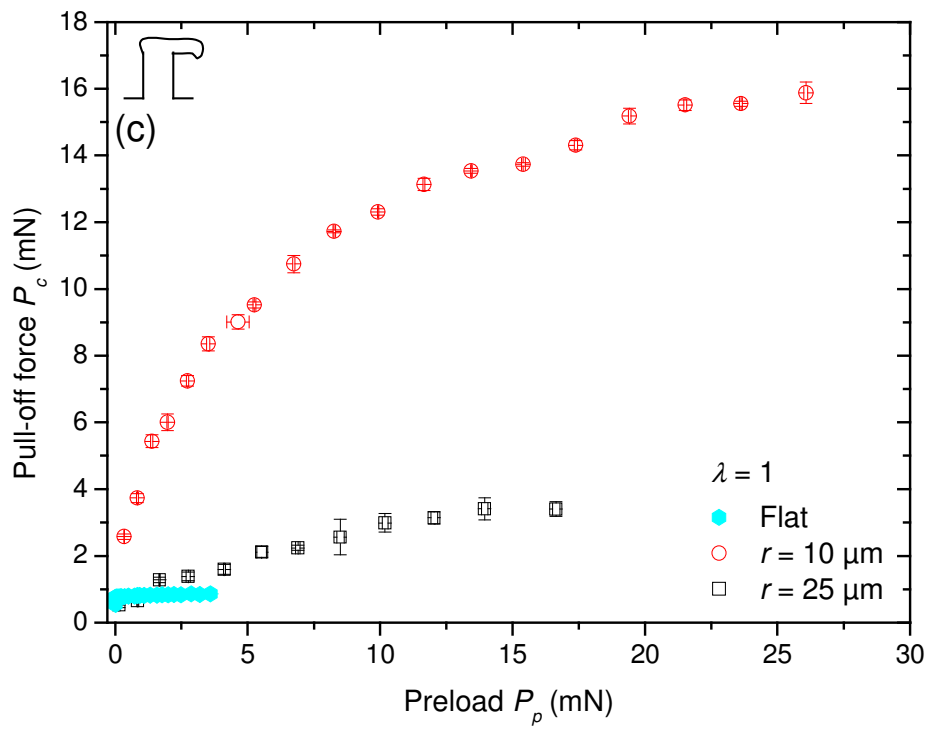
Contact shape	Pillar radius, r (μm)	Tip dimensions (μm)	E^* (MPa)	Splitting efficiency (at $P_p = 1\text{mN}$) Exp. (Theory)
Flat tip 	2.5	2.5	1.38	-0.48 (-0.5)
	5	5	1.30	
	10	10	0.95	
	25	25	0.76	
Spherical tip 	2.5	$r_1 = 9.3$	$1.34^{(*)}$	-1.00 (-1)
	5	$r_1 = 16.4$	$1.13^{(*)}$	
	10	$r_1 = 24.1$	$1.02^{(*)}$	
	25	$r_1 = 39.3$	$0.58^{(*)}$	
Flat tip with rounded edges 	2.5	$r = 2.9$ $r_2 = 2.7$	1.38	
	5	$r = 5.2$ $r_2 = 4.8$	1.00	
	10	$r = 10.0$ $r_2 = 9.0$	1.16	
	25	$r = 25.5$ $r_2 = 21.6$	0.85	
Mushroom tip (fabricated by printing) 	10	$r_1 \sim 12.9$	$2.50^{(*)}$	-2.26
	25	$r_1 \sim 32.0$	$1.81^{(*)}$	
Mushroom tip (fabricated by molding on quenched wafers)	9.1	$r_1 \sim 9.7$	2.29	
	23.5	$r_1 \sim 25.2$	1.47	

Contact shape	Pillar radius, r (μm)	Tip dimensions (μm)	E^* (MPa)	Splitting efficiency (at $P_p = 1\text{mN}$) Exp. (Theory)
	10	$r_1 = 11.3$ $r_2 = 10.1$	$2.29^{(*)}$	-1.54
	25	$r_1 \sim 33.8$ $r_2 \sim 30.1$	$1.81^{(*)}$	
	5	$r_1 \sim 3$ $h = 9$	0.60	
	10	$r_1 \sim 3$ $h = 9$	0.59	
	25	$r_1 \sim 6$ $h = 9$	0.50	

(*) These surfaces were cured twice during the fabrication process.

Figure 5.2 shows the measured pull-off forces, P_c , as functions of preload, P_p , for patterns with different tip shapes and radii. For comparison, the values obtained from a flat sample are also included. P_c measured on flat samples did not vary significantly with preload, as was expected from the Johnson-Kendall-Roberts (JKR) theory (18). In contrast, P_c increased strongly with preload for all patterned surfaces, except for the concave tips, until a plateau was reached. Pillars with concave tips behaved differently: starting with a very low plateau, P_c increased with preload and, finally, reached a higher saturation level; all pull-off values for concave tips were significantly below the ones for the other shapes.





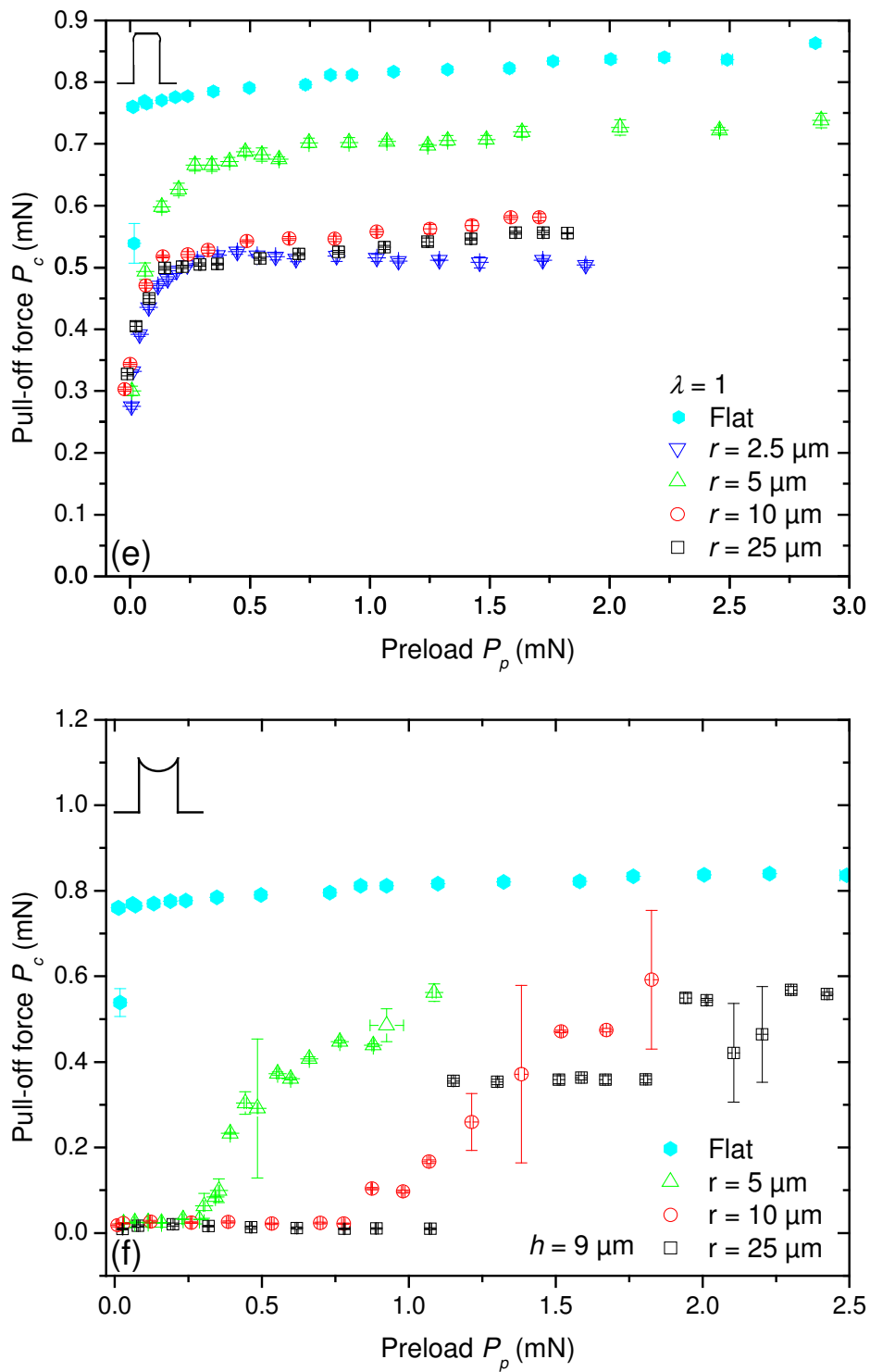


Figure 5.2: Pull-off force vs. preload for the different shapes: (a) flat tip, (b) spherical tip, (c) spatular tip, (d) mushroom-like tip, (e) flat tip with rounded edges and (f) concave tip. The data for the flat punch pillars is taken from chapter 4.

Patterned surfaces with planar, spherical, mushroom and spatular tip shapes showed increasing P_c for decreasing pillar radius at any preload, in agreement with the contact splitting principle (10-12). In the case of tips with rounded edges, a similar tendency was

found for pillars with radii 25, 10 and 5 μm ; however, P_c dropped for patterns with smaller radius (2.5 μm). At low preloads, patterns with concave tip shape showed very low adhesion independently of the radius. P_c started increasing at lower preloads for smaller radii, but reached similar plateau values for all radii. A split contact surface does not seem to favor adhesion for this shape.

Comparison with flat controls depends on the contact shape: The pull-off force of patterned surfaces with flat tips exceeded P_c of the flat surface for $r < 5 \mu\text{m}$. In the case of mushroom and spatular tips, P_c was much higher than for the flat surface for all measured radii. In contrast, spherical, rounded edge and concave tips showed lower P_c than the flat control substrate. This may be attributed to the loss of actual contact area in patterned cases, which does not seem to be outweighed by the adhesion enhancement due to contact splitting for these shapes. To check whether the high adhesion values of the mushroom-like pillars correlated with the diameter of the mushroom terminal, samples with the same pillar radius but different mushroom tip radii were measured. Results for the two fabrication methods are represented in Figure 5.3 for pillar radii 25 and 10 μm . No significant difference in the adhesion performance could be detected in samples with differences in the tip diameter of up to 7 μm .

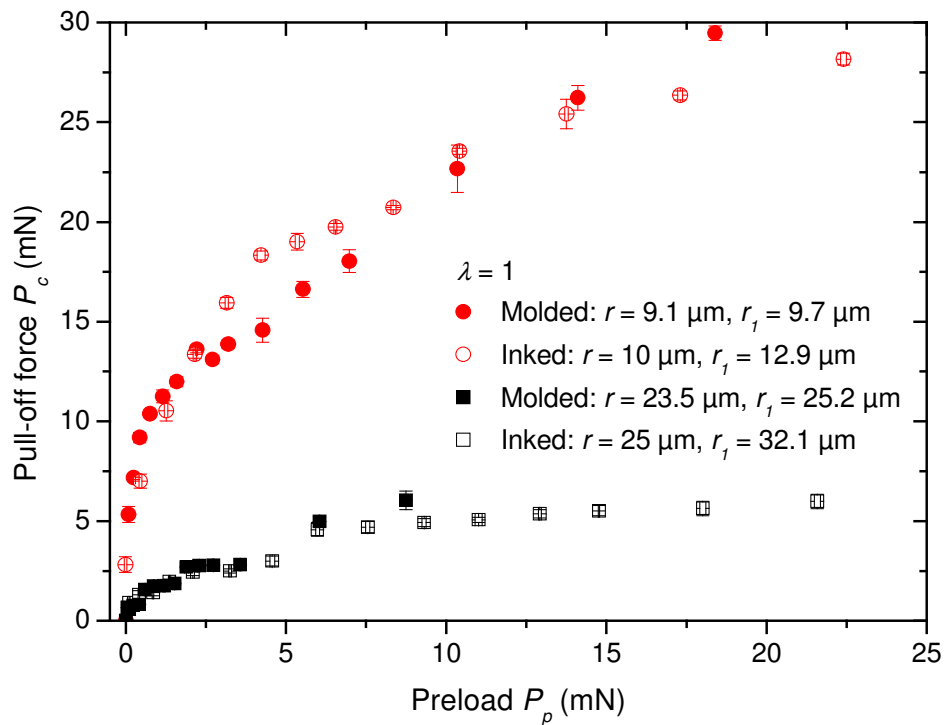


Figure 5.3: Pull-off force vs. preload for pillars with mushroom tips having the same pillar radius (10 or 25 μm) but different mushroom tip radius, obtained by different methods (printing or molding on quenched wafers).

A comparison of pull-off force vs. preload for pillars with different tip shapes but the same radius and height is given in Figure 5.4. Large P_c values were found for mushroom and spatular tips in comparison with all other shapes (note that the P_c -axis is split). The following ranking of adhesive performance for the different tip shapes can be extracted: mushroom tips are far superior, followed by spatula tips; flat tips have considerably weaker adhesion, but are stronger than flat tips with rounded edges, spherical and concave tips.

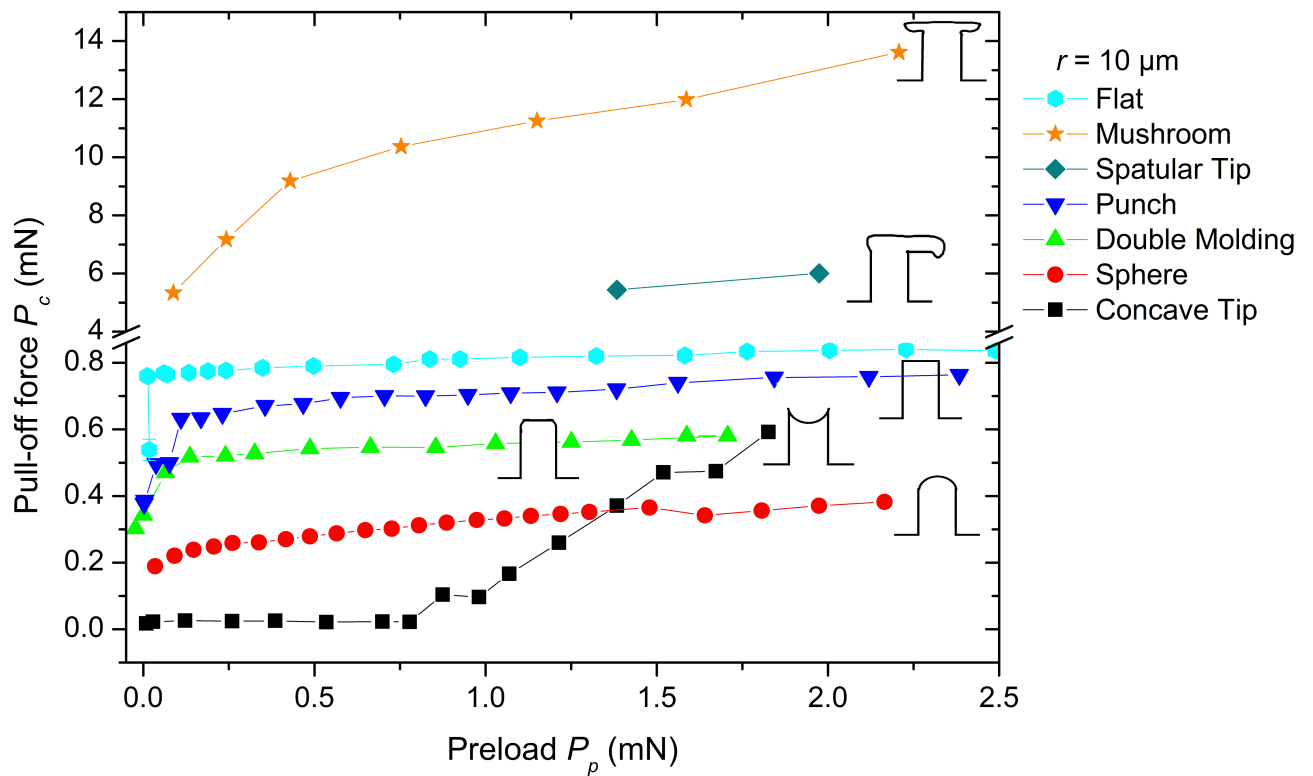
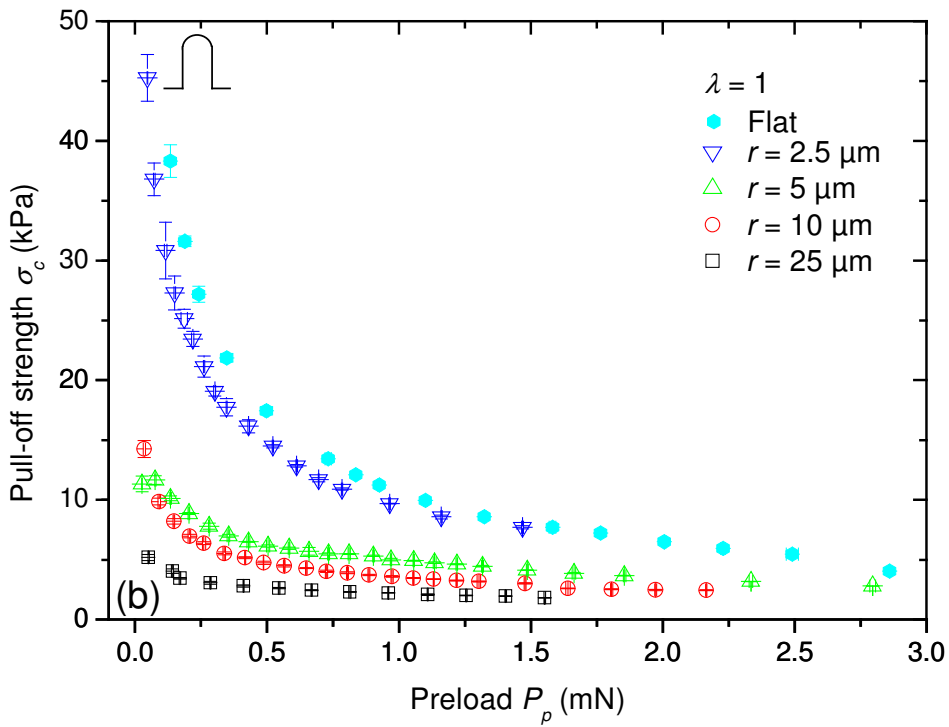
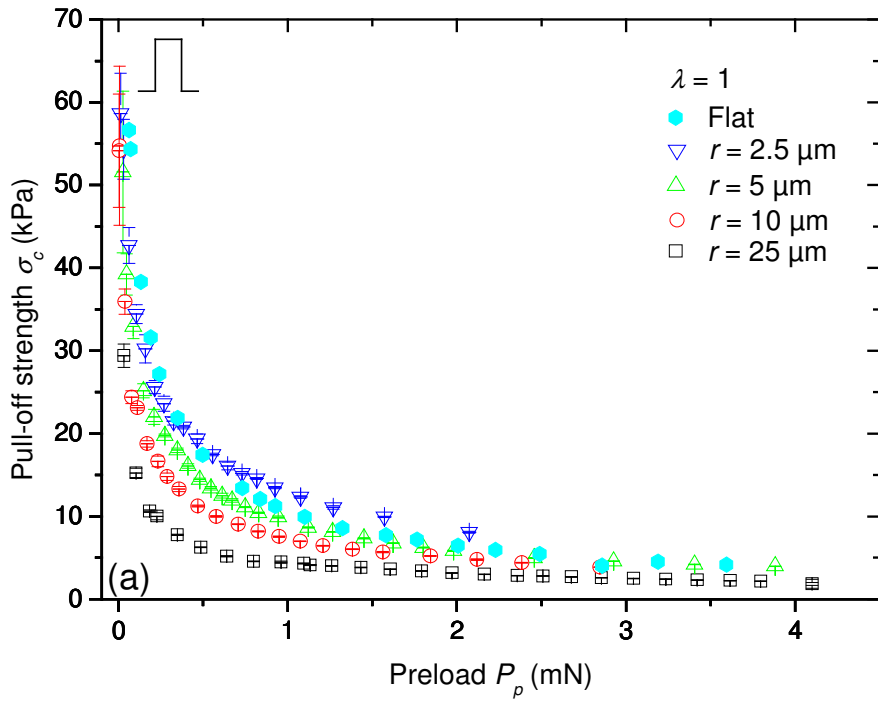
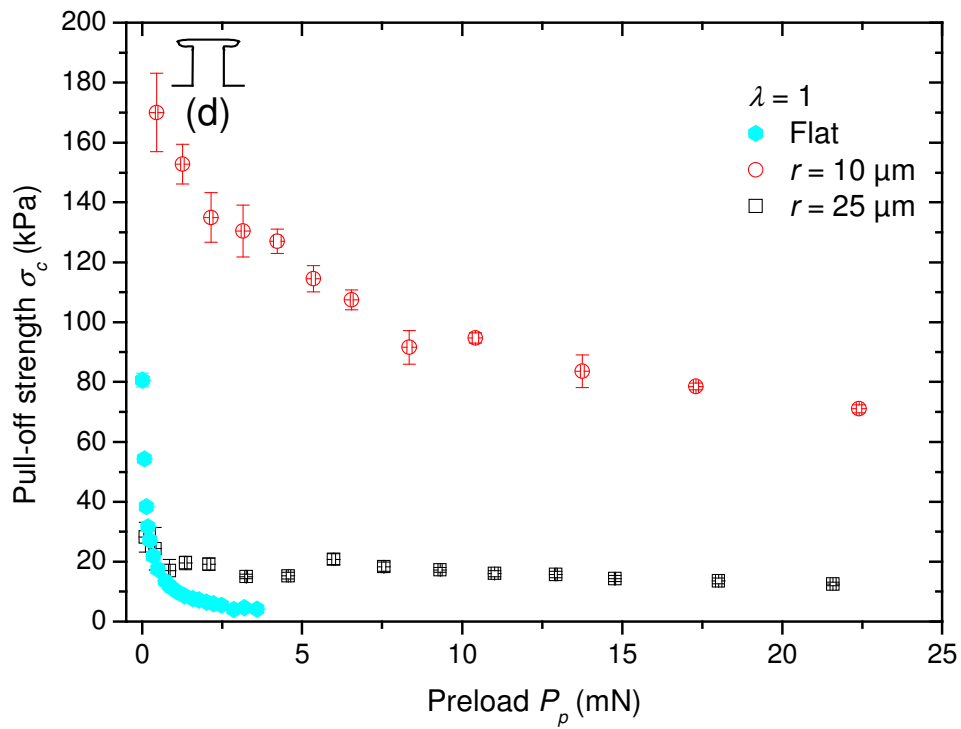
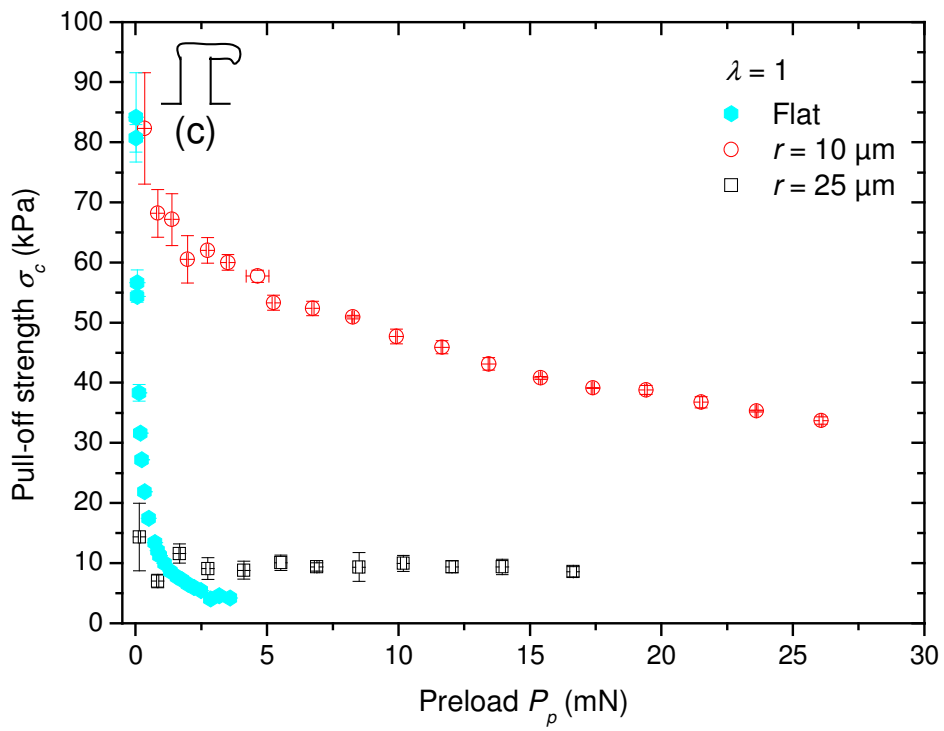


Figure 5.4: Comparison of pull-off force vs. preload data for the different shapes. Pillar radius is fixed at $10\ \mu\text{m}$. Note that the ordinate is split to include the experimental values for the mushroom tip. The experimental error is within the size of the symbols.

A more meaningful parameter to compare adhesion performance is given by the pull-off strength, σ_c , which is obtained by dividing P_c by the apparent contact area. This area is different for each preload value and can be calculated from the experimental indentation depth by simple geometrical considerations as πa^2 , where a is the radius of contact for the sphere with the substrate at maximum preload (same approach as in chapter 4). Figure 5.5 shows how σ_c decreases with increasing preload in all cases except for pillars with concave tip shape, which show a small increase in σ_c with preload.





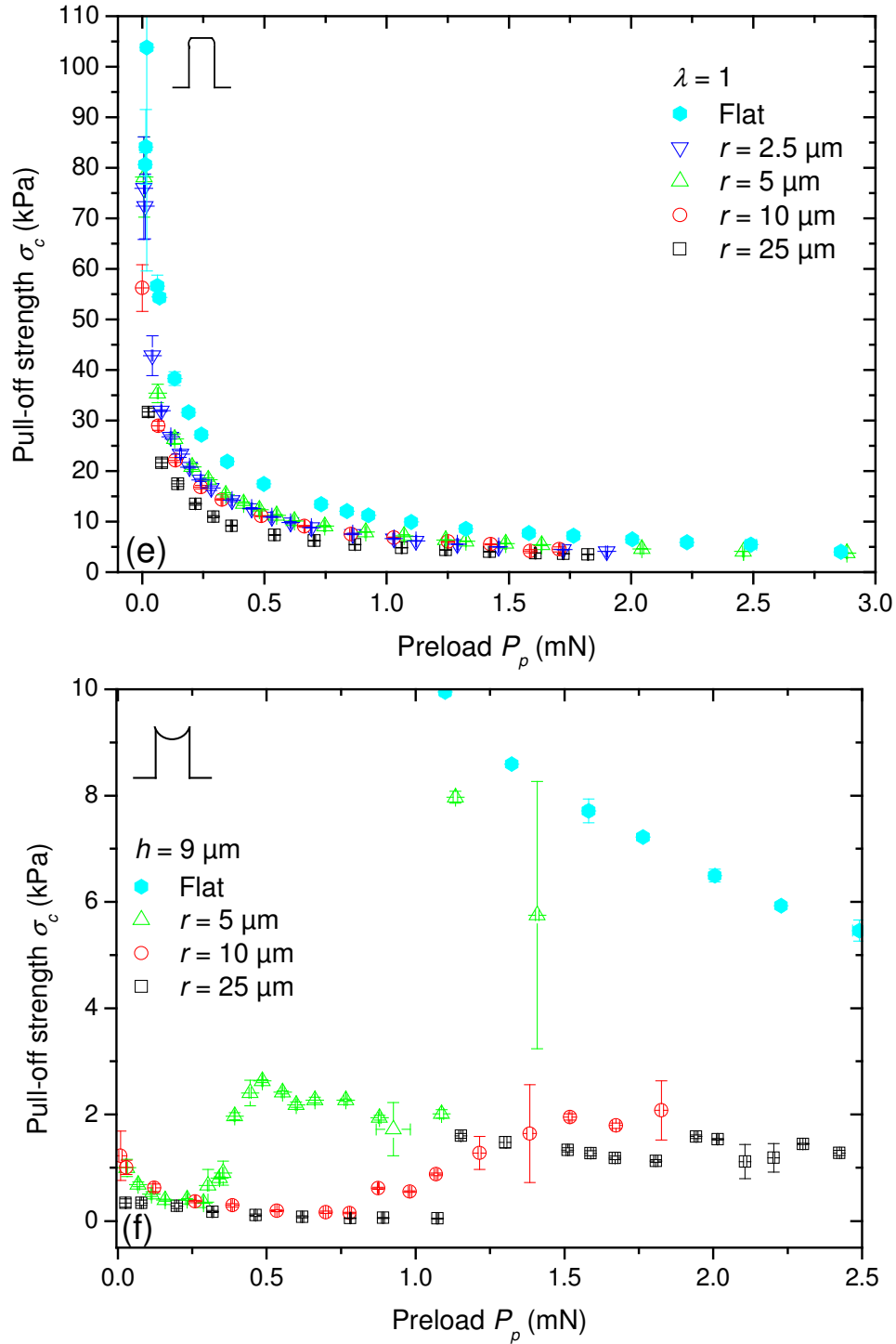


Figure 5.5: Pull-off strength vs. preload for the different shapes: (a) flat punch tip, (b) spherical tip, (c) spatular tip, (d) mushroom-like tip, (e) tip with rounded edges and (f) concave tip. The data for the flat punch pillars is taken from chapter 4.

5.3.2 Compressive behavior

The compressive parts of the load-displacement curves were further analyzed by applying the Hertz theory of elastic contact (16), neglecting the fibrillar nature of

the surfaces. An effective Young's modulus $E^* = E/(1-\nu^2)$, where $\nu = 0.5$ is Poisson's ratio, was obtained by fitting the experimental data to the expression:

$$P = \frac{4}{3} E^* \sqrt{R} \delta^3 \quad (5.1)$$

where P is the applied compressive load, R is the radius of the indenting sphere and δ the indentation depth. The fits are shown in Figure 5.6 for pillars with $r = 10 \mu\text{m}$ and the resulting values of E^* are listed in Table 5.1. For a given radius, pillars with flat, spherical and rounded edge tips gave similar results; pillars with concave tips showed much lower E^* , by up to a factor 1/2, presumably as a consequence of the thin, flexible tip walls. Surfaces with mushroom and spatular tips had significantly higher values, typically by a factor of 2 to 3.

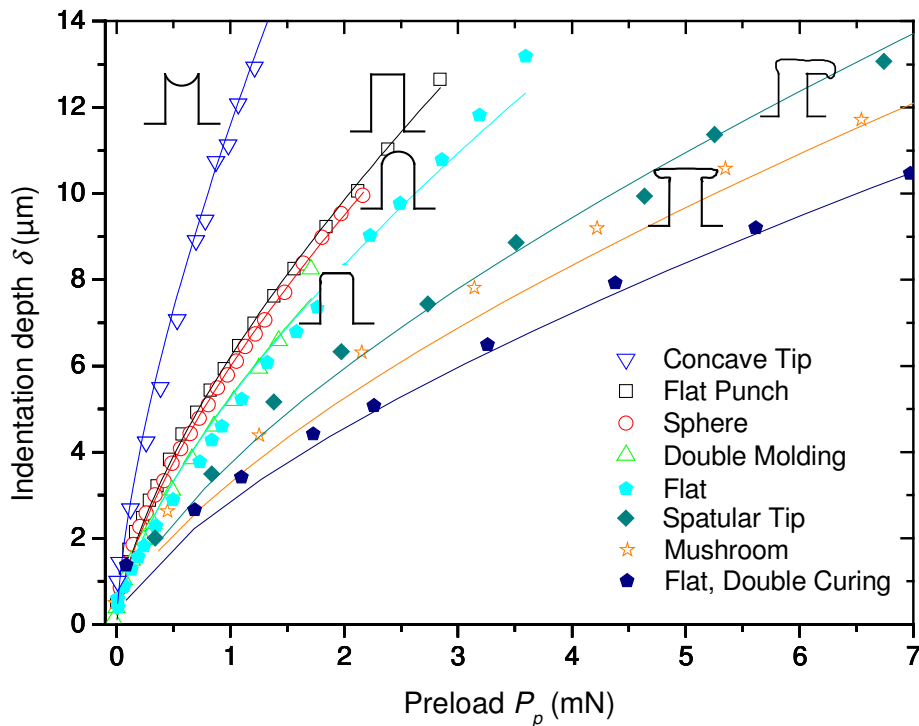


Figure 5.6: Compressive portions of the load-displacement curves for patterns with a radius of $10 \mu\text{m}$ and different contact shapes. Lines represent fits to the Hertz theory of elastic contact (16). The values of the effective Young's moduli, E^* , obtained from the fits are given in Table 5.1.

5.4 Discussion

This chapter reports on the first systematic study of the effects of fiber tip shape on adhesion. It is clear from the results that fiber shape augments the role of fiber radius, which was studied systematically for flat ends in chapter 4. In the following, these results are discussed in detail.

5.4.1 Influence of tip shape on pull-off force

The results presented here show clearly that contact shape strongly influences the adhesion behavior. For a given radius, pillars with flat punch tip shape have significantly higher P_c than spherical contacts. This is expected from contact mechanics considerations, e.g. ref. (12). The flat contact with rounded edges shows an intermediate behavior for pillar radii below 5 μm . Such pillars with smaller radius (2.5 μm) give a smaller P_c than spherical contacts. This could be due to the decreased flat to edge ratio for small pillar radius, which lowers the actual contact surface. The contact mechanics for such rounded structures has recently been described (108). It was shown that the pull-off force is different for a truncated sphere than for a flat punch with rounded edges. This sensitivity to the exact contact perimeter might be the reason why the experimental values drop for the smallest pillar radius.

Pillars with mushroom tips show the highest pull-off force, suggesting that the presence of a thin, compliant ring at the top of the pillar favors adhesion. The effect is considerable: the adhesion strength increases by a factor of 30 compared with the

flat control and amounts to 170 kPa in mushroom type pillars with $r = 10 \mu\text{m}$. This adhesion performance is comparable to that of the gecko (6).

Two recent studies have already shown results on mushroom type structures and also pointed out their benefit in adhesion (39, 52) – see also literature review in chapter 2. However, when comparing the effect of the pattern density, which is around 40 % in the above mentioned studies and about 22 % here, it is found that our structures possess superior adhesion performance, with equal (compared to Kim and Sitti, $\sigma_c = 180 \text{ kPa}$) – or higher adhesion strength (compared to Gorb *et al.*, $\sigma_c = 58 \text{ kPa}$), than the more densely patterned surfaces. In this more systematic study, the influence of the different parameters of the mushroom shape is also analyzed. Surprisingly, the radius and thickness of the upper ring does not seem to influence the final adhesion performance. Only the pillar radius, and therefore the number of contact points, seems to be important.

Pillars with spatular tips show an intermediate behavior between flat and mushroom tips. To the authors knowledge, this is the first example of an artificial adhesive surface with asymmetric pillars, close in design to attachment organs observed in flies. The adhesion performance of these asymmetric structures may change depending on the direction of the retracting force. This could be advantageous in applications where repeated attachment/release events are required, as in animal locomotion.

In comparison to all other shapes, concave tips give by far the lowest P_c . It is possible that such tips adhere through a suction mechanism, which would be insensitive to the fiber radius for a given pressure difference (12). If verified, this different adhesion mechanism could be an explanation for the variant behavior exhibited by concave tips in the measurements presented in this thesis.

According to theoretical models, the differences in adhesion force due to contact shape decrease with decreasing contact size and Young's modulus (i.e. softer materials) (130). For a material like Sylgard 184 ($E \approx 2$ MPa), these differences are predicted to become negligible for radii below 100 nm. 3D patterns with such small dimensions are difficult to obtain with the current procedures, but will be matter of future studies.

5.4.2 Size effect for different shapes: “splitting efficiency”

The results in Figures 5.2 and 5.5 show that a decrease in pillar radius causes a significant increase in pull-off force and strength in pillars with flat, spherical, spatular and mushroom tips. This is illustrated more clearly in Figure 5.7, where the pull-off strength is plotted against the pillar radius, on log-log scale, for a constant preload value of 1 mN. The slope of these data defines the potential for improving σ_c by down scaling of the contact size and has been termed “contact splitting efficiency” (12). Larger absolute values of the slopes result in higher gains in σ_c by splitting the contact. Values of the slopes are given in Table 1. A slope of -0.48 ± 0.03 was obtained for flat tips, close to the theoretical value of -0.50 (12). A higher negative slope was found for spherical contacts, where the experimental value of -1.00 ± 0.02 , also equals the theoretical predictions. The highest splitting efficiency is observed in mushroom and spatular contacts, with estimated slope values of -2.26 and -1.54 respectively. These values are yet to be explained theoretically.

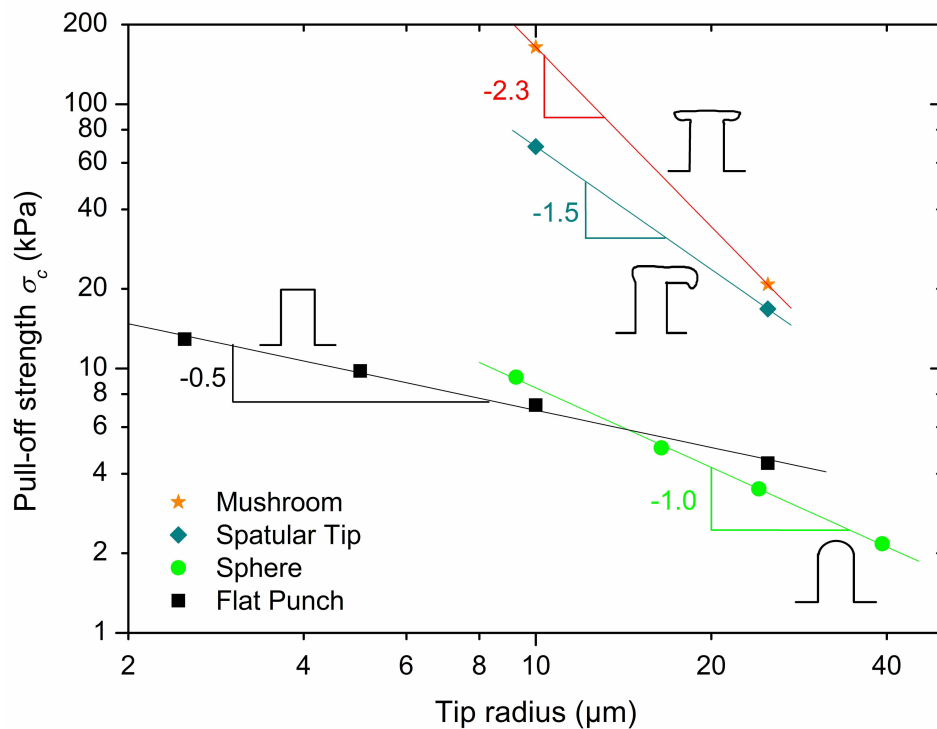


Figure 5.7: Tip radius dependence of the pull-off force (“splitting efficiency”) for flat, spherical, spatular and mushroom-like contacts. Data correspond to a preload of $P_p = 1$ mN. In the case of spherical tips, the radius corresponds to the radius of curvature measured by white light interferometry (Table 5.1). For all other shapes the pillar radius is used.

Not shown is the case of concave tips, where the fiber radius did not seem to influence P_c at low or high preloads. Only at intermediate P_p did these tips display slight radius effects. This insensitivity to scaling is a possible indication for a suction effect (12).

5.4.3 Preload dependence of pull-off force for different tip shapes

The preload dependence of P_c for patterned surfaces has been described theoretically (116) and shown experimentally for pillars with flat tips in chapter 4. By modeling the contact between the pillar pattern and the spherical indenter as an array of independent elastic springs attached to a rigid hemisphere and compressed against a flat surface, an increase of P_c with preload up to a plateau value, $P_{c(max)}$ was predicted (116). When applied to the experimental results (not shown here), this model seems to reproduce the preload dependence of P_c in spherical, rounded edge, mushroom and spatular tip shapes, but it does not describe the case of concave tips.

$P_{c(max)}$, as given by the fit to the spring model, is represented in Figure 5.8 for the different radii and shapes. An increase in $P_{c(max)}$ was found for decreasing pillar radii, as expected also from contact splitting (10). The indentation radius of the contacting sphere a_{crit} at which $P_{c(max)}$ is reached can also be obtained from the fit. Figure 5.8 shows that a_{crit} increases slightly with pillar radius (for constant aspect ratio) in the case of spherical, flat and rounded edge tips. Similar values of a_{crit} were found for these tip shapes at constant pillar radius. This was not the case for patterns with mushroom-like tips, which show much higher values of a_{crit} . Higher a_{crit} means that higher preloads are required in order to reach the maximum pull-off force of the patterned surface. Taking the preload dependence of P_c as an effective mechanism to modulate adhesion performance, pillars with mushroom-like patterns will thus offer a much wider modulation range than pillars with other shapes. This design can be advantageous for the fabrication of adhesives with tunable adherence.

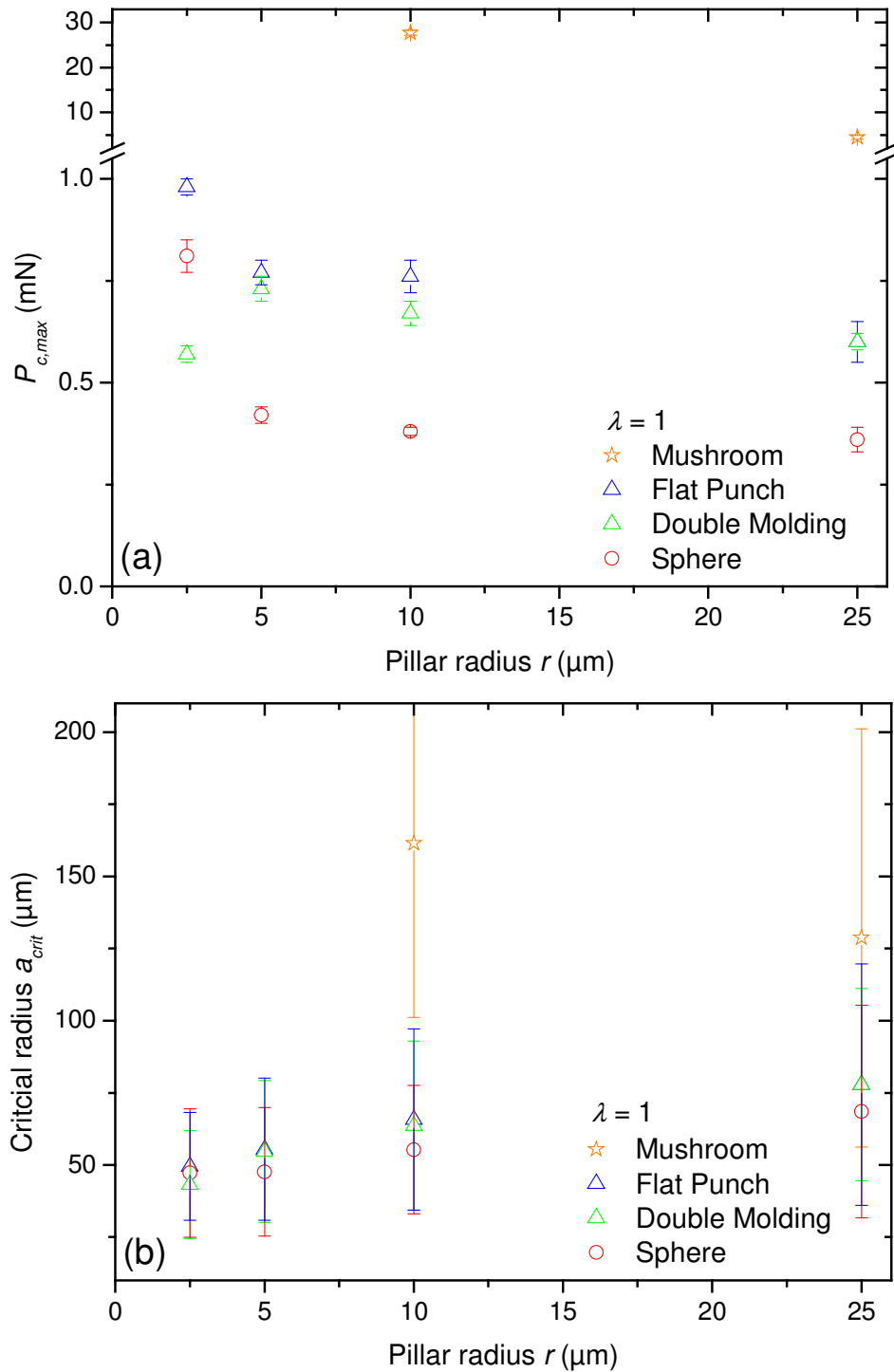


Figure 5.8: Maximum value (plateau) of the pull-off force, $P_{c(max)}$, and critical contact radius, a_{crit} , for different pillar radii and tip shapes. The values were determined by fitting the P_c vs. P_p data with the spring model (116). In (a), note the split ordinate in order to accommodate the values for the mushroom-like tips.

It is important to remember that the patterned surfaces with spherical, mushroom and spatular tips obtained by inking and printing have undergone two sequential curing processes. Because of more extensive crosslinking, this implies a higher Young's modulus of the pillar material. For flat Sylgard 184, E^* amounts to 1.42 MPa after a single, and to

3.04 MPa after a double curing process. However, this does not seem to be the determining factor for the values obtained since surfaces with mushroom terminals obtained by molding (single curing) or by printing and inking (double curing) show similar E^* values (to within 20 %).

Table 5.1 shows that E^* decreases notably with decreasing radius at constant aspect ratio for all shapes except for the concave tip. Regarding these data it is unclear whether the change can be attributed to the decreasing radius or to the increasing height of the pillars. In chapter 4 it was demonstrated for pillars with flat terminals that E^* is not influenced significantly by the pillar radius, but decreases with increasing pillar height or aspect ratio. For this reason, it is assumed that this effect is common to all the shapes.

Patterns with concave tips possess the same height (9 μm) for all radii. This is a consequence of the fabrication process, which entails reduced flexibility in the choice of pillar dimensions. In accordance with the reported invariance of E^* with radius at constant height, patterns with $h = 9 \mu\text{m}$ and $r = 5$ and $10 \mu\text{m}$ show similar E^* . Patterns with $h = 9 \mu\text{m}$ and $r = 25 \mu\text{m}$ show a slight smaller E^* , presumably due to their higher curvature.

5.5 Conclusions

From the results and discussions in this chapter, the following conclusions can be drawn:

- Patterned elastomeric surfaces with widely different tip shapes can be produced reproducibly using variations of lithography and soft molding methods. The pillar radii can be varied between 2.5 and 25 μm , with the aspect ratio kept constant at a value of 1.

- The contact shape strongly influences the adhesion behavior of patterned surfaces. The highest pull-off forces were found for mushroom-like pillars, which showed an increase of up to 30 times over the flat controls. Flat and spherical shapes showed lower adhesion, while concave shapes resulted in the poorest performance, coupled with an unusual preload dependence.
- The fiber radius effect studied previously augments the shape effect, creating vastly different “splitting efficiencies” for the different shapes. Within the size range tested, mushroom and spatular shapes hold the greatest promise for further adhesion improvement through size reduction.
- Further studies are required to explain the outstanding performance of the mushroom-type and the spatular shapes. They benefit very likely from a significant reduction of the deleterious stress concentration that is present at the perimeter of conventional flat punch contacts.

The chapter is based on the concept of adhesion driven by van der Waals type interactions and does not consider capillarity effects, although their contributions may also be significant (6). Recent theoretical calculations already indicated that capillary forces also depend on contact shape (115). Such effects will be the focus of future studies.

6 Design Criteria for Dry Adhesive Systems: The Effect of Shape

Abstract – The biomimetic reproduction of the gecko adhesion system has been a topic of intense research over the past years. Successes, however, has so far been limited. This is due to the extremely small structures in conjunction with complex shapes that need to be replicated. In previous studies, design and materials selection charts to determine the optimum materials and design combination for dry adhesive systems have been established. Also the effect of shape on the adhesive properties of single fibers and fiber arrays has been a research focus. In this chapter both approaches are combined to provide even better guidelines for the design of optimal adhesive structures.

6.1 Introduction

The origins of gecko adhesion are still under debate. It has recently become clear that van der Waals interactions are mostly responsible for the adhesive forces (7-9). In humid environments capillary forces may contribute equally to the adhesion mechanism (6). For the adhesion of a hemisphere to a semi-infinite half space both pull-off forces scale linearly with the hemisphere dimension. The splitting of big contacts into many smaller ones leads to an improvement of adhesion (10, 11) and is the explanation for the finding that bigger (heavier) animals exhibit finer adhesive structures. In a recent paper (15), these concepts were distilled into design maps that can guide the implementation of artificial adhesion systems by providing optimal materials and dimensional properties. In another paper, the deviation in shape from the ideal hemispherical contour was explored and a variety of scaling laws was found for different shapes (12). This chapter attempts to combine the influence of shape and the design predictions. Design maps will be developed for several contact shapes including such that exhibit an asymmetry and thus allow easy detachment in the appropriate pulling direction (Figure 6.1). Hemispherical tips have been treated in a previous publication on adhesion design maps (15), but will be discussed in this thesis mainly for comparison.

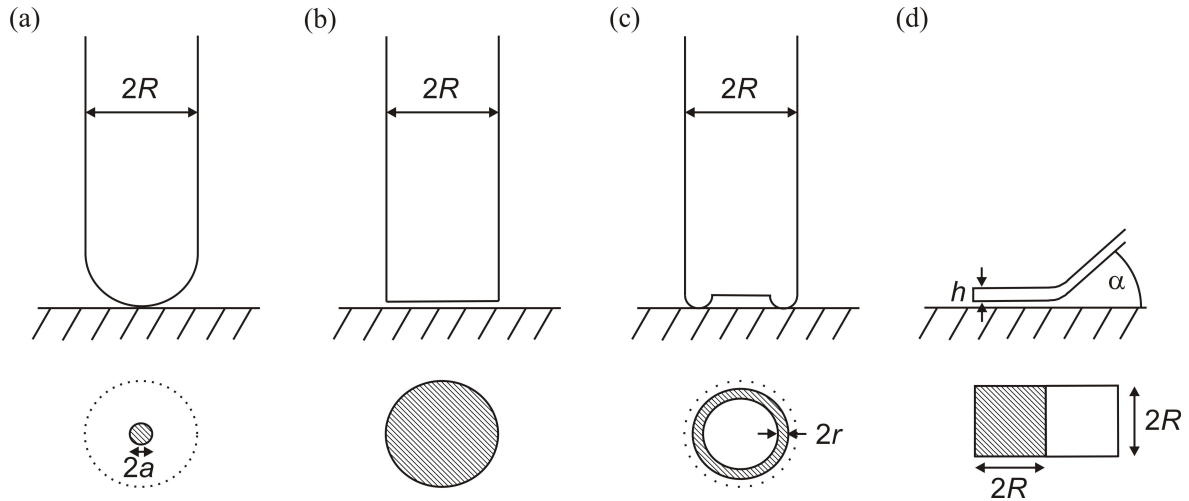


Figure 6.1: Side and plan view of contact shapes considered for adhesion design maps: (a) hemisphere, (b) flat tip, (c) toroidal tip, (d) elastic band. In each case, the shaded area indicates contact (adapted from ref. (12)).

6.2 Review of Design Maps

First, a brief overview of the general construction of adhesion design maps and the equations behind the different criteria is given. The equations for the pull-off force P_c can be found in a previous publication (12). There it is also shown that concentrating only on the Johnson-Kendall-Roberts theory (instead of the Derjaguin-Muller-Toporov approach) is justified. Nevertheless, DMT might be applicable for very small and stiff fibers. This can be seen when considering the Tabor parameter (see equation 2.9) (20) for multiwalled carbon nanotube based dry adhesives as published by Zhao *et al.* (58) and by Yurdumakan *et al.* (57). With typical values for the effective modulus (200 GPa), the relative radius (25 nm), the work of adhesion (0.05 J/m²) and the equilibrium separation of the contacting surfaces (0.4 nm), a Tabor parameter of around 0.03 is calculated. Thus, DMT theory should be applied in these cases, but the difference in pull-off forces is smaller than 25 % between the two theories and is not expected to overshadow general trends.

In adhesion design maps, the following five design criteria are displayed: “fiber fracture”, “condensation”, “ideal contact strength”, “adaptability” and “apparent contact strength”. The “fiber fracture criterion” acknowledges that for very thin fibers the adhesion strength might become larger than the theoretical fracture strength of the fibers σ_{th}^f . The axial stress σ_f in the fibers is:

$$\sigma_f = \frac{P_c}{A_f} \quad (6.1)$$

where P_c is the pull-off force for a single fiber and A_f is the cross-sectional area of a single fiber. Both take different values for the different fiber tip shapes which will be discussed in the following paragraphs.

The condition for fiber fracture is expressed as follows:

$$\sigma_f \geq \sigma_{th}^f \quad (6.2)$$

which gives a lower limit for the useful fiber radius R . For the theoretical fracture strength we use the approximation that σ_{th}^f equals $E/10$, where E is the Young’s modulus of the fiber material.

The limit of “ideal contact strength” describes the theoretical maximum contact strength which cannot be surpassed. It is transmitted at the moment of pull-off through the actual contact area and is expressed as follows:

$$\sigma_c = \frac{P_c}{A_c} \leq \sigma_{th} \quad (6.3)$$

In this equation σ_c is the contact strength, A_c the actual contact area at pull-off (a function of tip shape) and σ_{th} the ideal strength of van der Waals bonds, which can be described as:

$$\sigma_{th} \approx \frac{\gamma}{b} \quad (6.4)$$

Here, γ represents the work of adhesion and b the characteristic length of surface interactions. For both we choose typical values, which are $\gamma = 0.05 \text{ J/m}^2$ and $b = 2 \cdot 10^{-10} \text{ m}$. Solving equation 6.3 for R in the case of the different tip shapes will yield a lower limit for R .

As a certain elastic compliance is necessary to adapt to rough surfaces, the limit of “adaptability” was introduced in ref. (15). This will also address the fact that the elastic strain energy stored in the fibers cannot exceed the work of adhesion (129). Persson’s result (129) for the effective modulus prescribes an upper limit for the Young’s modulus as follows:

$$E < E_{eff} \frac{4\pi}{Cf} \lambda^2 \quad (6.5)$$

where E_{eff} is the effective Young’s modulus of the fiber structure. Here we chose to set E_{eff} to the – somewhat arbitrary – value of 1 MPa which should ensure contact adaptability. C is a dimensionless geometrical constant with a value close to 10 and f is the areal fiber packing density. The fiber aspect ratio λ is defined as $(L/2R)$ with L being the fiber length.

The “apparent contact strength” describes the pull-off force divided by the apparent contact area A_{app} , which is a function of tip shape. For the construction of the maps we consider different values for the apparent contact strength σ_{app} to ensure reasonable adhesion performance of the fibrillar system. Contours of constant σ_{app} will be superimposed in all maps.

For the “fiber condensation” criterion, different approaches can be chosen which will be discussed in the following. Sticking of fibers to each other, rather than to the contact surfaces will greatly diminish their adhesive capabilities.

6.2.1 What is the appropriate condensation criterion?

The condensation criterion used so far when constructing adhesion design maps is that derived by Sitti and Fearing (38). They modeled the fibers as elastic beams subjected to a point load at their tips. This load was considered as the JKR adhesion force between two fiber ends modeled as spheres. This results in a lower limit for the fiber radius which avoids condensation:

$$R \geq \frac{8\gamma' h_f^{1/2}}{E} \lambda^3 \quad (6.6)$$

In this equation, γ' denotes the work of adhesion between two fibers tips, which might differ from γ . The function h_f is defined as:

$$\frac{1}{h_f} = \frac{1}{h(f)} = \left(\sqrt{\frac{\pi}{4f}} - 1 \right)^2 \quad (6.7)$$

When using this condensation limit below, we will assume spherical tips, even for other tip shapes. For flat tips, this approach has proven to be reasonable as it describes experimental data well (131) (see chapter 4).

In another approach, Glassmaker *et al.* derived conditions to avoid fiber condensation by considering a line contact between the fibers (44, 88). They calculated the strain energy associated with bending the fibers so that they touched, and assumed that under equilibrium conditions this energy was equal to the energy required to separate the two surfaces. The end result again gives a lower limit for R :

$$R \geq 8.35 \frac{\lambda^3 \gamma}{\pi E} h_f^{3/4} \quad (6.8)$$

This criterion, which has been derived for fibers with circular cross-section disregarding the tip shape, will below be used for all shapes, even for the elastic tape. When comparing the theoretical predictions of this limit with experimental data, the criterion has proven to be useful (44, 131) (see chapter 4).

For a comparison between the criteria developed by Sitti and Fearing and by Glassmaker *et al.*, the quotient of eq. 6.6 and eq. 6.8 is plotted as a function of f in Figure 6.2.

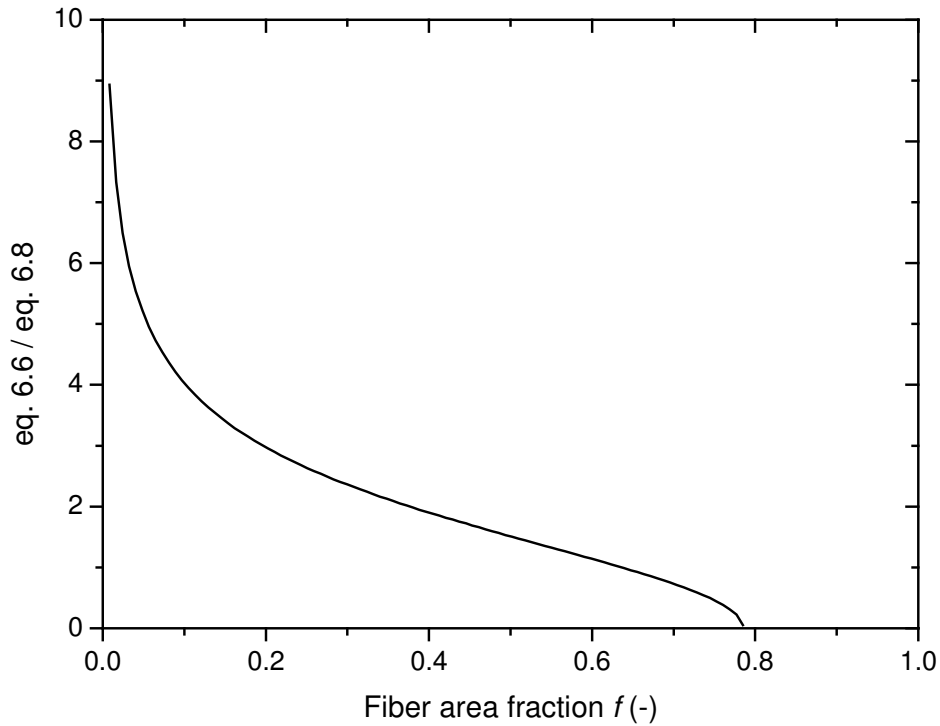


Figure 6.2: Quotient of equations 6.6 and 6.8, to illustrate the differences between the condensation criteria developed by Sitti and Fearing and Glassmaker *et al.* as a function of fiber area fraction f .

A third approach to the problem of fiber condensation was put forward by Persson (129). He considered thin and long elastic fibers which were attached perpendicular to a rigid substrate. Above a critical length, the fibers bend and form a compact layer of tilted fibers. With this model Persson calculated the elastic energy stored in the fibers, the van der Waals fiber-fiber binding energy per unit length and the total energy of the system. At the end, this yielded the following lower limit for R :

$$R \geq \left(\frac{12^2 b \gamma^2 \lambda^4}{E^2 \arccos^4 \left(\frac{f}{\pi} 2\sqrt{3} \right)} \right)^{1/3} \quad (6.9)$$

Note that Persson did not make any assumptions about the tip shape so that equation 6.9 can be used universally to describe the condensation criterion in all our cases.

6.2.2 Minimal number of contacts

In connection with the phenomenon of „contact splitting“ (10, 11), the question arises whether the gain in adhesion force can be offset by a smaller total contact area. Obviously, it will not increase total pull-off force when one big contact is substituted by only one small contact. Thus, a minimal number N_{min} of small contact elements is necessary to gain pull-off force. In the following this minimal number will be calculated as a function of tip shape.

Let us consider one big hemispherical contact with radius R . According to the JKR theory, this sphere will exert a pull-off force given by:

$$P_c = -\frac{3}{2}\pi\gamma R \quad (6.10)$$

The sphere occupies a projected apparent contact area A_{proj} :

$$A_{proj} = \pi R^2 \quad (6.11)$$

We now substitute this contact by a single smaller one with radius R' . For this small hemisphere, P'_c and A'_{proj} are as follows:

$$P'_c = -\frac{3}{2}\pi\gamma R' \quad (6.12)$$

$$A'_{proj} = \pi R'^2 \quad (6.13)$$

Since $R' < R$, it follows that $P'_c < P_c$, hence at least N_{min} small pillars are required to achieve the same adhesion force. These pillars will be packed with a finite areal density f , so that (fA_{proj}) is available for the small contacts. When N is the number of small pillars, we can write:

$$\pi R^2 = \frac{N\pi R'^2}{f} \quad (6.14)$$

or,

$$R' = \sqrt{\frac{f}{N}}R \quad (6.15)$$

We equate the pull-off forces for one and N_{min} contacts:

$$P_c = N_{min} P'_c \quad (6.16)$$

$$\frac{3}{2}\pi\gamma R = N_{min} \frac{3}{2}\pi\gamma \sqrt{\frac{f}{N_{min}}}R \quad (6.17)$$

This results in the following condition for the minimum number of small contacts to exceed the force of one contact:

$$N_{min} = \frac{1}{f} \quad (6.18)$$

Performing similar analyses for the other tip shapes – as they are described in ref. (12) – yields the solutions given in Table 6.1.

Table 6.1: Minimum number of small contacts N_{min} substituting a large one for efficient splitting for spherical, tape-, flat punch-like, toroidal and general axisymmetric tip shape (with q being a shape parameter (130)).

Tip shape	N_{min}
Sphere, Tape	$1/f$
Torus (self similar)	$1/f^2$
Flat punch	$1/f^3$
General axisymmetric profile	$\frac{1}{f^{\frac{3(q-1)}{q+1}}}$

6.3 Design Maps for Punches

For the construction of the adhesion design maps for flat punches we make the following assumptions:

- Perfect contact (no surface roughness)
- Condensation and adaptability criterion are unchanged compared to spherical contacts
- $E \approx E^*$, $\gamma \approx \gamma'$
- Modulus symmetry (hard punch on compliant substrate behaves similarly to soft punch on hard substrate)
- Young's moduli up to 200 GPa will be considered since for almost all technical contact pairs the reduced Young's modulus will not exceed this value

6.3.1 Contours of constant apparent contact strength

As described in section 6.2, we construct this limit with the pull-off force of a flat punch (12, 17, 117):

$$P_c = \sqrt{8\pi ER^3\gamma} \quad (6.19)$$

The apparent contact area is given by:

$$A_{app} = \frac{R^2\pi}{f} \quad (6.20)$$

Following Spolenak *et al.* (15) we determine the apparent contact strength:

$$\sigma_{app} = \frac{P_c}{A_{app}} = f \sqrt{\frac{8E\gamma}{\pi R}} \quad (6.21)$$

The result defines the maximum fiber radius if a specified apparent contact strength σ_{app} needs to be achieved:

$$R \leq \frac{8E\gamma f^2}{\pi\sigma_{app}^2} \quad (6.22)$$

Note that for the flat punch, the contours of apparent contact strength scale linearly with Young's modulus, in contrast to the scaling for the spherical contact, which is independent of Young's modulus (15).

6.3.2 The limit of fiber fracture

Fiber fracture is avoided when the apparent contact strength (eq. 6.21) is smaller than $f\sigma_{th}^f$, where $\sigma_{th}^f = E/10$. This gives the following lower bound for R :

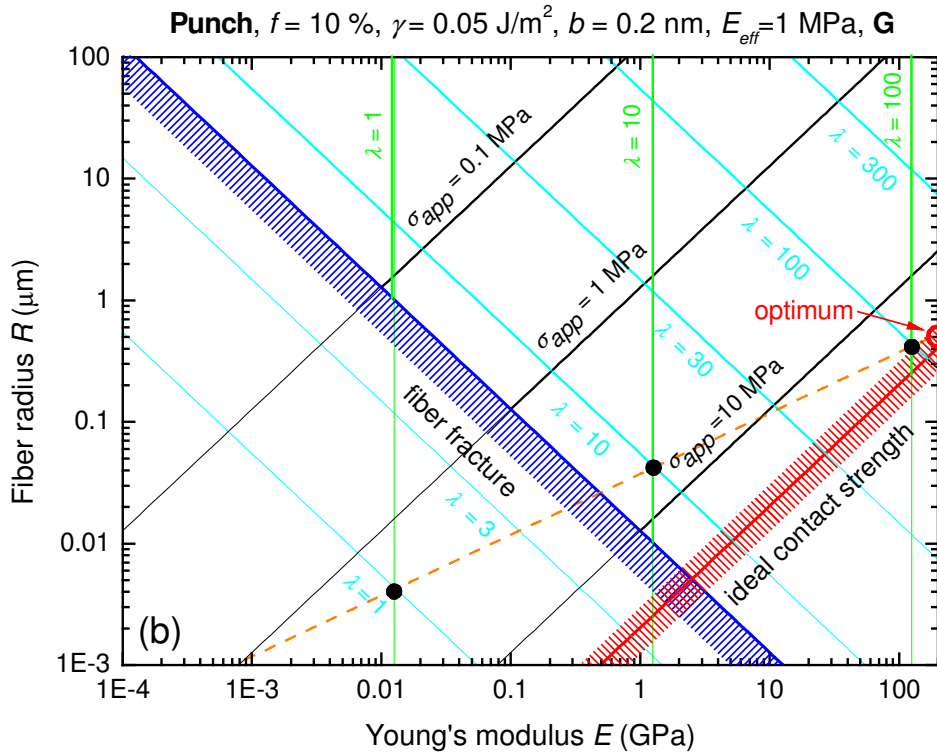
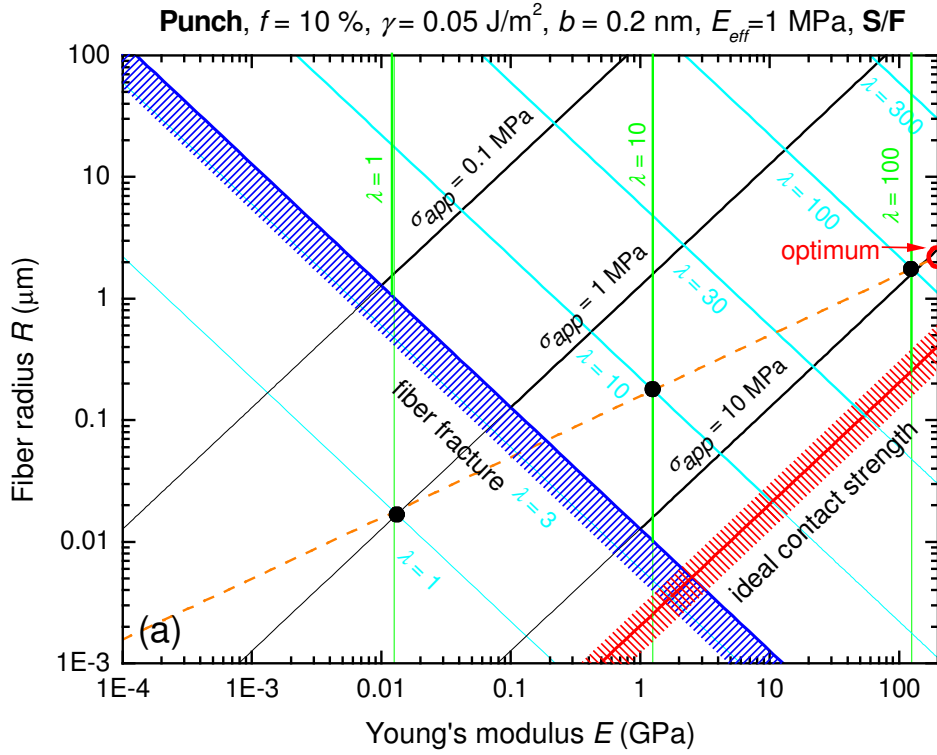
$$R \geq \frac{800\gamma}{\pi E} \quad (6.23)$$

6.3.3 The limit of ideal contact strength

Following the idea presented by Spolenak *et al.* (15) and explained in section 6.2 of this chapter, the following limit can be determined:

$$R \geq \frac{8Eb^2}{\pi\gamma} \quad (6.24)$$

Having now calculated all necessary limits, we can construct an adhesion design map. As condensation criteria, we choose the condition by Sitti and Fearing (eq. 6.6). The resulting plot is shown in Figure 6.3a.



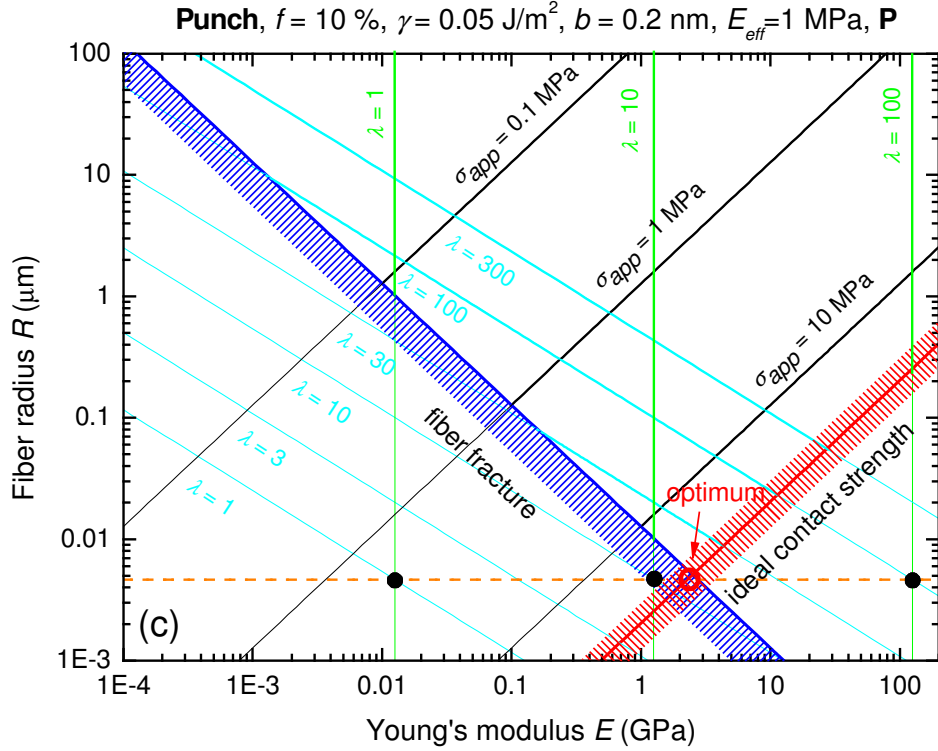


Figure 6.3: Adhesion design map for flat tips, constructed using the condensation limit developed by (a) Sitti and Fearing, (b) Glassmaker *et al.* and (c) Persson. The following parameters are assumed: $\gamma = 0.05 \text{ J/m}^2$, $f = 10\%$, $b = 0.2 \text{ nm}$ and $E_{\text{eff}} = 1 \text{ MPa}$. The criteria for fiber fracture (blue line) and ideal contact strength (red line) are indicated. The black lines are contours of equal apparent contact strength. The condensation limits for different aspect ratios are indicated by cyan lines, whereas the criterion of adaptability is drawn as green lines. The dashed line (orange) is the “conode”. In (a) and (b), its intersection with the ideal contact strength criterion would indicate optimum parameters, but leads to a Young’s modulus value which is above that of carbon nanotubes. The red circle thus indicates the optimum solution. In (c) the intersection of the “conode” with the ideal contact strength limit is below the criterion for fiber fracture; the optimum is nevertheless indicated.

6.3.4 Intersection with the conode

As suggested by Spolenak *et al.* (15) we can define a “conode” in the maps. It links the loci of optimum apparent contact strength, while avoiding condensation and ensuring adaptability. It is mathematically given by:

$$R = \gamma \sqrt{\frac{h(f)EC^3 f^3}{E_{\text{eff}}^3 \pi^3}} \quad (6.25)$$

In the log-log plot of the adhesion design map, the conode has a slope of 1/2. It is now instructive to compare the conode slope to the slope of the apparent contact strength criterion. In the case of a spherical contact, the slope of the apparent contact strength

criterion was smaller than the slope of the conode, namely nil (15). In this case optimum adhesion was ensured by moving to smaller fiber radii until the conode crossed the fiber fracture limit, which determined the absolute optimum. In the current case of the flat punch, the contours of apparent contact strength have a slope of one. Here, bigger radii would imply better adhesion and the absolute optimum would be found at the intersection between the conode and the ideal contact strength limit:

$$R = \gamma \sqrt{\frac{h_f EC^3 f^3}{E_{eff}^3 \pi^3}} = \frac{8Eb^2}{\pi\gamma} \quad (6.26)$$

This condition results in the following optimal modulus:

$$E_{opt} = h_f \frac{C^3 f^3 \gamma^4}{64E_{eff}^3 b^4 \pi} \quad (6.27)$$

The optimum values for the aspect ratio λ and the fiber radius R can be deduced in an analogous way (see Table 8.1). The result for the optimum apparent contact strength σ_{app}^{opt} is:

$$\sigma_{app}^{opt} = \frac{f\gamma}{b} \quad (6.28)$$

6.3.5 Condensation limit after Glassmaker *et al.*

As laid out in section 6.2.1, Glassmaker *et al.* developed another condition for fiber condensation which we will employ as an alternative input criterion for the maps (44). Using equation 6.8 yields Figure 6.3b. The conode is plotted as a dashed line. It is given by:

$$R = \sqrt{\frac{C^3 f^3 E \gamma_f^{3/2}}{E_{eff}^3 \pi^5}} \quad (6.29)$$

With equation 6.29 and its intersection with the ideal contact strength limit, we get the following results for the optimum Young's modulus E_{opt} and the optimal apparent contact strength σ_{app}^{opt} :

$$E_{opt} = \frac{188^{2/3} E_{eff} \pi^{5/3}}{C f h_f^{1/2}} \quad (6.30)$$

$$\sigma_{app}^{opt} = \frac{3 E_{eff} \pi^{5/3}}{15^{1/3} C^2 h_f^{1/2}} \quad (6.31)$$

6.3.6 Condensation limit after Persson

Using Persson's equation 6.9 we constructed the design map shown in Figure 6.3c. As above, for the calculation of the conode, the condensation and the adaptability limit are used. The result is the following:

$$R = \left(\frac{3 C f \gamma}{\pi E_{eff}} \right)^{2/3} \frac{b^{1/3}}{\arccos^{4/3} \left(\frac{f}{\pi} 2\sqrt{3} \right)} \quad (6.32)$$

which is independent of E ! In Figure 6.3c, the conode is shown as a dashed line. For the given set of parameters – $E_{eff} = 1$ MPa, $C = 10$, $f = 0.1$, $\gamma = 0.05$ J/m², $b = 0.2$ nm, the conode is found at $R \approx 4.65$ nm. In Figure 6.3c this is below the intersection of the fiber fracture and the ideal contact strength limit, so that in this particular case no ideal values are found; the intersection is nevertheless indicated with a red circle. For the general

optimum Young's modulus, we insert (6.32) into the limit of ideal contact strength. The result is shown in eq. 6.33. The optimum apparent contact strength is given in eq. 6.34:

$$E_{opt} = \frac{1}{8} \left(\frac{3Cf}{E_{eff}} \right)^{2/3} \left(\frac{\gamma}{b} \right)^{5/3} \frac{\pi^{1/3}}{\arccos^{4/3} \left(\frac{f}{\pi} 2\sqrt{3} \right)} \quad (6.33)$$

$$\sigma_{app}^{opt} = \frac{f\gamma}{b} \quad (6.34)$$

6.4 Surface Roughness in the Adhesion Design Maps for Flat Tips

So far, the effect of surface roughness is not considered. We now model the surface as having periodic roughness and approximate its contour by hemispheres. In a 2D representation, the surface is a series of half-circles (Figure 6.4). We still assume that the punches themselves are absolutely flat.

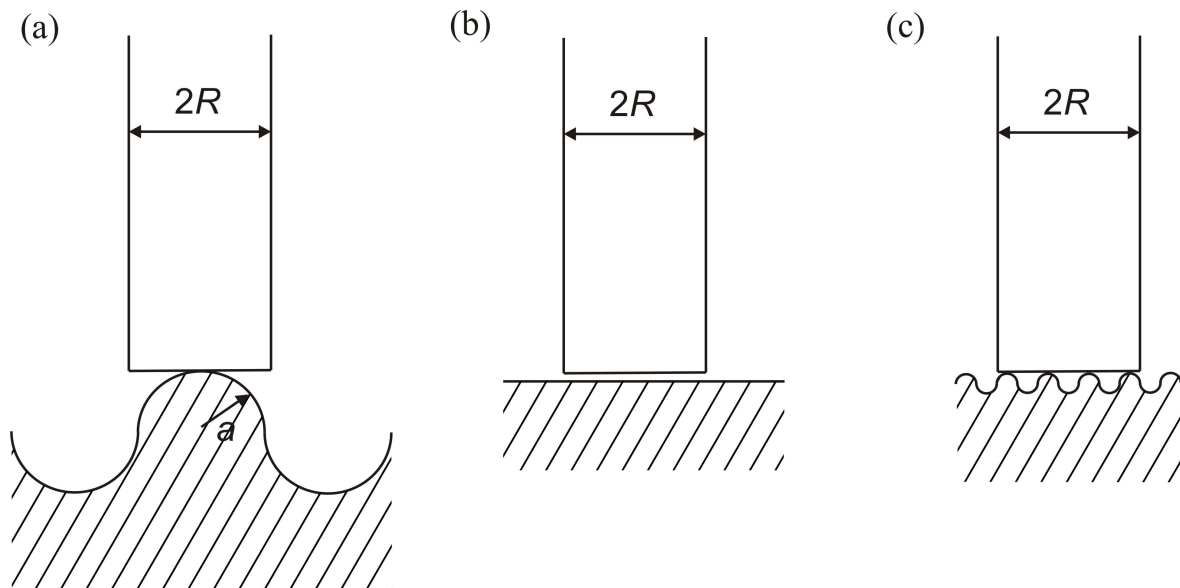


Figure 6.4: 2D sketch of the assumed periodic model for surface roughness. We model the individual arcs as half circles. Schematic of the three cases considered in the roughness analysis: (a) one sphere per punch, (b) flat on flat, (c) in-between case.

There are three cases imaginable:

- a) The periodicity of the roughness is of the same order as the punch diameter. Then we have only one sphere tough each punch (see Figure 6.4a). This case leads to the adhesion design map of spheres as previously published (15).
- b) The periodicity is so small that the substrate can be considered as a smooth surface (see Figure 6.4b). This leads to the adhesion design maps introduced in section 6.3.
- c) The in-between case (Figure 6.4c) will be analyzed in the following paragraph.

We assume that the hemispheres are in a closest 2D packing which leads to a maximum packing density of $\frac{\pi}{2\sqrt{3}}$, or approximately 90.7 %. From there on, we can calculate the number n of spheres in contact with a single flat punch of radius R . The surface roughness is described by the radius a of the hemispheres. According to surface roughness definitions (132), this radius corresponds to $R/2$. We find for the number of contacting spheres:

$$n = \frac{\pi R^2}{4\sqrt{3}a^2} \quad (6.35)$$

Since in the adhesion design maps, one of the parameters is R , a new equation for P_c has to be derived. As we model the surface roughness with hemispherical protrusions, the standard JKR solution for the pull-off force of spheres (eq. 2.6) can be used. Instead of R , a is inserted for the radius. It has to be taken into account the n spheres are in contact with the punch. Together with (6.35) the result is:

$$P_c = \frac{\sqrt{3}\pi^2\gamma R^2}{8a} \quad (6.36)$$

Note that P_c now has a quadratic dependence on R so that we can expect invariance to contact splitting. As can be seen in eq. 6.36, there are limits for the radius of the hemispheres: For very small values of a , P_c would reach unreasonably high values, whereas it would go close to zero for very large a . This has to be considered when constructing adhesion design maps with this model.

6.4.1 Construction of adhesion design map

The effect of introducing surface roughness is expected to be strongest in the maps constructed with the Sitti and Fearing condensation limit. Therefore we will consider only this approach to fiber condensation. To do so, we make the same assumptions as in section 6.3 for the flat punches against smooth surfaces and get the following results for the limits which are affected (the derivation is the same as laid out in chapters 6.2 and 6.3):

Apparent contact strength:

$$\sigma_{app} = f \frac{\sqrt{3}\pi\gamma}{8a} \quad (6.37)$$

Interestingly, equation 6.37 is independent of punch radius and Young's modulus, but depends on the surface roughness. Here we find a splitting effect: For smaller roughness (thus, smaller radius a), the apparent contact strength increases.

Fiber fracture:

$$E = \frac{10\pi\sqrt{3}\gamma}{8a} \quad (6.38)$$

We find that the fiber fracture limit is also independent of R . Therefore, invariance to contact splitting is expected.

Ideal contact strength:

Following Spolenak *et al.* (15), the contact radius α_c at the instant of pull-off is defined as:

$$\alpha_c = \left(\frac{9\pi\gamma a^2}{8E^*} \right)^{1/3} \quad (6.39)$$

for one spherical contact, so that for n hemispheres in contact we get:

$$\sigma_c = \frac{P_c}{n\alpha_c^2\pi} \leq \sigma_{th} \quad (6.40)$$

$$\sigma_c = 6a \left(\frac{\gamma E^{*2}}{81\pi^2 R^4} \right)^{1/3} \quad (6.41)$$

With this result, $\sigma_{th} \approx \frac{\gamma}{b}$, $E^* = \frac{E}{1-\nu^2}$ and the assumption that $\nu = 0.3$ we find the following limit:

$$R \geq 1.34(ab)^{3/4} \left(\frac{E}{\pi\gamma} \right)^{1/2} \quad (6.42)$$

Having calculated all the necessary criteria, we now construct the adhesion design map for flat tips against a substrate with periodic roughness. The result is shown in Figure 6.5, where a has been chosen with 500 nm. For $R \approx a$, when the punch is of the

same dimension as the hemispherical protrusions, the above derived model can no longer be applied. When $R \approx a/10$, the case for a flat punch against a smooth surface is reached and the map for this part is the same as in Figure 6.3a, with one exception: For the contours of constant apparent contact strength it has been taken into account that some of the punches do not contact the counter surface: eq. 6.22 is divided by a factor of 10. For the intermediate part of $a/10 \leq R \leq a$, we interpolated the limits of fiber fracture and ideal contact strength accordingly.

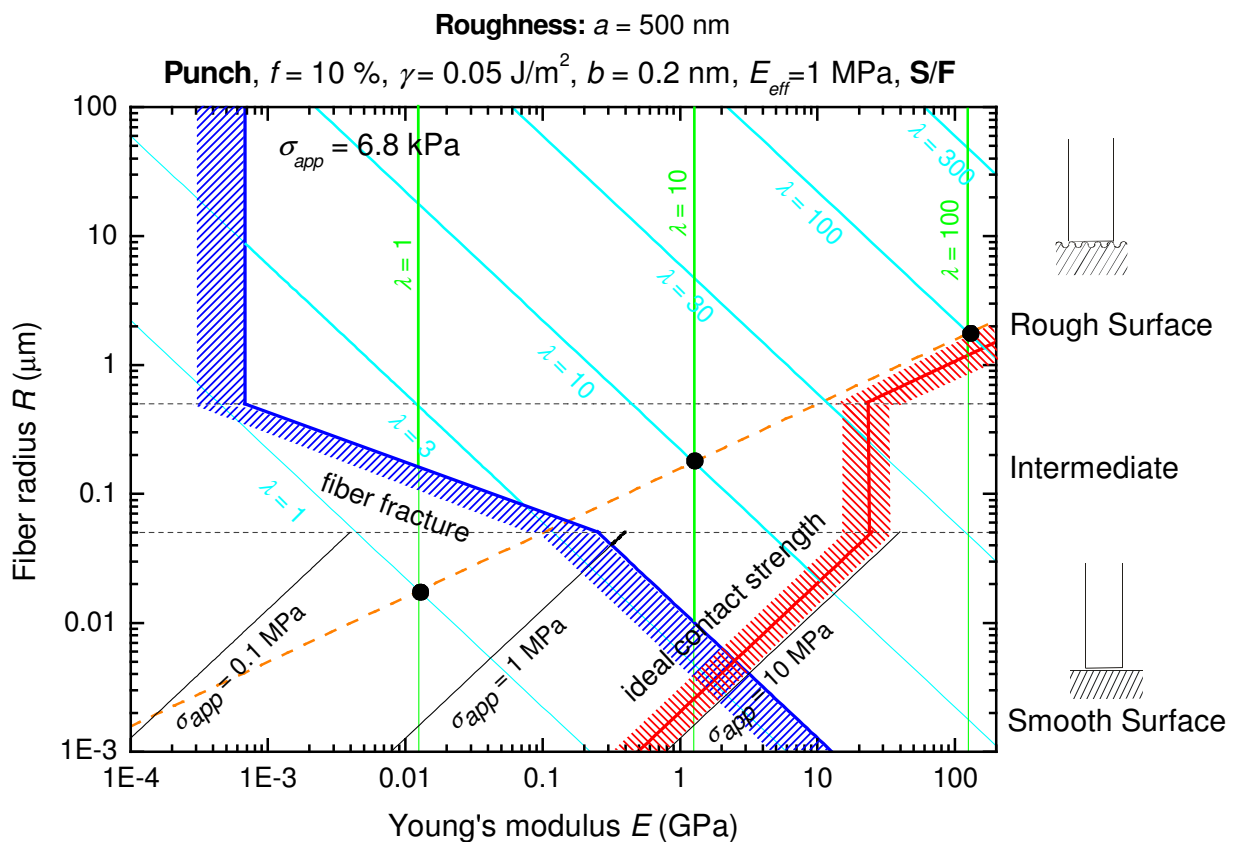


Figure 6.5: Adhesion design map for a flat tip against a substrate with periodical roughness. The condensation limit after Sitti and Fearing is employed and the following parameters are assumed: $\gamma = 0.05$ J/m², $f = 10\%$, $b = 0.2$ nm and $E_{eff} = 1$ MPa. For the surface roughness, a radius of the small spheres of $a = 500$ nm is considered. The dashed, orange line is the “conode”. For $R > 500$ nm, the presented model for a flat punch against a rough surface is employed and for $R < a/10$, where the contact is that of a flat punch against a smooth surface, the same limits as in Fig. 6.3a are used. For the contours of constant apparent contact strength the punches which don’t make contact with the counter surface, have been considered by dividing eq. 6.22 by a factor of 10. For the intermediate case of $a/10 \leq R \leq a$, the limits of fiber fracture and ideal contact strength were interpolated. For $R > a$, the apparent contact strength is constant over the entire map – contact splitting invariance – and the minimum Young’s modulus is determined by the fiber fracture limit.

Intersection with the conode:

As the apparent contact strength is constant for $R > a$, neither small nor large radii are favored. A minimum value for the Young's modulus is determined through the fiber fracture criterion. On and right of this vertical line all radii give the same adhesion performance. The fiber fracture limit is not altered for the different condensation limits, therefore this result is the same for the other two condensation approaches.

6.5 Design Maps for Toroidal Tips

When constructing design maps for toroidal tips we make the same assumptions as for the flat punches. As in (12) self-similar scaling is assumed, i.e. $r = R/10$, with r being the radius of the ring part of the torus (see Figure 6.1c).

6.5.1 Contours of constant apparent contact strength

From Spolenak *et al.* (12) we get the pull-off force of a torus:

$$P_c = (\pi E \gamma^2)^{1/3} \pi R^{4/3} \quad (6.43)$$

As described in section 6.2, we determine the apparent contact strength:

$$\sigma_{app} = \frac{P_c}{A_{app}} = f \left(\frac{\pi E \gamma^2}{R^2} \right)^{1/3} \quad (6.44)$$

which results in a limit for R of:

$$R \leq \left(\frac{f^3 \pi E}{\sigma_{app}^3} \right)^{1/2} \gamma \quad (6.45)$$

Note that for the torus, the contours of apparent contact strength scale with the square root of the Young's modulus. This is in contrast to the scaling for the spherical contact, which is independent of Young's modulus. It is also different from the flat tips, which scale linearly with E .

6.5.2 The limit of fiber fracture

Following the previously mentioned approach, we obtain the following fiber fracture limit:

$$R \geq \sqrt{1000\pi} \frac{\gamma}{E} \quad (6.46)$$

6.5.3 The limit of ideal contact strength

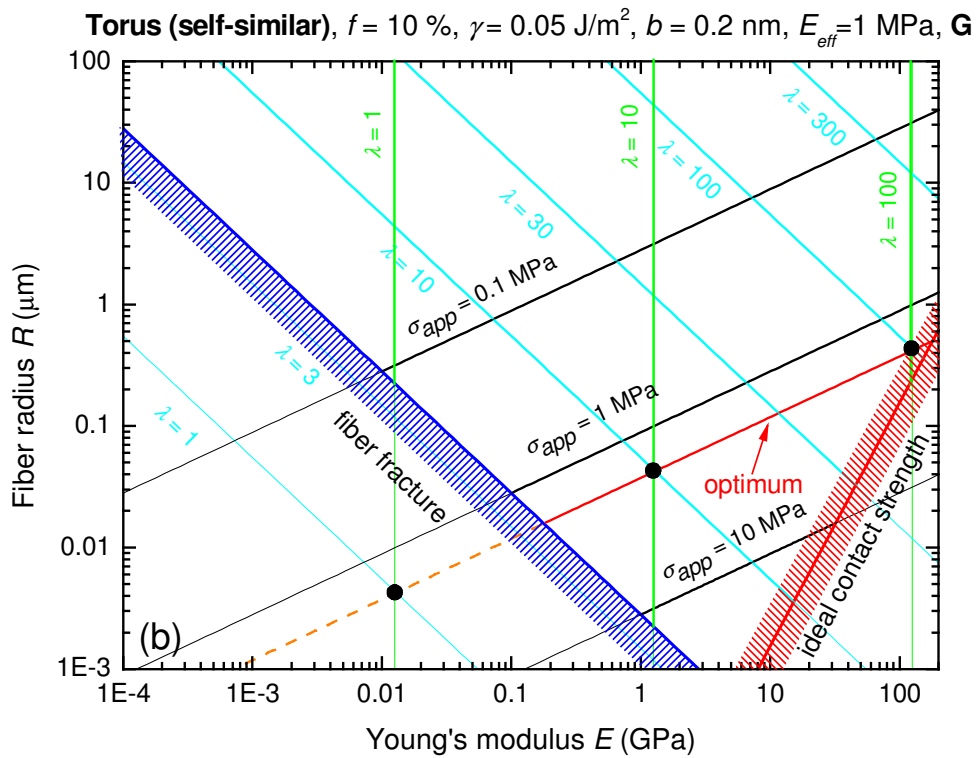
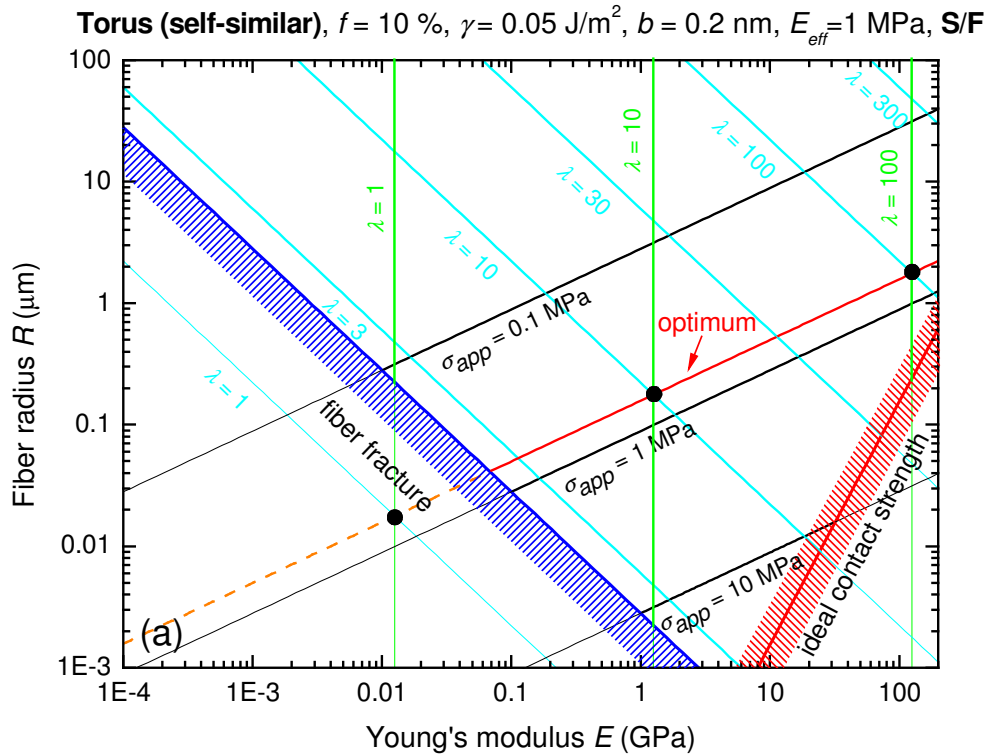
Following Spolenak *et al.* (15),

$$\sigma_c = \frac{P_c}{2a_c 2\pi R} = \frac{P_c}{4\pi R \left(\frac{32R^2 \gamma}{\pi E} \right)^{1/3}} \leq \sigma_{th} \approx \frac{\gamma}{b} \quad (6.47)$$

the following limit can be determined:

$$R > \frac{E^2 \pi^2 b^3}{2^{11} \gamma^2} \quad (6.48)$$

With all these limits at hand we can draw them into the double-logarithmic space of the adhesion design maps and for the condensation limit developed by Sitti and Fearing yield the plot shown in Figure 6.6a.



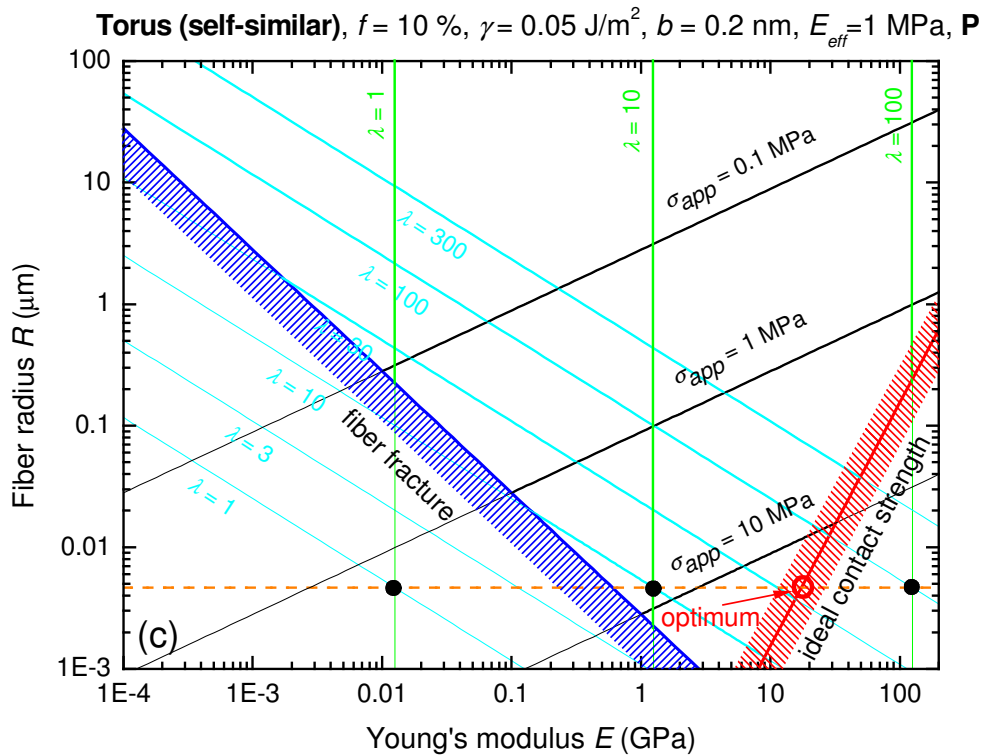


Figure 6.6: Adhesion design map for toroidal tips, constructed using the condensation limit developed by (a) Sitti and Fearing, (b) Glassmaker *et al.* and (c) Persson. The following parameters are assumed: $\gamma = 0.05 \text{ J/m}^2$, $f = 10\%$, $b = 0.2 \text{ nm}$ and $E_{\text{eff}} = 1 \text{ MPa}$. The dashed line (orange) is the “conode”. In (a) and (b) it has the same slope as the apparent contact strength limit. The whole sector between fiber fracture and ideal contact strength limit – indicated by the solid red line – yields optimal adhesive properties. In (c), the intersection of the “conode” with the ideal contact strength criterion indicates the optimum parameters and is highlighted with a red circle.

6.5.4 Intersection with the conode

For the condensation limit after Sitti and Fearing, as for the other ones, we can use the conode equations derived in the section about the maps for the punches, so that here only the optimal adhesion parameters will be derived. For the Sitti and Fearing (38) and for the Glassmaker *et al.* (44) limit, the conode equations, 6.25 and 6.29 respectively, have a slope of one half in the log-log plot of the maps. The adhesion design map for the latter limit is plotted in Figure 6.6b.

It is interesting that the conode and the apparent contact strength criterion have the same slope. This implies that all points on the conode have the same apparent

contact strength. The intersection of the conode with the ideal contact strength is defined by (Sitti and Fearing case):

$$\gamma \sqrt{\frac{h_f EC^3 f^3}{E_{eff}^3 \pi^3}} = \frac{E^3 \pi^2 b^3}{2^{11} \gamma^2} \quad (6.49)$$

resulting in the following maximum modulus:

$$E_{\max} = \frac{2^{22/3} Cf \gamma^2 h_f^{1/3}}{\pi^{7/3} b^2 E_{eff}} \quad (6.50)$$

The intersection with the fiber fracture criterion leads to:

$$\gamma \sqrt{\frac{h_f EC^3 f^3}{E_{eff}^3 \pi^3}} = \sqrt{1000\pi} \frac{\gamma}{E} \quad (6.51)$$

resulting in the following minimum modulus:

$$E_{\min} = \frac{10E_{eff} \pi^{4/3}}{Cf} \frac{1}{\sqrt[3]{h_f}} \quad (6.52)$$

The other parameters such as the aspect ratio and the radius can be deduced in an analogous way (see Table 8.1). The maximum and minimum apparent contact strength value is given below:

$$\sigma_{app}^{\max/\min} = \frac{E_{eff} \pi^{4/3}}{h_f^{1/3} C} \quad (6.53)$$

For the Glassmaker *et al.* approach (Figure 6.6b), we calculate the following maximum and minimum Young's moduli and apparent contact strength value:

$$E_{\max} = \frac{Cf\gamma^2 h_f^{1/2} 2^{22/3}}{E_{\text{eff}} \pi^3 b^2} \quad (6.54)$$

$$E_{\min} = \frac{10\pi^2 E_{\text{eff}}}{Cfh_f^{1/2}} \quad (6.55)$$

$$\sigma_{\text{app}}^{\max/\min} = \frac{E_{\text{eff}} \pi^2}{Ch_f^{1/2}} \quad (6.56)$$

For the condensation criterion after Persson (129) we get the adhesion design map shown in Figure 6.6c. For this limit the conode has been derived in equation 6.32. Here, the conode has a smaller slope than the contours of constant apparent contact strength, so that the intersection of the conode and the ideal contact strength limit determines the optimum design parameters. For the optimum Young's modulus and apparent contact strength, we get the following conditions:

$$E_{\text{opt}} = \frac{2^{11/2}}{\arccos^{2/3}\left(\frac{f}{\pi} 2\sqrt{3}\right)} \left(\frac{3Cf}{E_{\text{eff}}}\right)^{1/3} \left(\frac{\gamma}{\pi b}\right)^{4/3} \quad (6.57)$$

$$\sigma_{\text{app}}^{\text{opt}} = 2^{11/6} \left(\frac{\pi E_{\text{eff}}}{3C}\right)^{1/3} \left(\frac{f\gamma \arccos\left(\frac{f}{\pi} 2\sqrt{3}\right)}{b}\right)^{2/3} \quad (6.58)$$

6.6 Design Maps for Tapes

Next, adhesion design maps for elastic tapes are presented. We make the following assumptions:

- The tape has a square contact area of dimensions $2R \times 2R$
- Scaling of the tape thickness h is self similar: $h = R/10$
- In the first part, the peel-off angle will be kept constant at $\alpha = 60^\circ$
- The condensation and adaptability criterion are unchanged compared to spherical contacts
- Perfect contact without surface roughness

6.6.1 Contours of constant apparent contact strength

From Kendall (12, 133) we get the pull-off force of an elastic band:

$$P_c = 2\gamma R g(\alpha, \lambda) \quad (6.59)$$

where two variables are defined as follows:

$$g(\alpha, \lambda) = \frac{2 \sin \alpha}{\sqrt{(1 - \cos \alpha)^2 + 2\lambda + (1 - \cos \alpha)}} \quad (6.60)$$

$$\lambda = \frac{10\gamma}{ER}$$

With the assumptions stated above, this leads to the following expression for P_c :

$$P_c = \frac{4\gamma R}{\sqrt{1 + \frac{80\gamma}{3ER}}} \quad (6.61)$$

From this, we determine the condition for R (for a more detailed derivation see appendix D, 8.4.1.1) (15):

$$R \leq -\frac{40\gamma}{3E} + \sqrt{\frac{1600\gamma^2}{9E^2} + \frac{f^2\gamma^2}{\sigma_{app}^2}} \quad (6.62)$$

Note that for the elastic band, the contours of constant apparent contact strength are independent of Young's modulus for large moduli, but scale inversely with Young's modulus for small moduli.

6.6.2 The limit of fiber fracture

For the fiber fracture limit, we get (15),

$$\sigma_f = \frac{5P_c}{R^2} \leq \sigma_{th}^f \approx \frac{E}{10} \quad (6.63)$$

this yields (see appendix D, 8.4.1.2):

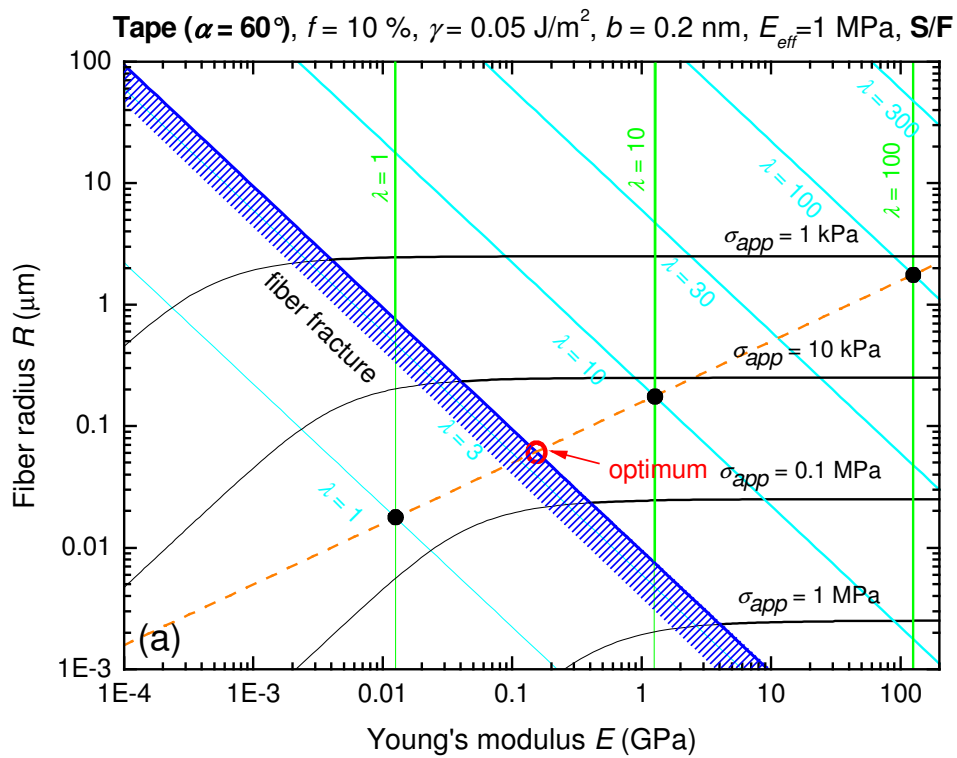
$$R \geq \frac{188\gamma}{E} \quad (6.64)$$

6.6.3 The limit of ideal contact strength

Following Spolenak *et al.* (15), we derive the following equation for R (see appendix D, 8.4.1.3, for a more detailed derivation):

$$R \geq -\frac{40\gamma}{3E} + \sqrt{\frac{1600\gamma^2}{9E^2} + b^2} \tag{6.65}$$

For the three different condensation criteria considered and the above derived limits, the resulting adhesion design maps for elastic tapes at a peel-off angle of 60° are presented in Figure 6.7.



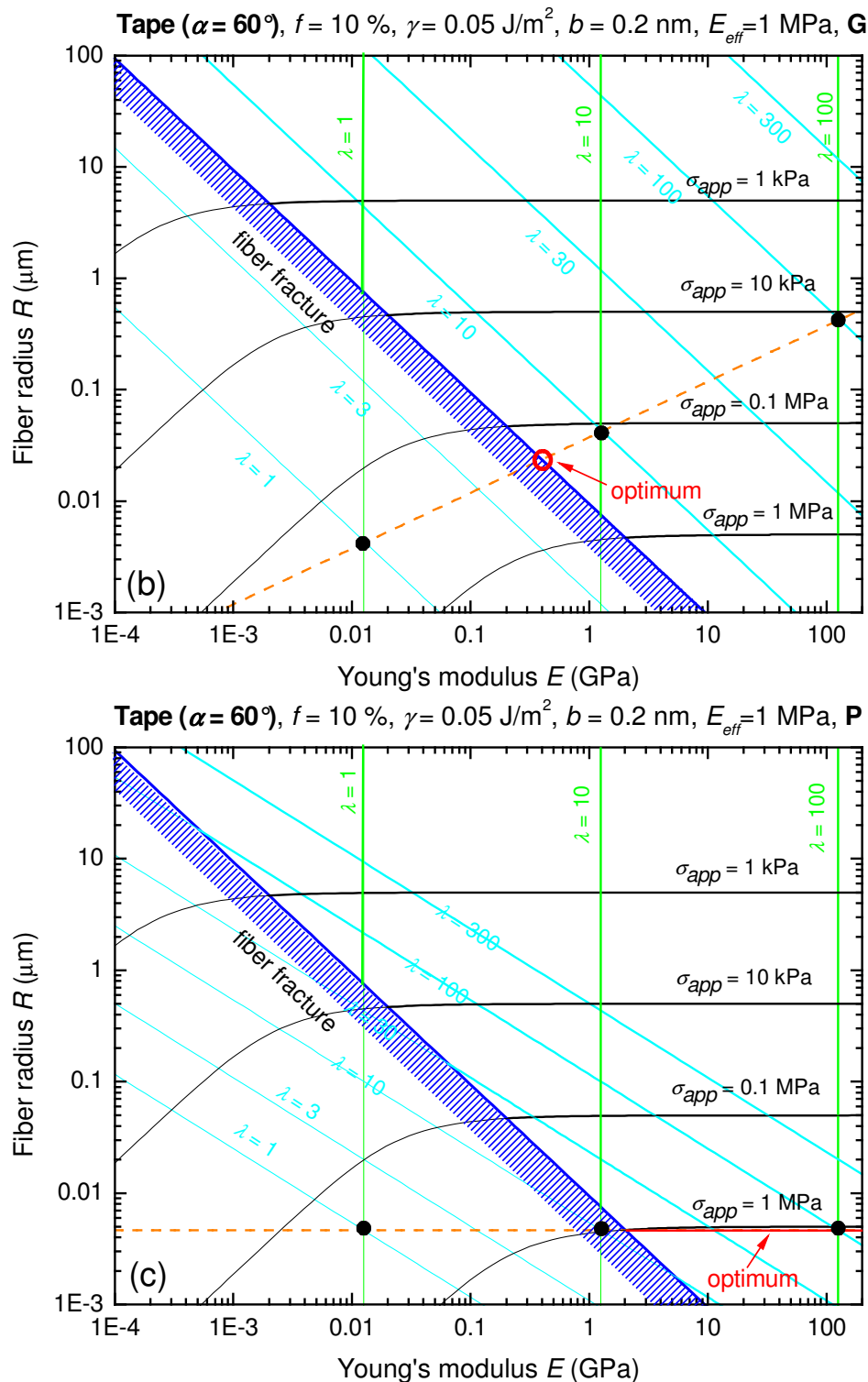


Figure 6.7: Adhesion design map for an elastic tape at a peel-off angle of 60° , constructed using the condensation limit developed by (a) Sitti and Fearing, (b) Glassmaker et al. and (c) Persson. The following parameters are assumed: $\gamma = 0.05 \text{ J/m}^2$, $f = 10\%$, $b = 0.2 \text{ nm}$ and $E_{\text{eff}} = 1 \text{ MPa}$. The dashed line (orange) is the “conode”. In (a) and (b), its intersection with the fiber fracture limit indicates the optimum parameters and is highlighted with a red circle. In (c), right of the fiber fracture criterion, the conode has about the same slope as the apparent contact strength limit, so that this entire domain – indicated by the solid line – yields optimum design parameters.

6.6.4 Intersection with the conode

In the log-log plot of Figure 6.7a, the conode for the condensation limit after Sitti and Fearing (38) has a slope of one half (eq. 6.25). It is now instructive to compare the conode slope to the slope of the apparent contact strength criterion. Here, the slope of the apparent contact strength criterion is zero at high moduli and -1 at low moduli. This means that the optimum can be found at the intersection between the conode and the fiber fracture criterion, which leads to the following condition:

$$\gamma \sqrt{\frac{h_f E C^3 f^3}{E_{eff}^e \pi^3}} = \frac{188\gamma}{E} \quad (6.66)$$

resulting in the optimum modulus:

$$E_{opt} = \frac{188^{2/3} E_{eff} \pi}{\sqrt[3]{h_f} C f} \quad (6.67)$$

The optimum apparent contact strength is given by:

$$\sigma_{app}^{opt} \approx \frac{1.10 E_{eff}}{C \sqrt{h_f}} \quad (6.68)$$

For the condensation criterion brought forward by Glassmaker *et al.* (44), we get the adhesion design map presented in Figure 6.7b. In equation 6.29 we calculated the according conode. As in the Sitti and Fearing case, the intersection between the conode and the fiber fracture limit gives the optimal design parameters. Here, we calculate E_{opt} and σ_{app}^{opt} (see Table 8.1 for R_{opt} and λ_{opt}):

$$E_{opt} \approx \frac{20E_{eff}\pi^{5/3}}{Cf\sqrt{h_f}} \quad (6.69)$$

$$\sigma_{app}^{opt} \approx \frac{1.10E_{eff}}{C\sqrt{h_f}} \quad (6.70)$$

For the condensation limit developed by Persson (129), the log-log plot of the design maps is shown in Figure 6.7c. In the region right of the fiber fracture criterion, the conode, see equation 6.32, has about the same slope as the apparent and the ideal contact strength limits (namely nil). So this entire domain, which in theory goes up to infinite Young's moduli, will yield optimal design parameters. We thus calculate the minimum Young's modulus E_{min} and the minimum apparent contact strength σ_{app}^{min} :

$$E_{min} = \frac{188\gamma^{1/3} \arccos^{4/3}\left(\frac{f}{\pi}2\sqrt{3}\right)}{b^{1/3}} \left(\frac{E_{eff}\pi}{3Cf}\right)^{2/3} \quad (6.71)$$

$$\sigma_{app}^{min} = \left(\frac{141}{161}\right)^{1/2} \left(\frac{f\gamma}{b}\right)^{1/3} \left(\frac{\pi E_{eff}}{3C}\right)^{2/3} \arccos^{4/3}\left(\frac{f}{\pi}2\sqrt{3}\right) \quad (6.72)$$

6.6.5 Limits and maps for other peel-off angles

As it might be instructive to compare adhesion design maps for elastic tapes for different peel-off angles α , we derive the limiting conditions as a function of α . Because the calculation itself is similar to the one described above, only the results for the limits and some basic steps will be given.

Apparent contact strength:

The general solution for the contours of constant apparent strength is found to be:

$$R \leq \frac{-\frac{10\gamma}{E} + \sqrt{\frac{100\gamma^2}{E^2} + \frac{Y \sin^2 \alpha \gamma^2 f^2}{\sigma_{app}^2}}}{Y} \quad (6.73)$$

with

$$Y = [(1 - \cos \alpha)^2 + (1 - \cos \alpha)] \quad (6.74)$$

Fiber fracture:

$$R \geq \frac{-\frac{10\gamma}{E} + \sqrt{\frac{100\gamma^2 + Y 200^2 \sin^2 \alpha \gamma^2}{E^2}}}{Y} \quad (6.75)$$

Ideal contact strength:

$$R \geq \frac{-\frac{10\gamma}{E} + \sqrt{\frac{100\gamma^2}{E^2} + Y b^2 \sin^2 \alpha}}{Y} \quad (6.76)$$

Because the design maps published so far (15) were constructed using the condensation limit after Sitti and Fearing and since the general trends for different peel-off angles α will be the same for all three condensation criteria, we only consider the Sitti and Fearing approach for the construction of maps at different angles. In Figure 8.10 (appendix D) the adhesion design maps are plotted for seven different peel-off angles, i.e. $\alpha = 5, 15, 30, 45, 60, 75$ and 90° .

Intersection with the conode:

As for the case of $\alpha = 60^\circ$, the optimal design parameters can be found at the intersection of the conode with the fiber fracture limit. This yields the following equation for the optimum Young's modulus:

$$E_{opt} = \frac{10^{2/3} \left(-h_f + \sqrt{h_f^2 + 400Y \sin(\alpha) h_f Y^2} \right)^{2/3} E_{eff} \pi}{Y^2 f C h_f} \quad (6.77)$$

With this knowledge of the optimal Young's modulus as a function of the peel-off angle, we ask the question at which angle E_{opt} is maximal. Here also R_{opt} would be largest. In order to determine those values, the maximum of the above derived equation is calculated. This is the case when the following equation is satisfied:

$$\frac{800}{3} \frac{10^{2/3} Y \pi E_{eff} h_f \sin(\alpha) \cos(\alpha)}{\left(-h_f Y^2 + Y^2 \sqrt{h(f)^2 + 400Y \sin(\alpha)^2 h_f^2} \right) f C \sqrt{h_f^2 + 400Y \sin^2(\alpha) h_f^2}} = 0 \quad (6.78)$$

Inserting values for $C = 10$, $f = 0.1$, $E_{eff} = 1$ MPa, results in a peel-off angle for the Young's modulus to be maximal of $\alpha \approx 39^\circ$.

6.7 Discussion

6.7.1 Critical number for change in hierarchy

The critical number of new contacts necessary to substitute one big contact strongly depends on tip shape, as is demonstrated in Table 6.1. Not surprisingly, this is correlated with what is called “splitting efficiency”, as shapes which benefit more from splitting will need less small contacts on a next level of hierarchy to increase total pull-off force. Considering a fiber packing density of $f = 0.1$, one needs 10 new fibers for hemispherical tip shape and 1.000 new ones for flat tips. The reason is that, the splitting efficiency of the punch is a factor of 2 smaller than that of the sphere. Since the splitting efficiency of the tape is the same as that of the sphere, N_{min} for tapes has the same dependence on f . For constructing hierarchical artificial adhesives it will thus be best to choose hemispherical or band-like shape. This is of importance, as fabrication techniques, or even more the limit of fiber condensation, will constrain the packing density, so that the only choice for reaching high numbers of contacts is going to very small fiber radii. That again is a severe challenge in the fabrication process. In first experiments, the fabrication of elastomeric pillars with different tip shapes – among them also ones which remind of gecko spatulae – has already been demonstrated (39, 52, 134, 135), see chapters 3, 4 and 5. Even though pillar dimensions were still in the micrometer range and the aspect ratios very small, these structures showed that the fabrication of complex tip shapes is possible. The concept of hierarchical systems is very important once surface roughness is considered, as was theoretically demonstrated by Kim and Bhushan, who showed that multi-level hierarchical structures are beneficial for adapting to rough surfaces (136).

6.7.2 Comparison of spheres and tapes

When looking at the gecko adhesive system with modern scanning electron microscopy, one discovered the spatular structure that terminates the individual attachment hairs (setae). Therefore, it is reasonable to assume that among the tip shapes treated in this chapter, the elastic tape is best suited to describe what we find with the gecko. Interestingly, the elastic tape and the hemispherical tip shape have the same splitting efficiency (12), even though they differ in their modulus dependence. According to classic JKR theory, the adhesion of spheres is independent of Young's modulus, whereas the pull-off force of elastic tapes scales with the square root of E . Because of this and the different peel-off angles that have to be considered, the contact mechanical treatment of tapes is more complicated than that of spheres. As they both show the same splitting efficiency, the idea of approximating the tape with spheres is evident. In this paragraph, we ask the question whether this is an appropriate assumption, or not. Therefore, we plot the limits for spherical and tape contact in one adhesion design map, considering peel-off angles between 15° and 90° for the elastic band. The resulting plot is presented in Figure 6.8 where the intervals for constant apparent contact strength and the fiber fracture limit are marked as hatched areas.

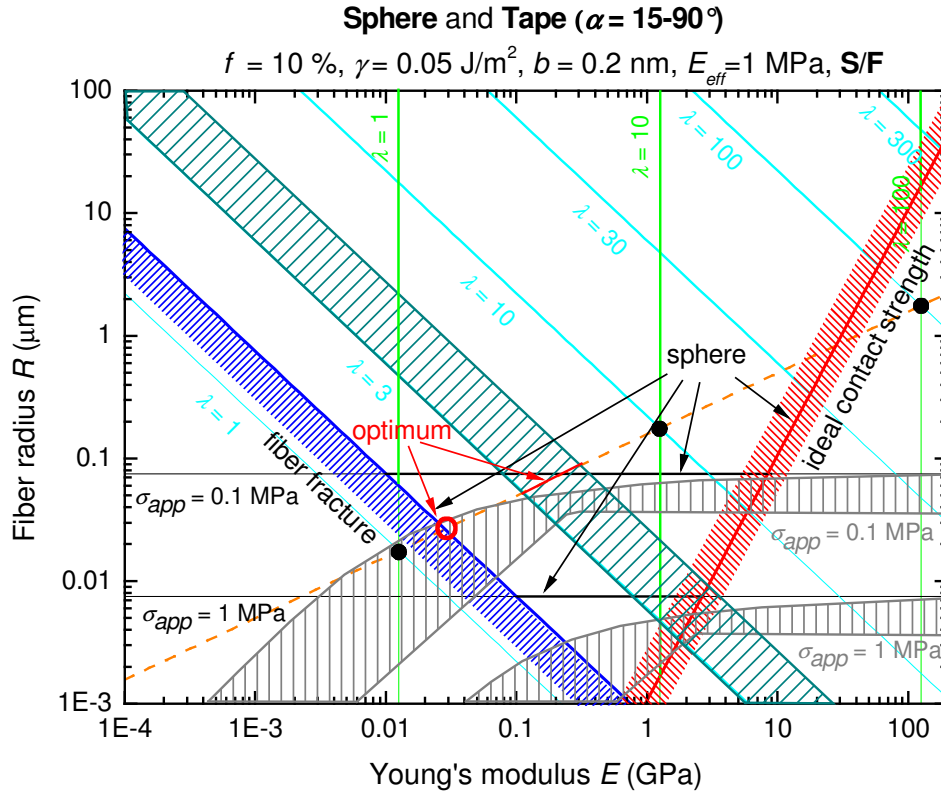


Figure 6.8: Adhesion design map for hemispherical and band-like tip shape, constructed using the condensation limit developed by Sitti and Fearing. The following parameters are assumed: $\gamma = 0.05 \text{ J/m}^2$, $f = 10\%$, $b = 0.2 \text{ nm}$ and $E_{\text{eff}} = 1 \text{ MPa}$. For the elastic band, peel-off angles between 15° and 90° are considered and the resulting areas for constant apparent contact strength (gray lines) and for the fiber fracture limit (light blue) are hatched. The limits belonging to the spherical contact are indicated. The adaptability and condensation criteria are invariant to contact shape. The dashed line (orange) is the “conode”. Its intersections with the fiber fracture limits yield the optimum parameters and are indicated with a red circle in the case of the sphere and by a solid red line for the tape contact.

A first observation in Figure 6.8, is the strong dependence of the apparent contact strength on Young’s modulus for the tape contact. For small moduli it scales inversely with E , whereas for high E , it is independent of the Young’s modulus and reaches the value for the hemispherical contact for which the apparent contact strength is no function of E . The point most interesting to mention when considering only hemispheres instead of elastic bands are the optimum values. For the spheres, an optimum Young’s modulus of around 30 MPa and an optimum fiber radius of approx. 30 nm was found. In the case of the elastic band, the regimes for those parameters are 100 - 300 GPa for E_{opt} and 50 - 100 nm for R_{opt} . This shows that for finding the optimal fiber radius, the hemispherical approximation is appropriate, whereas for the Young’s modulus it yields values about one order of magnitude higher than for the tape itself. Generally speaking, it is surprising how

little the modulus effect is, and how well the spherical contact can be used as a first order approximation for the elastic band.

6.7.3 Discussion of adhesion design maps

In Figure 6.3, the adhesion design maps for the flat tips are shown. As for all three condensation models the slope of the conode is smaller than that for the contours of apparent contact strength, the intersection of the conode with the ideal contact strength yields the optimum design parameters. This is somewhat surprising as we usually experience that softer materials “stick” more than stiffer ones. The reason for this surprising result is found in the relationship between pull-off force and Young’s modulus for the flat punch (eq. 6.19): The pull-off force scales with the square root of the modulus. Thus, the stiffer the punch, the higher the adhesion force. This relationship, which is valid only for a punch stiffer than the half space it is in contact with, was derived neglecting surface roughness. Introducing roughness changes those results as is demonstrated by the periodical model presented in this chapter. With roughness, the adhesion performance of the punch is dramatically reduced (Figure 6.4) and the results are more like what one would expect intuitively. This strong roughness influence has already been investigated by Fuller and Tabor in 1975. They theoretically treated the reduction in adhesion force due to a gaussian distribution of surface asperities heights on a rough flat, in contact with a smooth sphere (137). Fuller and Tabor found that even a relatively small surface roughness (in the nanometer regime) can reduce adhesion to very small values. Also in 1975, Johnson treated the effect of surface roughness on adhesion forces very similar to the approach taken by Fuller and Tabor (138). He chose an exponential distribution of asperity heights and found that the influence of surface roughness can be so strong that no overall adhesion is developed (138). More recently, Persson in his theory for the adhesion between rough bodies, described the surfaces with a roughness power spectrum (139, 140). In good

qualitative agreement with experimental results by Fuller and Tabor, he found that the pull-off force was dramatically reduced with increasing roughness (139, 140). Persson's theory can also be applied for the contact between two rough plates; the combination we are dealing with in the maps for the flat tips. Compared with those approaches for rough surfaces, our model is very simplified and could be improved by introducing a statistic distribution for the radii of the hemispheres. Still, it very well demonstrates the dramatic influence of surface roughness on adhesion performance. For Persson's approach to fiber condensation (129), in Figure 6.3c the intersection of the conode with the ideal contact strength limit is below the criterion for fiber fracture, so that here no optimum would be found for the given parameters. As the conode is only slightly below the cross-over of the fiber fracture and the ideal contact strength limit, the optimum parameters are calculated nevertheless and are presented in Table 6.2 (see below).

For the toroidal tips presented in Figure 6.6, the conodes for the condensation models developed by Sitti and Fearing (38) and Glassmaker *et al.* (44), have the same slope as the contours of constant apparent contact strength. Thus, the whole conode between the fiber fracture and the ideal contact strength limit yields optimum parameters. For the Sitti and Fearing case this means that one can change the Young's modulus by over three orders of magnitude (from ca. 0.6 to 200 GPa) and still obtain the same adhesion performance. The optimum radius would change from about 0.04 to 2 μm in this process. The reason for this behavior is a balance between contact splitting and the dependence of the pull-off force on Young's modulus. The latter scales with $E^{1/3}$ and favors larger moduli, whereas contact splitting shifts optimum values to smaller radii.

For the tapes, which have the same splitting efficiency as spheres (12), contact splitting is "stronger" than the dependence on Young's modulus ($P_c \sim E^{1/2}$). For the

condensation limits after Sitti and Fearing and Glassmaker *et al.*, the optimum values are found at smaller Young's moduli and radii. Both, the contours of constant apparent contact strength and the limit of ideal contact strength are shifted to smaller radius values than in the maps for the other shapes. The limit of ideal contact strength, for the Young's moduli considered, is found at radii smaller than the ones included in the maps. As the contours of apparent contact strength for $\sigma_{app} = 0.1$ and 1 MPa are at such small radius values, in Figure 6.6 contours for $\sigma_{app} = 1$ and 10 kPa are added. Inserting values for $C = 10$, $f = 0.1$, $E_{eff} = 1$ MPa, yields a peel-off angle for the Young's modulus to be maximal of $\alpha \approx 39^\circ$. E_{opt} then is 66 MPa. Interestingly, the angle at which gecko spatulae make contact with a substrate (109) is between 50 and 55° which is quite close to our result. As well, other theoretical treatment of gecko attachment by Gao *et al.* demonstrated that the attachment force was maximal for a pulling angle of around 30° (141). Again, this is close to what was found here. What is quite different than in natural systems is the optimum Young's modulus, which is around 1 - 10 GPa in nature (142), whereas we calculated a value of 66 MPa. This difference might originate in the assumptions made when constructing the maps and which seem to have more influence on the modulus than on the peel-off angle.

6.7.4 What is the optimum shape?

As we constructed adhesion design maps for several contact shapes, it is only fitting to ask the question which shape will yield the optimal adhesive. For each contour, the conditions for the optimum Young's moduli and the optimum apparent contact strengths have already been presented. In Table 8.1 (appendix D) these results are summarized and supplemented with the equations for the optimum radii and aspect ratios. In order to be able to compare all contact shapes, including the hemisphere which was treated in an earlier publication (15), the results for spheres have been added. As it is quite

difficult to see trends with these equations only, we insert the typical values for b , C , f , E_{eff} , α and γ that were used to construct the maps in Figures 6.3 to 6.8 ($b = 0.2$ nm, $C = 10$, $f = 0.1$, $E_{eff} = 1$ MPa, $\alpha = 60^\circ$, $\gamma = 0.05$ J/m²). The resulting numerical values for the optimal design parameters are summarized in Table 6.2.

Table 6.2: To ease the comparison between the different tip shapes and fiber condensation models, we insert typical values ($E_{eff} = 1$ MPa, $C = 10$, $f = 0.1$, $\gamma = 0.05$ J/m², $b = 0.2$ nm) into the equations for E_{opt} , R_{opt} , λ_{opt} and the ultimate apparent contact strength σ_{app}^{opt} , listed in Table 8.1, and present the numerical results. In (a) for the condensation limit after Sitti and Fearing, in (b) for the Glassmaker *et al.* approach and in (c) for the condition developed by Persson. For the spherical tips a Poisson's ratio of $\nu = 0.3$ is assumed.

(a) Condensation limit after Sitti and Fearing

Tip shape	E_{opt} (Pa)	R_{opt} (m)	λ_{opt} (-)	σ_{app}^{opt} (Pa)
Sphere	$2.83 \cdot 10^7$	$2.65 \cdot 10^{-8}$	1.50	$2.83 \cdot 10^6$
Flat punch	$5.98 \cdot 10^{12}$	$1.22 \cdot 10^{-5}$	735.80	$2.5 \cdot 10^7$
Torus (self similar)	$4.71 \cdot 10^{11}$	$3.42 \cdot 10^{-6}$	193.60	$6.81 \cdot 10^5$
	$6.81 \cdot 10^7$	$4.11 \cdot 10^{-8}$	2.30	
Elastic tape ($\alpha = 60^\circ$)	$1.53 \cdot 10^8$	$6.16 \cdot 10^{-8}$	3.49	$7.44 \cdot 10^4$

(b) Condensation limit after Glassmaker *et al.*

Tip shape	E_{opt} (Pa)	R_{opt} (m)	λ_{opt} (-)	σ_{app}^{opt} (Pa)
Sphere	$1.07 \cdot 10^8$	$6.99 \cdot 10^{-9}$	2.90	$1.07 \cdot 10^6$
Flat punch	$3.36 \cdot 10^{11}$	$6.85 \cdot 10^{-7}$	163.50	$2.50 \cdot 10^7$
Torus (self similar)	$1.78 \cdot 10^8$	$5.02 \cdot 10^{-7}$	119.80	$1.78 \cdot 10^6$
	$1.80 \cdot 10^{11}$	$1.58 \cdot 10^{-8}$	3.76	
Elastic tape ($\alpha = 60^\circ$)	$3.99 \cdot 10^8$	$2.36 \cdot 10^{-8}$	5.63	$1.98 \cdot 10^5$

(c) Condensation limit after Persson

Tip shape	E_{opt} (Pa)	R_{opt} (m)	λ_{opt} (-)	σ_{app}^{opt} (Pa)
Sphere	$1.61 \cdot 10^8$	$4.65 \cdot 10^{-9}$	3.58	$1.61 \cdot 10^6$
	$2.11 \cdot 10^9$	$4.65 \cdot 10^{-9}$	12.95	$1.61 \cdot 10^6$
Flat Punch	$2.28 \cdot 10^9$	$4.65 \cdot 10^{-9}$	13.47	$2.50 \cdot 10^7$
Torus (self similar)	$1.74 \cdot 10^{10}$	$4.65 \cdot 10^{-9}$	37.16	$1.85 \cdot 10^7$
Elastic tape ($\alpha = 60^\circ$)	$2.02 \cdot 10^9$	$4.65 \cdot 10^{-9}$	12.69	$1.01 \cdot 10^6$

With these values and for all three condensation criteria, the flat punch results in the highest values for the optimum apparent contact strength. It reaches a value of $\sigma_{app}^{opt} = 25$ MPa, which is well above that of the gecko (0.1 to 0.2 MPa (6, 8)). The resulting values for the optimal Young's moduli reach numbers which for the Sitti and Fearing condensation model ($E_{opt} = 6$ TPa) even surpass moduli reached by to-date materials (1 TPa). In the maps, we limited the Young's modulus to a maximum of 200 GPa, as in real contact pairs the effective modulus will very rarely exceed this value. The radius values seem to be more plausible in the Persson case, as one would expect that pillars in the nanometer regime are superior to those in the micrometer range. Interestingly, the value for the pillar aspect ratio is very small for the Persson criterion ($\lambda_{opt} \approx 17$) and thus much more feasible than the high numbers predicted by the other two limits ($\lambda_{opt} \approx 160$ and 735). For a fiber packing density of 10 %, simple geometrical considerations yield a minimum aspect ratio of around 8 for the Persson limit to be applicable. Thus, only the minimal aspect ratio in the hemispherical case is below what is describable after Persson. Introducing surface roughness and using our simple model of periodic hemispherical bumps, the performance of the punch drops dramatically and the apparent contact strength for a roughness of $R_z = 1 \mu\text{m}$ is no higher than approx. 7 kPa (about a factor of 80.000

smaller than without roughness!). As discussed in the previous section, such drastic reductions in adhesion performance were modeled in the literature and found experimentally (111, 137, 139, 140) as well.

For the other tip shapes, it depends on the condensation model which shape has the second highest value for the optimum apparent contact strength. For the Sitti and Fearing limit, the spherical contact shows the second highest adhesion performance ($\sigma_{app}^{opt} = 2.8$ MPa) followed by the torus (0.7 MPa) and the elastic tape (74 kPa). In all three cases, the predicted optimal Young's modulus and radius values are plausible and in the range possible in artificial systems.

In the case of the other two condensation criteria, the torus adheres second best ($\sigma_{app}^{opt} = 1.8$ MPa for the Glassmaker *et al.* limit and 18.5 MPa for the Persson criterion), and is followed by the hemispherical contact (about 1 MPa for both limits). The elastic tape always shows the lowest adhesion performance (0.2 and 1.0 MPa), but we still calculated apparent contact strengths in the range of gecko attachment (0.1 to 0.2 MPa) (6, 8). This is remarkable, as the elastic tape does thereby not only promise significant adhesion, but due to its asymmetric nature allows easy detachment; a property very desirable in technical systems. For the Glassmaker *et al.* limit, the optimum Young's moduli are all in the 0.1 GPa range and the radii are between 7 and 500 nm. This is quite small, but still feasible with today's fabrication techniques; especially as the optimal aspect ratios for these three tip shapes are below 10. We can state that all optimal aspect ratio values, with the exception of the flat punch, are quite small; the highest being about 40 for the torus after Persson, and the rest mainly being below 10. In summary, for ideal surfaces without roughness, flat tips are by far the ones with the best adhesion performance. This breaks down once roughness comes into play. For the ideal case, the flat punches are either

followed by the torii, or the hemispheres, depending on the condensation limit, whereas the elastic tape always adheres least. But even the tapes give maximum values for the apparent contact strength well in the range of gecko adhesion. All shapes, independent of the condensation limit, take high optimum Young's modulus values, which are above the MPa range and, with the exception of the flat punch and the torus after Sitti and Fearing, optimum radii below one micrometer. The optimum aspect ratios for the elastic tape, the torus and the sphere are mainly below ten, but even exceed 700 for the flat punch.

The question which condensation limit is best suited for the construction of adhesion design maps is difficult to answer. For the punch, the Sitti and Fearing model leads to an intersection point of the conode with the ideal contact strength limit at a Young's modulus above those realized in up-to-date materials. We thus expect the strongest adhesion for the stiffest materials at hand. Interestingly, there are two experimental studies showing very promising adhesion performance of carbon nanotube based dry adhesives (57, 58). Also for the Glassmaker *et al.* approach the intersection point of the conode with the ideal contact strength limit is at a Young's modulus value of 300 GPa, which is still very high. The model after Persson thus seems to be best suited to describe the punch shape as it yields the most reasonable results. It has to be stated though that, when being compared with experimental data from microstructured elastomer surfaces, both the Sitti and Fearing and the Glassmaker *et al.* approach, describe the experimental reality very well (131), see chapter 4. For the other tip shapes, the model after Persson demands for the smallest radii, with the optimum being independent of tip shape. As one would expect that the optimum radius is a function of contact shape, one could argue that the Glassmaker *et al.* approach (in our context) is more feasible than that developed by Persson. The Sitti and Fearing model, which assumes spherical tips for all contact shapes, perhaps should only be used for hemispheres. At the end, the Glassmaker *et al.* limit might be the one of choice for the

construction of adhesion design maps. In this context it is interesting to mention that considering the quite different approach for calculating the attractive forces between two fibers, the Sitti and Fearing and the Glassmaker *et al.* model give surprisingly similar results. This is demonstrated in Figure 6.2 where the ratio between the condensation condition after Sitti and Fearing and after Glassmaker *et al.* is plotted as a function of fiber area fraction f . For most technical systems f will range between 0.1 and 0.6. In this regime the ratio of the two limits is between one and four, demonstrating how little the difference between them really is. Still, this small difference in some cases can yield quite different optimum design parameters in the log-log plot of the maps. Another idea to circumvent condensation problems is to choose a quadratic fiber cross-section and packing the fibers such that they can touch their nearest neighbors only with the edges and not with the faces. By doing so, the attractive forces between the fibers and thus the problem of fiber condensation is minimized. Additionally, one could coat the fiber surface, not the tip, with a material with low work of adhesion, reducing attractive forces. The same effect could be achieved by roughening the fiber surfaces.

6.7.5 Limitations and problems

A word of caution is necessary. The adhesion design maps presented in this chapter are based on severe simplifications. For example, the fiber fracture limit is based on the approximation that the theoretical fracture strength is one tenth of the Young's modulus. This can only be derived for perfect crystalline materials (143), but is not valid for polymers. For PDMS, the fracture strength is about a factor of four higher than the Young's modulus (see Table 3.3). As polymers very often are amorphous, or have large amorphous fractions, it is not possible to derive a similar, elegant relationship between fracture strength and modulus. Moreover, the mechanical properties of polymers depend on parameters that do not exist in metals and ceramics, e.g. polydispersity.

Thus, $\sigma_{th}^f = E/10$ is used knowing that it is under debate. It still is a good first order approximation over the entire modulus range covered in the maps. Especially as the limit of fiber fracture is shifted to smaller radii for higher ratios like $\sigma_{th}^f \approx 4E$ and therefore becomes even less important compared to the criterion of fiber condensation.

For the flat punch contact, the equation for the pull-off force (eq. 6.19) was originally derived assuming that the contact radius is equal to the radius of the punch. This is only valid for a punch with higher stiffness than that of the substrate it is in contact with. This will not be the case for the entire modulus range of the design maps. Spolenak *et al.* showed that for the contact radius being reduced to 80 % of the punch radius, the pull-off force is reduced by ca. 10 % (12). We follow this argument and use eq. 6.19 for all moduli considered in the maps.

Examples for results that might be misleading, are the low optimum aspect ratios that are predicted in this chapter. One possible reason has already been mentioned; the neglect of surface roughness. As in the real world animals with fibrillar adhesives have to adhere to surfaces with considerable roughness, they are equipped with setae of larger aspect ratios (about 25 for the gecko (144)). In the future, it would be interesting to include roughness into the maps for all shapes and in a more sophisticated manner than presented in this chapter. As well, there is experimental evidence that the gecko adhesion benefits from humidity and that capillary effects might play a role (6). One can imagine artificial adhesives combining capillary and van der Waals type interactions. This might also be part of future design maps, in order to find out about the optimum design parameters in wet or humid environments. Finally, a parameters which should be considered more in the future is the effect of aspect ratio on adhesion performance. Both, theoretical and experimental investigations have shown that adhesion increases with aspect ratio (118-120, 131), see

chapter 4. This effect has so far not been considered in the maps, but it would favor higher aspect ratios automatically.

The adhesion design maps as they are presented here, are meant as first approximations to learn more about the effect of shape on the adhesion behavior. They are another step to find out how different tip shapes influence the process of choosing the right design parameters for optimal adhesives and they give first indications which shape is most promising when it comes to maximizing adhesion performance. They also might help to understand biological attachment systems as nature provides a variety of different contact shapes (12).

6.8 Conclusions

In the present chapter we extended the existing concept of adhesion design maps for hemispherical contacts to three other tip shapes. These shapes are flat, toroidal and elastic band. Keeping in mind the assumptions made when constructing the maps, and comparing the three new shapes with the already presented hemispherical one (15), we draw the following main conclusions when it comes to the design of an optimal adhesive system:

- When hierarchical structures are considered, one has to keep in mind that there is a critical number for new pillars substituting one big contact so that this change is beneficial for the adhesion performance. This critical number is a function of fiber packing density and tip shape, reflecting the different splitting efficiencies. It is easiest to switch to another level of hierarchy for spherical and band-like structures. One has to create most new contacts for adhesives with flat tips.
- For ideal surfaces without any roughness, flat tips yield the strongest adhesives. This breaks down once roughness is considered. The second best adhesion performance results from toroidal tips, followed by spheres and tapes. For the elastic band, maximum adhesion performance is still found to be in the range of the gecko. This is very promising as the asymmetric tape allows for an easy release of the contact.
- Among the three condensation models considered, the one put forward by Glassmaker *et al.* seems to be best suited for the construction of adhesion design maps, as it is independent of contact shape and could even be expanded to square fiber cross sections.

7 Summary and Outlook

The present study clearly demonstrates that there are significant size and shape effects in bioinspired dry adhesives. To understand these phenomena in more detail, different 3D tip shapes were fabricated from standard 2D SU-8 molds which were microstructured using contact mode photolithography. By variations of the soft molding techniques, standard flat punch, spherical, concave, spatula-like and mushroom-shaped tip geometries, as well as flat punches with rounded edges were successfully fabricated. With the development of a two step process, first hierarchical model systems were demonstrated. Synthesis of these structures was possible homogeneously over one square centimeter, but up-scaling to entire wafer level is expected to be feasible. The feature dimensions of the fabricated structures ranged from 2 to 50 μm in diameter and from 2.5 to 200 μm in height.

Systematic adhesion experiments on these structures revealed a number of size and shape effects. First, the principle of contact splitting was found to be valid for flat tips and such terminated by hemispheres. The splitting efficiencies were in strikingly exact agreement with JKR-based adhesion theory. When comparing the performance of the other shapes, it is most interesting that spatula- and mushroom-shaped pillars generated very high pull-off forces. For the mushroom shape pull-off strengths in the region of gecko adhesion were determined. A flat control specimen was exceeded by over a factor of 30, even for large pillar diameters. Since the splitting efficiency of the mushroom shape is largest, even higher strengths with decreasing feature size will be possible in the future. Flat and spherical shapes showed lower adhesion, while concave tips resulted in the

poorest performance, coupled with an unusual preload dependence. In Figure 7.1 the same literature data as in Figure 2.3 are presented as adhesion strength plotted versus feature radius on a log-log scale. Additionally, the data presented in this thesis were added. They fit well into the published results and demonstrate the influence of size and shape on the adhesion of fibrillar systems.

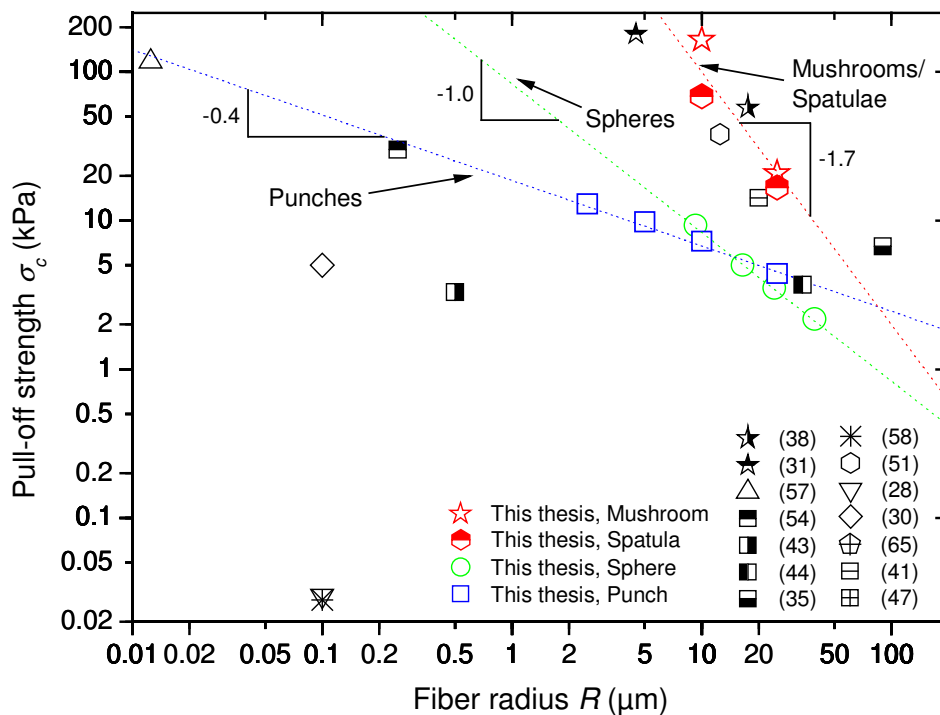


Figure 7.1: A comparison of the published adhesion strength (pull-off force per area, σ_c) data represented as pull-off strength versus fiber radius and the data presented in this thesis (all for aspect ratio one and at $P_p = 1$ mN).

The adhesion testing also revealed a strong preload dependence of the pull-off force, which increased with increasing preloads. This effect was more pronounced in pillars with higher aspect ratios and could be explained by the spherical nature of the indenter used to measure adhesion. Interestingly, not only a reduction of feature size increased adhesion performance but also an increase of pillar aspect ratio. A possible explanation for this result was found in a model originally developed for the rupture of rubbery solids, which describes the behavior found in this work very well. Thus, the highest pull-off forces can be expected for pillars with small radii and high aspect ratios, while avoiding fiber

condensation. This highlights again the need for a trade-off between geometrical and elastic parameters as it is demonstrated by the adhesion design maps which in this thesis have been extended to further contact shapes besides the hemispherical one. These shapes were that of a flat punch, a torus and of an elastic tape, for which different peel-off angles were considered. For contact with an ideal smooth surface it was found that flat tips give the strongest adhesives followed by toroidal tips, spheres and tapes. The elastic tapes seem to be very promising, as the adhesion performance is in the regime of natural systems and their asymmetric shape allows for easy release. By putting forward a simple model for rough surfaces it was demonstrated that even small roughnesses reduce adhesion dramatically.

There is still a lot that can and should be done for future experiments on fibrillar model systems. First, the analysis presented in this thesis is based on van der Waals interactions only, not considering any humidity or capillary effects. Since experiments on natural fibrillar systems showed a strong humidity dependence of the pull-off forces (6), it would be interesting to see if such effects are found with artificial surfaces as well. Recent theoretical calculations already indicated that capillary forces also depend on contact shape (115). First experiments in this direction are under way. Of course, the high splitting potential of the spatula- and the mushroom-like tip shape should be investigated further, mainly by scaling down the contact size to confirm the high pull-off strengths of these structures predicted by the data shown in this thesis. In 2005 Suh *et. al* already presented a method of fabricating high aspect ratio nanostructures with diameters around 150 nm based on capillary lithography which allowed them to generate spatula-like structures (145). To exploit this method further and to measure adhesion performance of such small structures would be fascinating and should yield unprecedented pull-off forces. In order to further understand the high splitting efficiencies and the absolute pull-off forces, it would also be

necessary to model the contact mechanics of mushroom and spatular structures either numerically or analytically. They benefit very likely from a significant reduction of the deleterious stress concentration that is present at the perimeter of conventional flat punch contacts. With this theoretical understanding at hand the fabrication of optimized structures with even better adhesion performance might be possible.

A structure that is presented in this thesis but only as far as the fabrication is concerned and without any adhesion measurements performed, are the hierarchical systems. Performing adhesion tests on these structures, once they are successfully fabricated in PDMS and not only in SU-8, should help to better understand the role of hierarchy on the adhesion of fibrillar systems, especially when combining this method with gradients in Young's modulus and different pillar packing densities and shapes. By doing so, an experimental investigation of the minimum number of small contacts necessary for efficient splitting derived in chapter 6 will be possible. First experiments in this direction have already been performed successfully.

Finally, active systems are very interesting since they allow the switching of the pull-off behavior from a sticky to a non-sticky state. First adhesives based on shape memory polymers (146) or magnetic actuation (66) have already successfully been fabricated but still many approaches for designing and fabricating active systems remain open for future developments. Such efforts will benefit from the knowledge gained about size and shape effects on fibrillar adhesives presented in this thesis.

8 Appendices

8.1 Appendix A: Additional Information to Chapter 3

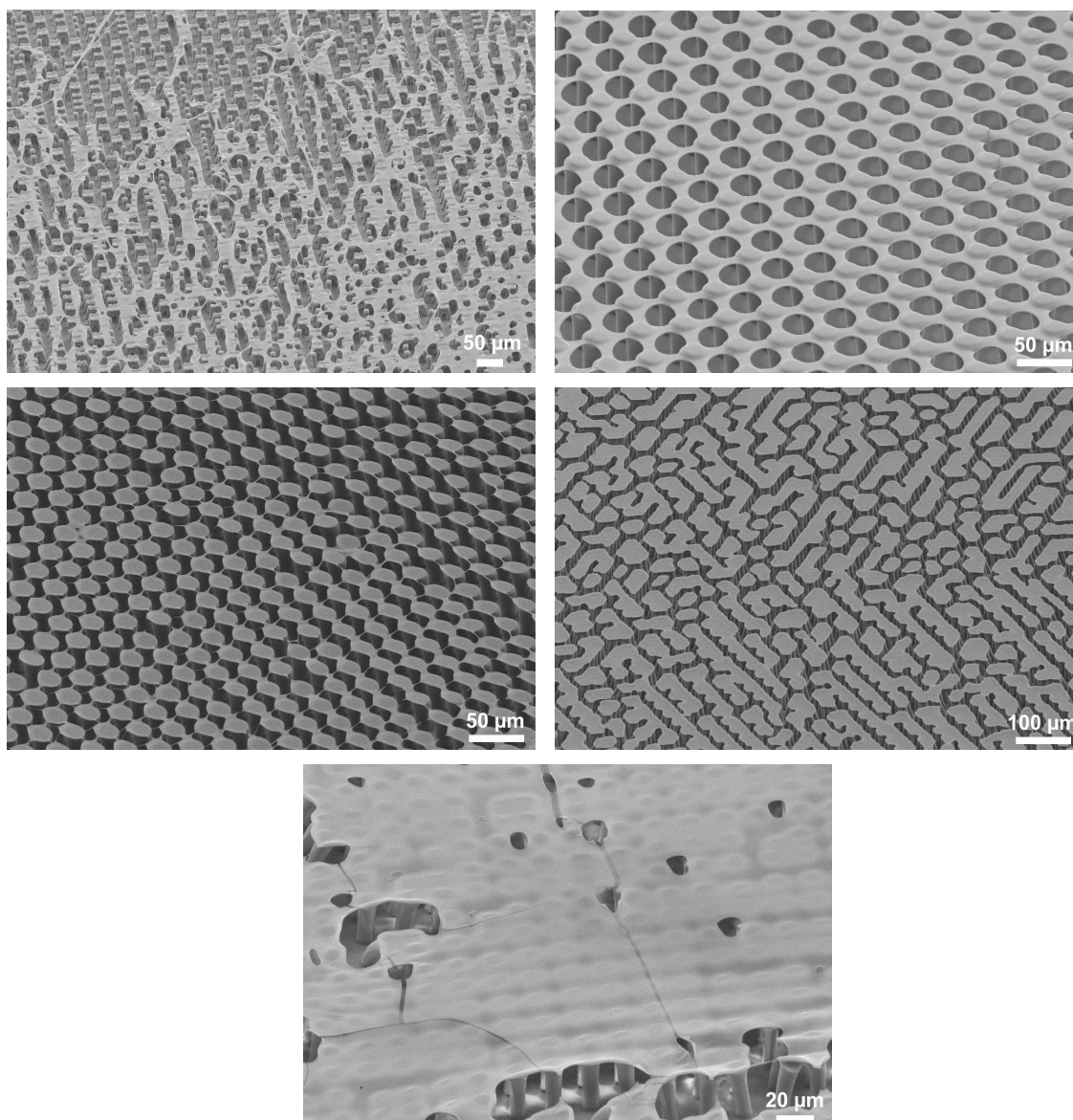


Figure 8.1: SEM micrographs showing examples of failed inking and printing experiments.

8.2 Appendix B: Additional Information to Chapter 4

8.2.1 SEM micrographs of selected pillars structures

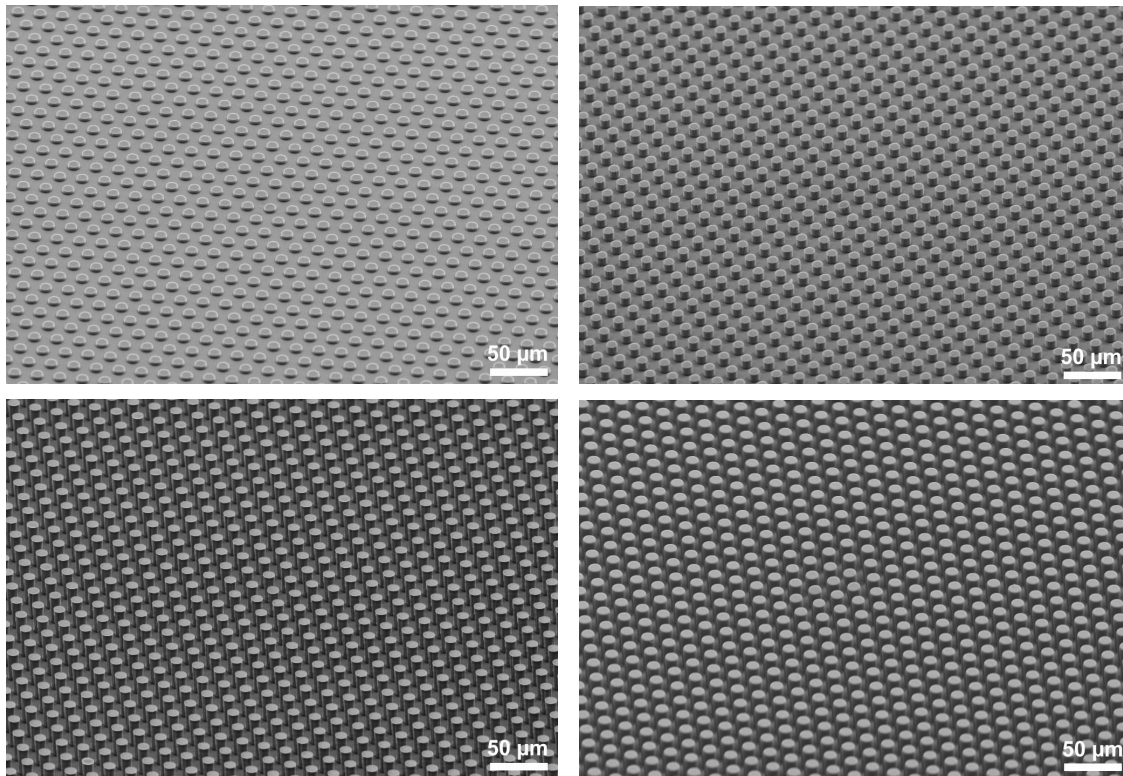


Figure 8.2: SEM micrographs of selected pillar structures with $r = 5 \mu\text{m}$ and $\lambda = 0.5, 1, 2$ and 4 . Specimens were coated with 10 nm Au/Pd before taking pictures.

8.2.2 Load-displacement curves

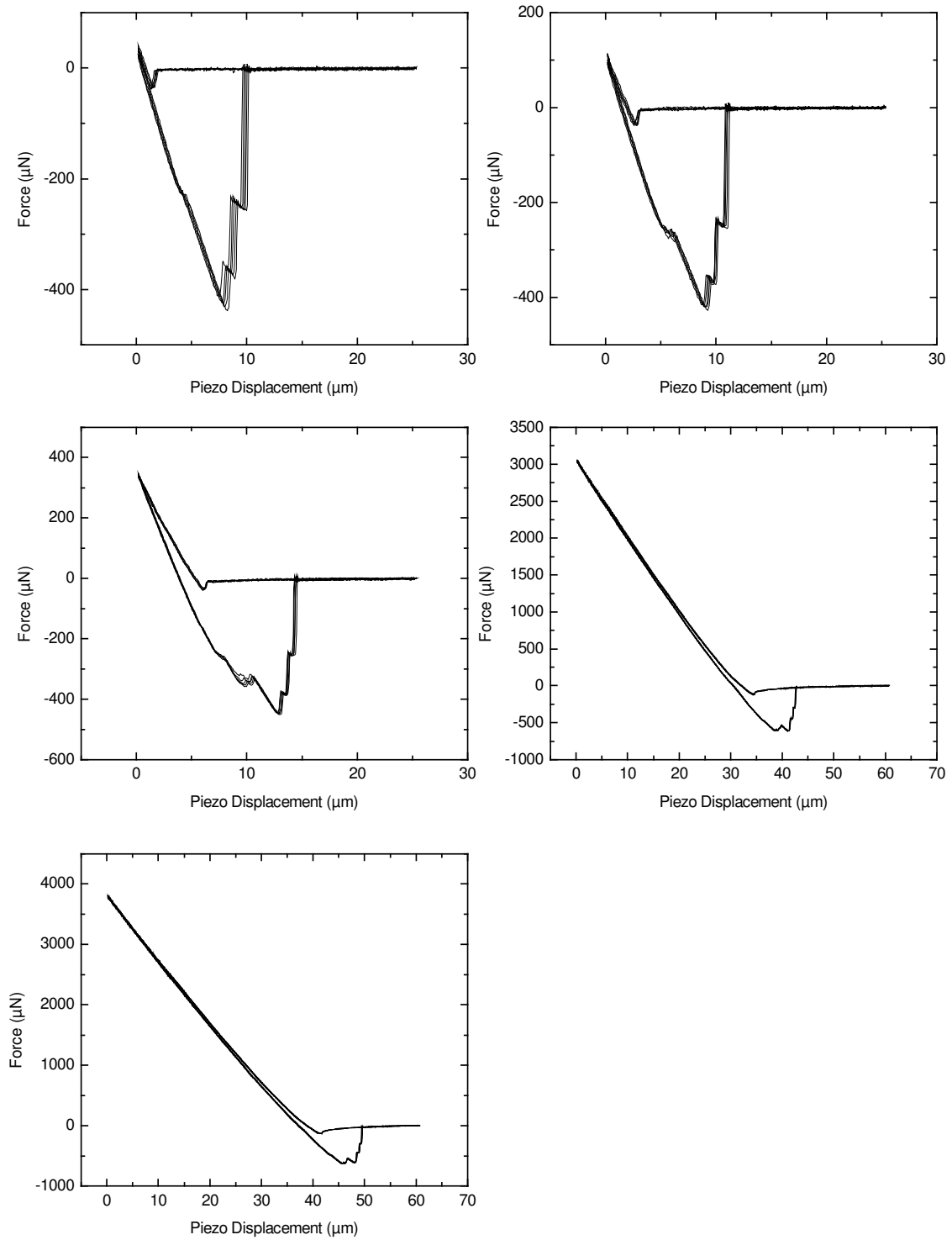


Figure 8.3: Load-displacement curves at different preloads obtained on patterned surfaces ($r = 25 \mu\text{m}$, $\lambda = 1$). Each graph contains data corresponding to five experiments to demonstrate the high reproducibility of the measurements.

8.2.3

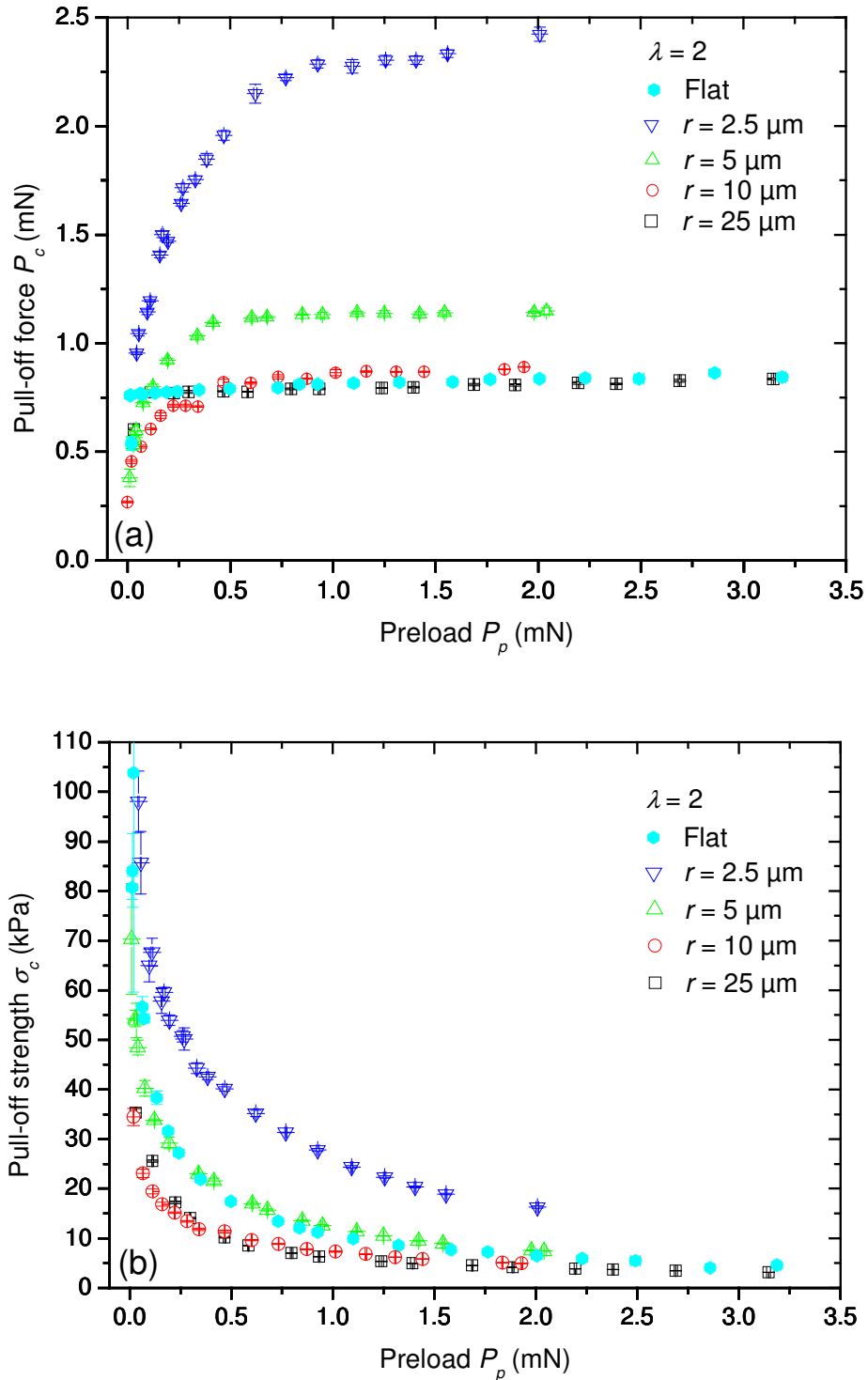
Pull-off force and strength vs. preload for aspect ratio $\lambda = 2$ 

Figure 8.4: Dependence of the pull-off force, P_c , and the pull-off strength, σ_c , on the preload, P_p , in adhesion experiments on flat and patterned surfaces with pillars of different radii and constant aspect ratio ($\lambda = 2$).

8.2.4

Tenacity

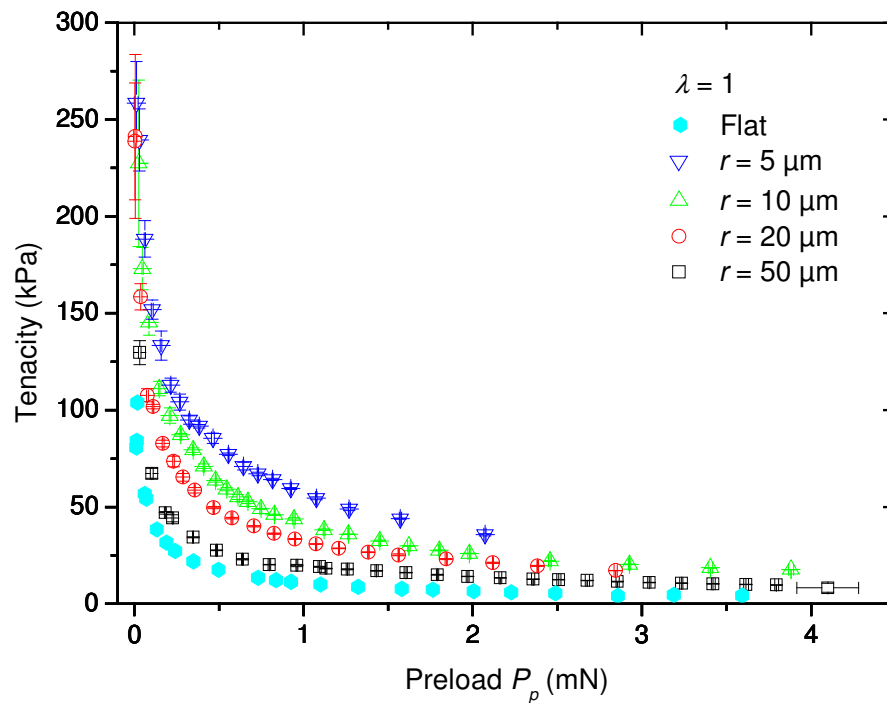


Figure 8.5: Tenacity of pillars arrays of different radius ($\lambda = 1$) compared to flat surface.

8.2.5

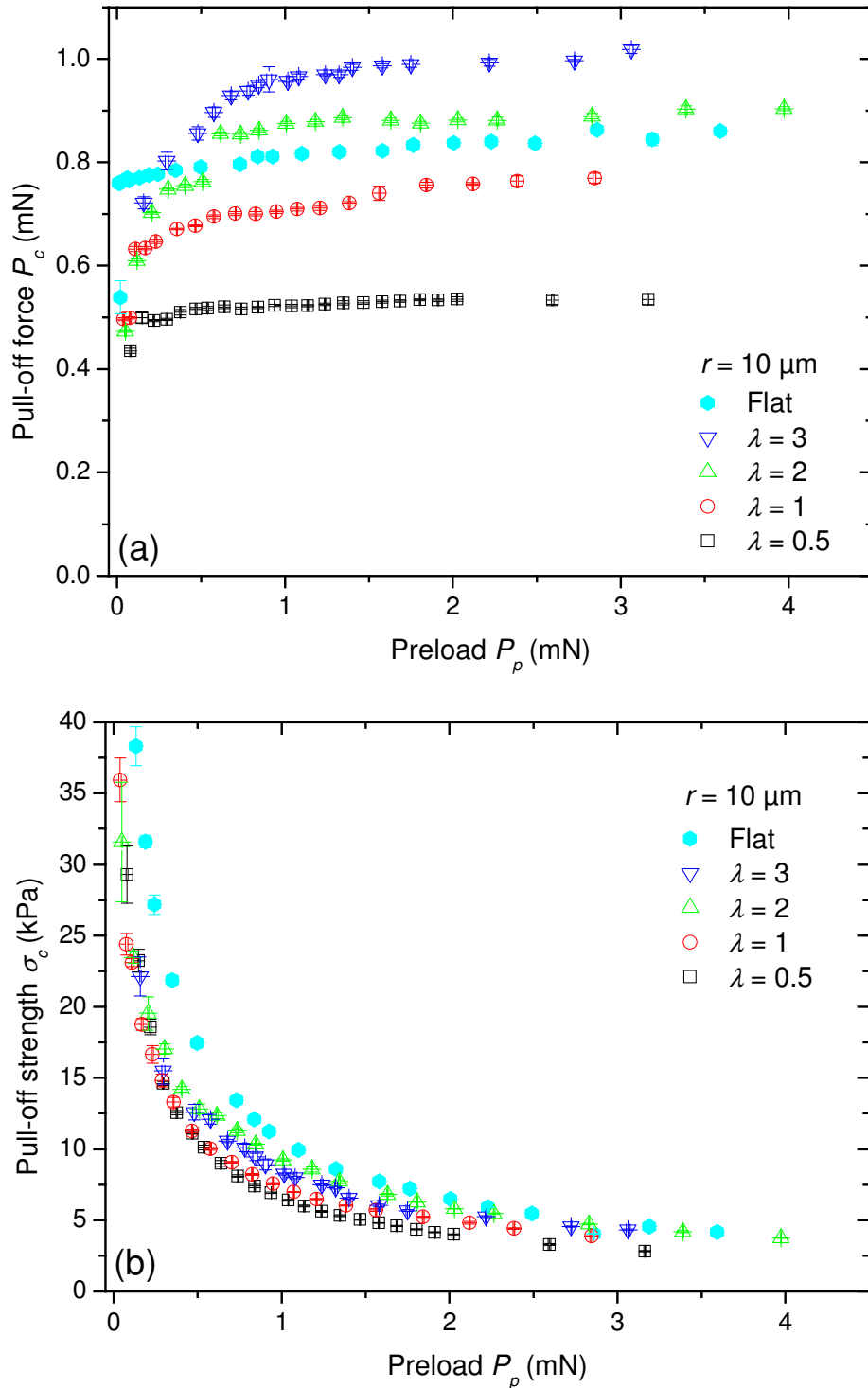
Pull-off force as a function of aspect ratio at radius $r = 10 \mu\text{m}$ 

Figure 8.6: The influence of the aspect ratio on adhesion of patterned surfaces. Data correspond to pillar patterns with radius $10 \mu\text{m}$ and different heights, measured at different preloads.

8.2.6

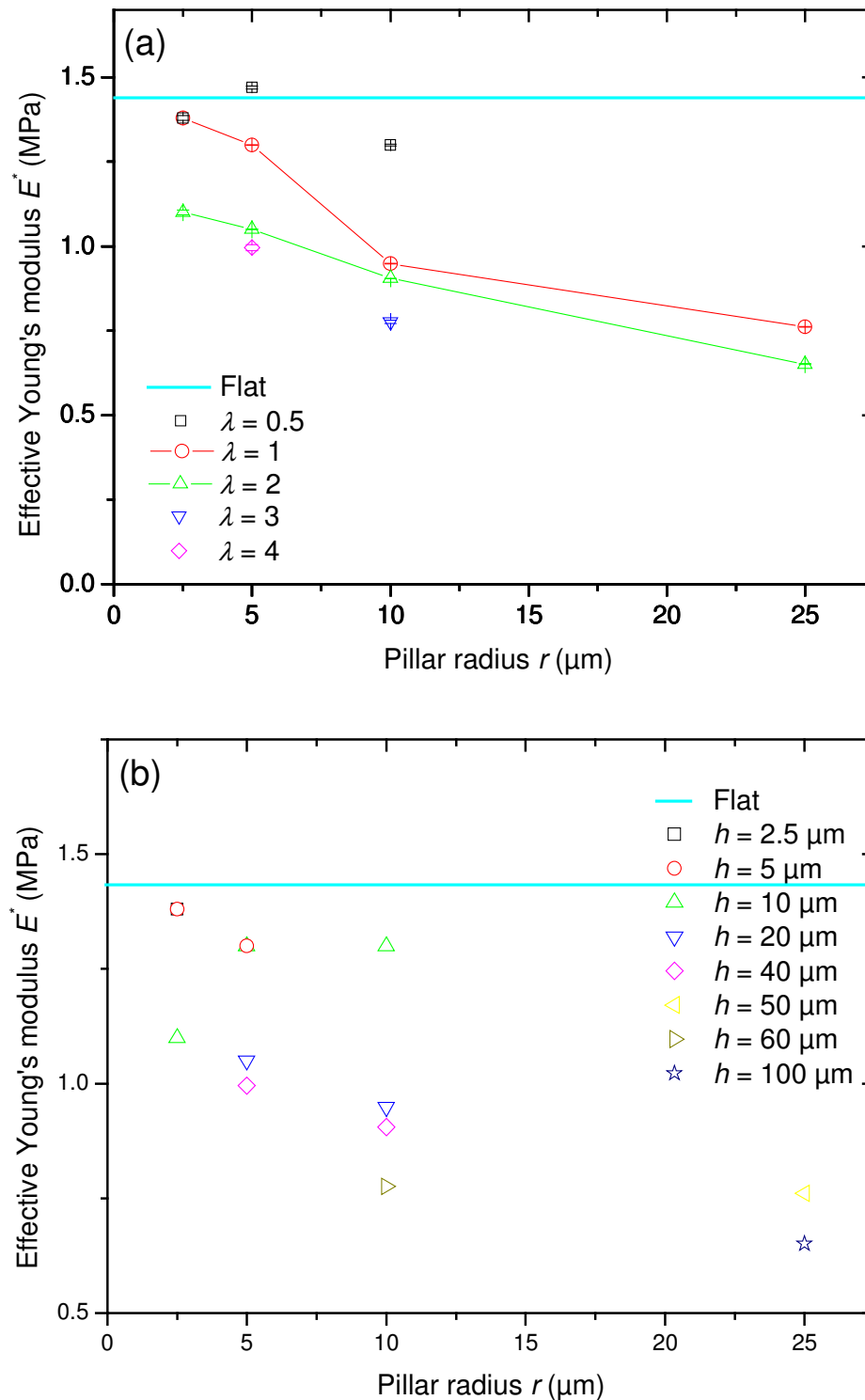
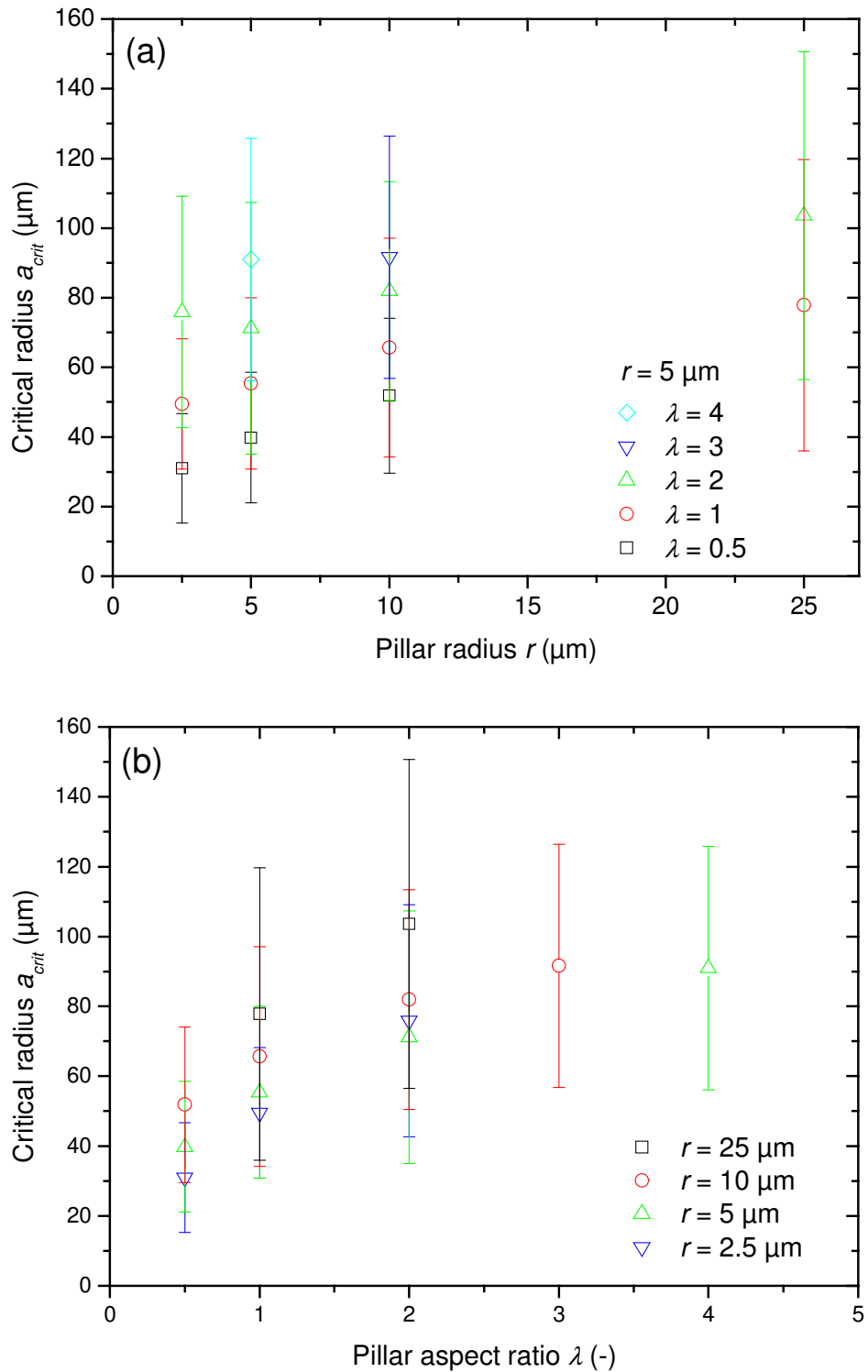
Dependence of E^* on radius, height and aspect ratio

Figure 8.7: Variation of E^* of patterned surfaces with different radii, heights and λ . E^* has been calculated by fitting the loading curves to the Hertz model.

8.2.7

Critical contact radius and number of pillars in contact at a_{crit} 

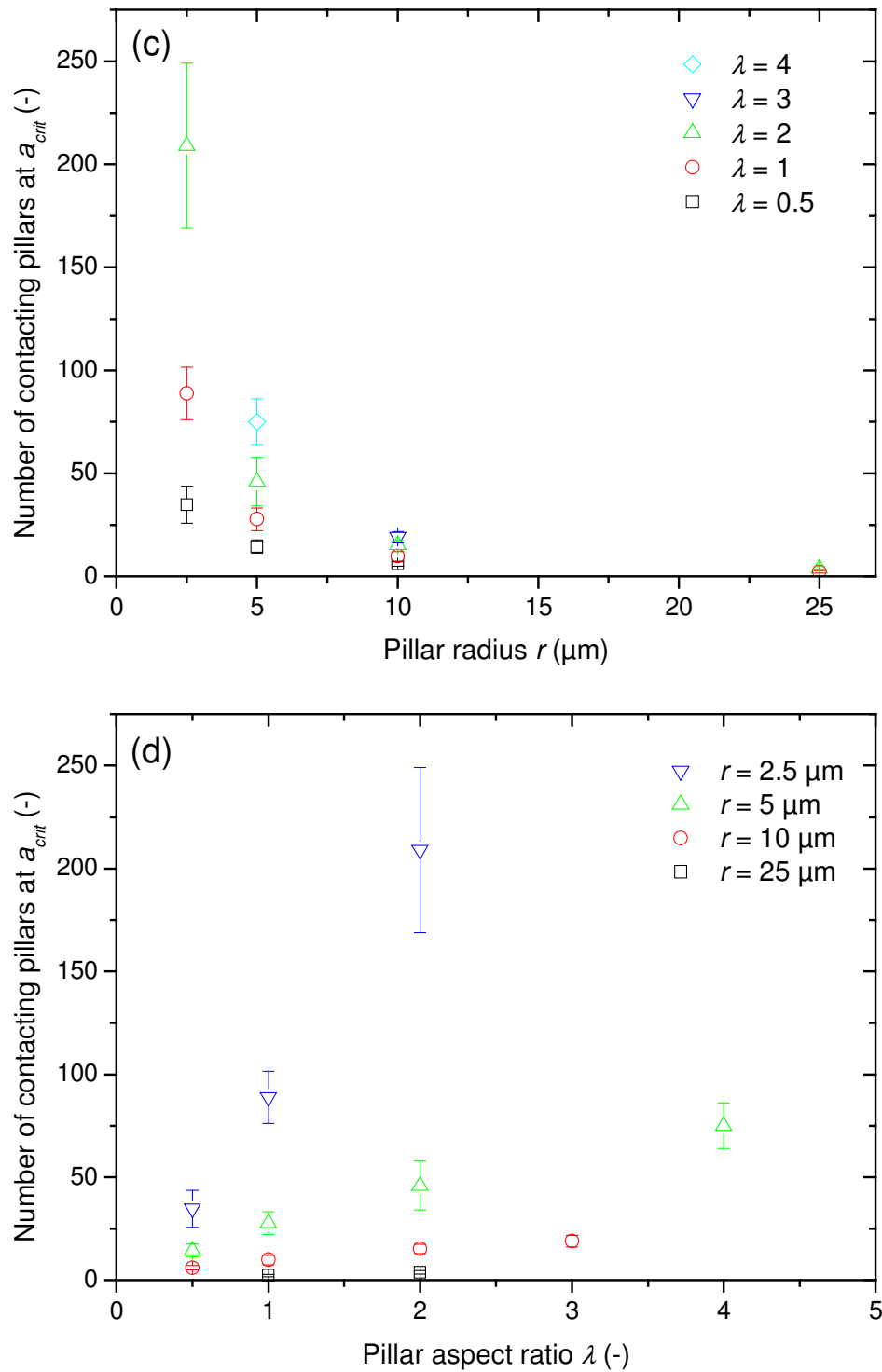


Figure 8.8: Critical contact radius, a_{crit} and number of pillars in contact at a_{crit} for different pillar radii, heights and λ . The values for a_{crit} were determined by fitting the P_c - P_p data with the spring model (116).

8.3 Appendix C: Additional Information to Chapter 5

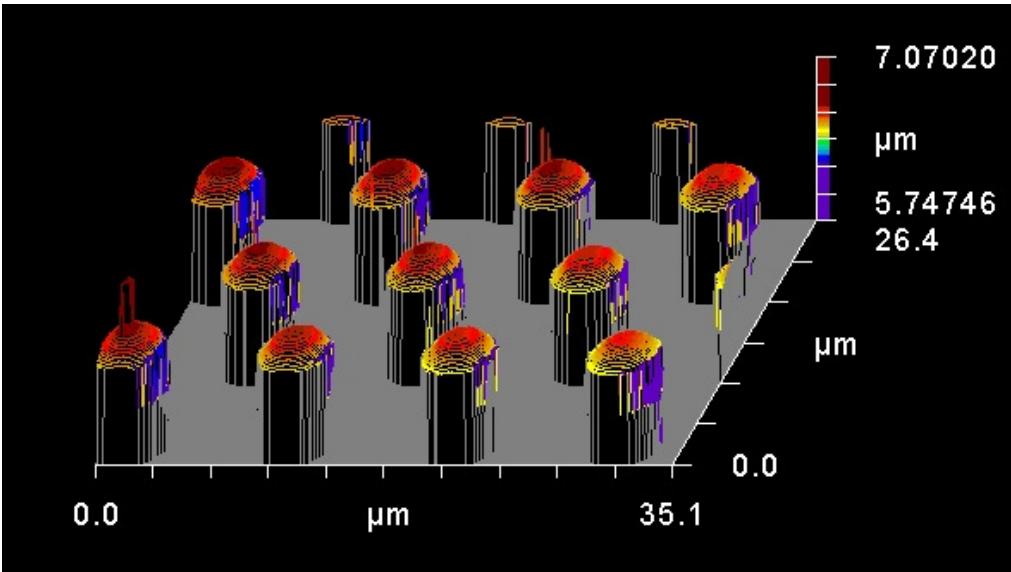


Figure 8.9: White light interferometer profile of a sample with spherical tips confirming the hemispherical tip shape.

8.4 Appendix D: Additional Information to Chapter 6

8.4.1 Design maps for tapes: detailed derivation

8.4.1.1 Contours of constant apparent contact strength

The apparent area fraction is given by:

$$A_{app} = \frac{4R^2}{f} \quad (8.1)$$

From this and with eq. 6.61, we determine the apparent contact strength (15):

$$\sigma_{app} = \frac{P_c}{A_{app}} = \frac{f\gamma}{R\sqrt{1 + \frac{80\gamma}{3ER}}} \quad (8.2)$$

which results in a limit of:

$$\sigma_{app}^2 R^2 + \sigma_{app}^2 \frac{80\gamma}{3E} R - f^2 \gamma^2 = 0 \quad (8.3)$$

$$R_{1/2} = -\frac{40\gamma}{3E} \pm \sqrt{\frac{1600\gamma^2}{9E^2} + \frac{f^2 \gamma^2}{\sigma_{app}^2}} \quad (8.4)$$

Since only positive values for R have a physical meaning we write:

$$R \leq -\frac{40\gamma}{3E} + \sqrt{\frac{1600\gamma^2}{9E^2} + \frac{f^2\gamma^2}{\sigma_{app}^2}} \quad (8.5)$$

8.4.1.2 The limit of fiber fracture

For the fiber fracture limit, we get (15),

$$\sigma_f = \frac{5P_c}{R^2} \leq \sigma_{th}^f \approx \frac{E}{10} \quad (8.6)$$

and derive the following criterion:

$$R^2 + \frac{80\gamma}{3E}R - \frac{40000\gamma^2}{E^2} = 0 \quad (8.7)$$

Since only positive R values have a physical meaning, this yields:

$$R(\text{positive}) \approx \frac{188\gamma}{E} \quad (8.8)$$

$$R \geq \frac{188\gamma}{E} \quad (8.9)$$

8.4.1.3 The limit of ideal contact strength

Following Spolenak *et al.* (15),

$$\sigma_c = \frac{P_c}{4R^2} \leq \sigma_{th} \approx \frac{\gamma}{b} \quad (8.10)$$

results in the following limit (again, only positive R values have physical meaning):

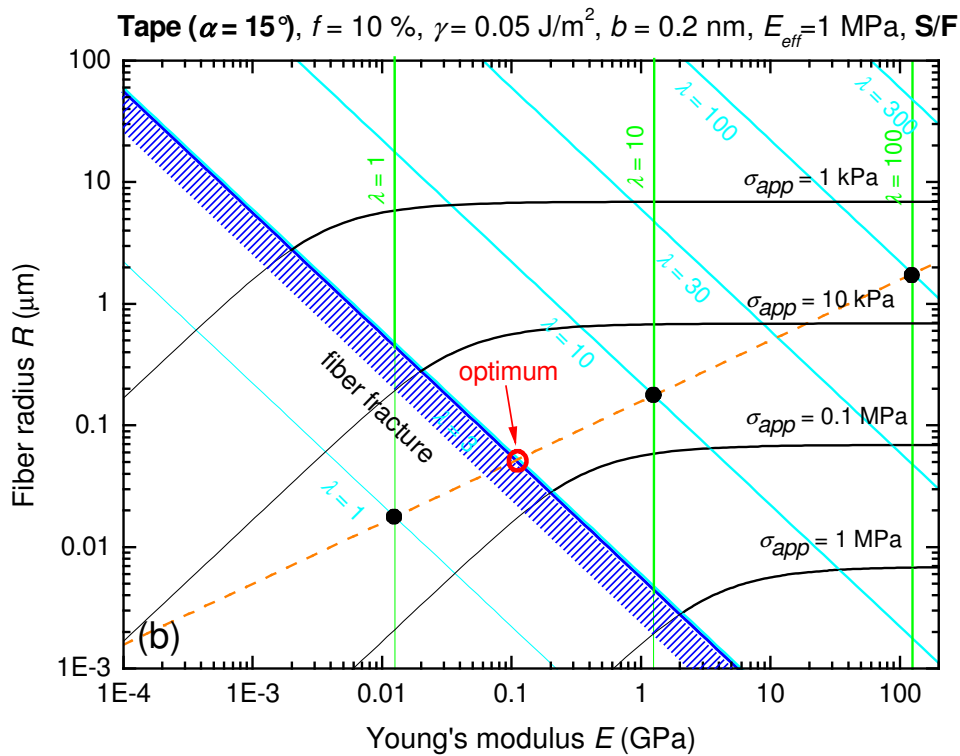
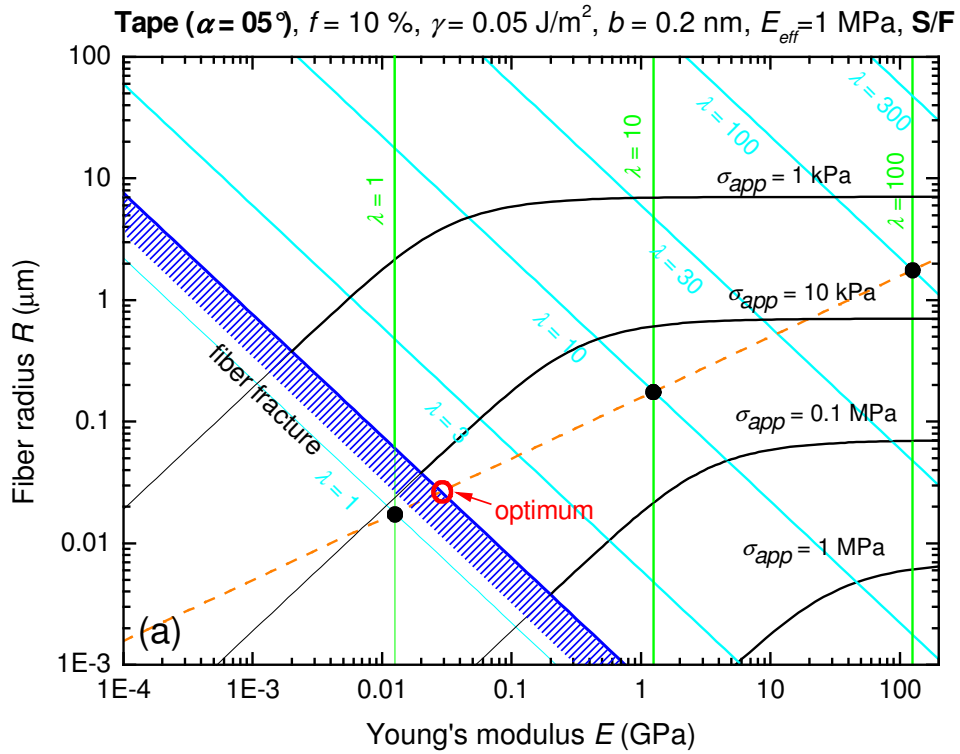
$$R^2 + \frac{80\gamma}{3E}R - b^2 = 0 \quad (8.11)$$

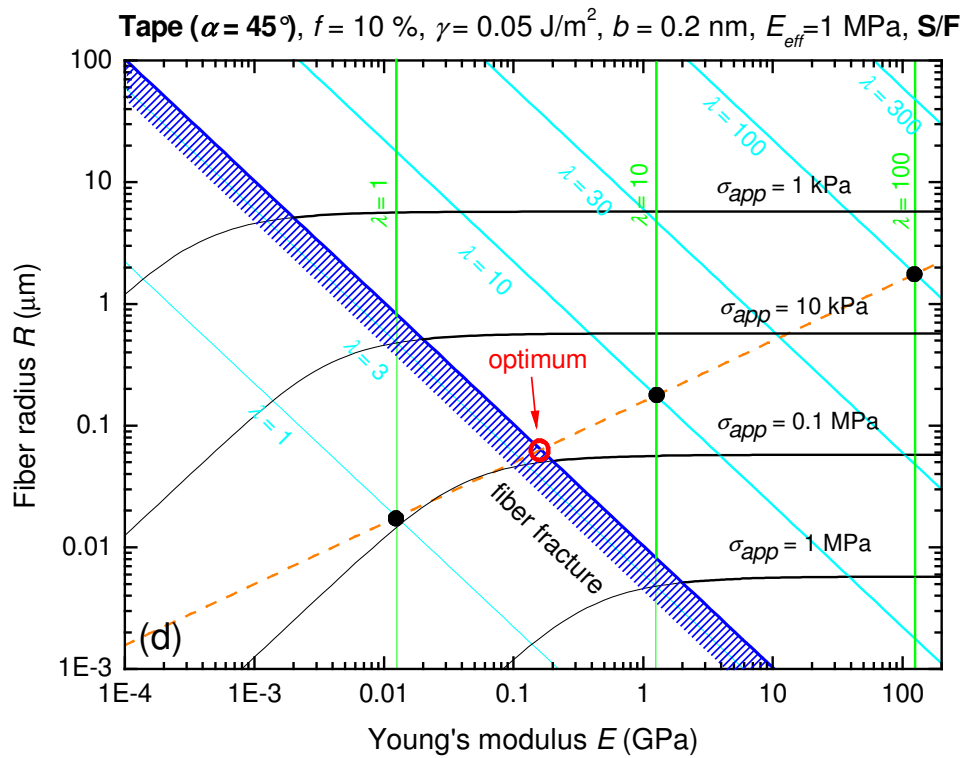
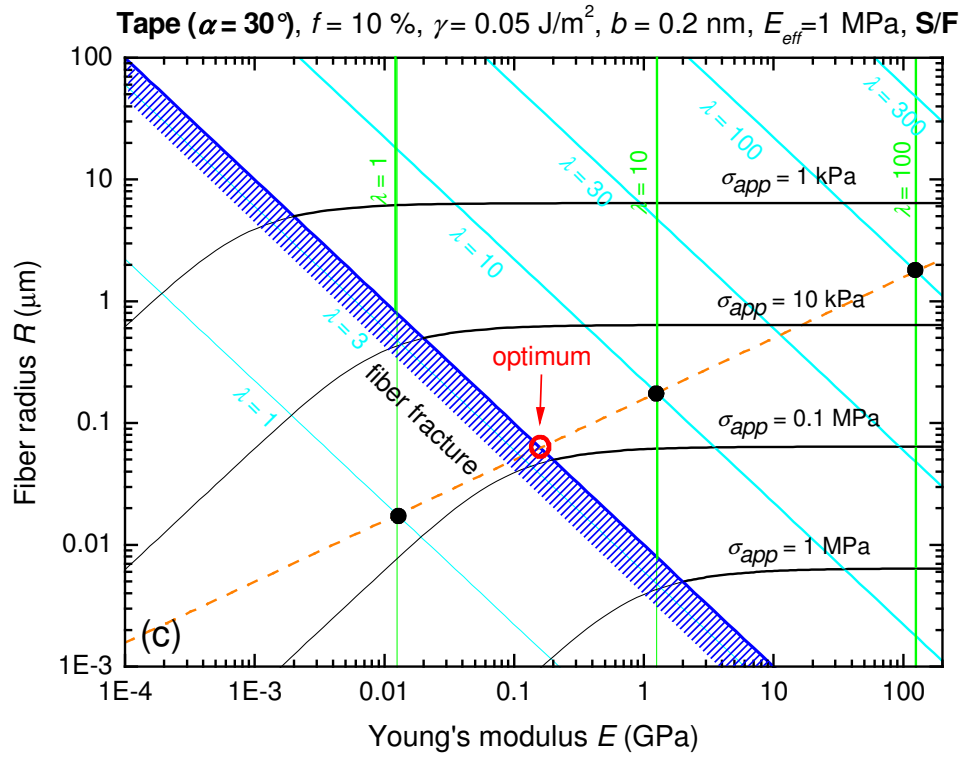
$$R(\text{positive}) = -\frac{40\gamma}{3E} \pm \sqrt{\frac{1600\gamma^2}{9E^2} + b^2} \quad (8.12)$$

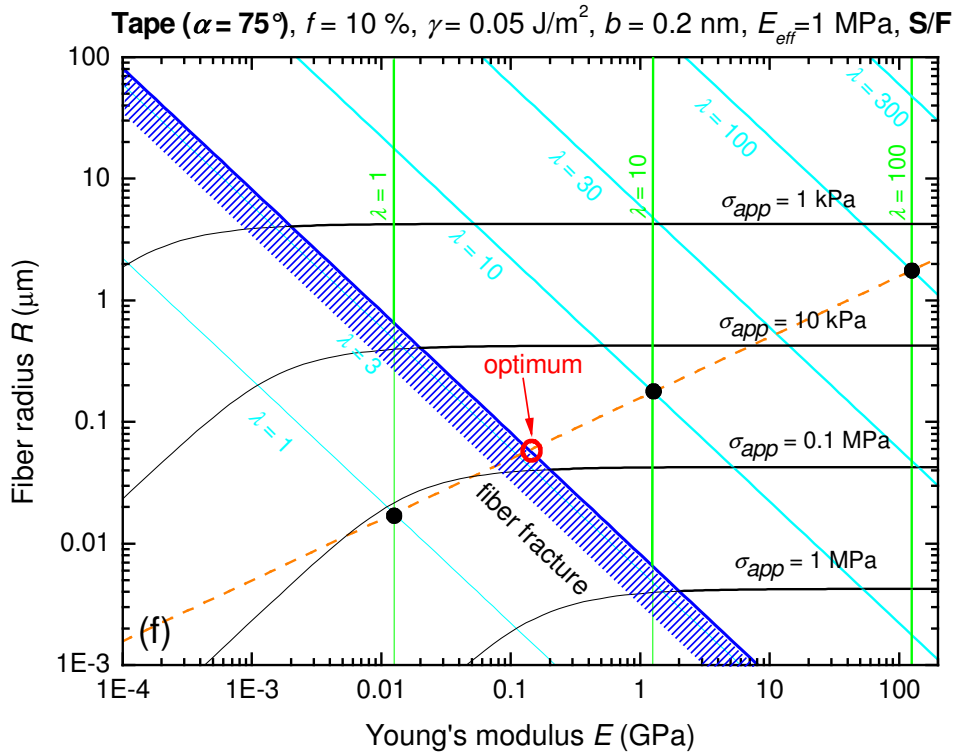
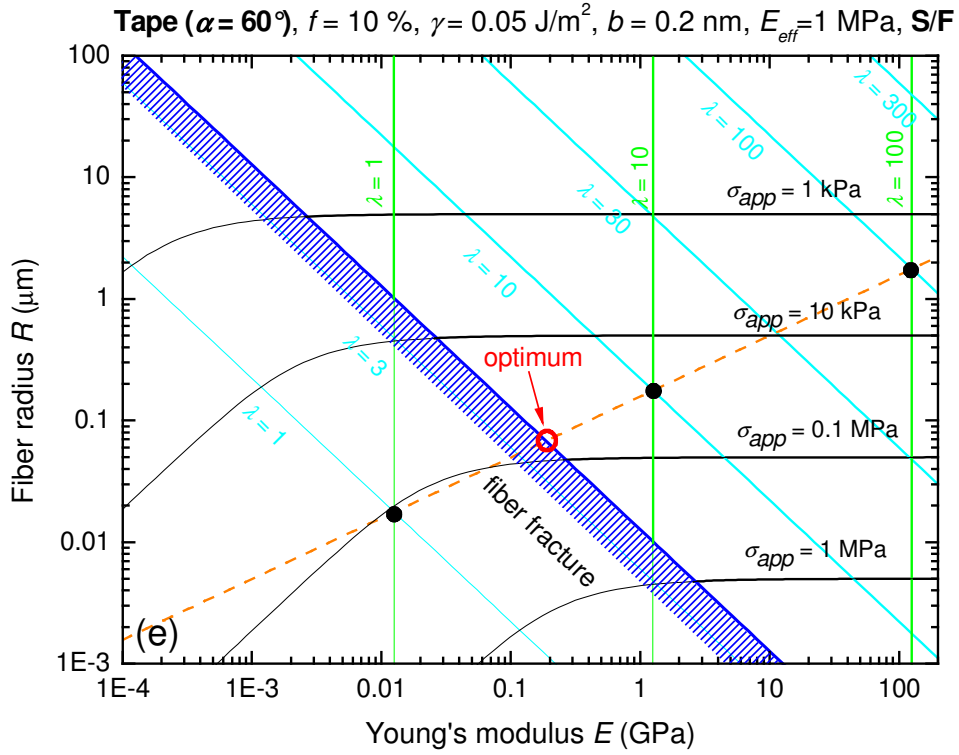
$$R \geq -\frac{40\gamma}{3E} + \sqrt{\frac{1600\gamma^2}{9E^2} + b^2} \quad (8.13)$$

8.4.2

Adhesion design maps for tapes at different peel-off angles







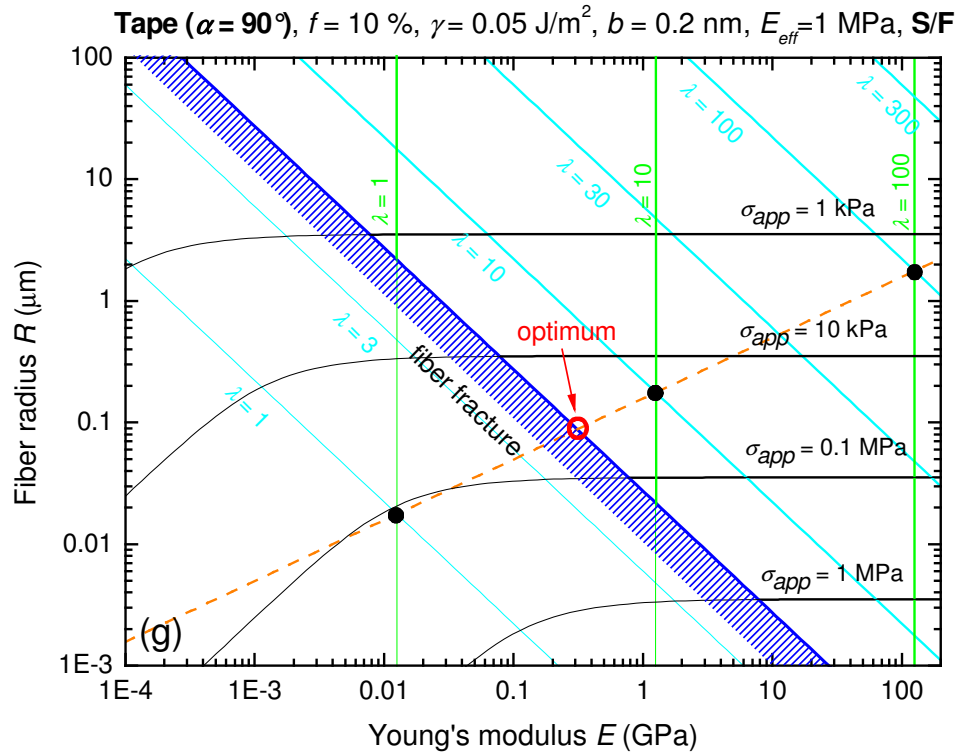


Figure 8.10: Adhesion design maps for elastic tapes at different peel-off angles α , constructed using the condensation limit developed by Sitti and Fearing. The following parameters are assumed: $\gamma = 0.05 \text{ J/m}^2$, $f = 10\%$, $b = 0.2 \text{ nm}$ and $E_{\text{eff}} = 1 \text{ MPa}$. The dashed line is the “conode”. Its intersection with the fiber fraction limit indicates the optimum parameters and is highlighted with a red circle. The following angles α were considered: (a) 5° , (b) 15° , (c) 30° , (d) 45° , (e) 60° , (f) 75° , (g) 90° .

8.4.3

Adhesion design maps for spherical tip shape

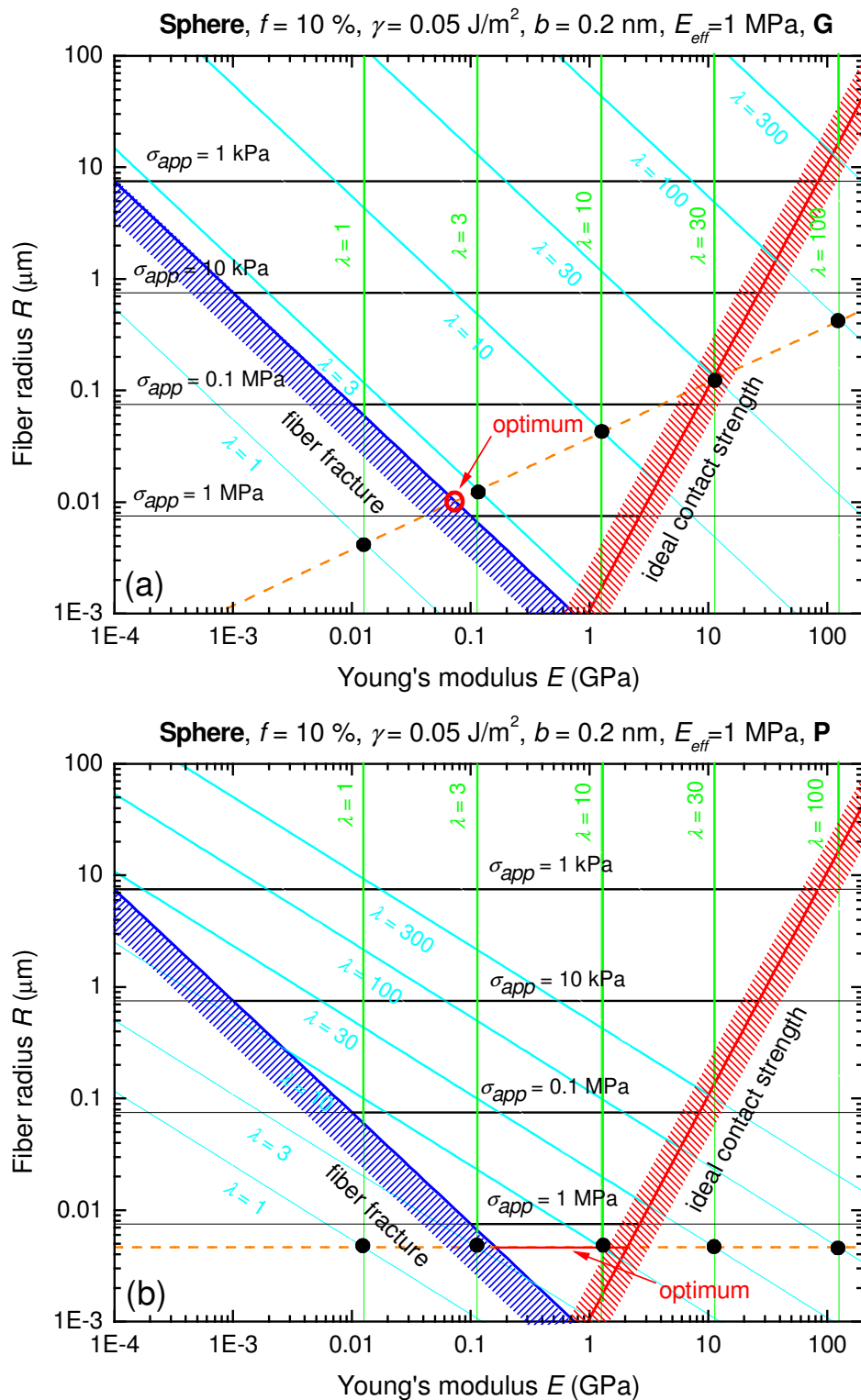


Figure 8.11: Adhesion design maps for hemispherical contact shape and the condensation limits after (a) Glassmaker et al. and (b) Persson.

The conode equation after Glassmaker *et al.*:

$$R = \sqrt{\frac{C^3 f^3 E \mathcal{M}_f^{3/2}}{E_{eff}^3 \pi^5}} \quad (8.14)$$

Equating the conode with the fiber fracture limit yields E_{opt} and σ_{opt} :

$$E_{opt} = \frac{15^{2/3} E_{eff} \pi^{5/3}}{fCh_f^{1/2}} \quad (8.15)$$

$$\sigma_{app}^{opt} = \frac{3E_{eff} \pi^{5/3}}{15^{1/3} C2h_f^{1/2}} \quad (8.16)$$

The conode after Persson:

$$R = \left(\frac{3Cf\gamma}{\pi E_{eff}} \right)^{2/3} \frac{b^{1/3}}{\arccos^{4/3} \left(\frac{f}{\pi} 2\sqrt{3} \right)} \quad (8.17)$$

As the conode has the same slope as the contours of constant apparent contact strength, E_{max} and E_{min} can be calculated. In-between these two parameters, the optimal adhesive can be found.

$$E_{max} = \frac{\sqrt{\frac{3}{8}} \pi (1 - \nu^2)}{\arccos^{2/3} \left(\frac{f}{\pi} 2\sqrt{3} \right)} \left(\frac{3Cf}{\pi E_{eff}} \right)^{1/3} \left(\frac{\gamma}{b} \right)^{4/3} \quad (8.18)$$

$$E_{\min} = 15 \arccos^{4/3} \left(\frac{f}{\pi} 2\sqrt{3} \right) \left(\frac{\gamma}{b} \right)^{1/3} \left(\frac{\pi E_{\text{eff}}}{3Cf} \right)^{2/3} \quad (8.19)$$

The optimum apparent contact strength is:

$$\sigma_{\text{app}}^{\text{max/min}} = \frac{\arccos^{4/3} \left(\frac{f}{\pi} 2\sqrt{3} \right)}{2} \left(\frac{3f\gamma}{b} \right)^{1/3} \left(\frac{\pi E_{\text{eff}}}{C} \right)^{2/3} \quad (8.20)$$

8.4.4 Optimum design parameters for all three condensation limits

Table 8.1: Summary of the optimum design parameters found by intersecting the conode with the appropriate limit. Besides the optimum Young's modulus E_{opt} , the optimal fiber radius, R_{opt} , aspect ratio, λ_{opt} , and the ultimate apparent contact strength, $\sigma_{\text{app}}^{\text{opt}}$ are presented. All three models for fiber condensation are considered: In (a) Sitti and Fearing, in (b) Glassmaker et al. and in (c) Persson.

(a) Condensation limit after Sitti and Fearing

Tip shape	E_{opt}	R_{opt}
Sphere	$E_{\text{opt}} = \frac{15^{2/3} \pi E_{\text{eff}}}{Cf h_f^{1/3}}$	$R_{\text{opt}} = \frac{C 15^{1/3} \gamma h_f^{1/3}}{\pi E_{\text{eff}}}$
Flat punch	$E_{\text{opt}} = h_f \frac{C^3 f^3 \gamma^4}{64 E_{\text{eff}}^3 b^4 \pi}$	$R_{\text{opt}} = \frac{h_f C^3 f^3 \gamma^3}{8 b^2 \pi^2 E_{\text{eff}}^3}$
Torus (self similar)	$E_{\text{max}} = \frac{2^{22/3} C f \gamma^2 h_f^{1/3}}{\pi^{7/3} b^2 E_{\text{eff}}}$	$R_{\text{max}} = \frac{2048^{1/3} C^2 f^2 \gamma^2 h_f^{2/3}}{\pi^{8/3} b E_{\text{eff}}^2}$
	$E_{\min} = \frac{10 E_{\text{eff}} \pi^{4/3}}{Cf} \frac{1}{\sqrt[3]{h_f}}$	$R_{\min} = \frac{1000^{1/2} \gamma C f h_f^{1/3}}{10 \pi^{5/6} E_{\text{eff}}}$
Elastic tape ($\alpha = 60^\circ$)	$E_{\text{opt}} = \frac{188^{2/3} E_{\text{eff}} \pi}{\sqrt[3]{h_f} Cf}$	$R_{\text{opt}} = \frac{188^{1/3} \gamma h_f^{1/3} Cf}{\pi E_{\text{eff}}}$

Tip shape	λ_{opt}	σ_{app}^{opt}
Sphere	$\lambda_{opt} = \frac{15^{1/3}}{2h_f^{1/6}}$	$\sigma_{app}^{opt} = \frac{3\pi E_{eff}}{2C15^{1/3} h_f^{1/3}}$
Flat punch	$\lambda_{opt} = \frac{h_f^{1/2} C^2 f^2 \gamma^2}{15E_{eff}^2 b^2 \pi}$	$\sigma_{app}^{opt} = \frac{\gamma f}{b}$
Torus (self similar)	$\lambda_{max} = \frac{2048^{1/3} h_f^{1/6} C f \gamma}{2E_{eff} b \pi^{5/3}}$ $\lambda_{min} = \left(\frac{5}{2}\right)^{1/2} \left(\frac{\pi}{h_f}\right)^{1/6}$	$\sigma_{app}^{max/min} = \frac{E_{eff} \pi^{4/3}}{h_f^{1/3} C}$
Elastic tape ($\alpha = 60^\circ$)	$\lambda_{opt} = \frac{188^{1/3}}{2h_f^{1/6}}$	$\sigma_{app}^{opt} \approx \frac{0.16\pi E_{eff}}{h_f^{1/3} C}$

(b) Condensation limit after Glassmaker *et al.*

Tip shape	E_{opt}	R_{opt}
Sphere	$E_{opt} = \frac{15^{2/3} E_{eff} \pi^{5/3}}{f C h_f^{1/2}}$	$R_{opt} = \frac{15^{1/3} \gamma C h_f^{1/2}}{E_{eff} \pi^{5/3}}$
Flat punch	$E_{opt} = \frac{188^{2/3} E_{eff} \pi^{5/3}}{C f h_f^{1/2}}$	$R_{opt} = \frac{C^6 f^6 \gamma^3 h_f^{3/2}}{8E_{eff}^3 b^2 \pi^4}$
Torus (self similar)	$E_{max} = \frac{C f \gamma^2 h_f^{1/2} 2^{22/3}}{E_{eff} \pi^3 b^2}$ $E_{min} = \frac{10\pi^2 E_{eff}}{C f h_f^{1/2}}$	$R_{max} = \frac{C^2 f^2 \gamma^2 2048^{1/3} h_f}{E_{eff}^2 \pi^4 b}$ $R_{min} = \frac{10^{1/2} C f h_f^{1/2}}{E_{eff} \pi^{3/2}}$
Elastic tape ($\alpha = 60^\circ$)	$E_{opt} \approx \frac{20E_{eff} \pi^{5/3}}{C f h_f^{1/2}}$	$R_{opt} = \frac{188^{1/3} \gamma C h_f^{1/2}}{E_{eff} \pi^{5/3}}$

Tip shape	λ_{opt}	σ_{app}^{opt}
Sphere	$\lambda_{opt} = \frac{15^{1/6} \pi^{2/6}}{2h_f^{1/8}}$	$\sigma_{app}^{opt} = \frac{3E_{eff} \pi^{5/3}}{15^{1/3} C 2h_f^{1/2}}$
Flat punch	$\lambda_{opt} = \frac{C^{7/2} f^{7/2} \gamma^2 h_f^{3/4}}{16E_{eff}^2 b^2 \pi^2}$	$\sigma_{app}^{opt} = \frac{3E_{eff} \pi^{5/3}}{15^{1/3} C^2 h_f^{1/2}}$
Torus (self similar)	$\lambda_{max} = \frac{Cf\gamma 2048^{1/3} h_f^{1/4}}{E_{eff} 2\pi^2 b}$ $\lambda_{min} = \frac{5^{1/2} \pi^{1/2}}{2^{1/2} h_f^{1/4}}$	$\sigma_{app}^{max/min} = \frac{E_{eff} \pi^2}{Ch_f^{1/2}}$
Elastic tape ($\alpha = 60^\circ$)	$\lambda_{opt} = \frac{1}{2h_f^{1/4}} 188^{1/3} \pi^{1/3}$	$\sigma_{app}^{opt} \approx \frac{1.10E_{eff}}{Ch_f^{1/2}}$

(c) Condensation limit after Persson

Tip shape	E_{opt}
Sphere	$E_{max} = \frac{\sqrt{\frac{3}{8}} \pi (1-\nu^2)}{\arccos^{2/3} \left(\frac{f}{\pi} 2\sqrt{3} \right)} \left(\frac{3Cf}{\pi E_{eff}} \right)^{1/3} \left(\frac{\gamma}{b} \right)^{4/3}$ $E_{min} = 15 \arccos^{4/3} \left(\frac{f}{\pi} 2\sqrt{3} \right) \left(\frac{\gamma}{b} \right)^{1/3} \left(\frac{\pi E_{eff}}{3Cf} \right)^{2/3}$
Flat punch	$E_{opt} = \frac{1}{8} \left(\frac{3Cf}{E_{eff}} \right)^{2/3} \left(\frac{\gamma}{b} \right)^{5/3} \frac{\pi^{1/3}}{\arccos^{4/3} \left(\frac{f}{\pi} 2\sqrt{3} \right)}$
Torus (self similar)	$E_{opt} = \frac{2^{11/2}}{\arccos^{2/3} \left(\frac{f}{\pi} 2\sqrt{3} \right)} \left(\frac{3Cf}{E_{eff}} \right)^{1/3} \left(\frac{\gamma}{\pi b} \right)^{4/3}$
Elastic tape ($\alpha = 60^\circ$)	$E_{min} = \frac{188 \gamma^{1/3} \arccos^{4/3} \left(\frac{f}{\pi} 2\sqrt{3} \right)}{b^{1/3}} \left(\frac{E_{eff} \pi}{3Cf} \right)^{2/3}$

Tip shape	R_{opt}
Sphere	$R_{opt} = \left(\frac{3Cf\gamma}{\pi E_{eff}} \right)^{2/3} \frac{b^{1/3}}{\arccos^{4/3} \left(\frac{f}{\pi} 2\sqrt{3} \right)}$
Flat punch	$R_{opt} = \left(\frac{3Cf\gamma}{\pi E_{eff}} \right)^{2/3} \frac{b^{1/3}}{\arccos^{4/3} \left(\frac{f}{\pi} 2\sqrt{3} \right)}$
Torus (self similar)	$R_{opt} = \left(\frac{3Cf\gamma}{\pi E_{eff}} \right)^{2/3} \frac{b^{1/3}}{\arccos^{4/3} \left(\frac{f}{\pi} 2\sqrt{3} \right)}$
Elastic tape ($\alpha = 60^\circ$)	$R_{min} = \left(\frac{3Cf\gamma}{\pi E_{eff}} \right)^{2/3} \frac{b^{1/3}}{\arccos^{4/3} \left(\frac{f}{\pi} 2\sqrt{3} \right)}$
Tip shape	λ_{opt}
Sphere	$\lambda_{max} = \frac{3^{1/6} \left(\frac{3}{8} \pi^2 (1 - \nu^2) \right)^{1/4}}{2 \arccos^{1/3} \left(\frac{f}{\pi} 2\sqrt{3} \right)} \left(\frac{\gamma C f}{\pi b E_{eff}} \right)^{2/3}$
Sphere	$\lambda_{min} = \frac{15^{1/2}}{2} \left(\frac{\arccos^2 \left(\frac{f}{\pi} 2\sqrt{3} \right)}{3} \right)^{1/3} \left(\frac{\gamma C f}{\pi b E_{eff}} \right)^{1/6}$
Flat punch	$\lambda_{opt} = \frac{3^{1/3}}{\pi^{1/3} 32^{1/2} \arccos^{2/3} \left(\frac{f}{\pi} 2\sqrt{3} \right)} \left(\frac{\gamma C f}{b E_{eff}} \right)^{5/6}$
Torus (self similar)	$\lambda_{opt} = \frac{2^{7/4}}{\arccos^{1/3} \left(\frac{f}{\pi} 2\sqrt{3} \right)} \left(\frac{3}{\pi^7} \right)^{1/6} \left(\frac{C f \gamma}{b E_{eff}} \right)^{2/3}$
Elastic tape ($\alpha = 60^\circ$)	$\lambda_{min} = \frac{188^{1/2} \arccos^{2/3} \left(\frac{f}{\pi} 2\sqrt{3} \right)}{2 \cdot 3^{1/3}} \left(\frac{C f \gamma}{\pi b E_{eff}} \right)^{1/6}$

Tip shape	σ_{app}^{opt}
Sphere	$\sigma_{app}^{max/min} = \frac{\arccos^{4/3}\left(\frac{f}{\pi} 2\sqrt{3}\right)}{2} \left(\frac{3f\gamma}{b}\right)^{1/3} \left(\frac{\pi E_{eff}}{C}\right)^{2/3}$
Flat punch	$\sigma_{app}^{opt} = \frac{f\gamma}{b}$
Torus (self similar)	$\sigma_{app}^{opt} = 2^{11/6} \left(\frac{\pi E_{eff}}{3C}\right)^{1/3} \left(\frac{f\gamma \arccos\left(\frac{f}{\pi} 2\sqrt{3}\right)}{b}\right)^{2/3}$
Elastic tape ($\alpha = 60^\circ$)	$\sigma_{app}^{min} = \left(\frac{141}{161}\right)^{1/2} \left(\frac{f\gamma}{b}\right)^{1/3} \left(\frac{\pi E_{eff}}{3C}\right)^{2/3} \arccos^{4/3}\left(\frac{f}{\pi} 2\sqrt{3}\right)$

9 References

1. Aristotle (350 B.C.) *Historia Animalium*, translated by Thomson, D.A.W. (1918), Clarendon, Oxford.
2. Hiller, U. & Blaschke, R. (1967) *Naturwissenschaften* **54**, 344-345.
3. Hiller, U. (1968) *Z. Morphol. Tiere* **62**, 307-362.
4. Stork, N. E. (1983) *J. Nat. Hist.* **17**, 829-835.
5. Haase, A. (1900) *Archiv für Naturgeschichte* **66**, 321-345.
6. Huber, G., Mantz, H., Spolenak, R., Mecke, K., Jacobs, K., Gorb, S. N. & Arzt, E. (2005) *Proc. Natl. Acad. Sci. U. S. A.* **102**, 16293-16296.
7. Autumn, K. & Peattie, A. M. (2002) *Integr. Comp. Biol.* **42**, 1081-1090.
8. Autumn, K., Liang, Y. A., Hsieh, S. T., Zesch, W., Chan, W. P., Kenny, T. W., Fearing, R. & Full, R. J. (2000) *Nature* **405**, 681-685.
9. Autumn, K., Sitti, M., Liang, Y. C. A., Peattie, A. M., Hansen, W. R., Sponberg, S., Kenny, T. W., Fearing, R., Israelachvili, J. N. & Full, R. J. (2002) *Proc. Natl. Acad. Sci. U. S. A.* **99**, 12252-12256.
10. Arzt, E., Gorb, S. & Spolenak, R. (2003) *Proc. Natl. Acad. Sci. U. S. A.* **100**, 10603-10606.
11. Arzt, E., Enders, S. & Gorb, S. (2002) *Z. Metallk.* **93**, 345-351.
12. Spolenak, R., Gorb, S., Gao, H. J. & Arzt, E. (2005) *Proc. R. Soc. London, Ser. A* **461**, 305-319.
13. Del Campo, A. & Arzt, E. (2007) *Macromol. Biosci.* **7**, 118-127.
14. Chan, E. P., Greiner, C., Arzt, E. & Crosby, A. J. (2007) *MRS Bull.* **32**, 496-503.
15. Spolenak, R., Gorb, S. & Arzt, E. (2005) *Acta Biomater.* **1**, 5-13.
16. Hertz, H. (1882) *J. reine angew. Math.* **92**, 156-171.
17. Maugis, D. (2000) *Contact, Adhesion and Rupture of Elastic Solids* (Springer, Heidelberg), pp. 203-343.
18. Johnson, K. L., Kendall, K. & Roberts, A. D. (1971) *Proc. R. Soc. London, Ser. A* **324**, 301-313.
19. Derjaguin, B. V., Muller, V. M. & Toporov, Y. P. (1975) *J. Colloid Interface Sci.* **53**, 314-326.
20. Tabor, D. (1977) *J. Colloid Interface Sci.* **58**, 2-13.
21. Muller, V. M., Yushchenko, V. S. & Derjaguin, B. V. (1980) *J. Colloid Interface Sci.* **77**, 91-101.

22. Scherge, M. & Gorb, S. N. (2001) *Biological Micro and Nanotribology: Nature's Solutions* (Springer Verlag, Berlin), pp. 141-145.
23. Glassmaker, N. J., Jagota, A. & Hui, C. Y. (2005) *Acta Biomater.* **1**, 367-375.
24. Chung, J. Y. & Chaudhury, M. K. (2005) *J. R. Soc. Interface* **2**, 55-61.
25. Ghatak, A., Mahadevan, L., Chung, J. Y., Chaudhury, M. K. & Shenoy, V. (2004) *Proc. R. Soc. London, Ser. A* **460**, 2725-2735.
26. Sitti, M. & Fearing, R. S. (2003) *J. Adhes. Sci. Technol.* **17**, 1055-1073.
27. Majidi, C., Groff, R. & Fearing, R. (2004) in *2004 ASME International Mechanical Engineering Congress & Exposition* (Anaheim, CA, U.S.A.), pp. 1-6.
28. Sitti, M. & Fearing, R. S. (2003) in *IEEE International Conference on Robotics and Automation* (Taiwan), pp. 1164-1170.
29. Sitti, M. (2003) in *ASME Congress* (Washington D.C., U.S.A.), pp. 42787-42792.
30. Menon, C., Murphy, M. & Sitti, M. (2004) in *IEEE International Conference on Robotics and Biomimetics (ROBIO)* (Shenyang, China), pp. 431-436.
31. Campolo, D., Jones, S. & Fearing, R. S. (2003) in *IEEE-NANO 2003*. (San Francisco, CA, U.S.A.), pp. 856-859.
32. Shah, G. J. & Sitti, M. (2004) in *IEEE International Conference on Robotics and Biomimetics (ROBIO)* (Shenyang, China), pp. 873-878.
33. Majidi, C., Groff, R. E., Maeno, Y., Schubert, B., Baek, S., Bush, B., Maboudian, R., Gravish, N., Wilkinson, M., Autumn, K. & Fearing, R. S. (2006) *Phys. Rev. Lett.* **97**.
34. Jin, M. H., Feng, X. J., Feng, L., Sun, T. L., Zhai, J., Li, T. J. & Jiang, L. (2005) *Adv. Mater.* **17**, 1977-1981.
35. Kim, D. S., Lee, H. S., Lee, J., Kim, S., Lee, K. H., Moon, W. & Kwon, T. H. (2007) *Microsyst. Technol.* **13**, 601-606.
36. Peressadko, A. & Gorb, S. N. (2004) *J. Adhes.* **80**, 247-261.
37. Peressadko, A. (2004), personal communication.
38. Sitti, M. & Fearing, R. S. (2002) in *2nd IEEE Conference on Nanotechnology* (Washington D.C., U.S.A.), pp. 137-140.
39. Gorb, S. N., Varenberg, M., Peressadko, A. & Tuma, J. (2006) *J. Roy. Soc. Interface* **4**, 271-275.
40. Varenberg, M. & Gorb, S. (2007) *J. Roy. Soc. Interface*, accepted for publication, 10.1098/rsif.2007.0222.
41. Bhushan, B. & Sayer, R. A. (2007) *Microsyst. Technol.* **13**, 71-78.
42. Varenberg, M., Peressadko, A., Gorb, S. & Arzt, E. (2006) *Appl. Phys. Lett.* **89**, 121905.
43. Varenberg, M., Peressadko, A., Gorb, S., Arzt, E. & Mroczek, S. (2006) *Rev. Sci. Instrum.* **77**.
44. Glassmaker, N. J., Jagota, A., Hui, C. Y. & Kim, J. (2004) *J. Roy. Soc. Interface* **1**, 23-33.
45. Crosby, A. J., Hageman, M. & Duncan, A. (2005) *Langmuir* **21**, 11738-11743.

46. Thomas, T. & Crosby, A. J. (2006) *J. Adhes.* **82**, 311-329.
47. Cheung, E., Karagozler, M. E., Park, S., Kim, B. & Sitti, M. (2005) in *IEEE/ASME International Conference on Advanced Intelligent Mechatronics* (Monterey, CA, U.S.A.), pp. 551-557.
48. Aksak, B., Murphy, M. P. & Sitti, M. (2007) *Langmuir* **23**, 3322-3332.
49. Han, M., Lee, W., Lee, S. K. & Lee, S. S. (2004) *Sens. Actuator A-Phys.* **111**, 14-20.
50. Roca-Cusachs, P., Rico, F., Martinez, E., Toset, J., Farre, R. & Navajas, D. (2005) *Langmuir* **21**, 5542-5548.
51. Kustandi, T. S., Samper, V. D., Yi, D.-K., Ng, W.-S., Neuzil, P. & Sun, W. (2007) *Adv. Funct. Mater.*, in press.
52. Kim, S. & Sitti, M. (2006) *Appl. Phys. Lett.* **89**, 261911.
53. Choi, S. J., Yoo, P. J., Baek, S. J., Kim, T. W. & Lee, H. H. (2004) *J. Am. Chem. Soc.* **126**, 7744-7745.
54. Yoon, E. S., Singh, R. A., Kong, H., Kim, B., Kim, D. H., Jeong, H. E. & Suh, K. Y. (2006) *Tribol. Lett.* **21**, 31-37.
55. Geim, A. K., Dubonos, S. V., Grigorieva, I. V., Novoselov, K. S., Zhukov, A. A. & Shapoval, S. Y. (2003) *Nat. Mater.* **2**, 461-463.
56. Hui, C. Y., Glassmaker, N. J., Tang, T. & Jagota, A. (2004) *J. Roy. Soc. Interface* **1**, 35-48.
57. Yurdumakan, B., Raravikar, N. R., Ajayan, P. M. & Dhinojwala, A. (2005) *Chem. Commun.*, 3799-3801.
58. Zhao, Y., Tong, T., Delzeit, L., Kashani, A., Meyyappan, M. & Majumdar, A. (2006) *J. Vac. Sci. Technol. B* **24**, 331-335.
59. Northen, M. T. & Turner, K. L. (2005) *Nanotechnology* **16**, 1159-1166.
60. Northen, M. T. & Turner, K. L. (2006) *Sens. Actuator A-Phys.* **130**, 583-587.
61. Northen, M. T. & Turner, K. L. (2006) *Curr. Appl. Phys.* **6**, 379-383.
62. Lin, Z., Kerle, T., Baker, S. M., Hoagland, D. A., Schaffer, E., Steiner, U. & Russell, T. P. (2001) *J. Chem. Phys.* **114**, 2377-2381.
63. Schaffer, E., Thurn-Albrecht, T., Russell, T. P. & Steiner, U. (2000) *Nature* **403**, 874-877.
64. Northen, M. T. (2005), personal communication.
65. Northen, M. T., Greiner, C., Arzt, E. & Turner, K. L. (2007) *submitted to Nat. Mater.*
66. Northen, M. T., Greiner, C., Arzt, E. & Turner, K. L. (2006) in *Solid-State Sensors, Actuators, and Microsystems Workshop* (Hilton Head Island, SC, U.S.A.), pp. 43-46.
67. Manciola, J. D. (2007), *Nano- and micro-structured polymer surfaces*, PhD-Thesis, Fakultät für Chemie und Geowissenschaften, Universität Heidelberg.
68. La Spina, G., Stefanini, C., Menciassi, A. & Dario, P. (2005) *J. Micromech. Microeng.* **15**, 1576-1587.

69. Nain, A. S., Amon, C. & Sitti, M. (2006) *IEEE Transactions on Nanotechnology* **5**, 499-510.
70. Jeong, H. E., Lee, S. H., Kim, P. & Suh, K. Y. (2006) *Nano Lett.* **6**, 1508-1513.
71. Harfenist, S. A., Cambron, S. D., Nelson, E. W., Berry, S. M., Isham, A. W., Crain, M. M., Walsh, K. M., Keynton, R. S. & Cohn, R. W. (2004) *Nano Lett.* **4**, 1931-1937.
72. Williams, J. D. & Wang, W. (2004) *Microsyst. Technol.* **10**, 694-698.
73. Kudryashov, V., Yuan, X. C., Cheong, W. C. & Radhakrishnan, K. (2003) *Microelectron. Eng.* **67-8**, 306-311.
74. Teh, W. H., Durig, U., Drechsler, U., Smith, C. G. & Guntherodt, H. J. (2005) *J. Appl. Phys.* **97**.
75. Xia, Y. N. & Whitesides, G. M. (1998) *Angew. Chem.-Int. Edit.* **37**, 551-575.
76. Whitesides, G. M., Ostuni, E., Takayama, S., Jiang, X. Y. & Ingber, D. E. (2001) *Annu. Rev. Biomed. Eng.* **3**, 335-373.
77. Carrillo, F., Gupta, S., Balooch, M., Marshall, S. J., Marshall, G. W., Pruitt, L. & Puttlitz, C. M. (2006) *J. Mater. Res.* **21**, 535-537.
78. Information about Dow Corning brand Silicone Encapsulants (2006), <http://www.dowcorning.com/applications/search/default.aspx?R=131EN>.
79. Krogh, M. & Asberg, P. (2003) *My Little Guide to Soft Lithography*, pp. 8-9.
80. Lee, J. N., Jiang, X., Ryan, D. & Whitesides, G. M. (2004) *Langmuir* **20**, 11684-11691.
81. Carrillo, F., Gupta, S., Balooch, M., Marshall, S. J., Marshall, G. W., Pruitt, L. & Puttlitz, C. M. (2005) *J. Mater. Res.* **20**, 2820-2830.
82. Del Campo, A. & Arzt, E. (2007) *Chem. Rev.*, in press.
83. Pfaff, H. (2005), *Synthesis and adhesion of biomimetic contact elements*, PhD-Thesis, Fakultät Chemie, Universität Stuttgart.
84. Del Campo, A., Álvarez, I., Filipe, S. & Wilhelm, M. (2007) *Adv. Funct. Mater.*, in press.
85. Zhao, Y. & Zhang, X. (2006) *Sens. Actuator A-Phys.* **127**, 216-220.
86. Lee, T. W., Jeon, S., Maria, J., Zaumseil, J., Hsu, J. W. P. & Rogers, J. A. (2005) *Adv. Funct. Mater.* **15**, 1435-1439.
87. Delamarche, E., Schmid, H., Michel, B. & Biebuyck, H. (1997) *Adv. Mater.* **9**, 741-746.
88. Hui, C. Y., Jagota, A., Lin, Y. Y. & Kramer, E. J. (2002) *Langmuir* **18**, 1394-1407.
89. Sharp, K. G., Blackman, G. S., Glassmaker, N. J., Jagota, A. & Hui, C. Y. (2004) *Langmuir* **20**, 6430-6438.
90. Odom, T. W., Love, J. C., Wolfe, D. B., Paul, K. E. & Whitesides, G. M. (2002) *Langmuir* **18**, 5314-5320.
91. Schmid, H. & Michel, B. (2000) *Macromolecules* **33**, 3042-3049.
92. Bietsch, A. & Michel, B. (2000) *J. Appl. Phys.* **88**, 4310-3418.

-
93. Choi, K. M. & Rogers, J. A. (2003) *J. Am. Chem. Soc.* **125**, 4060-4061.
 94. Rogers, J. A., Paul, K. E. & Whitesides, G. M. (1998) *J. Vac. Sci. Technol. B* **16**, 88-97.
 95. Choi, D. G., Jeong, J. H., Sim, Y. S., Lee, E. S., Kim, W. S. & Bae, B. S. (2005) *Langmuir* **21**, 9390-9392.
 96. Csucs, G., Kunzler, T., Feldman, K., Robin, F. & Spencer, N. D. (2003) *Langmuir* **19**, 6104-6109.
 97. Suh, K. Y. & Langer, R. (2003) *J. Appl. Phys.* **83**, 4250-4252.
 98. Khang, D. Y., Kang, H., Kim, T. I. & Lee, H. H. (2004) *Nano Lett.* **4**, 633-637.
 99. Khang, D. Y. & Lee, H. H. (2004) *Langmuir* **20**, 2445-2448.
 100. Rolland, J. P., Hagberg, E. C., Denison, G. M., Carter, K. R. & De Simone, J. M. (2004) *Angew. Chem.-Int. Edit.* **43**, 5796-5799.
 101. Eo, Y. J., Lee, T. H., Kim, S. Y., Kang, J. K., Han, Y. S. & Bae, B. S. (2005) *J. Polym. Sci. Pt. B-Polym. Phys.* **43**, 827-836.
 102. Eo, Y. J., Kim, J. H., Ko, J. H. & Bae, B. S. (2005) *J. Mater. Res.* **20**, 401-408.
 103. Kim, S. Y., Augustine, S., Eo, Y. J., Bae, B. S., Woo, S. I. & Kang, J. K. (2005) *J. Phys. Chem. B* **109**, 9397-9403.
 104. Kim, W. S., Kim, K. S., Eo, Y. J., Yoon, Y. & Bae, B. S. (2005) *J. Mater. Chem.* **15**, 465-469.
 105. Jeong, J. H., Sim, Y. S., Sohn, H. & Lee, E. S. (2004) *Microelectron. Eng.* **75**, 165-171.
 106. Yoo, P. J., Choi, S. J., Kim, J. H., Suh, D., Baek, S. J., Kim, T. W. & Lee, H. H. (2004) *Chem. Mat.* **16**, 5000-5005.
 107. Ge, H. X., Wu, W., Li, Z. Y., Jung, G. Y., Olynick, D., Chen, Y. F., Liddle, J. A., Wang, S. Y. & Williams, R. S. (2005) *Nano Lett.* **5**, 179-182.
 108. Ma, L., McMeeking, R. & Arzt, E. (2006), submitted for publication.
 109. Huber, G., Gorb, S. N., Spolenak, R. & Arzt, E. (2005) *Biol. Lett.* **1**, 2-4.
 110. Full, R. J., Fearing, R. S., Kenny, T. W. & Autumn, K. (2001), Adhesive microstructure and its fabrication based on the adhesive mechanism of the Gecko, Patent, Wo, 2001049776.
 111. Peressadko, A., Hosoda, N. & Persson, B. N. J. (2005) *Phys. Rev. Lett.* **95**, 124301.
 112. Chaudhury, M. K. & Whitesides, G. M. (1991) *Langmuir* **7**, 1013-1025.
 113. Burton, Z. & Bhushan, B. (2005) *Nano Lett.* **5**, 1607-1613.
 114. De Souza, E. J., Mohrdieck, C., Brinkmann, M. & Arzt, E. (2006) *submitted for publication*.
 115. Farshchi-Tabrizi, M., Kappl, M., Cheng, Y. J., Gutmann, J. & Butt, H. J. (2006) *Langmuir* **22**, 2171-2184.
 116. Schargott, M., Popov, V. L. & Gorb, S. (2006) *J. Theor. Biol.* **243**, 48-53.
 117. Kendall, K. (1971) *J. Phys. D-Appl. Phys.* **4**, 1186-1195.
 118. Jagota, A. & Bennison, S. J. (2002) *Integr. Comp. Biol.* **42**, 1140-1145.

-
119. Tang, T., Hui, C. Y. & Glassmaker, N. J. (2005) *J. Roy. Soc. Interface* **2**, 505-516.
 120. Lake, G. J. & Thomas, A. G. (1967) *Proc. R. Soc. London, Ser. A* **300**, 108-119.
 121. Niederegger, S., Gorb, S. & Jiao, Y. K. (2002) *J. Comp. Physiol. A* **187**, 961-970.
 122. Gorb, S. N. (1998) *Proc. R. Soc. London, Ser. B* **265**, 747-752.
 123. Autumm, K., Majidi, C., Groff, R. E., Dittmore, A. & Fearing, R. (2006) *J. Exp. Biol.* **209**, 3558-3569.
 124. Jiao, Y. K., Gorb, S. & Scherge, M. (2000) *J. Exp. Biol.* **203**, 1887-1895.
 125. Gorb, S. N. (2001) *Attachment devices of insect cuticle* (Kluwer Academic Publishers, Dordrecht), pp. 135-176.
 126. Hansen, W. R. & Autumn, K. (2005) *Proc. Natl. Acad. Sci. U. S. A.* **102**, 385-389.
 127. Hui, C. Y., Glassmaker, N. J. & Jagota, A. (2005) *J. Adhes.* **81**, 699-721.
 128. Persson, B. N. J. & Gorb, S. (2003) *J. Chem. Phys.* **119**, 11437-11444.
 129. Persson, B. N. J. (2003) *J. Chem. Phys.* **118**, 7614-7621.
 130. Gao, H. J. & Yao, H. M. (2004) *Proc. Natl. Acad. Sci. U. S. A.* **101**, 7851-7856.
 131. Greiner, C., Del Campo, A. & Arzt, E. (2007) *Langmuir* **23**, 3495-3502.
 132. Bhushan, B. (2002) *Introduction to Tribology* (John Wiley & Sons, Inc., New York), pp. 18-21.
 133. Kendall, K. (1975) *J. Phys. D-Appl. Phys.* **8**, 1449-1452.
 134. Del Campo, A., Greiner, C., Álvarez, I. & Arzt, E. (2007) *Adv. Mater.*, in press.
 135. Del Campo, A., Greiner, C. & Arzt, E. (2007) *Langmuir*, in press.
 136. Kim, T. W. & Bhushan, B. (2007) *J. Adhes. Sci. Technol.* **21**, 1-20.
 137. Fuller, K. N. G. & Tabor, D. (1975) *Proc. R. Soc. London, Ser. A* **345**, 327-342.
 138. Johnson, K. L. (1975) in *The mechanics of the contact between deformable bodies*, eds. De Pater, A. D. & Kalker, J. J. (Delft University Press, Delft), pp. 33-39.
 139. Persson, B. N. J. & Tosatti, E. (2001) *J. Chem. Phys.* **115**, 5597-5610.
 140. Persson, B. N. J. (2002) *Phys. Rev. Lett.* **89**, 245502.
 141. Gao, H. J., Wang, X., Yao, H. M., Gorb, S. & Arzt, E. (2005) *Mech. Mater.* **37**, 275-285.
 142. Orso, S., Wegst, U. G. K., Eberl, C. & Arzt, E. (2006) *Adv. Mater.* **18**, 874-877.
 143. Courtney, T. H. (1990) *Mechanical Behavior of Materials* (McGraw-Hill Publishing Company, New York), pp. 383-385.
 144. Williams, E. E. & Peterson, J. A. (1982) *Science* **215**, 1509-1511.
 145. Suh, K. Y., Choi, S. J., Baek, S. J., Kim, T. W. & Langer, R. (2005) *Adv. Mater.* **17**, 560-564.
 146. Reddy, S., Del Campo, A. & Arzt, E. (2007) *Adv. Mater.*, in press.
 147. Del Campo, A. & Greiner, C. (2007) *J. Micromech. Microeng.* **17**, R81-R95.

10 Deutsche Kurzfassung der Dissertation

10.1 Motivation und Literaturüberblick

Seit Jahrtausenden fasziniert es den Menschen wie sich Geckos, Spinnen und einige Insekten scheinbar mühelos an der Wand und kopfüber an der Decke hängend fortbewegen. So schrieb schon der griechische Philosoph und Naturforscher Aristoteles in seinem Werk "De Anima" über die erstaunliche Fähigkeit des Geckos kopfüber einen Baum hinunterklettern zu können (1). Allerdings gelang es erst in der zweiten Hälfte des 20. Jahrhunderts die Struktur der Haftorgane des Geckos zu untersuchen (2, 3). Dies hat mit ihrer Aufspaltung in Milliarden feinsten Hafelemente, sog. Spatulae, zu tun, deren Dimensionen im 100 nm Bereich liegen und somit erst mit verbesserter rasterelektronenmikroskopischer Technik aufzulösen waren. Durch Wissenschaftler um den amerikanischen Biologen Kellar Autumn gelang es zu Beginn des neuen Jahrtausends auch die Natur der Wechselwirkungskräfte, auf denen die Adhäsion des Geckos beruht zu klären. Diese sind Van-der-Waals-Kräfte (VdW-Kräfte) und somit universell zwischen allen Oberflächen vorhanden, da sie auf induzierten Dipolen beruhen (7-9). Dies erklärt auch, warum Geckos auf nahezu allen Materialien haften können. Neuere Messungen an einzelnen Gecko-Spatulae weisen jedoch darauf hin, dass auch kapillare Effekte einen nicht zu vernachlässigend Beitrag zur Haftkraft dieser Tiere leisten (6). Vergleicht man die Haftorgane verschiedener Spezies, die die Eigenschaft besitzen in der Senkrechten und kopfüber laufen zu können, so fallen mehrere Dinge auf: Zum einen werden die

Haftstrukturen mit zunehmendem Körpergewicht kleiner, zum anderen finden sich verschiedene Formen in denen der Endkontakt ausgeführt ist. Die erste Beobachtung wurde theoretisch durch das sog. “Prinzip des Kontaktaufspaltens” erklärt. Dieses beruht auf der am meisten angewandten kontaktmechanischen Theorie für VdW-Wechselwirkungen die nach den Wissenschaftlern die sie entwickelt haben – Johnson, Kendall und Roberts (JKR) – benannt ist. Das Prinzip des Kontaktaufspaltens besagt, dass wenn man unter Beibehaltung der projizierten Kontaktfläche einen großen, bspw. hemisphärischen, Kontakt in viele kleine Kontakte aufspaltet, die Haftkraft zunimmt (10, 11). Eben jenes Phänomen verdeutlicht warum schwerere Tiere ihre Hafthaare in feinere Strukturen aufspalten müssen. Es wird auf Grund einer höheren Anzahl an Einzelkontakten mehr Haftkraft gewonnen. Berechnet man die Effizienz des Aufspaltens, so stellt man fest, dass diese eine Funktion der Endkontur des Kontaktes ist und sich z.B. für stempelförmige Elemente deutlich von der für Halbkugeln unterscheidet (12). All jene Überlegungen führten zur Entwicklung von sog. “Adhesion Design Maps” (Design-Karten), die ein strategisches Auslegen von künstlichen, fibrillären Haftstrukturen erleichtern sollten. In ihnen werden in einem doppelt-logarithmischen Radius-E-Modul-Raum, limitierende Bedingungen für diese Systeme aufgetragen und letztlich das Optimum für Radius, E-Modul und Aspektverhältnis der Strukturen ermittelt, bei denen die Haftkräfte maximal sind. Ein Beispiel für eine solche limitierende Randbedingung ist die sog. Kondensation einzelner Säulen, bei der sich auf Grund eines zu hohen Aspektverhältnisses (bei gegebener Steifigkeit) eher ein Kontakt zwischen zwei Säulen, als der beiden einzeln mit der gegenüberliegenden Oberfläche, ausbildet. Dieses Phänomen ist der Haftkraft stark abträglich und gilt es zu vermeiden. Alles bisher Angeführte über die Leistungsfähigkeit des biologischen Vorbildes, die Theorie der Kontaktaufspaltung sowie die Design-Karten, zeigt auf, welch hohes Potential in künstlichen Haftstrukturen steckt. Dies ist Grund und Anreiz genug für zahlreiche Forschungsgruppen weltweit die Entwicklung von

funktionsfähigen fibrillären Haftsystemen voranzutreiben. Dennoch wurde in der Literatur der Einfluss einer Radiusverkleinerung auf die Haftkräfte sowie die Rolle der Endkontur der Säulen bis heute nicht systematisch untersucht. Um sich diesen Fragen experimentell zu nähern und Licht auf die Effekte von Größe und Form der Haftkontakte zu werfen, wurden in der vorliegenden Arbeit fibrilläre Modellsysteme, die sich für kontrollierte und reproduzierbare Messungen eignen hergestellt und auf ihre Hafteigenschaften hin untersucht. Des Weiteren wurde das bereits erwähnte Konzept der “Adhesion Design Maps” auf zusätzliche Endkonturen erweitert. Das experimentelle Vorgehen wird im Folgenden beschrieben sowie die wichtigsten Ergebnisse vorgestellt.

10.2 Experimentelles

Es war das Ziel dieser Arbeit präzise Messungen an Modellsystemen fibrillärer Haftsysteme vorzunehmen. Um sowohl Radius, als auch Aspektverhältnis der Säulen, welche als Modell fibrillärer Haftsysteme verwendet wurden, unabhängig voneinander variieren und kontrollieren zu können, wurden mittels optischer Lithographie Masterstrukturen angefertigt. Ausgehend von Siliziumwafern, welche man mit Piranha-Lösung (fünf Teile Wasserstoffperoxyd auf einen Teil Schwefelsäure) gereinigt hatte, wurden in Reinraumatmosferae mittels Spincoating verschieden dicke Schichten eines Photolacks aufgebracht. Verwendet wurde SU-8, ein epoxidbasierender UV-sensitiver Negativ-Photolack, der sich besonders für sehr dicke Lackschichten eignet (147). Durch die Wahl geeigneter chromfreier Stellen auf der verwendeten lithographischen Maske konnte der Durchmesser der späteren Säulen festgelegt werden, wobei die Lackdicke die Höhe vorgab. Die mit Erfolg hergestellten Strukturdurchmesser lagen zwischen 2 und 50 μm , die Höhen zwischen 2 und 200 μm . In die SU-8-Schicht wurden im Normalfall Löchern strukturiert und diese mit einem siloxanbasierenden Elastomer namens

Polydimethylsiloxan (PDMS) (Dow Corning Sylgard 184) abgeformt. Das Ergebnis dieses Schrittes waren nach dem Aushärten des PDMS (14 h bei 65°C) und einem vorsichtigem Ablösen der Elastomerstruktur vom Wafer, Säulen im Mikrometerbereich die sich auf Grund des niedrigen E-Moduls von PDMS (ca. 2 MPa) sehr gut für Adhäsionsmessungen eignen. Dies war mit SU-8-Säulen, die ebenfalls hergestellt wurden, auf Grund einer Steifigkeit von ca. 5 GPa nicht der Fall. Um das Ablösen des PDMS vom Photolack zu vereinfachen, wurden die Wafer vor dem erstmaligen Abgießen einem Silanisierungsschritt, bei dem sich mittels eines Perfluorosilans (Heptadecafluoro-1,1,2,2-tetrahydrooctyltrichlorosilan) eine teflonartige Oberflächenschicht ausbildete, unterworfen. Durch diese Art des sog. "Soft Molding" konnten aber nur Säulen mit dem Profil eines flachen Stempels hergestellt werden. Um den Einfluss verschiedener Endkonturen der Säulen auf die Adhäsionseigenschaften untersuchen zu können, wurde deshalb ein Verfahren entwickelt, um unter Verwendung der lithographischen Master komplexere Formen darstellen zu können (siehe dazu Kapitel 3 dieser Arbeit). Dazu wurden zuerst Säulen mit der Kontur eines flachen Stempels hergestellt. Diese ergaben sich aus dem oben beschriebenen Abformen der SU-8-Masterstrukturen. In einem zweiten Schritt wurde mittels Spincoating eine Schicht von unvernetztem PDMS mit einer Dicke von ca. 6 µm auf einem Siliziumwafer aufgebracht. Von Hand wurden nun die Spitzen der Elastomersäulen in diese Schicht eingetaucht und wieder herausgezogen. Wurden die Säulen nun mit ihrem Ende nach unten weisend in einem Ofen kuriert, so ergaben sich unter dem Einfluss der Oberflächenspannung des unvernetzten PDMS und der Schwerkraft, Säulen mit halbkugelförmiger Endkontur. Wurden die Säulen nach dem Eintauchen in flüssiges PDMS, auf einen waagrecht liegenden, silanisierten Wafer gegeben, so konnten Säulen pilzförmiger Natur hergestellt werden. Lag der Wafer hingegen leicht gekippt, ergaben sich Säulen mit spatelförmigen Spitzen. Durch einen sog. Doppelabguß ausgehend von SU-8-Säulen, über PDMS welches nach dem Abziehen

silanisiert und erneut mit PDMS abgegossen wurde, gelang es stempelförmige Säulen mit abgerundeten Kanten anzufertigen. Ausgehend von sog. Dentalwachsen (PDMS-basierenden Elastomeren, die in Zahnarztpraxen Verwendung finden und die deutlich schneller vernetzen als Sylgard 184) gelang die Herstellung von Säulen mit konkaver Geometrie (siehe Figure 3.5 für das Fabrikationsschema der Endkonturen). Die Herstellung hierarchischer Modellsysteme gelang durch zwei aufeinanderfolgende lithographische Belichtungsschritte an deren Ende beide Ebenen zusammen entwickelt wurden (siehe dazu Figure 3.4 in Kapitel 3).

Die Untersuchung der Adhäsionseigenschaften solch mikrostrukturierter PDMS-Oberflächen erfolgte mittels eines im Eigenbau entstandenen Adhäsionsmeßgerätes. Dieses beruht auf der Auslenkung eines Glascantilevers welche laseroptisch bestimmt wird. Durch eine präzise Kalibrierung der Federkonstante des Cantilevers konnte später auf die Kraft zurückgerechnet werden. An das Ende des Cantilevers wurde in den hier präsentierten Versuchen eine polierte Saphirkugel mit 5 mm Durchmesser angebracht. Um die Haftkräfte einer Probe zu bestimmen, wurde der gesamte Cantilever mittels eines Piezoaktuators in Richtung der durch einen Hexapod positionierten Probe bewegt. Die Saphirkugel wurde bis zu einer gewissen Vorlast in die Probe gedrückt und anschließend wieder von jener abgezogen. Hierbei sorgte die Adhäsion für eine gewisse Haftkraft (siehe Figure 4.2b in Kapitel 4 für eine typische Kraft-Abstands-Kurve). Die Messungen wurden bei Raumtemperatur und Luftfeuchtigkeiten um 20 % durchgeführt. In allen Versuchen wurde die Vorlast schrittweise erhöht.

10.3 Ergebnisse und Diskussion

Das erste wichtige Ergebnis der vorliegenden Arbeit ist, dass es gelang auf elegante Art und Weise Säulen mit dreidimensionalen Spitzengeometrien aus einfachen lithographischen Mastern herzustellen. Dazu wurden wie oben beschrieben die Viskositätseigenschaften von PDMS und PDMS-basierenden Elastomeren ausgenutzt. Die hier vorgestellten Geometrien sind die eines flachen Stempels, halbkugel-, spatel- und pilzförmig. Ebenso wurden konkave Säulen und flache Stempel mit abgerundeten Kanten, neben hierarchischen Modellsystemen, erzeugt.

Bei den Adhäsionsmessungen zeigte sich, dass die ermittelten Haftkräfte eine Funktion der Vorlast waren (siehe dazu z.B. Figure 4.3 in Kapitel 4). Mit steigender Vorlast, nahm die Haftkraft zuerst zu, um dann in einem Plateau zu saturieren. Beides konnte erfolgreich mit einem einfachen Federmodell (116) erklärt werden. In diesem Modell werden die einzelnen Säulen als rein elastische und voneinander unabhängig Federn angenähert. Sie stehen auf einer Seite in Kontakt mit einer Kugel und einer Ebene andererseits. Vereinfacht formuliert, nimmt die Haftkraft anfangs zu, da mit steigender Vorlast eine zunehmende Anzahl an Säulen (Federn) in Kontakt mit der Kugel kommt und somit auch mehr einzelne Kontakte zur Adhäsion beitragen. Steigt die Indentationstiefe weiter, sie ist über die Steifigkeit der Probe direkt mit der Vorlast verknüpft, kommt es im Moment des Kontaktabrisses aber zu einem Gleichgewicht zwischen Federn im Zentrum und am Rand des Kontaktes. Die Säulen im Zentrum befinden sich in Kompression und wirken der Adhäsion entgegen. Die Strukturen am Rand sind im Zug und sorgen für die eigentliche, aktuelle Haftkraft. Ist das Gleichgewicht zwischen beiden Beiträgen erreicht, erhöht eine größere Vorlast die Haftkraft nicht weiter. Dieses Modell beschreibt den experimentell gefundenen Verlauf der Haftkräfte über der Vorlast sehr zufriedenstellend, wenn auch für verschiedene Säulenradien unterschiedlich gut (siehe Figure 4.3 in

202

Kapitel 4). Diese Vorlastabhängigkeit spielt eine große Rolle beim Vergleich der Daten untereinander sowie mit in der Literatur veröffentlichten Ergebnissen. Im letztgenannten Fall wird nur sehr selten die gesamte Haftkraft-Vorlastkurve angegeben, bzw. erläutert bei welcher Vorlast die Haftkräfte ermittelt wurden. Dieser Umstand erschwert eine sinnvolle Interpretation der Literaturdaten häufig beträchtlich.

Durch die systematische Reduktion des Säulenradius von 25 über 10 und 5 auf 2.5 μm zeigte sich, dass die Haftkräfte mit kleiner werdendem Säulenradius zunehmen. Da die Absolutkräfte eine Funktion der Größe der für die Versuche verwendeten Saphirkugel waren, wurden die Kräfte durch die sog. projizierte Kontaktfläche – die maximale Kontaktfläche zwischen Probe und Kugel (siehe Figure 4.2a Kapitel 4) – normiert und dadurch die Kontaktfestigkeit ermittelt. Da die Kontaktfestigkeit unabhängig von der Größe der Saphirkugel ist, stellt diese Haftkraft pro Fläche das wohl beste Maß zum Vergleich des Adhäsionsverhaltens verschiedener Strukturen dar (siehe Figure 4.4 in Kapitel 4 für eine Auftragung der Haftfestigkeit gegen die Vorlast für Strukturen mit einem konstanten Aspektverhältnis von eins). Durch die doppelt-logarithmische Auftragung der Haftfestigkeit gegen den Säulenradius ergab sich die Effizienz der Kontaktaufspaltung. Diese wurde für stempelförmige Säulen mit -0.5 bestimmt. Somit bestätigte sich die theoretische Erwartung, die nach JKR ebenfalls diesen Wert vorsieht.

In weiteren Versuchen an ähnlichen Strukturen wurde der Säulenradius konstant gehalten (5 μm) und gleichzeitig das Aspektverhältnis von 0.5 über 1 und 2 auf 4 erhöht. Hierbei zeigte sich, dass die Haftkräfte und Festigkeiten mit steigendem Aspektverhältnis zunahmten. Dieses Verhalten könnte mit einer Theorie die ursprünglich für die Festigkeit von kautschuk-elastischen Materialien entwickelt (120) und später auf fibrilläre Adhäsive erweitert wurde (118, 119), erklärt werden (siehe dazu Figure 4.5 in Kapitel 4).

Um Einblick in die Frage zu erhalten, wie sehr die Spitzenkontur der Säulen die Hafteigenschaften der Adhäsive beeinflusst, wurden von allen sechs oben erwähnten Formen die Haftkräfte als Funktion der Vorlast bestimmt. Dabei zeigte sich, dass das Prinzip der Kontaktaufspaltung bei allen Formen, bis auf die Stempel mit abgerundeten Kanten und die konkaven Spitzen, Gültigkeit zu haben scheint. Bei den Stempeln mit abgerundeten Kanten, nimmt der flache gegenüber dem runden Anteil der Spitze mit kleiner werdendem Radius ab. Somit sank für den kleinsten der untersuchten Durchmesser (5 μm) die Haftkraft sogar unter die für den größten (50 μm). Die konkave Säulenform scheint invariant gegenüber einer Veränderung des Säulendurchmessers zu sein. Die Ergebnisse für diese und die anderen Konturen als Auftragungen der Kraft, bzw. der Festigkeit gegen die Vorlast sind in Figures 5.2 bzw. 5.5 in Kapitel 5 dargestellt. Trägt man wiederum die Haftfestigkeit bei einer konstanten Vorlast von einem Millinewton gegen den Säulen, bzw. Spitzenradius doppelt-logarithmisch auf, so ergibt sich der in Abbildung 10.1 gezeigte Graph.

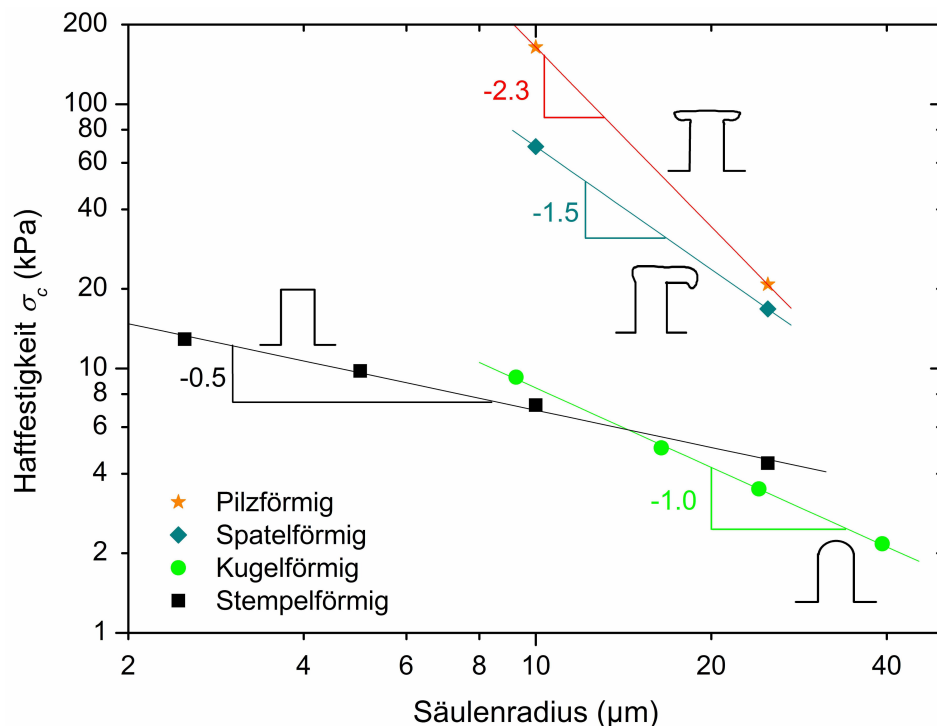


Abbildung 10.1: Abhängigkeit der Haftspannung vom Säulen bzw. Spitzenradius (für die hemisphärische Kontur) in einer doppelt-logarithmischen Auftragung. Gezeigt sind Daten für Säulen mit der Form eines flachen Stempels, Spitzen mit hemisphärischer, spatulärer und pilzförmiger Struktur. Die Vorlast ist konstant bei 1 mN und das Aspektverhältnis beträgt in allen Fällen 1.

Diese Abbildung illustriert das Prinzip der Kontaktaufspaltung: Die Haftspannung nimmt für kleiner werdende Strukturen jeweils zu. Für die Säulen mit hemisphärischer Endkontur ergibt sich eine Aufspaltungseffizienz von -1, was mit dem nach der JKR-Theorie zu erwarteten Wert übereinstimmt. Für die spatuläre und pilzförmige Spitzenform, existieren bislang noch keine theoretischen Vorhersagen für die Aufspaltungseffizienz. Es ist aber hervorzuheben, dass beide experimentell sehr hohe Werte erreichen, so dass sich eine weitere Miniaturisierung der Kontakte besonders anbietet, da sich die Haftfestigkeit dadurch nochmals deutlich erhöhen lassen sollte. Dies gilt im Besonderen für die pilzförmigen Strukturen, da diese Absolutwerte für die Haftfestigkeit von annähernd 200 kPa erreichen. Dies liegt im Bereich der Haftfestigkeiten einzelner Geckospatulae, die je nach Meßmethode zwischen 100 kPa (8) und 200 kPa (6) erreichen. Damit wäre es also für noch kleinere, aber im Mikrometerbereich befindliche, Strukturen möglich, die Hafteigenschaften des Geckos, zumindest was die Kräfte betrifft, zu übertreffen. Auch in der Literatur (39, 52) findet sich, dass die pilzförmigen Säulen an dieser Stelle besonders vielversprechend sind.

Um diese z.T. erstaunlich starke Abhängigkeit der Hafteigenschaften fibrillärer Systeme von einzelnen Variablen nicht nur experimentell zu untersuchen und den Prozeß der Material- und Parameterauswahl zu vereinfachen, wurden im Rahmen der vorliegenden Arbeit die für hemisphärische Kontakte bereits bekannten "Adhesion Design Maps" auf weitere Endkonturen ausgeweitet. Diese waren die des flachen Stempels, des Toruses und der eines bandförmigen Kontaktes (siehe Figure 6.1). Für letzteren wurden verschiedene Winkel zur Oberfläche untersucht, während für den flachen Stempel auch ein einfaches Rauheitsmodell angenommen wurde. Hierdurch sollten erste Hinweise auf den Einfluss der Oberflächenrauigkeit auf die Hafteigenschaften erhalten werden. Ein Vergleich zwischen den verschiedenen Endkonturen zeigte, dass für den Kontakt mit einer ideal

glatten Oberfläche, flache Stempel am stärksten haften, gefolgt, von toroidalen Spitzen und Halbkugeln, während das elastische Band die schwächste Adhäsion aufweist. Es ist aber hervorzuheben, dass auch für das Band Haftspannungen in der Größenordnung natürlicher Systeme gefunden wurden. Dadurch ist diese Kontur sehr vielversprechend, da sie stark haftet und durch ihre Asymmetrie gleichzeitig leicht abzulösen sein sollte. Für die „Adhesion Design Map“ für die flachen Stempel in Kontakt mit einer rauhen Oberfläche (Figure 6.5) ergab sich, dass die Haftspannung um einen Faktor von ungefähr 80.000 reduziert wurde. Dies verdeutlicht den starken Effekt selbst kleinster Rauigkeiten auf die Adhäsionseigenschaften und fügt sich sehr gut in das aus der Literatur bekannte Bild ein (137, 138, 140). Da in der Literatur drei verschiedene Modelle für die Berechnung des Kondensationslimits, also für die Vermeidung des Verklumpens der einzelnen Säulen zu größeren Bündeln, existieren, wurde alle drei Kriterien für die Rechnungen herangezogen und verglichen. Dabei zeigte sich, dass das Modell von Glassmaker *et al.* (44) für die Konstruktion der Maps am besten geeignet zu sein scheint.

Insgesamt konnte im Rahmen der vorliegenden Arbeit gezeigt werden, dass es möglich ist komplexe dreidimensionale Endkonturen für wohldefinierte Modellsysteme fibrillärer Adhäsive herzustellen. Diese Modellsysteme wurden anschließend auf ihre Hafteigenschaften hin untersucht und festgestellt, dass sich ein Aufspaltungs- und somit ein Größeneffekt einstellt. Die Haftkräfte nahmen mit kleiner werdendem Säulenradius zu. Höhere Aspektverhältnisse führten ebenso zu verbesserten Hafteigenschaften. Sowohl die experimentellen, als auch die theoretischen Untersuchungen zum Einfluss der Spitzenkontur der Säulen zeigten eine sehr starke Abhängigkeit der Hafteigenschaften von diesem Parameter. Insbesondere die pilzförmigen Säulen ergaben sehr hohe Absolutwerte der Haftfestigkeit. Diese lagen im Bereich der Geckoadhäsion. Gleichzeitig wiesen Säulen dieser Form die günstigste Effizienz für weiteres Aufspalten auf, so dass für kleinere

Strukturen noch deutlich höhere Kräfte zu erwarten sind. Mit den hier dargelegten experimentellen Erkenntnissen, insbesondere in Verbindung mit den Leitlinien für die Konstruktion fibrillärer Haftsysteme wie sie in den Designkarten vorgestellt wurden, sollte die vorliegende Arbeit einen wichtigen Beitrag zur zukünftigen, strategischen Entwicklung bio-inspirierter, fibrillärer Haftsysteme leisten.